

Jordan Journal of Mechanical and Industrial Engineering (JJMIE)

JJMIE is a high-quality scientific journal devoted to fields of Mechanical and Industrial Engineering. It is published by Hashemite University in cooperation with the Jordanian Scientific Research and Innovation Support Fund, Ministry of Higher Education and Scientific Research.

EDITORIAL BOARD

Editor-in-Chief

Prof. Moh'd Sami Ashhab

Assistant Editors

Dr. Ahmad AlMigdady

Dr. Mohannad Jreissat

Editorial Board

Prof. Tariq A. ALAzab

Al Balqa Applied University

Prof. Jamal Jaber

Al- Balqa Applied University

Prof. Mohamad Al-Widyan

Jordan University of Science and Technology

Prof. Mohammed Taiseer Hayajneh

Jordan University of Science and Technology

Prof. Mohammad Al-Tahat

The University of Jordan

Dr. Ali M. Jawarneh

The Hashemite University

THE INTERNATIONAL ADVISORY BOARD

Abu-Qudais, Mohammad

Jordan University of Science & Technology, Jordan

Tzou, Gow-Yi

Yung-Ta Institute of Technology and Commerce, Taiwan

Abu-Mulaweh, Hosni

Purdue University at Fort Wayne, USA

Jubran, Bassam

Ryerson University, Canada

Afaneh Abdul-Hafiz

Robert Bosch Corporation, USA

Kakac, Sadik

University of Miami, USA

Afonso, Maria Dina

Institute Superior Tecnico, Portugal

Khalil, Essam-Eddin

Cairo University, Egypt

Badiru, Adedji B.

The University of Tennessee, USA

Mutoh, Yoshiharu

Nagaoka University of Technology, Japan

Bejan, Adrian

Duke University, USA

Pant, Durbin

Iowa State University, USA

Chalhoub, Nabil G.

Wayne State University, USA

Riffat, Saffa

The University of Nottingham, U. K

Cho, Kyu-Kab

Pusan National University, South Korea

Saghir, Ziad

Ryerson University, Canada

Dincer, Ibrahim

University of Ontario Institute of Technology,
Canada

Sarkar, MD. Abdur Rashid

Bangladesh University of Engineering &
Technology, Bangladesh

Douglas, Roy

Queen's University, U. K

Siginer, Dennis

Wichita State University, USA

El Bassam, Nasir

International Research Center for Renewable
Energy, Germany

Sopian, Kamaruzzaman

University Kebangsaan Malaysia, Malaysia

Haik, Yousef

United Arab Emirates University, UAE

EDITORIAL BOARD SUPPORT TEAM

Language Editor

Dr. Baker M. Bani-khair

Publishing Layout

Eng. Ali Abu Salimeh

SUBMISSION ADDRESS:

Prof. Moh'd Sami Ashhab, Editor-in-Chief
Jordan Journal of Mechanical & Industrial Engineering,
Hashemite University,
PO Box 330127, Zarqa, 13133, Jordan
E-mail: jjmie@hu.edu.jo



Hashemite Kingdom of Jordan



Hashemite University

Jordan Journal of
Mechanical and Industrial Engineering

JJMIE

An International Peer-Reviewed Scientific Journal

Financed by Scientific Research Support Fund

Volume 14, Number 1, March 2020

Special Issue: Instrumentation & Measurements in Engineering

<http://jjmie.hu.edu.jo/>

ISSN 1995-6665

Jordan Journal of Mechanical and Industrial Engineering (JJMIE)

JJMIE is a high-quality scientific journal devoted to fields of Mechanical and Industrial Engineering. It is published by Hashemite University in cooperation with the Jordanian Scientific Research and Innovation Support Fund, Ministry of Higher Education and Scientific Research.

Introduction: The Editorial Board is very committed to build the Journal as one of the leading international journals in mechanical and industrial engineering sciences in the next few years. With the support of the Ministry of Higher Education and Scientific Research and Jordanian Universities, it is expected that a heavy resource to be channeled into the Journal to establish its international reputation. The Journal's reputation will be enhanced from arrangements with several organizers of international conferences in publishing selected best papers of the conference proceedings.

Aims and Scope: *Jordan Journal of Mechanical and Industrial Engineering* (JJMIE) is a refereed international journal to be of interest and use to all those concerned with research in various fields of, or closely related to, mechanical and industrial engineering disciplines. *Jordan Journal of Mechanical and Industrial Engineering* aims to provide a highly readable and valuable addition to the literature which will serve as an indispensable reference tool for years to come. The coverage of the journal includes all new theoretical and experimental findings in the fields of mechanical and industrial engineering or any closely related fields (Materials, Manufacturing, Management, Design, Thermal, Fluid, Energy, Control, Mechatronics, and Biomedical). The journal also encourages the submission of critical review articles covering advances in recent research of such fields as well as technical notes.

Guide for Authors

Manuscript Submission:

High-quality submissions to this new journal are welcome now and manuscripts may be either submitted online or email.

Online: For online and email submission upload one copy of the full paper including graphics and all figures at the online, submission site, accessed via <http://jjmie.hu.edu.jo>. The manuscript must be written in MS Word Format. All correspondence including notification of the Editor's decision and requests for revision, takes place by e-mail and via the Author's homepage, removing the need for a hard-copy paper trail

Submission address and contact :

Prof. Moh'd Sami Ashhab

Editor-in-Chief

Jordan Journal of Mechanical & Industrial

Engineering, Hashemite University

PO Box 330127, Zarqa, 13115, Jordan

E-mail: jjmie@hu.edu.jo

Types of contributions: Original research papers and Technical reports

Corresponding author: Clearly indicate who is responsible for correspondence at all stages of refereeing and publication, including post-publication. Ensure that telephone and fax numbers (with country and area code) are provided in addition to the e-mail address and the complete postal address. Full postal addresses must be given for all co-authors.

Original material: Submission of an article implies that the work described has not been published previously (except in the form of itstan abstract or as part of a published lecture or academic thesis), that it is not under consideration for publication elsewhere, the publication is approved by all authors and that, if accepted, it will not be published elsewhere in the same form, in English or in any other language, without the written consent of the Publisher. Authors found to be deliberately contravening the submission guidelines on originality and exclusivity shall not be considered for future publication in this journal.

Withdrawing: If the author chooses to withdraw his article after it has been assessed, he shall reimburse JJMIE with the cost of reviewing the paper.

Manuscript Preparation:

General: Editors reserve the right to adjust style to certain standards of uniformity. Original manuscripts are discarded after publication unless the Publisher is asked to return original material after use. Please use MS Word for the text of your manuscript

Structure: Follow this order when typing manuscripts: Title, Authors, Authors title, Affiliations, Abstract, Keywords, Introduction, Main text, Conclusions, Acknowledgements, Appendix, References, Figure Captions, Figures and then Tables. Please supply figures imported into the text AND also separately as original graphics files. Collate acknowledgements in a separate section at the end of the article and do not include them on the title page, as a footnote to the title or otherwise.

Text Layout: Use 1.5 line spacing and wide (3 cm) margins. Ensure that each new paragraph is clearly indicated. Present tables and figure legends on separate pages at the end of the manuscript. If possible, consult a recent issue of the journal to become familiar with layout and conventions. All footnotes (except for table and corresponding author footnotes) should be identified with superscript Arabic numbers. To conserve space, authors are requested to mark the less important parts of the paper (such as records of experimental results) for printing in smaller type. For long papers (more than 4000 words) sections which could be deleted without destroying either the sense or the continuity of the paper should be indicated as a guide for the editor. Nomenclature should conform to that most frequently used in the scientific field concerned. Number all pages consecutively; use 12 or 10 pt font size and standard fonts.

Corresponding author: Clearly indicate who is responsible for correspondence at all stages of refereeing and publication, including post-publication. The corresponding author should be identified with an asterisk and footnote. Ensure that telephone and fax numbers (with country and area code) are provided in addition to the e-mail address and the complete postal address. Full postal addresses must be given for all co-authors. Please consult a recent journal paper for style if possible.

Abstract: A self-contained abstract outlining in a single paragraph the aims, scope and conclusions of the paper must be supplied.

Keywords: Immediately after the abstract, provide a maximum of six keywords (avoid, for example, 'and', 'of'). Be sparing with abbreviations: only abbreviations firmly established in the field may be eligible.

Symbols: All Greek letters and unusual symbols should be identified by name in the margin, the first time they are used.

Units: Follow internationally accepted rules and conventions: use the international system of units (SI). If other quantities are mentioned, give their equivalent quantities in SI

Maths: Number consecutively any equations that have to be displayed separately from the text (if referred to explicitly in the text).

References: All publications cited in the text should be presented in a list of references following the text of the manuscript.

Text: Indicate references by number(s) in square brackets in line with the text. The actual authors can be referred to, but the reference number(s) must always be given.

List: Number the references (numbers in square brackets) in the list in the order in which they appear in the text.

Examples:

Reference to a journal publication:

[1] M.S. Mohsen, B.A. Akash, "Evaluation of domestic solar water heating system in Jordan using analytic hierarchy process". Energy Conversion & Management, Vol. 38 (1997) No. 9, 1815-1822.

Reference to a book:

[2] Strunk Jr W, White EB. The elements of style. 3rd ed. New York: Macmillan; 1979.

Reference to a conference proceeding:

[3] B. Akash, S. Odeh, S. Nijmeh, "Modeling of solar-assisted double-tube evaporator heat pump system under local climate conditions". 5th Jordanian International Mechanical Engineering Conference, Amman, Jordan, 2004.

Reference to a chapter in an edited book:

[4] Mettam GR, Adams LB. How to prepare an electronic version of your article. In: Jones BS, Smith RZ, editors. Introduction to the electronic age, New York: E-Publishing Inc; 1999, p. 281-304

Free Online Color : If, together with your accepted article, you submit usable color and black/white figures then the journal will ensure that these figures will appear in color on the journal website electronic version.

Tables: Tables should be numbered consecutively and given suitable captions and each table should begin on a new page. No vertical rules should be used. Tables should not unnecessarily duplicate results presented elsewhere in the manuscript (for example, in graphs). Footnotes to tables should be typed below the table and should be referred to by superscript lowercase letters.

Notification: Authors will be notified of the acceptance of their paper by the editor. The Publisher will also send a notification of receipt of the paper in production.

Copyright: All authors must sign the Transfer of Copyright agreement before the article can be published. This transfer agreement enables Jordan Journal of Mechanical and Industrial Engineering to protect the copyrighted material for the authors, but does not relinquish the authors' proprietary rights. The copyright transfer covers the exclusive rights to reproduce and distribute the article, including reprints, photographic reproductions, microfilm or any other reproductions of similar nature and translations.

Proof Reading: One set of page proofs in MS Word format will be sent by e-mail to the corresponding author, to be checked for typesetting/editing. The corrections should be returned within 48 hours. No changes in, or additions to, the accepted (and subsequently edited) manuscript will be allowed at this stage. Proofreading is solely the author's responsibility. Any queries should be answered in full. Please correct factual errors only, or errors introduced by typesetting. Please note that once your paper has been proofed we publish the identical paper online as in print.

PAGES	PAPERS
1-6	Optimization Design and Analysis of Rotary Indexing Mechanism of Tool Magazine in Machining Center <i>Jun Zhang, Shuli Sun, Hoang Anh Tuan</i>
7-14	Online Monitoring and Early Warning Technology of Repeated Multiple Blackouts in Distribution Network Based on Multi-source Information Fusion and Delphi Method <i>Wensi Cao, Mingming Xu, Rongze Niu, Qing Wu, Ruirui Xie</i>
15-24	Contact Mechanics Analysis and Optimization of Shape Modification of Electric Vehicle Gearbox <i>Qingyong Zhang, Yaru Wang, Weiping Lin, Yongjun Luo, Xingjian Wu</i>
25-36	Design of Digital Aerial Photography System for Unmanned Aerial Vehicle Based on Wireless Sensor Network <i>Rui Wang, Nian-chu Wu, Xin-li Yu</i>
37-41	The Application of Closed Hydraulic System of Hoisting Mechanism in Auto Crane <i>Duwei Nie, Changxing Fu</i>
43-52	Monitoring Algorithm for Speed Information of Autonomous Vehicles Based on Magneto-resistive Sensor <i>Yu Tang</i>
53-60	An Adaptive Scheduling Method for Resources in Used Automobile Parts Recycling <i>Pengfei Ning</i>
61-70	Intelligent Remote Monitoring System for Minor Faults of Intelligent Unmanned Vehicle <i>Jia Tao, Yuchen Jia, Yuan Gao</i>
71-79	Review Study of Physical and Mechanical Characteristics on Mixed Soil with Scrap Tire Rubber Particles <i>Jianguang Bai, Yan Zhang, Shuzheng Wu</i>
81-88	Design of Intelligent Obstacle Avoidance System for Fully Automated Unmanned Vehicle Based on Laser Ranging <i>Chunyu Li</i>
89-99	Distributed Multi-level Inventory Algorithms for Automotive Maintenance Spare Parts Based on Centralized Control Model <i>Jiangang Li</i>
101-108	Design of Path Tracking Control System for UAV Based on Adaptive Preview Method <i>Yiping Li</i>
109-117	Optimization of Clutchless AMT Shift Control Strategy for Electric Vehicles <i>Jingpu Li, Pengcheng Sheng, Kaikai Shao</i>
119-128	Deep Drainage Detection System for Inland Vessels Based on Machine Vision <i>Hechuang Wang</i>

- 129-137** **Regional Coordination Control Method of Rail Transit Signal Based on Unmanned Driver**
Yongcheng Wu, Changqiong Yang, Lanlan Huangfu
- 139-147** **Unmanned Vehicle Route Tracking Method Based on Video Image Processing**
Yiyi Zhu, Na Guo
- 149-158** **Acceleration Sensor Abnormality Detection Method for Axle Box of Unmanned Vehicle**
Jianhu Gong
- 159-165** **Driving Pattern Recognition of Hybrid Electric Vehicles Based on Multi-hierarchical Fuzzy Comprehensive Evaluation**
Qingyong Zhang, Zhenfei Lu, Yaru Wang, Weiping Lin
- 167-173** **Vibration Fatigue Analysis and Optimization Design of a Light-truck Urea Box Bracket**
Zhenqi Yu, Huifang Jia, Xingyuan Huang
- 175-182** **Application of Improved Particle Swarm Optimization in Gear Fault Diagnosis of Automobile Transmission**
Aibing Wang, Jianwei Liang, Yapeng Liu
-

Optimization Design and Analysis of Rotary Indexing Mechanism of Tool Magazine in Machining Center

Jun Zhang^{a*}, Shuli Sun^a, Hoang Anh Tuan^b

^aSchool of Engineering, Zhejiang University City College, Hangzhou 310015, China

^bDepartment of Science and Technology, Ho Chi Minh city University of Transport, Vietnam

Received OCT 16 2019

Accepted JAN 10 2020

Abstract

In order to achieve a faster rotation speed and lower impact load of the machining center armless type tool magazine during the rotary indexing process, the rotation and positioning characteristics of the rotary indexing mechanism were studied. The structural design of the Geneva mechanism used to drive the tool magazine was completed, and the optimized design scheme of the new double-pins without the locking arc Geneva mechanism to replace the single-pin locking arc Geneva mechanism was finally determined. The two schemes were modeled and compared by kinematics based on NX and ADAMS. The results of kinematics contrast simulation show that the double-pins Geneva mechanism structure without locking arc has the advantages of being faster in rotational speed, smaller in impact load and more stable running condition, so that the speed of machine tool change while greatly reducing device wear and improve the durability of the device.

© 2020 Jordan Journal of Mechanical and Industrial Engineering. All rights reserved

Keywords: Geneva mechanism, optimization design, tool magazine, machining center.

1. Introduction

CNC machining center is the mainstream and popular equipment of the current manufacturing industry [1, 2]. Its biggest feature is the tool storage and automatic tool change function, which is mainly realized by the tool magazine and automatic tool changer [3, 4]. At present, the operating efficiency and reliability of the tool magazine components have become an important factor restricting the operation efficiency and reliability of CNC machine tools. Although domestic and international research has been done to improve the tool change speed and tool change stability [5-12], but there is still a lot of improvement. Therefore, it is necessary to study the rotation and positioning characteristics of the tool magazine drive mechanism to achieve a faster rotation speed and a lower impact load during the tool change process.

In this study, the 16T armless type rotary indexing mechanism was taken as the research object. Firstly, the initial scheme of the rotary indexing mechanism was designed. Then, through the optimization design calculation of the mechanism, the final rotary indexing mechanism was determined to be a double-pin without

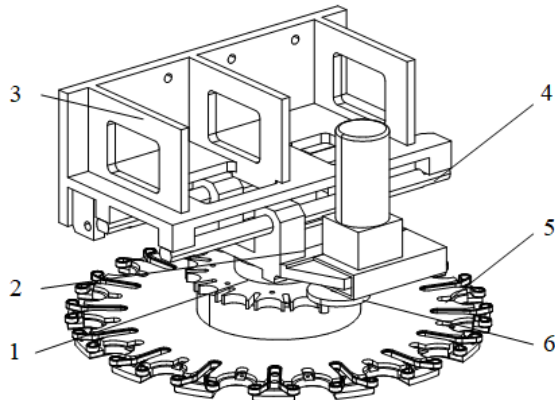
locking arc, which is a brand-new tool magazine drive mechanism, which increases the rotation speed while reducing the impact load, reduces the tool magazine wear, and improves the tool magazine durability. Based on NX and ADAMS software, the 3D modeling and kinematics comparison analysis of the pre-optimized and optimized mechanisms were carried out, and the rotation and positioning characteristics of the mechanism were obtained. From the comparison of the kinematics simulation results, the rotational speed of the optimized structure was doubled compared with the old structure, and the impact load was greatly reduced. Consequently, the wear of the tool magazine was reduced, and the durability of the tool magazine was improved.

2. Methodology of design and optimization for rotary indexing mechanism

2.1. Analysis of tool change process in tool magazine

The main part of the armless type tool magazine is mainly composed of the base body, the connecting seat, the sliding rail, the indexing plate, the tool magazine plate and the driver plate pins. The main part of the armless type tool magazine is shown in Figure 1.

* Corresponding author e-mail: zucczj@163.com.



1. Indexing plate 2. Connecting seat 3. Base body
4. Sliding rail 5. Tool magazine plate 6. Driver plate & pin

Figure 1: Armless type tool magazine main part structure diagram

The following is a simple analysis of the tool change action of the armless type tool magazine.

1. The spindle moves to the tool change position;
2. The spindle is stopped;
3. The tool magazine moves to the tool change position (grabbing the old tool);
4. The spindle releases the old tool;
5. The spindle moves upwards (let the tool magazine rotate the positioning space);
6. The tool magazine is rotated and positioned to the new tool position;
7. The spindle moves downward (moving to the tool change position);
8. The spindle grasps the new tool;
9. The tool magazine is retracted to the initial position (end tool change).

During this entire tool change process, the forward and backward movement of the tool magazine is completed by the cylinder drive. This action can already achieve a faster speed. Therefore, the efficiency of the entire tool change process is mainly determined by the speed of the indexing plate rotation and positioning. It is necessary to select a more suitable rotational positioning scheme to increase the indexing plate rotation speed while ensuring a smooth rotation process and to reduce impact during positioning and startup

2.2. Determination of the rotary indexing mechanism

The rotary indexing mechanism is mainly used to realize the indexing and turning motion of the tool magazine, so it is very important to ensure the speed and reliability of the tool magazine. At present, most of the armless type tool magazines use the single-head double-lead worm gear mechanism, the double-lead cylindrical cam mechanism and the Geneva mechanism to realize the rotary indexing of the tool magazine. Among them, the single-head double-lead worm gear mechanism can adjust the transmission gap of the worm and worm at any time to achieve accurate indexing index, but the structure of the transmission mechanism is complicated and difficult to process. The double-lead cylindrical cam mechanism has strong bearing capacity and stable indexing, and is suitable for a mechanism with a large load, but at the same time, its disadvantage is that the structure is complicated and the

processing cost is high [13]. The Geneva mechanism has high rotational efficiency, small impact load, stable operation, simple structure and easy manufacture [14]. Therefore, the rotary indexing mechanism of the tool magazine is realized by the Geneva mechanism.

The Geneva mechanism is a mechanism that can convert the continuous rotation of the active part into a periodic intermittent motion of the driven part, and is commonly used in various rotary indexing mechanisms. The Geneva mechanism can be classified into external meshing, internal meshing and spherical Geneva mechanism according to different meshing modes. The armless type tool magazine adopts an external meshing Geneva mechanism to realize the rotary indexing action. The active part of the external meshing Geneva mechanism is the driver plate and the pin, and the driven part is the indexing plate. The working principle is as follows: the active part performs a continuous rotary motion at a constant angular velocity, and the driven part performs a periodic intermittent rotary motion. When the pin does not enter the indexing plate, the locking limit action is completed by the concave locking arc of the indexing plate and the convex locking arc of the driver plate. After the pin enters the indexing plate, the lock arc is released and the driver plate drives the indexing plate to rotate. In this way, a one-way intermittent rotational motion is outputted in a loop.

2.3. Calculation of the parameters of the Geneva mechanism

Different slot number can result in different angular velocity and angular acceleration changes: the less the slot, the greater the change in angular acceleration and the greater the impact and wear. Therefore, the number of slots of the external meshing Geneva mechanism for the tool magazine should not be less than 8. The known research object is a 16T armless type tool magazine, so the number of slots is set to 16. According to the working requirements of the tool magazine, the number of driver plate pin is initially selected as 1.

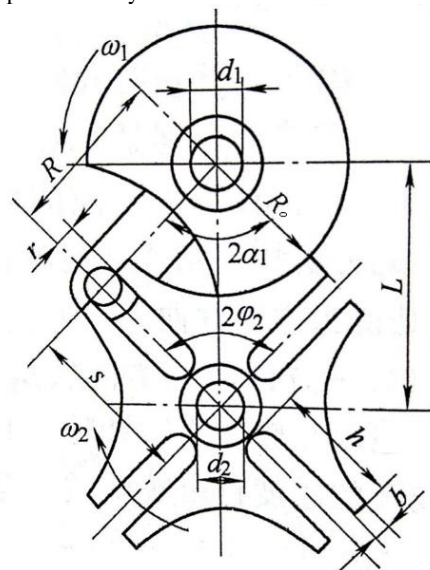


Figure 2: External meshing Geneva mechanism size parameter

The size parameters of the external meshing Geneva mechanism are shown in Figure 2. Specific values can be obtained by the following design calculations:

Center distance: The value of the center distance is determined by the size of the machine space and the form of the tool magazine structure. The larger center distance makes the indexing plate indexing process more stable, but at the same time, the quality of the indexing plate is increased, and the motor driving power is synchronously improved. The smaller center distance can cause the impact at the meshing of the mechanism to become larger. Taking into account the above factors, the value is determined as: $L = 150\text{mm}$

$$\text{Indexing plate movement angle: } 2\varphi_2 = 2\pi / Z = 22.5^\circ \quad (1)$$

$$\text{Driver plate movement angle: } 2\alpha_1 = \pi - 2\varphi_2 = 157.5^\circ \quad (2)$$

$$\text{Pin center track radius: } R = L \times \sin \varphi_2 \approx 30\text{mm} \quad (3)$$

$$\text{Pin radius: } r \geq R/6 = 5\text{mm} \quad (4)$$

$$\text{Slot top radius: } s = \sqrt{r^2 + (L \cos \varphi_2)^2} \approx 147\text{mm} \quad (5)$$

$$\text{Slot top sidewall thickness: } b = 3 \sim 5\text{mm} \quad (7)$$

Slot depth:

$$h = [s - (L - R - r)] + (3 \sim 5\text{mm}) = 35\text{mm} \quad (8)$$

$$\text{Radius of locking arc: } R_0 = R - r - b = 20\text{mm} \quad (9)$$

$$\text{Motion coefficient: } \tau = 2\alpha_1/2\pi = (Z - 2)/2Z = 0.4372 \quad (10)$$

The geometric parameters of the Geneva mechanism are listed in Table 1:

Table 1: Geneva mechanism geometric parameters

Parameters	Value
Number of slots/Z	16
Number of pins/n	1
Center distance/L	150 mm
Indexing plate movement angle/ $2\varphi_2$	22.5°
Driver plate movement angle/ $2\alpha_1$	157.5°
Pin center track radius/R	30 mm
Pin radius/r	5 mm
Slot top radius/s	147 mm
Slot top sidewall thickness/b	5 mm
Slot depth/h	35 mm
Motion coefficient/ τ	0.4372
Locking arc radius/ R_0	20 mm

2.4. Parametric modeling of Geneva mechanism based on NX

NX is an interactive CAD/CAE/CAM software system that is powerful enough to easily construct a variety of complex parametric entities and models, as well as kinematics and dynamics simulation of related models [15]. It has been widely used by multidisciplinary researchers.

The modelling dimensions of the Geneva mechanism are determined by the above parameters, the 2D drawing is drawn first, and the 3D model is finally completed by NX. The 3D model of the Geneva mechanism is shown in Figure 3.

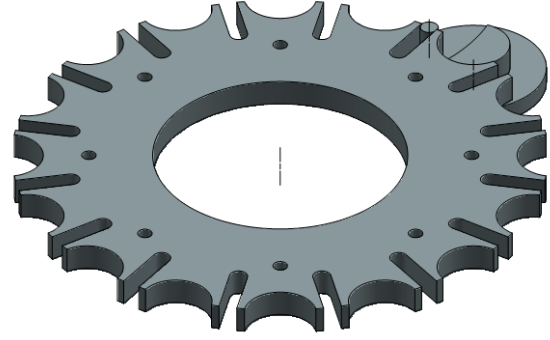


Figure 3: 3D model of Geneva mechanism

2.5. Optimization design of the Geneva mechanism

In order to achieve a higher rotational speed and stability of the tool magazine, the Geneva mechanism is optimized by the following two steps.

2.5.1. Increase rotation speed

It is known that the number of the driver plate pins of the Geneva mechanism is 1 ($n = 1$), and the number of slots is 16 ($Z = 16$), that is, the driver plate is rotated for one week, and the indexing plate is rotated by 22.5 degrees, thereby realizing the rotary indexing operation of the tool magazine. At the same time, when $n = 1$, its motion coefficient $\tau = 0.4372 < 0.5$, that is, the indexing plate movement time is less than the stop time, and the motion efficiency is low. In order to increase the rotational speed of the indexing plate and increase the coefficient of motion without increasing the rotational speed of the driver plate, it is necessary to increase the number of pins of the driver plate.

When the number of slots of the external meshing Geneva mechanism is greater than or equal to 6, the number of pins cannot be greater than 2, so the numbers of pins are 2 ($n = 2$). In this way, without increasing the driver plate rotation speed, the rotation speed of the indexing plate is doubled, the motion coefficient is also doubled, and the movement time is greater than the stop time.

However, the increase in the number of pins of the Geneva mechanism causes the central angle of the locking arc to become smaller, and its value is calculated by the following formula (11):

$$\gamma = 2\pi / n - 2\alpha_1 = 180^\circ - 157.5^\circ = 22.5^\circ \quad (11)$$

In the formula (11): n is the number of pin, and $2\alpha_1$ is the driver plate movement angle.

Figure 4 is a comparison diagram of the structure of the Geneva mechanism in the case where the number of round pins is equal to 1 (Figure 4a) and equal to 2 (Figure 4b). The double pins in Figure 4b double the rotational speed, but because there is still a locking arc in the structure, it still needs to complete the typical intermittent movement. During the positioning process, a large impact load is generated when the pin enters the slot every time, and it can be seen from the figure that the locking arc of the double-pins mechanism becomes very small only 22.5 degrees. This results in a locking arc that is prone to wear and its durability is greatly reduced. Therefore, it is necessary to further optimize the design.

2.5.2. Improve stability

In order to improve the stability of the rotary indexing movement of the tool magazine, we have determined the following improvement requirements: avoiding the rigid impact during the operation of the mechanism and reducing the wear during the operation of the mechanism to obtain a precise positioning position. According to the above design requirements, the double pins structure is still adopted, and the parameters, such as the center distance, the indexing plate movement angle, the driver plate movement angle, the pin center track radius, the pin radius, and the slot depth are unchanged. An optimized double-pins Geneva mechanism without locking arc was redesigned as shown in Figure 5 below.

As can be seen from the above Figure 5, the optimized slot top radius ($s1$) is larger than the initial slot top radius (s). It can be seen from the above Figure 5 that the value of $s1$ is calculated by the formula (12):

$$s1 = \sqrt{L^2 + (R - r)^2} \approx 152mm \quad (12)$$

In the formula (12): L is the center distance, R is the pin center track radius, and r is the pin radius.

It can be seen from Figure 5 that a transitional arc is newly designed between the initial slot top circle and the optimized slot top circle. When the pin 1 is disengaged from the slot along the transitional arc, the pin 2 just enters the transitional arc of the slot. The transitional arc acts as a lock and positioning. At the moment of Figure 4, the Geneva mechanism is in a stationary state. When the Geneva mechanism is in this state, the line between the centers of the two pins and the line between the center of the indexing plate and the center of the driver plate are perpendicular to each other, that is, the instantaneous angular velocity of the rotation of the indexing plate is 0 ($\omega = 0$), thereby avoiding the rigidity of the mechanism. At the same time, the optimization mechanism cancels the original small locking arc design, which reduces the wear during operation and improves the durability of the mechanism, thus achieving the optimal design requirements.

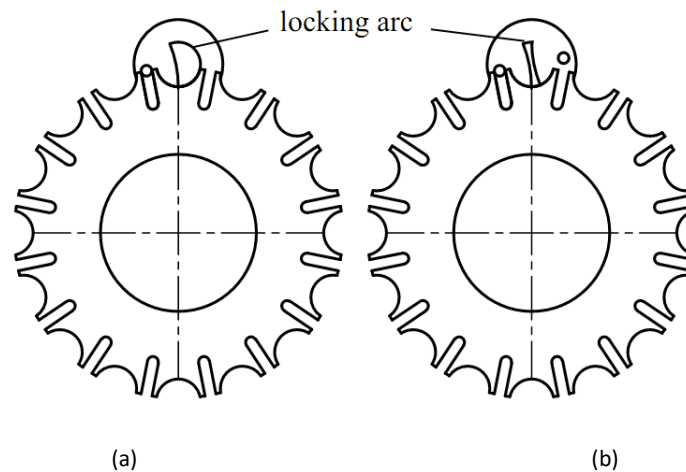


Figure 4: Different number of pins comparison chart

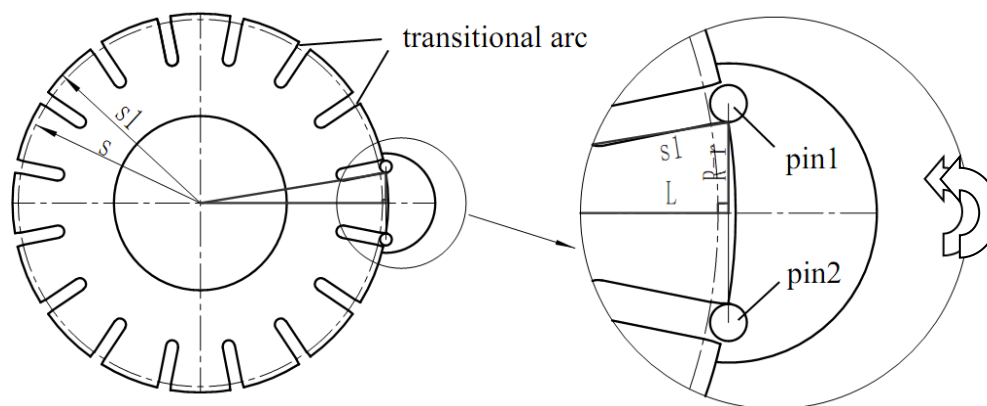
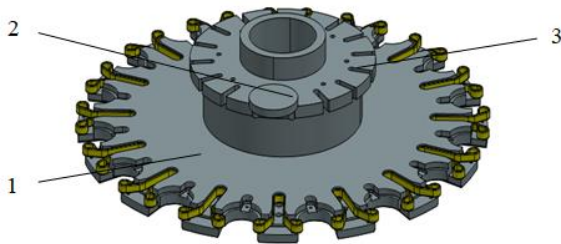


Figure 5: Optimized Geneva mechanism 2D drawing

3. Comparative analysis of kinematics for rotary indexing mechanism

3.1. Parametric modeling of rotary indexing mechanism based on NX

The optimized Geneva mechanism model and other parts models of the tool magazine are built in NX 3D modeling software. These parts are assembled together as required, and finally assembly model of the rotary indexing mechanism of the tool magazine as shown in Figure 6.



1. Tool magazine plate 2. Driver plate & pin 3. Indexing plate

Figure 6: Assembly model of rotary indexing mechanism

3.2. Comparative analysis of mechanism kinematics based on ADAMS

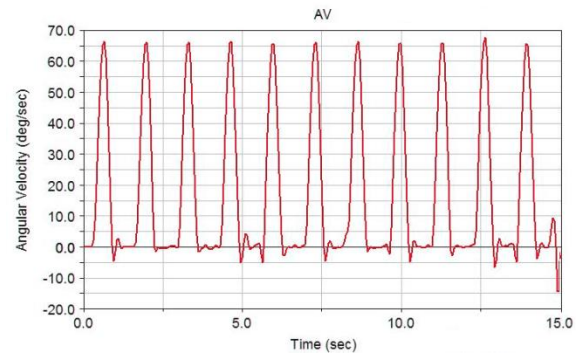
In order to verify the optimization effect of the new Geneva mechanism, the ADAMS software was used to compare the kinematics of the old and new Geneva mechanisms.

The first step is to simplify the tool magazine assembly model in the NX software, remove excess parts, and finally retain only the necessary components such as indexing plate, driver plate and pins. Export the Parasolid format (.x_t format file) and import it into the ADAMS software. Set the unit to MMKS, add the gravitational acceleration and material properties, and finally complete the pre-processing.

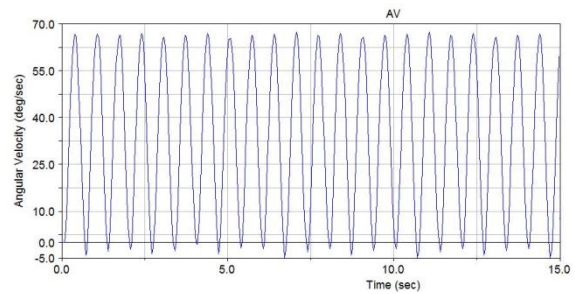
The second step is to constrain the indexing plate and the ground through the revolute joint in the ADAMS software. The driver plate and the ground are constrained by the revolute joint. The pin and the driver plate are constrained by the revolute joint. The driver plate and the indexing plate, the pin and the indexing plate are constrained by the contact joint. The specific parameters of the contact joint are set as follows: the stiffness is $10e6$, the force exponent is 1.5, the damping is 10, the penetration depth is 0.01, and the static friction factor is 0.1, the dynamic friction factor is 0.08. A rotational drive with a rotational speed of 45r/min was applied to the driver plate, and finally the simulation model was constructed.

4. Results and discussion

The new and old simulation models are submitted to the solution, and the angular velocity and angular acceleration curves of the indexing plates in the old and new mechanisms are plotted in the post-processing section. The results are shown in Figure 7 and Figure 8.

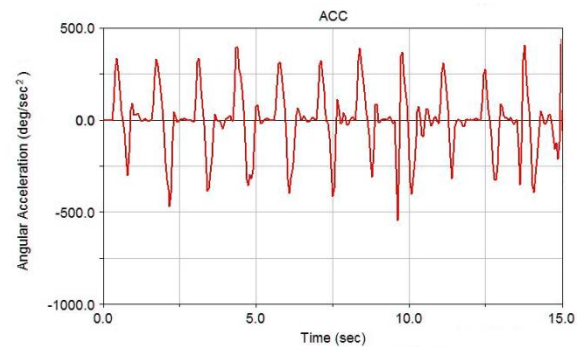


(a)

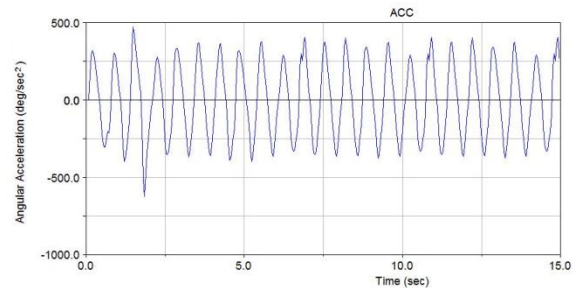


(b)

Figure 7: AV-Curve comparison chart of old & new mechanisms



(a)



(b)

Figure 8: ACC-Curve comparison chart of old & new mechanisms

In Figure 7, the red curve is the angular velocity curve of the old mechanism indexing plate in [16], and the blue curve is the angular velocity curve of the new mechanism indexing plate. In Figure 8, the red curve is the angular acceleration curve of the old mechanism indexing plate in [16], and the blue curve is the angular acceleration curve of the new mechanism indexing plate.

After comprehensively comparing and analyzing the curves of Figure 7 and Figure 8, the following conclusions can be drawn:

1. In the same 10 seconds, when the new mechanism turned 15 indexing stations, the old mechanism only turned 7.5 indexing stations, so the new mechanism's rotation speed doubled.
2. In both the old and the new mechanisms, the angular velocity and angular acceleration of the indexing disc are constantly changing. The angular velocity is maximized when the center of the indexing plate, the driving plate and the pin are collinear. The angular acceleration is exactly zero when the angular velocity is maximum.
3. The old mechanism indexing plate has a period in which the angular velocity is equal to 0 in the cycle, so that an impact phenomenon occurs during acceleration. The angular velocity of the indexing plate of the new mechanism is not in the state of 0 for a long time, and it is not necessary to repeatedly overcome the static inertia, so the impact load is greatly reduced, the wear is reduced and the durability is improved.

In summary, the optimized new Geneva mechanism doubles in rotational speed and is approximately in continuous motion. The reduction in the angular velocity variation causes the mechanism to not repeatedly overcome the static inertia. At the same time, because of the existence of a transition arc, the impact and vibration are also smaller than the old mechanism. These have proven that the optimized new Geneva mechanism can completely replace the old Geneva mechanism.

5. Conclusion

In this study, the rotary indexing mechanism of the tool magazine was designed and optimized. The newly designed double-pins without locking arc Geneva mechanism has been proved by motion simulation to prove that it can completely replace the old single-pin Geneva mechanism with locking arc. At the same time, the simulation analysis results show that the new mechanism rotation speed is doubled and the impact load is greatly reduced, which provides an important reference for subsequent research.

In the next stage, this study will test the movement of the new mechanism under actual conditions to further verify the angular velocity and angular acceleration of the mechanism. The research on the influence of the manufacturing process on the running state of the Geneva mechanism is completed to achieve a more optimized design of the rotary indexing mechanism.

Acknowledgements

This work was financially supported by Zhejiang Province Laboratory Work Research Project for University (YB201827), Zhejiang Province Education Science

Planning Research Project for University (2019SCG196), and Department of Education of Zhejiang Province Research Project (Y201839021).

References

- [1] Barbosa, M., Silva, F.J.G., Pimentel, C., Gouveia, R.M. A novel concept of CNC machining center automatic feeder, *Procedia Manufacturing*, 2018, 17: 952-959.
- [2] Usop, Z., Sarhan, A.A.D., Mardi, N.A., Wahab, M.N.A. Measuring of positioning, circularity and static errors of a CNC Vertical Machining Centre for validating the machining accuracy, *Measurement*, 2015, 61: 39-50.
- [3] Sardhara, T., Tamboli, K. Design and development of automatic lubrication system for ATC of CNC, *Materials Today: Proceedings*, 2018, 5(2): 3959-3964.
- [4] Dereli, T., Filiz, I.H. Allocating optimal index positions on tool magazines using genetic algorithms, *Robotics and Autonomous Systems*, 2000, 33(2): 155-167.
- [5] Lee, J.J., Jan, B.H. Design of Geneva mechanisms with curved slots for non-undercutting manufacturing, *Mechanism and Machine Theory*, 2009, 44(6): 1192-1200.
- [6] Zhang, Y.M., Ji, S.T., Zhao, J. Study on the geometric characteristics of mating surfaces of globoidal cam mechanisms, *Mechanism and Machine Theory*, 2016, 100: 44-62.
- [7] Hsieh, J.F. Design and analysis of indexing cam mechanism with parallel axes, *Mechanism and Machine Theory*, 2014, 81: 155-165.
- [8] Ji, S.T., Zhao, J., Zhang, Y.M. An application of geodesics to the calculation of the rib-thickness of globoidal cam mechanisms, *Mechanism and Machine Theory*, 2015, 87: 163-176.
- [9] Li, G.M., Tao, W.J., Feng, H.T. Development status and key technologies of automatic tool changer, *Machine Tool & Hydraulics*, 2013,41(05):174-176.
- [10] Hsieh, J. Design and machining of cylindrical cam with meshing indexing disc, *Proceedings of the Institution of Mechanical Engineers, Part C: Journal of Mechanical Engineering Science*, 2007,221(3):341-351.
- [11] Li, G.F., Li, Y., Wang, D.C. Research on status monitoring and fault warning for reliability testing of circular tool magazine, *Modular Machine Tool & Automatic Manufacturing Technique*,2018,9:86-89.
- [12] Yu, J.W., Luo, H., Shu, X. Modeling and profile analysis of globoidal cam in automatic tool changer, *Journal of Mechanical Transmission*,2017,41(7):88-92.
- [13] Yang, C.B., Liu, Y.F., Wang, C.Z. Application of dual lead cylindercam indexing mechanism in vertical lathe, *Manufacturing Technology & Machine*, 2014, 9: 113-114.
- [14] Zhang, Y., Xia, X.P. Designing of tool changer in bamboo hat ATC of machine centre, *Coal Mine Machinery*, 2009, 30(03): 100-102.
- [15] Nikitchenko A., Artiukh V., Shevchenko D., et al. Modeling of Operation of Elastic-frictional Draft Gear by NX Motion Software, *Procedia Engineering*, 2017,187:790-796.
- [16] Zou, H.J., Yin, H. L. Design and Application Innovation of Intermittent Motion Mechanism. China Machine Press, 2008.

Online Monitoring and Early Warning Technology of Repeated Multiple Blackouts in Distribution Network Based on Multi-source Information Fusion and Delphi Method

Wensi Cao ^{a*}, Mingming Xu ^b, Rongze Niu ^b, Qing Wu ^a, Ruirui Xie ^b

^aSchool of Electric Power, North China University of Water Resources and Electric Power, Zhengzhou 450045, China

^bState Grid Henan Electric Power Research Institute, Zhengzhou 450002, China

Received OCT 16 2019

Accepted JAN 8 2020

Abstract

The service-oriented architecture model (SOA) is highly open, hierarchical, and can support parallel / distributed information interaction. Through well-defined interfaces and contracts to contact different services of applications, it has many applications in the field of power system. The SOA architecture is used to realize multi-source power outage information fusion and provide data support for power outage risk assessment and hierarchical early warning. For the problem of repeated multiple blackouts in the distribution network, based on the SOA framework design, the multi-source information fusion technology of the distribution network is used to provide data exchange for online monitoring and early warning technology. By analyzing the factors affecting the repeated multiple blackouts risk and the blackout grading warning of the distribution network, every impact factor scoring standards are given respectively. The Delphi method is used to establish an indicator evaluation system to evaluate the repeated multiple blackouts risks and the indicators of power outage classification warnings in the distribution network, and calculate the weights of each indicator. A repeated multiple blackouts assessment was conducted for an actual blackouts instance, and the comprehensive probability value and hierarchical warning level of repeated multiple blackouts are obtained to realize online monitoring and early warning, which provided a new technology for dealing with repeated multiple blackouts.

© 2020 Jordan Journal of Mechanical and Industrial Engineering. All rights reserved

Keywords: Delphi; Repeated multiple blackouts; grading early warning; multi-source information fusion; Service-Oriented Architecture.

1. Introduction

Many problems exist in the distribution network, such as weak grid, low equipment reliability, backward information level, insufficient scheduling capability and so on. Thereby, repeated multiple blackouts led to frequent accidents and frequent user complaints, which seriously affected the service quality and social image of the power supply company. According to the "Clear description of the acceptance criteria for low-voltage and frequent blackout complaints" by the marketing department of State Grid Corporation, Repeated Multiple Blackouts is defined as: 3 or more power blackouts occurred in a station for two consecutive months. Domestic and foreign research gaps on Repeated Multiple Blackouts, lack of effective governance methods. The causes for power blackouts can be divided into two categories: Planned blackouts and Fault blackouts. Planned blackouts can be known in advance through announcements, etc. Therefore, the Fault blackouts is studied mainly.

There is a lot of Equipment in distribution network, the current operational and historical data come from multiple

systems. It is difficult and inaccurate to evaluate the status of a certain area or line based on a single information. Compared with the single source information evaluation method, multi-source information fusion technology can improve the robustness and accuracy of the system. It is the basic links of realizing blackouts monitoring and early warning to achieve integration of multi-source blackouts information in distribution networks and the cross-system service linkage mechanism. This study adopts the SOA architecture based on Web Service to realize the fusion of multi-source information and online detection and early warning.

The causes of Repeated Multiple Blackouts are complex, including human factors, external factors, natural factors and equipment factors. How to target different causes, it is the key and difficult point of solving repeated Multiple Blackouts effectively to govern blackouts differently. Index weights are used to reflect the influence of various factors on the blackouts and the relative importance of the indicators. Determining the weight of the indicators is an important issue in the comprehensive evaluation. At present, the methods for determining the weight coefficient are: subjective weighting method,

* Corresponding author e-mail: 493441872@qq.com.

objective weighting method, and subjective and objective comprehensive weighting method.

In reference [2], OPA model is applied to power grid outage accident simulation to calculate the risk value of power grid security events, which is suitable for high-voltage transmission system. Literature [3] Based on fault tree and analytic hierarchy process (AHP), established four levels of indicators based on large-scale outage fault tree, and analyzed structural risk, technical risk and equipment risk layer by layer, so as to calculate the comprehensive risk degree of large-scale outage risk. In reference [4], by analyzing the outage probability caused by various emergencies, the outage risk of distribution network under emergencies is calculated, and the emergency warning level is determined based on this criterion. In reference [5], a risk assessment model of distribution network considering various factors is proposed. In the model, a new method is adopted to calculate the outage cost of distribution network. This method reflects the comprehensive influence of outage frequency, outage duration and outage power on outage cost. In the existing research results of distribution network risk assessment, the assessment method combining empirical analysis and qualitative analysis based on subjective factors is more common, there is no standard unified assessment system, and some quantitative assessment methods consider relatively single risk factors [1-5], and most of them are not applied in practice, only stay in theoretical analysis. In this paper, based on the SOA architecture to achieve multi-source outage information fusion, the Delphi evaluation system is used to evaluate and analyze the indicators of various influencing factors, and the risk and classification early warning model of repeated multiple outage in distribution network is constructed to realize online monitoring and early warning, providing new help for the governance of repeated multiple outage in distribution network.

2. Multi-source Information Fusion and Literature Review

The source system related to the multi-source information of the distribution network includes: PMS2.0 (Lean management system for equipment (property) operation and maintenance), Distribution Automation System (A kind of automation system that can make the distribution enterprise monitor, coordinate and operate the distribution equipment in real time in the distance) Power Collection System (Through the collection and analysis of power consumption data of distribution transformers and end users, the power consumption monitoring, step pricing, load management and line loss analysis are

realized), OMS (A scheduling integrated management system which integrates scheduling production, professional management and scheduling business processing), and the like. Multi-source information fusion technology was launched in the 1970s to study the comprehensive processing and utilization of multi-source uncertainty information[5]. Common information fusion methods are: Artificial Neural Network method [6-8], Bayesian Network method [9], Fuzzy Reasoning method [10-11], Dempster-Shafer Reasoning method, etc. [12]. Service-Oriented Architecture (SOA) is a highly open, hierarchical, component model that supports parallel/distributed information interaction and loose coupling [13]. It links the different services of the application through well-defined interfaces and contracts between these services, it links the different services of the application through well-defined interfaces and contracts between these services, whose interface specifications generally complying with the IEC61968 and IEC61970 protocols. And has been applied widely in the field of power systems [14-16]. The SOA architecture solves the coupling problem of the subsystem to the greatest extent and minimizes the coupling degree of each subsystem. It is an effective mechanism to solve the encapsulation, interaction, integration, and reuse of each subsystem.

Web Service is used to implement the SOA architecture, the Web Service interface adopts Apache Axis2 technology. The client and the server interact with each other with the SOAP protocol through HTTP. The client generates a SOAP request message according to the WSDL description document and sends it to the server. The client generates a SOAP request message according to the WSDL description document and sends it to the server, the server parses the received SOAP request, invokes the Web Service, and then generates a corresponding SOAP response and sends it back to the client.

The Web Service server adopts the dual-system hot backup mechanism. Through the dynamic IP drift mechanism, when the running machine fails, the IP automatically drifts and points to the hot backup machine to achieve trouble-free operation. Web services are published in the JBOSS server using the Axis2 framework.

All source system data (model, real-time data, fault information, etc.) is pushed to the enterprise information bus through the Web Service, and pushed to the data adapter from the bus to the multi-source blackouts information buffer pool to perform model checking, model conversion, model splicing and model fusion. Then it is stored in the multi-source blackouts information database to provide data support for the risk assessment, prevention and control application of the distribution network Repeated Multiple Blackouts, as shown in Figure 1.

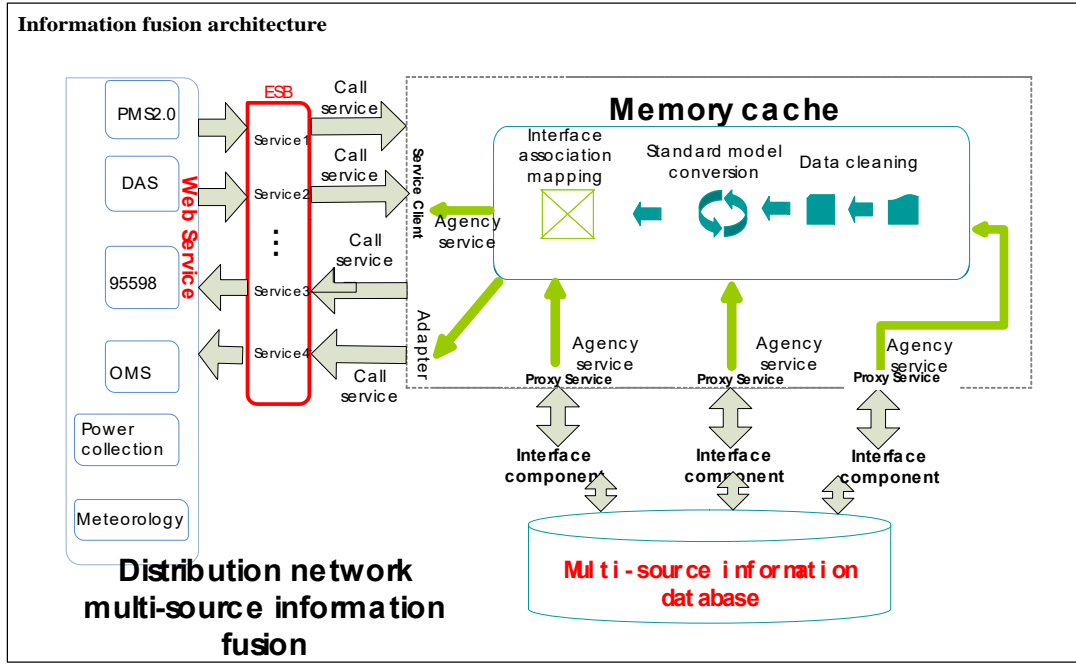


Figure1. Information fusion architecture

3. Delphi method evaluation system

Delphi is a method that fully integrates expert knowledge, experience and information in the field, also known as expert scoring. The key of Delphi’s method is that it seeks expert opinions in an anonymous manner, and the decision opinions tend to be consistent and approximate the actual value through information communication and cyclic feedback experts, n indicators (assuming each expert evaluates all indicators).

3.1. Delphi method main statistical analysis function

3.1.1. Expert authority level

Expert authority level has an important influence on the accuracy of the weight coefficient judgment results. The higher the authority of the pert, the more reliable the weight coefficient obtained. Expert authority level is generally decided by the basis of expert judgment and expert familiarity with the index. The calculation formula is:

$$C_{Ri} = \frac{C_{ai} + C_{si}}{2} \quad (i = 1, 2 \dots m) \quad (1)$$

3.1.2. Weighted arithmetic mean C_{Ej}

C_{Ej} reflects the concentration of expert ratings. The larger the C_{Ej} , the more important the indicator. The calculation formula is:

$$C_{Ej} = \frac{1}{m} \sum_{i=1}^m C_{Ri} * C_{ji} \quad (i = 1, 2 \dots m, j = 1, 2 \dots n) \quad (2)$$

C_{Ej} : the weighted arithmetic mean of indicator j,

C_{ji} :the score of expert i on indicator j.

3.1.3. Coefficient of variation

The coefficient of variation v_j mainly reflects the volatility of the experts’ evaluation of the indicators, that is the degree of coordination. The calculation formula is:

$$v_j = \frac{S_i}{C_{Ei}} \quad (3)$$

S_i : the standard deviation of the evaluation index i score.

$$S_i = \sqrt{\frac{1}{m-1} \sum_{i=1}^m (C_{ji} - C_{Ej})^2} \quad (4)$$

3.1.4. Coordination coefficient of expert opinion w

The expert opinion coordination coefficient W reflects the coordination degree of the expert group’s weighting coefficients for all indicators, ranging from 0 to 1. Generally, after 2 to 3 rounds of consultation and coordination, the coordination coefficient generally fluctuates within the range of 0.5 and the error control is better.

$$w = \frac{12}{(m^2(n^3 - n) - m \sum_{j=1}^m T_j)} \sum_{j=1}^n (R_j - R)^2 \quad (j = 1, 2 \dots n) \quad (5)$$

n: the total number of indicators; R_j : the index i evaluation level and; R: the evaluation level and the mean value of all indicators;

$$T_j = \sum_{l=0}^L (t_l^3 - t_l) \quad (6)$$

L: the number of groups having the same evaluation value among the expert evaluation values;

t_l : the same number of levels in the L group.

3.1.5. Expert positive coefficient

k_j is the interest level of experts on indicator i. The calculation formula is:

$$k_j = \frac{m_j}{m} \tag{7}$$

m_j : the number of experts who evaluated the indicator j. Under the assumption of this paper, $k=1$.

3.1.6. indicator weight

The indicator weight is the weight coefficient of the index j:

$$k_{wj} = \frac{C_j}{\sum_{j=1}^n C_j} \tag{8}$$

4. Risk model of distribution network Repeated Multiple Blackouts

4.1. Risk indicators of distribution network Repeated Multiple Blackouts

The repeated multiple blackouts risk assessment of the distribution network accounts for the main characteristics of the repeated multiple blackouts scenarios. There are

three main factors affecting the repeated multiple blackouts in the distribution network: equipment level, operation and maintenance level, and grid structure level. At the same time, it also takes into account the influence of external factors such as meteorological and historical blackouts, and makes full use of the current situation data and historical data of the distribution network in the multi-source information fusion system, which effectively reflects the comprehensive probability level of repeated multiple blackouts in the distribution network.

4.1.1. Equipment level

The probability of distribution network blackouts is closely related to the equipment level. The advanced and reliable power equipment is the hardware guarantee for safe operation of the distribution network. The indicators affecting the equipment level and scoring criteria are shown in Table 1

4.1.2. Operation and maintenance level

In the operation and management of the distribution network, whether the inspection is in place and whether the defects are eliminated is in time, which is related to whether the hidden dangers of the equipment can be detected and solved in time, thus affecting the failure rate. The index scores that affect the level of operation and maintenance are shown in Table 2.

Table 1. Scoring standard of sub-indicators affecting the level of equipment

Sub indicator	Score		
	10-20	30-40	50-80
Protection level against lightning	Lightning arrester Perfectly installed	Install lightning arrester only on the high voltage side of the power transformer	No lightning arresters
Insulation level	All lines are insulated	Some lines are insulated	Unused insulated wire
Number of old equipment	No old equipment	Small amount of old equipment	Large quantity of old equipment
Distribution network protection device configuration	All configured	Partial configured	No configured

Table 2. Scoring standard of sub-indicators affecting the level of operation and maintenance

Sub indicator	Score		
	10-20	30-40	50-80
Uninterruptible operation level	Third and fourth types of operational capabilities	Only the first and second types of simple operation capabilities	No ability
Repair ability	Stronger	Medium	Insufficient
Live detection and online monitoring technology	Stronger	Medium	Not possess

4.1.3. Grid structure level

Many problems exist in the distribution network, such as weak grid, and the repeated multiple blackouts led to frequent accidents and frequent user complaints. So, the grid structure needs to be strengthened. The index scores that affect the level of the grid structure are shown in Table 3.

Table 3. Scoring standard of sub-indicators affecting the level of grid structure

Score Sub indicator	10-20	30-40	50-80
Line “N-1” pass rate	Stronger transfer ability	Medium transfer capacity	No ability
Section switch installation	3 paragraphs and above	Less than 3	None
Power supply radius	Standards compliant	—	Exceeding provisions

4.2. Distribution network repeated multiple blackouts risk indicator weight

4.2.1. Indicator weights

Figure 2 shows the process of determining the weight coefficient of each index. According to the statistical analysis function of the Delphi method in Section 2.1, the scores of all experts are analyzed and summarized circularly. Synthesizing many power experts’ understanding for the importance of distribution network repeating multiple blackouts risk assessment indicators and the ratio of complaints held by the comprehensive management department, combined with the multi-source information fusion platform. After corresponding mathematical calculations, the weights of each indicator are obtained, and finally the weights of the 10 indicator features in the indicator system can be obtained, as shown in Table 4.

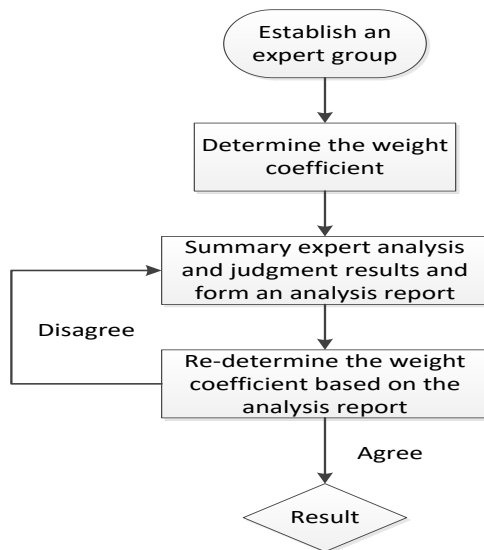


Figure 2. Process to get the index weight

Table 4. The coefficient of each index weight

Specific indicators	Weights
Protection level against lightning	0.12
Insulation level	0.08
Number of old equipment	0.08
Distribution network protection device configuration	0.12
Uninterruptible operation level	0.06
Repair ability	0.06
Live detection and online monitoring technology	0.08
Line “N-1” pass rate	0.16
Section switch installation	0.16
Power supply radius	0.08

Note : Number of experts : 10

4.2.2. External factors

External factors mainly include meteorological conditions and repeated power outages. The value of the repeated power outage factor is 1 for the power outage in the previous month and 1.5 for the power outage last month.

4.3. Evaluation results

The cumulative probability of repeated multiple blackouts can be derived from equations (9) and (10).

$$P = P_0 * Q * T \tag{9}$$

$$P_0 = \sum_{i=1}^n k_{wi} * U_i \tag{10}$$

P:the comprehensive probability of repeated multiple power outages;P₀:the base probability of repeated multiple blackouts; Q: the meteorological condition factor; T:the repeated blackouts factor; U_i: the score of each indicator. The comprehensive probability value of repeated multiple blackouts ranges from 0 to 100, and if the calculated value exceeds 100, it is calculated as 100.

According to the comprehensive probability value of repeated multiple blackouts in the distribution network, the probability of repeated multiple blackouts is divided into five levels(from large to small): I, II, III, IV, V, as shown in Table 5. The comprehensive probability value is a comprehensive score that takes into account various influencing factors, and reflects the repeated multiple blackouts probability level of the whole distribution network, and does not represent the percentage probability of repeated multiple blackouts.

Table 5. Repeated multiple outages of comprehensive probability of hierarchical and quantification

Level	I	II	III	IV	V
P	>70	40-70	20-40	10-20	<10

5. Classification early warning model of distribution network repeated multiple blackouts

According to the comprehensive probability value of repeated multiple blackouts, when the probability exceeds 70, that is, when repeated multiple blackouts occur “very likely”, an early warning should be issued.

According to the different consequences of repeated blackouts, a grading warning is carried out. That is, the risk is quantified in combination with the consequences of repeated blackouts. According to the risk grading results, the corresponding level of early warning is issued, and the corresponding measures are taken to provide the basis for prevention and control.

5.1. Consequences of repeating multiple blackouts

The factors affecting the consequences of repeated multiple blackouts mainly include four aspects: the importance of power load, the repeated blackouts complaint rate, the time and scope of blackouts. Therefore, different impacts should be considered in the repeated multiple blackouts warnings, and graded warning should be implemented. Quantitative scoring of each influencing factor index is analyzed and calculated by Delphi method, and the effect value of repeated multiple blackouts is obtained finally. The risk level of repeated multiple blackout events is determined according to the magnitude of the consequence value, and a corresponding level of warning is issued.

5.1.1. Consequence indicators of repeating multiple blackouts

1. The importance of blackouts load

For the distribution network, the greater the proportion of important loads, the greater the loss caused by blackouts. The load factor will be determined based on the specific gravity of the level I and II loads, as shown in Table 6.

Table 6. The importance of the load

Proportion of level I and II load	30%	60%	80%	100%
Score	60	70	80	90

When the load weight data is not available, the distribution of the load has regional characteristics, which can be used to reflect the importance of the load. Four types of areas—the center of city, urban area, town, village—are selected. Each type of area corresponds to a load area characteristic factor, which is used to characterize the load importance factor, as shown in Table 7.

Table 7. The importance of the load

Characteristics of load area	the center of city	urban area	Town	village
Score	90	80	70	60

2. Complaint information of repeated blackouts

The areas with more repeated blackouts complaint taking place will lead to more complaints, so consider the repeated blackouts complaint rate indicator in the region to

characterize the region’s tolerance to repeated blackouts, as shown in Table 8.

$$P_T = \frac{T_0}{T} \times 100\% \quad (11)$$

P_T : the repeated multiple blackouts complaint rate; T_0 : the number of repeated power outage complaints in the region; T : the number of user complaints in the region.

Table 8. The index of outages complaint history information

Complaint rate (%)	0-10	10-20	20-30	30-40	40-50	>50
Score	50	60	70	80	90	100

3. Time of blackouts

The time factor considers three cases: general working days, holidays, and special power supply periods, as shown in Table 9.

Table 9. The index of time of occurrence of Repeated multiple outages

Time factor	General working days	Holidays	Special power supply periods
Score	50-60	70-90	90-100

4. The scope of blackouts

For the distribution network, the range of blackouts, such as the whole line outage and the branch line outage, have different effects on the repeated blackouts of the distribution network, as shown in Table 10.

Table 10. Influence sphere of Repeated multiple outages

Range of blackouts	Branch line outage	Whole line outage
Score	20-50	80-90

5.1.2. Consequences indicator weights of repeating multiple blackouts

The Delphi method is also used to derive the weight of each indicator, as shown in Table 11.

Table 11. Each index weight of consequence of Repeated multiple outages

Influencing factor indicator	Weights
The importance of load	0.3
Historical blackout complaint information	0.2
Time of blackouts	0.1
Range of blackouts	0.4

5.1.3. Quantitative assessment of the consequences of repeated multiple blackouts

After obtaining the scores of the indicators that affect the consequences of repeated multiple blackouts in the distribution network, according to the formula (3-1) (3-2), the scores of the repeated multiple blackouts are obtained. According to the magnitude of the consequences of the blackouts, the severity of the consequences is divided into five levels, as shown in Table 12.

Table 12. Hierarchical and quantification of consequence of Repeated multiple outages

Loss of LevelII	Loss of Level II	Loss of LevelIII	Loss of LevelIV	Loss of LevelV
>70	40-70	20-40	10-20	<10

5.2. Failure risk classification warning

According to the quantified distribution network failure consequence value, the risk of repeated multiple blackouts in the distribution network is classified, and the warning level is determined according to the classification of the corresponding risks, so that the risk response measures can be taken conveniently in management. According to the normal distribution network risk grading theory, the distribution network repeated multiple blackouts risk warning is divided into five levels, namely, level I, level II, level III, level IV and V, as shown in Table 13.

Table 13. Hierarchical and quantification of consequence of Repeated multiple outages

Alert level	Consequence value
Level I	≥ 70
Level II	[40-70)
Level III	[20-40)
Level IV	[10,20)
Level V	<10

6. Example analysis

6.1. Case introduction

In July 2016, a distribution network line in a county town suffered blackouts due to two lightning arrester breakdown accidents during the summer. This line supplies power to some enterprises in the county. Collecting basic data such as power equipment, network structure, operation and maintenance records, and fault records in the area where the blackouts occurred in the multi-source information system, the equipment with a long operating life in this area is put into operation early, most of the equipment is aging seriously, and the relay protection device is simple in configuration. The scores of the benchmark probability indicators for evaluating repeated multiple blackouts are given in four aspects: comprehensive equipment level, operation and maintenance level, external force protection level and grid structure level.

In the region, lightning was frequent in the summer of June-August, and the meteorological factor was 1.2. The blackouts had occurred 2 times last month, and the repeated multiple blackouts factor was 1.5.

6.2. Score of evaluation index

The collected distribution network basic data is processed, and the scores of the respective indicators are given. The results are shown in Table 14.

Table 14. Score of factors

Index	Score
Lightning protection level	70
Insulation level	80
Ratio of old equipment	80
Distribution network protection device	60
Uninterruptible operation level	30
Repair ability	30
Live detection and online monitoring technology	70
Line "N-1" pass rate	30
Section switch installation	60
Power supply radius	10

The calculated baseline probability index value is 52.8. After considering the meteorological factors and the repeated blackouts factor, the comprehensive probability value is 95.04. A repeated multiple blackouts warning should be issued.

Table 15. Score of consequence

Influencing factor indicator	Score
The importance of load	70
Historical blackout complaint information	50
Time of blackouts	60
Range of blackouts	30

The value of calculated repeated blackouts consequence is 48. Therefore, the warning level should be level II.

6.3. Analysis of case evaluation results

The probability of the event evolving into repeated multiple blackouts exceeds 70. The event is "very likely" for repeated blackouts, and an early warning should be issued. According to the calculation of the consequence indicator value, the early warning level is determined to be a level II. The event will evolve into repeated multiple events, and measures should be taken in time to avoid the occurrence of repeated multiple events. Therefore, the electricity sector should formulate corresponding measures according to different repeated multiple blackouts warning levels and consequence risk levels, and the operation and maintenance personnel can take corresponding measures accordingly to prevent the blackouts event from evolving into repeated multiple blackouts events, causing serious consequences.

7. Conclusion

1. Using SOA framework of Webservice service, multi-source outage information fusion is realized, which provides data support for on-line monitoring, early warning and control of repeated multiple outages in distribution network;
2. Based on the analysis of multi-source information, the influencing factors, scoring standards and quantitative

scope of the two models are analyzed. Based on the Delphi method evaluation system, the risk model and outage classification early warning model of repetitive outage in distribution network are established to provide new technologies for the control of repetitive outage in distribution network.

3. In the future application process, the the risk model and outage classification early warning model of repeated multiple blackouts will be improved and improved

Acknowledgment

This work is supported by the Key Scientific Research Projects Plan of Henan Higher Education Institutions (19A470006); Key Scientific and Technological Research Projects of Henan Province (192102210229); Cultivation plan of young backbone teachers in Colleges and universities of Henan Province (2019GGJS104).

References

- [1] Wu Zimei, Liu Dong, Zhou Han. Preventive control decision analysis of risk-based power system security early warning [J]. Electric Power Automation Equipment, 2009,29 (9): 105-109
- [2] Lu en, Lu Xiaojun, Long Fei, et al. Power system outage risk assessment indicators and methods [J]. Electric Power Automation Equipment, 2015,35 (3): 68-74
- [3] Wang Bo, you Haihai, Yin Xianggen, et al. Security risk assessment system of complex power system based on multi factor analysis [J]. Power System Technology, 2011,35 (1): 40-45
- [4] Li Rui, Chen Ying, Mei Shengwei, et al. Emergency warning method of urban distribution network based on outage risk assessment [J]. Automation of Electric Power Systems, 2010,34 (16): 19-23
- [5] Su Haifeng, Jiang Xiaojing, Liang Zhirui. Risk assessment of distribution network operation considering various influencing factors [J]. Electrical Measurement & Instrumentation, 2014,51 (6): 34-38
- [6] Xu Jiayuan, Zhang Bin, Lin Xin, et al. Application of energy spectrum entropy vector method and RBF neural networks optimized by the particle swarm in high-voltage circuit breaker mechanical fault diagnosis. High Voltage Engineering, 2012, 38(6):1299-1306.
- [7] Fu Qiang, Chen Tefang, Zhu Jiaojiao. Transformer fault diagnosis using self-adaptive RBF neural network algorithm. High Voltage Engineering, 2012, 38(6):1368-1375.
- [8] Li Xin, Qi Hongwei, Teng Yun, et al. Evaluation method of high voltage circuit breaker running state based on matter element theory and AHP. In: International Conference on E-Product E-Service and E-Entertainment (ICEEE). [S.l.]:IEEE, 2010:7-9.
- [9] Lan Hua, Sun Chuanmeng, Wang Yunran, Yang Jianbiao, et al. Fault diagnosis of distributed transmission network based on Bayesian network. Electrical Measurement & Instrumentation, 2012,11:1-5.
- [10] Li Haiying, Feng Dong, Song Jiancheng. Fuzzy-DS evidence theory online assessment model of MV vacuum circuit breaker. High Voltage Apparatus, 2013, 49(1):40-45.
- [11] Liao Ruijin, Wang Qian, Luo Sijia, et al. Condition assessment model for power transformer in service based on fuzzy synthetic evaluation. Automation of Electric Power Systems, 2008, 32(3):70-75.
- [12] Chen Weigen, Wei Yanqin, Liao Ruijin. Variable weight fuzzy comprehensive evaluation method for operation condition of high voltage circuit breaker. High Voltage Apparatus, 2009, 45(3):73-77.
- [13] Kang Chaoqun, Li Erxia, Sheng Wanxing, et al. Research on dynamic state evaluation of distribution vacuum switchgear based on multi - source Information fusion. High Voltage Apparatus, 2017,03(53):235-241
- [14] Yuan Wenguang, Zhou Wenjun, Li Chunjian. Study on real-time SOA architecture of distribution automation system. Power System Protection and Control, 2012,40(17):150-155.
- [15] Zhou Zhi-ting, Jiang Hong-tu, Xiong Ye. Design of information integrated system of distribution transformer monitoring based on SOA. Power System Protection and Control, 2008, 36(23): 60-64.
- [16] Gui Xun, Liu Zhi-gang, Qian Qing-quan. Research on the general architecture of analysis software for powersystem with remarkable extensible characteristic. Relay, 2008, 36(11):13-18, 87.

Contact Mechanics Analysis and Optimization of Shape Modification of Electric Vehicle Gearbox

Qingyong Zhang^{a,b*}, Yaru Wang^a, Weiping Lin^a, Yongjun Luo^a, Xingjian Wu^a

^aSchool of Mechanical and Automotive Engineering, Fujian University of Technology, Fuzhou 350118, China

^bFujian Provincial Key Laboratory of Automotive Electronics and Electric Drive, Fujian University of Technology, Fuzhou 350118, China

Received OCT 16 2019

Accepted JAN 17 2020

Abstract

The performance of transmission gears has a great influence on the overall reliability, NVH performance and transmission efficiency of a gearbox. When the gear strength requirement is met, the gear transmission with low vibration and low noise is designed. In view of the NVH problem of automobile transmissions, the third pair of gear pairs of an electric vehicle gearbox is taken as the research object. Based on the nonlinear dynamic model theory of the gear transmission system, the gear profile modification and tooth orientation are comprehensively used to select a reasonable shape modification scheme. The stiffness matrix, mass matrix and position information of the shell extracted from the finite element software are combined with dynamic model of MASTA and the gear pair is optimized for microscopic shaping. Observing the simulation results, it can be seen that the gear pair transmission error and the maximum contact stress after the shape modification are significantly reduced compared with those before the shape modification, and the contact stress map distribution is more uniform. Therefore, selecting a suitable modification scheme can significantly improve the gear meshing effect. The gear transmission error is reduced, and the stress concentration of the gear teeth caused by the assembly error and the elastic deformation is improved, thereby reducing the vibration and noise generated by the gear transmission process.

© 2020 Jordan Journal of Mechanical and Industrial Engineering. All rights reserved

Keywords: Gear; micro-modification; optimization; transmission error; contact stress.

1. Introduction

As the core component of the automobile gearbox, the smooth running of the gear will have a great impact on the overall reliability NVH (Noise Vibration and Harshness) performance and transmission efficiency of a gearbox. With the development of modern industry, the gear transmission is gradually developing in the direction of high efficiency, precision and intelligence, and the requirements for the working performance of the gear are getting higher and higher. When the gear strength requirement is met, the gear transmission with low vibration and low noise becomes the goal of the study of gear dynamics research. Correct design of the parameters and accuracy of the gear can reduce its dynamic meshing force, and proper dynamic shaping can also reduce the impact. Based on the dynamic model and analysis of the gear transmission system, the overall simulation of the gearbox is carried out to obtain the NVH response of the gearbox, which helps to reduce its vibration and optimize its design. At this stage, the NVH performance of the gearbox is improved mainly by improving the structure, optimizing the process and the control method, gear shaping, and so on. And the gear shaping is an effective

method of the lowest cost. Gear shaping is widely used in traditional vehicle transmissions, but there is currently no mature solution for electric vehicles [1-3].

The methods of tooth profile modification are mainly divided into the following five methods: empirical formula method, differential geometry method, elastic mechanics method, function method and finite element method [4, 5].

The empirical formula method considers various factors that affect the deformation of gears under different working conditions, and gives the corresponding empirical formula to determine the amount of modification [6]. Yang Tingli et al. synthetically considered the factors, such as the manufacturing error and elastic deformation of gear teeth, and finally determined the optimum modification amount of gear teeth according to the corresponding formula [7].

Elasticity mechanics method is to use the theory of elasticity to analyze the forces acting on the gears in meshing, and calculate the modification amount needed for the elastic deformation of the tooth surface [8]. Cheng Yikang et al. used the finite element method to analyze the contact strength of the tooth surface under the condition of different tooth tip modification [9].

The function method is to determine the curve equation of the modified section by establishing the shape

* Corresponding author e-mail: zhqy@fjut.edu.cn.

increment function of the tooth top section, the middle section of the tooth profile and the root section of the tooth profile, or by using the curve transition method to determine the modification amount. Singh and Comparin studied the undamped vibration phenomenon of multi-degree-of-freedom systems, and obtained its approximate solution by harmonic balance method and function description method^[10].

Finite element method (FEM) is a popular modification method in modern times. It is a discrete numerical simulation method. The basic idea of the finite element method is to discretize the solution object and divide the solution domain of the problem into a series of units. Each unit is connected by nodes, and the unit node quantity equation is established from the energy relationship and the balance relationship, then form each unit equation group into an overall algebraic equation group, and select an appropriate calculation method to solve according to the specific conditions of the equation group^[11]. Gao Xiaoyu obtained the involute equation, the root transition curve equation and the spiral equation according to the involute gear meshing principle and three-dimensional modeling of the helical gear was carried out and the contact finite element analysis was carried out^[12]. Combined with the tooth profile modification theory, the amount of tooth tip modification of the helical gear was determined according to the contact simulation result. The two types of shaping curves were used to modify the helical gears. The comparison of the shaping effects determined the gear shaping curve of the wind turbine gearbox under certain working conditions. Oguz Kayabasi first analyzed and calculated the load distribution on the gear tooth profile by experimental methods. Then the mathematical model of gear tooth profile was established, the tooth profile was optimized by finite element method, and various stress distribution clouds are drawn^[13]. Wang Yi et al. used the finite element method to analyze the gear transmission process, determine the shape modification parameters and perform tooth surface modification to reduce gear vibration and noise^[14].

As for the tooth orientation modification, Litvin^[15] gave the design method of tooth orientation and tooth width direction to optimize the gear transmission error. Xiang Ya calculated the effective contact width and drum shape of gears based on the meshing tooth error and gear tooth deformation, and gave the tooth-shaped drum shape modification curve equation. By creating three-dimensional models of gear pairs with different drum shapes, the three-dimensional contact finite element method was used to calculate the longitudinal load distribution of tooth^[16]. Xing Bin et al. considered the influence of installation error and used the finite element quasi-static analysis method to quantitatively calculate the meshing stiffness and load distribution coefficient of different modified gears. The influence of installation error, gear modification amount on gear meshing stiffness and load distribution coefficient is obtained^[17]. Xiong Hegen et al. studied a two-stage helical gear reducer by static strength analysis and transmission error analysis, it was found that the contact strength safety factor of high-speed gears was low and there existed danger of pitting corrosion; The low-speed transmission error was relatively large. In order to improve the transmission performance, it

was considered to adopt a comprehensive modification method combining the tooth direction drum shape modification and the tooth inclination degree modification. Based on the Romax Designer software, the genetic algorithm was selected to optimize the comprehensive modification of the tooth direction, and the corresponding optimization and modification scheme was obtained^[18].

Although a lot of research on tooth shape modification has been done, the tooth shape modification in the dynamic analysis, especially the nonlinear dynamic analysis, is often neglected, and the final result can not truly reflect the influence of the shape modification. In view of the above deficiencies, this paper takes a three-speed gearbox of an electric vehicle as the research object, based on the nonlinear dynamic model theory of gear transmission system, the gear profile modification and tooth orientation are comprehensively used to select a reasonable shape modification parameter. The gear pair is optimized to provide a theoretical basis for improving the NVH performance of the transmission.

2. Modeling of transmission drive system

2.1. Dynamic modeling of the gearbox without body

The mechanical model of the gearbox is built based on MASTA. The model is shown in Fig. 1. The vehicle transmission studied in this paper is a three-speed automatic transmission. The gears are helical ones, which are mainly used in the powertrain of new energy vehicles to improve the dynamics of the vehicle and the operating conditions of motors. At the same design power, the use of the gearbox increases the rated motor speed and reduces motor torque, thereby reducing the size, weight and manufacturing cost of the motor.

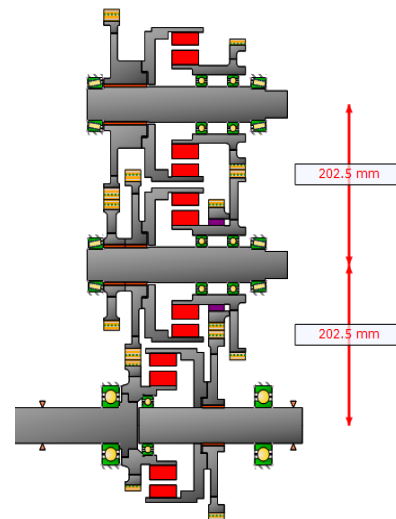


Figure 1. Gearbox two-dimensional model diagram

2.2. Importing of the gearbox housing

When the traditional transmission system is modeled, the gears and bearings are regarded as rigid bodies, and the boundary conditions are set to infinite stiffness. The elastic deformation of the shell, bearing, gear hub and other parts during working is not taken into account. Apparently, there is a certain difference from the actual situation, which can

not accurately reflect the actual working state of gearboxes. Therefore, it is necessary to consider the effect of actual stiffness of shell and other parts to get more accurate calculation results.

In this paper, the MASTA software is used to establish the node finite element model. Combined with the MASTA structural flexible module, the stiffness matrix, mass matrix and position information of the shell extracted from the finite element software are imported into the

MASTA. The partial data of the stiffness matrix and the mass matrix are shown in Tables 1 and 2^[19].

The assembly of the shell is completed by matching the condensed joints with the corresponding bearings, thus introducing the stiffness effect of the whole system, which is more in line with the actual situation, as shown in Fig. 2 and Fig. 3. Considering the actual stiffness effect, the system deformation analysis and gear micro-modification simulation analysis are carried out.

Table 1. Stiffness matrix of the shell

	Node 1 Dx	Node 1 Dy	Node 1 Dz	Node 1 Rx	Node 1 Ry	Node 1 Rz
Node 1 Fx	5004146300	2489301.5	1310509.4	203011.71	91125243	935473.21
Node 1 Fy	2489301.5	248991450	15394431	-1634935.2	232809.22	289414.83
Node 1 Fz	1310509.4	15394431	7339887000	-915190.66	-187594.06	138778.59
Node 1 Mx	203011.71	-1634935.2	-915190.66	2629860.7	-83975.229	17659.09
Node 1 My	91125243	232809.22	-187594.06	-83975.229	59606291	-202385.85
Node 1 Mz	935473.21	289414.83	138778.59	17659.09	-202385.85	2276400.8

Table 2. Mass matrix of the shell

	Node 1 Dx	Node 1 Dy	Node 1 Dz	Node 1 Rx	Node 1 Ry	Node 1 Rz
Node 1 Fx	24.54375	0.02878	0.01885	0.00091	-0.47793	-0.07083
Node 1 Fy	0.02878	5.2774	2.04046	0.07637	-0.00056	0.00076
Node 1 Fz	0.01885	2.04046	15.00319	0.12783	-0.00218	0.00154
Node 1 Mx	0.00091	0.07637	0.12783	0.01037	-0.00017	0.00015
Node 1 My	-0.47793	-0.00056	-0.00218	-0.00017	0.02934	0.00284
Node 1 Mz	-0.07083	0.00076	0.00154	0.00015	0.00284	0.00922

The position information of the housing is as shown in Table 3

Table 3. Location information of the housing

Name	Position (m)		
	X	Y	Z
4766	2.1631E-19	0.0375	-3.4694E-18
4767	-0.101	0.0375	0.17494
4768	0.101	0.0375	0.17494
4769	-2.7039E-19	-0.212	-3.4694E-18
4770	-0.101	-0.212	0.17494
4771	0.101	-0.212	0.17494

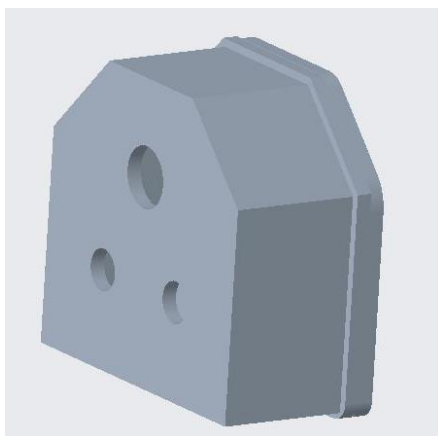


Figure 2. The model of the shell

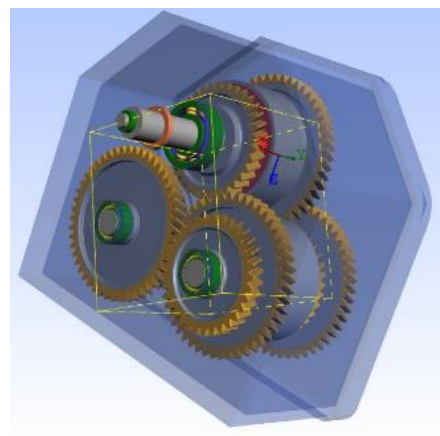


Figure 3. Overall model of the gearbox

3. Nonlinear vibration model and equation of gear system

3.1. Nonlinear vibration model

The concentrating mass method is used to establish the dynamic model of the automobile gearbox [20]. The frictional force and the influence of the oil film during the meshing process are neglected. The helical gear system can be simplified into the gear-bend-torsion-shaft coupling vibration system and the power of a couple of helical gear pairs. The model is shown in Fig. 4, where the system is a three-dimensional vibration system [21].

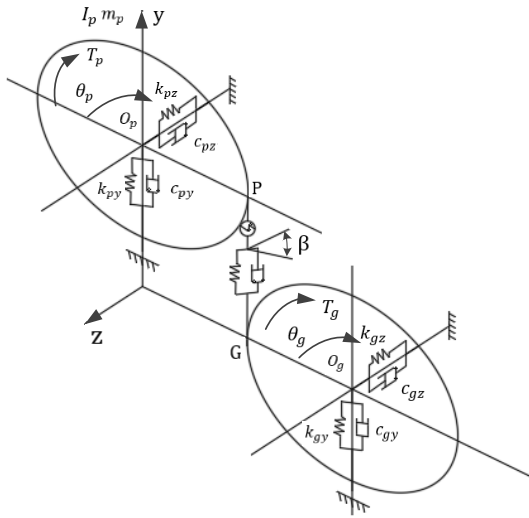


Figure 4. Dynamic model of the helical gear pair

3.2. Nonlinear vibration differential equation

From Fig. 5, assuming that the direction of rotation of the driving gear is right-handed and the helix angle is β , the relationship between the lateral direction and the axial vibration at the meshing point can be expressed as:

$$x = y \tan \beta \quad (1)$$

Regardless of the inter-tooth surface friction, the system has 6 degrees of freedom, and its generalized displacement array is:

$$\{\beta\} = \{y_p, z_p, \theta_p, y_g, z_g, \theta_g\}^T \quad (2)$$

where: y_i, z_i, θ_i ($i = p, g$) are the translational and angular vibration displacements of the driving wheel midpoint O_p and the passive wheel midpoint O_g in the Y direction and the Z direction, respectively.

Therefore, the relationship between the vibration displacement at point O_p and the vibration displacement of the driving wheel and O_g point and the generalized displacement of the passive wheel is:

$$\begin{cases} \bar{y}_p = y_p + \theta_p R_p \\ \bar{y}_g = y_g - \theta_g R_g \\ \bar{z}_p = z_p - \bar{y}_p \tan \beta \\ \bar{z}_g = z_g - \bar{y}_g \tan \beta \end{cases} \quad (3)$$

Assuming that the normal stiffness of the tooth engagement is k_m , normal damping is c_m and normal meshing error is e , their components in the Y and Z directions are:

$$\begin{cases} k_{my} = k_m \cos \beta \\ c_{my} = c_m \cos \beta \\ e_y = e \cos \beta \end{cases} \quad (4)$$

$$\begin{cases} k_{mz} = k_m \sin \beta \\ c_{mz} = c_m \sin \beta \\ e_z = e \cos \beta \end{cases} \quad (5)$$

Therefore, the tangential dynamic meshing force F_y of the system is:

$$F_y = k_{my} (\bar{y}_p - \bar{y}_g - e_y) + c_{my} (\dot{\bar{y}}_p - \dot{\bar{y}}_g - \dot{e}_y) \quad (6)$$

The axial dynamic meshing force F_z of the system is:

$$F_z = k_{mz} (\bar{z}_p - \bar{z}_g - e_z) + c_{mz} (\dot{\bar{z}}_p - \dot{\bar{z}}_g - \dot{e}_z) \quad (7)$$

Therefore, the dynamic equation of the model can be derived as follows:

$$\begin{cases} m_p \ddot{y}_p + c_{py} \dot{y}_p + k_{py} y_p = -F_y \\ m_p \ddot{z}_p + c_{pz} \dot{z}_p + k_{pz} z_p = F_z \\ I_p \ddot{\theta}_p = -T_p - F_y R_p \\ m_g \ddot{y}_g + c_{gy} \dot{y}_g + k_{gy} y_g = F_y \\ m_g \ddot{z}_g + c_{gz} \dot{z}_g + k_{gz} z_g = -F_z \\ I_g \ddot{\theta}_g = -T_g - F_y R_g \end{cases} \quad (8)$$

4. Gear microscopic modification

4.1. Gear tooth direction microscopic modification

The tooth orientation modification is to trim the tooth surface in a slight amount along the tooth direction, so as to deviate from the theoretical tooth surface, thereby improving the uneven distribution of the load along the tooth contact line and improving the bearing capacity of gears. The tooth direction modification mainly includes three methods of drum shaping, tooth end thinning and spiral angle modification.

The drumming is to make the teeth bulge in the middle of the tooth width, and the two sides are symmetrically distributed. Drumming is a well-adapted shaping method that compensates for the elastic deformation of gears, as

shown in Fig. 5. The parameters for the drum shaping are generally used as the initial value of the elastic deformation of the tooth contact, and the formula for calculating the elastic deformation δ is:

$$\delta = 1.16 \frac{F_n}{LE} \tag{9}$$

where: F_n is the normal load (N) of the gear meshing;

L is the length of the contact line (mm); E is the elastic modulus.

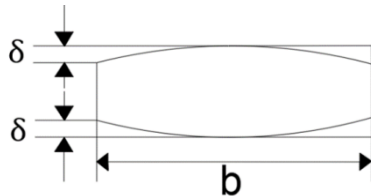


Fig.5 Drumming modification

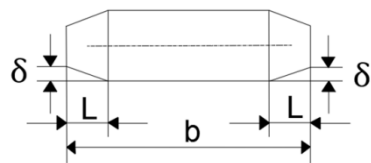


Figure 6. Tooth end thinning

Tooth end thinning means that one end or both ends of the gear teeth are gradually thinned toward the end at a small length of the tooth width, as shown in Fig. 6. The amount of modification is determined only by the amount of elastic deformation. For helical gears, the range of modification is $0.013mm \leq \delta \leq 0.035mm$, $L = 0.25b$,

b is the effective width (mm) of the gear. The helix angle modification refers to a slight change in the helix angle of the gear so that the actual tooth surface deviates from the theoretical tooth surface position, as shown in Fig. 7.

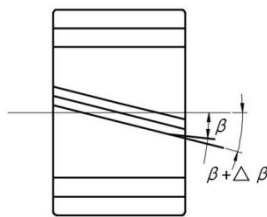


Figure 7. Spiral angle modification

4.2. Gear profile micro-shaping

During the gear meshing transmission, since gears are alternately engaged by single and double teeth, there is a significant abrupt change in the load distribution. As the load changes, the gear teeth also undergo corresponding deformation, resulting in an increase in the transmission error of gears, which in turn generates vibration, shock, noise and other issues. The tooth profile modification is to cut off the interference part of the tooth surface during the gear meshing process to reduce the transmission error and increase the meshing transmission stability, thereby

avoiding the phenomenon of sudden load change. The profile modification mainly includes the top edge trimming and the root modification. The tipping edge is the position at which the teeth contact the line when the tooth begins to enter the engagement at the addendum of the driven wheel and the root of the drive wheel. To avoid early contact, the driven wheel is generally trimmed near a portion of the crest. The roots are shaped to not only be in the vicinity of the crests, but also to correct the roots of the mating gear teeth that are intended to mesh.

The profile modification parameters are mainly the amount, the length and the curve of modification. The initial shape modification is generally acquired by the calculation of the tooth profile elastic deformation amount δ_a :

$$\delta_\alpha = \frac{\omega_t}{C_r} \tag{10}$$

where: ω_t is the unit tooth width load (N / mm);

C_r is the meshing stiffness of the gear (N / mm • μm).

The calculation ω_t of is as follows:

$$\omega_t = \frac{F_t}{b} \tag{11}$$

where: F_t is the tangential force (N) on the gear index circle.

The C_r is acquired as follows:

$$C_r = \sum_i^n \frac{1}{\delta_{1i} + \delta_{2i}} \tag{12}$$

where δ_{1i} and δ_{2i} are the comprehensive deformation of the driving wheel and the driven wheel respectively; F_i is the contact force of gears (N); n is the number of contacting teeth.

The modification length can be divided into long modification and short modification. The long modification is from the starting point (or termination point) of meshing to the alternation of single and double pairs of teeth. Short modification is one-half of the starting point (or termination point) of meshing to long modification. The long modification will cause the meshing part of gears to be less than one base pitch, which easily causes the meshing discontinuity of gears to produce impact. Therefore, the short modification is often used in the profile modification. The long modification is calculated according to formula (13) and the short modification is calculated according to formula (14).

$$\begin{cases} l_t = (E_\alpha - 1) p_{bt} \\ l_r = p_{bt} \end{cases} \tag{13}$$

$$\begin{cases} l_t = \frac{E_\alpha - 1}{2} p_{bt} \\ l_r = \frac{E_\alpha + 1}{2} p_{bt} \end{cases} \tag{14}$$

where: E_α is the contact ratio of gears; ρ_{bt} is the pitch of gears.

The shape of gear modification varies with the parameters. The general formulas are as follows:

$$\Delta = \Delta_{\max} \left(\frac{X}{L} \right)^\beta \quad (15)$$

Where X is the length from any point in the meshing area to the point meshing in or meshing out; L is the length of the meshing area of two teeth; Δ_{\max} is the maximum modification amount of gears; β is the index, and $1 < \beta < 2$ can be taken.

5. Gear modification design and result analysis

5.1. Scheme design

The gearbox is a three-speed gearbox with four pairs of gears engaged in meshing. The gear parameters are shown in Table 4.

Table 4 Gear pair parameters

Gear pair	Modulus	Number of teeth	Helical angle (°)	Pressure angle (°)	Rotation direction
The First pair	5	33	6	20	Left
Input	5	47	6	20	Right
The second pair	5	33	6	20	Right
Input	5	47	6	20	Left
The third pair	5	33	10	20	Left
Input	5	47	10	20	Right
The fourth pair	5	31	13	20	Right
Input	5	48	13	20	Left
Output					

Before defining the load spectrum, input and output power flows should be added to the input and output axes of the gearbox model respectively. The loads on the transmission system are constantly changing and the frequency with which different gears are used at work, that is, the time taken for each gear is also different, so the relation forms a load spectrum. The load spectrum of the actual working of the gearbox provides accurate input conditions for the operation of the transmission system, so that accurate calculation results of the force of each part can be obtained.

The working conditions of the third gearbox are shown in Table 5.

Table 5. First gear condition of gearbox

Load Case (%)	Duration (hr)	Ambient Air (°C)	Speed (r/min)	Torque (N·m)
25	60	20	1000	400
50	30	20	1000	600
75	60	20	2000	800
100	30	20	2000	1000

The input of the gearbox model is defined mainly according to the load spectrum, which is the combination of different working conditions of the gearbox, and the working conditions refer to the speed, torque and acting time on the gearbox under a certain power flow. For the same vehicle, the actual load spectrum will be affected by road conditions and driver operation. Therefore, a number of tests are carried out on different roads and driving habits by special testing instruments. Statistical data are extracted as the reference load spectrum for the design of transmission system. The load spectrum is defined according to Table 5, as shown in Table 6.

Because all gears engage in meshing when the gearbox works in first gear, and the gearbox loads are the largest at this time, this paper mainly checks the influence of loads on each pair of gears in first gear.

Table 6. Load Spectrum of First Gear of Gearbox

Design state	Load Case	Duration (hr)	Power Load	Speed (r/min)	Torque (N·m)
1st Design State	25% Load	60	Input Power Load	1000	400
			Output Power Load	223.5469	-1789.3336
	50% Load	30	Input Power Load	1000	600
			Output Power Load	223.5469	-2684.0004
	75% Load	60	Input Power Load	2000	800
			Output Power Load	447.0939	-3578.6672
	100% Load	30	Input Power Load	2000	1000
			Output Power Load	447.0939	-4473.3339

Without any optimization of gears, the damage rate and safety factor of each pair of gears can be obtained by implementing the advanced system deformation, as shown in Table 7. The safety factor is that in engineering design, in order to prevent the consequences caused by material defects, manufacturing and assembly errors, and external force surges, the theoretically capable force of the force part must be greater than the actual force, that is, the ratio of allowable stress and actual stress, the theoretical safety factor of the gear should be greater than 1. If equal to 1, that is, the allowable stress and the actual stress are equal, the safety factor has no meaning; if it is less than 1, the gear system will be close to the critical value, which will cause unsafe accidents in case of external load surge. Different pairs of gears have different safety factors due to different manufacturing quality, reliability, external load force and other factors. From Table 7, it can be seen that the bending safety factor of the third pair of gears does not meet the theoretical requirements, which is the weakest link in the whole system.

Table 7. Gear safety factor and damage rate

Gear pair		Contact		Bending	
		Safety factor	Damage rate	Safety factor	Damage rate
First pair	Input	1.5921	0	1.3141	0
	Output	1.6439	0	1.2823	0
Second pair	Input	1.4273	0	1.6099	0
	Output	1.4745	0	1.0089	92.49
Third pair	Input	1.0684	41.12	0.9712	129.88
	Output	1.1048	26.36	0.9678	141.71
Fourth pair	Input	1.0896	31.76	1.1193	21.82
	Output	1.1247	20.87	1.2431	121.7

Therefore, in order to optimize the contact stress of the tooth surface and improve the service life of the gear pair, the micro-modification of the third pair of gears is carried out in this paper. According to the calculation results, the initial modification parameters of the pinion and big gear are determined. By comparing the simulation results, the modification parameters are adjusted and optimized. The contact spots, transmission errors and the reduction of maximum tooth contact and root bending stress are taken as evaluation criteria. Finally, the micro-modification quantity of pinion and big gear is determined as shown in Table 8.

Table 8. Results of micro-modification results of the third pair of gears

Shape modification	Tooth drum shape (μm)	Tooth helix angle (μm)	Tooth Profile Drum Quantity (μm)
Pinion	5	35	15
Big gear	30	40	22

The modification curve is shown in Fig. 8 and Fig. 9.

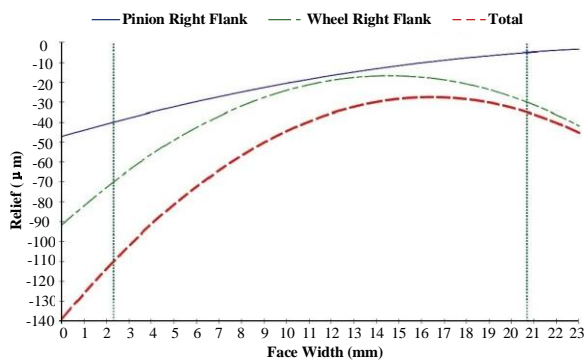


Figure 8. Tooth modification

5.2. Analysis of micro-modification results

After modification, the safety factor and damage rate of the third pair of gears are shown in Table 9. The damage rate decreases, the bending safety factor of pinion increases from 0.9712 to 1.2342, the bending safety factor of big gear increases from 0.9678 to 1.233, the bending safety factor of gears is greater than 1, and the contact safety factor also increases, which all meet the theoretical requirements of the gear safety factor. Therefore, the results show that the micro-modification of gears can improve the safety factor of the gear and prolong its service life.

Table 9. Gear safety factor and damage rate after modification

Gear pair		Contact		Bending	
		Safety factor	Damage rate	Safety factor	Damage rate
The third pair	Input	1.2825	1.63	1.2342	0.033
	output	1.3258	0.92	1.233	0.18

Fig. 10 is a comparison of the transmission error of the third pair of gears before and after shaping at different torques. Fig. 10(a) is the comparison of the transmission error before and after the gear modification at 25% torque, and Fig. 10(b) is the comparison of the transmission error at 50% torque. Fig. 10(c) is the comparison of the transmission error before and after the gear modification at 75% torque. Fig. 10(d) is the comparison of the transmission error before and after the gear modification at 100% torque. The overall analysis shows that the periodic variation of the transmission error curve after gear modification is smoother.

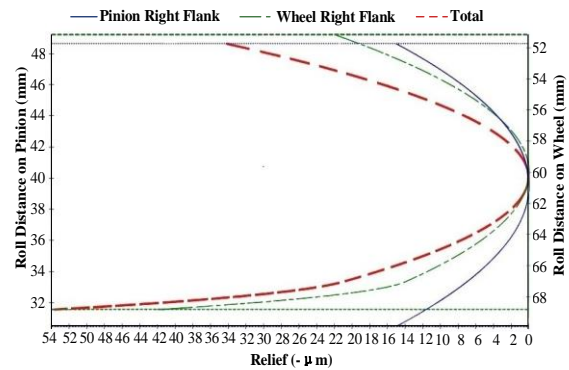


Figure 9. Tooth profile modification

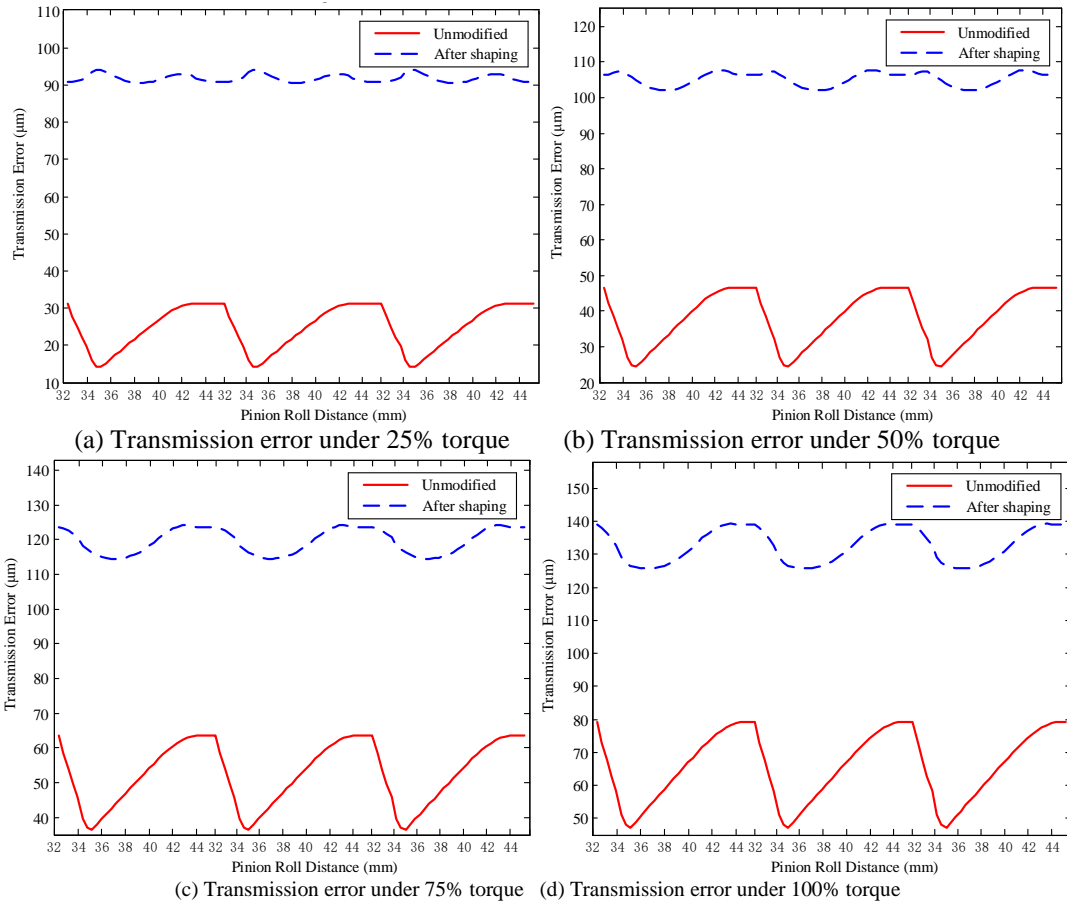


Figure 10. Comparison of transmission error before and after gear shaping

Although the transmission error value after modification is larger than that before the modification, the variation range of the transmission error under the four conditions after modification is known from Fig. 11, which are significantly smaller. The peak value is reduced by about 60% and the modification effect is remarkable. Among them, the transmission error of pinion and large gear is reduced from $22.2\mu\text{m}$ to $5.7\mu\text{m}$ under 50% torque, and the transmission error of pinion and large gear is reduced from $27.2\mu\text{m}$ to $9.6\mu\text{m}$ at 75% torque. Therefore, it can be seen that the micro-modification of gears can reduce the fluctuation range of the transmission error of the gearbox of the electric vehicle, so that the gear transmission is more stable and the vibration noise is reduced.

Fig. 12 shows the change of contact spot before and after modification under different torques. It can be concluded that the stress on the front tooth surface is not uniform, the stress on the left end of the gear is large, the gear teeth are prone to fracture during meshing, and the service life of the gear is low. After modification, the eccentric load of tooth surface is eliminated, the contact spot is uniformly stressed, and the maximum contact stress is close to the center of the gear. The load per unit length

of the tooth surface is reduced by about 25% under different torques and the effect is remarkable. The maximum stress at 50% torque decreased from 1679 Mpa to 1212 Mpa, and the maximum stress at 75% torque decreased from 1894 Mpa to 1363 Mpa. Therefore, considering the transmission error and contact stress of the modified gear, the micro-modification can prolong the service life of the gear teeth and improve the gear meshing performance, achieving the expected effect.

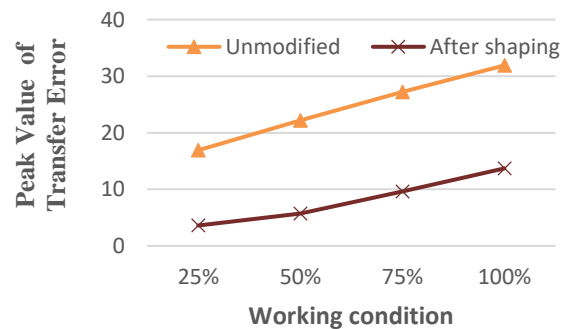


Figure 11. Comparison of peak value before and after modification

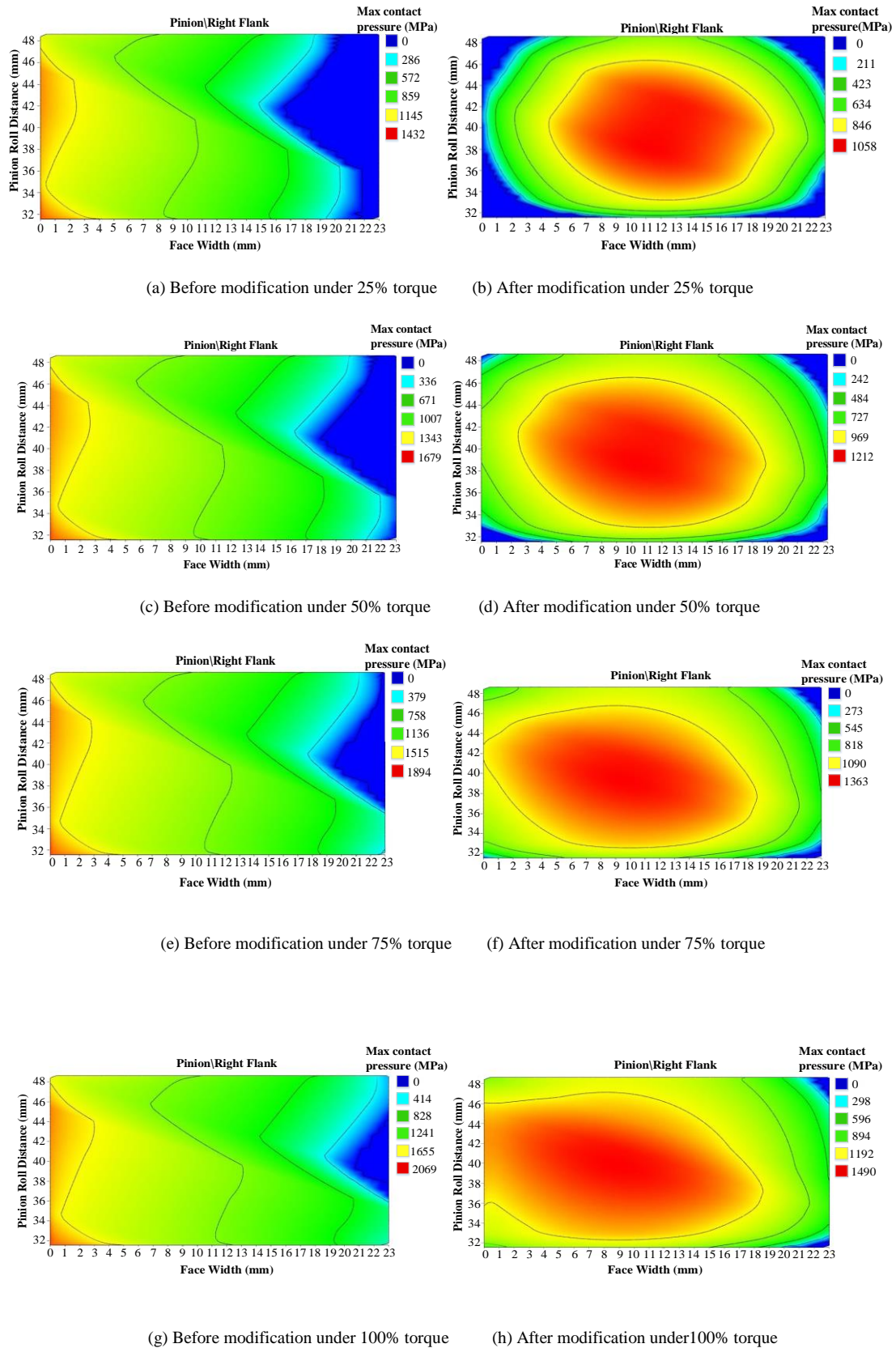


Figure 12. Comparison of contact spots before and after gear modification

6. Conclusion

1. The finite element model of the gearbox joint is established through the software of MASTA. The safety factor and damage rate of the four pairs of gear pairs of the gearbox are obtained through system deformation analysis. It is judged that the safety factor of the third pair of gears is less than 1, which is easy to cause damage, and this is used as the modification target gear. The transmission error, maximum contact stress, and contact spot diagrams are obtained by simulation. The optimum shape is determined by comparison and analysis before modification, so as to improve the safety factor and optimize the gear meshing performance.
2. Based on the common operating conditions of electric vehicles, at 75% torque, the transmission error of the third pair of gears decreased from 27.2 m to 9.6 m after the modification, which was about 65% lower than that before the modification, and the transmission error curve changed more smoothly periodically. The maximum contact stress of the gear after modification decreased from 1894Mpa to 1363Mpa, about 28% lower than that before modification, and the contact spot becomes even, eliminating the off-load phenomenon of the tooth surface, which greatly improves the stability of the gearbox in work, and extending the service life of the gear transmission system.
3. Gear transmission error analysis and load contact analysis play a good role in optimizing the performance of transmission NVH. Through the contact analysis of the gear, the contact situation can be directly judged, and the gear shape modification can be guided to improve the transmission error of the gear and the contact between the gear teeth.

Acknowledgments

This project is supported by the projects of technological innovation and strategic emerging industries of Fujian provincial economic and information commission, the projects of industry-university collaboration of Fuzhou municipal economic and information commission.

References

- [1] Shi RN. Design and experimental study on gear shaping of automotive transmission. Taiyuan University of Technology, 2015.
- [2] Zeng H, Wu RL. Research on gear modification technology of electric vehicle gearbox. *Automotive Parts*, 2014, (4): 34-36.
- [3] Ni G, Zhu C, Song C, Du X, Zhou Y. Tooth contact analysis of crossed beveloid gear transmission with parabolic modification. *Mechanism & Machine Theory*, 2017, 113:40-52.
- [4] Pan HX. Research on gear shaping technology. *China New Technology and New Products*, 2011, (13): 122-122.
- [5] Liu Y. Research on gear shaping strategy for internal helical non-circular gears and performance analyses for linkage models. *Journal of Mechanical Science and Technology*, 2014, 28(7):2749-2757.
- [6] KongX, Kang M, Fei XG, Liu W. Research on tooth profile modification of involute helical gear with high speed. *Modern Manufacturing Engineering*, 2013.
- [7] Yang TL, Ye X. Tooth modification of involute high speed gears. *Gears*, 1982, 6(3): 1-13.
- [8] Wang Y, Ma JS, Deng HY, Liu HP. Finite element analysis for tooth profile modification of gear-box of tracklayer. *Advanced Materials Research*, 2010, 156-157:621-624.
- [9] Cheng YK, Chen LF, Yu YD, Wang J. Finite element analysis of heavy-duty gear tooth profile modification based on elastic meshing theory. *Journal of Hunan University of Science and Technology (Natural Science Edition)*, 2005, (04): 34-37.
- [10] Kubo A, Kiyono S. Vibrational excitation of cylindrical involute gears due to tooth form error. *Bulletin of JSME*, 1980, 23(183):1536-1543.
- [11] Ding NS. Dynamic response analysis and study on the seismic characteristics of the beam string structure [D]. Lanzhou University of Technology, 2005.
- [12] Gao XX. Finite element analysis of gear-tooth contact of wind power gearbox. Dalian: Dalian University of Technology, 2008.
- [13] Kayabasi O, Erzincanli F. Shape optimization of tooth profile of a flexspline for a harmonic drive by finite element modelling. *Materials & Design*, 2007, 28(2): 441-447.
- [14] Wang Y. Contact analysis and modification research of automobile gearbox gears. Northeast University, 2010.
- [15] Litvin FL, Fuentes A. Gear geometry and applied theory. Cambridge: Cambridge University Press, 2004: 404-440.
- [16] Xiang Y. Research on tooth drum modification method for involute cylindrical gears. *Mechanical Transmission*, 2018,42(06): 44-48.
- [17] Xing B, Hou MX, Kong XF. Study on the calculation of meshing stiffness and load distribution coefficient of tooth profile modification gears. *Mechanical transmission*, 2017, 41(10): 96-103.
- [18] Xiong HG, Liu MF, Li GF. Study on the optimization of tooth profile modification of secondary helical cylindrical gear transmission. *Mechanical design and manufacture*, 2017, (01): 227-230.
- [19] Deng L. Vibration Analysis and Optimization Design of Automobile Gearbox. Chongqing University, 2013.
- [20] Guo Y, Kelley J, Parker RG. Nonlinear dynamics and stability of wind turbine planetary gear sets under gravity effects. *European Journal of Mechanics-A/Solids*, 2014, 47:45-57.
- [21] Zhu Y, You QQ. Modeling of gear transmission system and analysis of dynamic response characteristic. *Journal of Mechanical Transmission*, 2018, 42(10):160-165.

Design of Digital Aerial Photography System for Unmanned Aerial Vehicle Based on Wireless Sensor Network

Rui Wang^{*}, Nian-chu Wu, Xin-li Yu

School of Mechanical Engineering, Liaoning Shihua University, Fushun 113001, China

Received OCT 16 2019

Accepted JAN 25 2020

Abstract

The traditional UAV aerial photography system has the disadvantages of unclear imaging, low system efficiency and poor flight control effect. Thus, a digital aerial photography system based on wireless sensor network is proposed. Firstly, the principle of aerial photography system is analyzed, and the wireless sensor network is set up. A large number of wireless sensor nodes are deployed in the interval whose functions such as wireless communication and calculation are completed by nodes. For example, the SN-RN data acquisition layer, the RN-UAV relay transmission layer, and the UAV-DC mobile aggregation layer are designed to form a wireless sensor network architecture, and the UAV digital aerial photography technology is combined to form the wireless sensor network. Experiments show that the medium error, maximum error and medium error limit of the digital aerial photography of the UAV are low, the total working time of the system is short, and the accuracy of the flight execution of the UAV is maintained between 93%-95%, and always stable. Therefore, the overall imaging effect of this method is better, the system work efficiency is higher, the system control effect is better, and it is more practical and advantageous.

© 2020 Jordan Journal of Mechanical and Industrial Engineering. All rights reserved

Keywords: wireless sensor network; UAV; node; aerial photography; system design.

1. Introduction

Unmanned aerial vehicles (uavs), referred to as uavs, are unmanned aircraft operated by radio-controlled equipment and self-contained programmed controls, or operated autonomously, either completely or intermittently, by onboard computers. With the development of science and technology, UAV technology has been continuously improved. The digital aerial photography of UAV plays an increasingly important role in various fields due to its simple operation and high efficiency [1]. A set of UAV digital aerial photography system is mainly composed of flight platform, aerial photography system, ground control system and influence processing system. It uses UAV as flight platform and uses high-resolution CCD digital camera, air and ground control system and other equipment to achieve route planning and monitoring, video capture, acquisition, transmission pre-processing functions such as digital aerial photography system [2].

Wireless sensor network (WSN) is a combination of embedded technology, network technology, and sensor technology. It is used in military, industrial, agricultural, and other fields for information acquisition and object tracking, which is a hot topic at home and abroad. [3].

In the WSN of the UAV digital aerial photography system, a large number of nodes with low power consumption are often randomly scattered [4]. A node is a

micro-embedded system that senses and collects information from the environment. The UAV digital aerial photography system WSN requires self-assembled network and data transmission as a whole. Each node is required to be able to collect, process and transmit local information and data. It is also required to perform operations, such as storage, calculation, and aggregation on data forwarded by other nodes. Since the nodes are generally powered by batteries, the functional design requires that the nodes must be low-power, so the processing power, storage capacity and communication capabilities of the nodes are relatively weak [5, 6]. Due to the complex environmental conditions of aerial photography, it is unrealistic to replace the energy of a node or a supplementary node. Therefore, how to use fewer nodes to achieve efficient and reliable aerial photography has become one of the hotspots in recent years.

Literature [7] proposed a method for designing wireless sensor networks on UAV. This method gave the overall architecture and hardware and software design of the wireless sensor network combined with UAV application by analyzing the demand monitoring status of the UAV. However, the resulting aerial image resolution is not ideal. The method of literature [8] was based on the aerial photography system of the micro-autopilot. The method was mainly composed of the following parts: micro-automatic pilot aircraft (platform), aerial photography subsystem (i.e. ordinary or digital camera and electronic

* Corresponding author e-mail: wangrui@lnpu.edu.cn.

shutter control), aerial photography subsystem (digital CCD camera or digital video camera) and image real-time transmission, display and the recording subsystem, which could simultaneously carry the meteorological sounding subsystem. Atmospheric temperature, pressure and humidity could be obtained simultaneously during aerial photography or aerial photography, but the system performed poorly on planned routes. Literature [9] proposed the design of a multi-rotor UAV route planning system, introduced the architecture of the multi-rotor UAV aerial photogrammetry system, analyzed the characteristics of the multi-rotor UAV, and summarized its advantages. Based on the calculation method of related parameters, a route planning algorithm was developed based on this algorithm, and a multi-rotor UAV route planning system that could be used with the multi-rotor UAV ground station was designed and implemented. The overall work efficiency was not ideal.

Avoiding the shortcomings of traditional methods, this paper proposes a digital aerial photography system based on wireless sensor network. Firstly, the principle of aerial photography system is analyzed. On this basis, the wireless sensor network is set up, a large number of wireless sensor nodes are deployed in the interval, and the wireless communication and computing functions are completed by the nodes. the SN-RN data acquisition layer, the RN-UAV relay transmission layer and the UAV-DC mobile aggregation layer are designed to form a wireless sensor network architecture, and the UAV digital aerial photography technology is combined to form a UAV digital aerial photography system based on the wireless sensor network. At the same time, the system architecture can extend the life of the sensor node by alleviating the transmission task of the sensor node in the WSN; by increasing the function and power supply of the relay node, the resource consumption caused by the failure of the transmission node is reduced; the data acquisition efficiency and system life of the UAV digital aerial photography system are improved by the good network communication quality provided by mobile nodes.

2. Material and Methods

2.1. Principle Analysis of Digital Aerial Photography System for UAV Based on Wireless Sensor Network

When the fluid is flowing in the pipeline, on the surface of the plate or on the surface of an object with a certain shape, some or all of the fluid will change from laminar flow to turbulent flow with the change of conditions. At this point, friction coefficient and resistance coefficient will change significantly. The Reynolds number at the transition point is the Reynolds number technique. There are many characteristics analysis based on IEEE 802.15.4 low-power network and cellular network. Therefore, this study mainly analyzes the characteristics and performance between UAV and RN. The schematic diagram of the data exchange between UAV and RN is shown in Figure 1 [10].

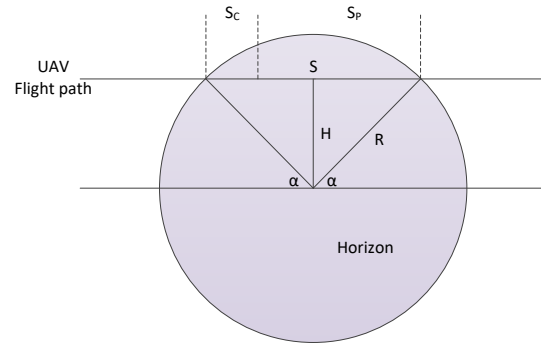


Figure 1. Plan of data exchange between UAV and RN

Note: H is flight height, m; S is flight distance, m; S_c is communication flight distance, m; S_p is change flight distance, m; R is communication radius, m; α is angel, ($^\circ$).

According to Figure 1, the following equation can be obtained:

$$H = R \cdot \sin \alpha \quad (1)$$

where: H is the height of the UAV from the ground, that is, the flying height; R is the communication radius of the RN; α is the angle between the connecting line between the UAV and the RN and the horizontal plane.

$$S = 2R \cdot \cos \alpha \quad (2)$$

where: S is the distance that the UAV and RN actually fly within the communicable range.

$$S = S_c + S_p \quad (3)$$

where: S_c is the distance the UAV can fly from the time the UAV enters the RN communication range to the time it can establish communication with each other. S_p is the distance the UAV flies during the data exchange between the UAV and the RN [11].

$$R = \sqrt{H^2 + (S/2)^2} \quad (4)$$

The time between UAV and RN for data exchange should meet the following equation:

$$t_e = \frac{S_p}{V} \quad (5)$$

where: t_e is the time required for the data exchange and processing of the UAV and the RN, and V is the flight speed of the UAV. The data exchange between the RN and the UAV should satisfy the following equation [12]:

$$L = (b \cdot t_e) / 8 \quad (6)$$

where: L is the length of the number of data bytes exchanged between the RN and the UAV; b is the data transmission rate between the RN and the UAV.

Equation (5) is substitute into equation (6), it can get:

$$L = \left(b \cdot \frac{D_p}{S} \right) / 8 \quad (7)$$

To ensure that all data cached in the RN can be collected by the UAV during the communication time, the RN's cache size should be greater than or equal to L . The

actual communication time between the UAV and the RN is greater than or equal to the sum of the time between the establishment of the connection and the time of data exchange [13, 14].

$$t \geq t_c + t_e \quad (8)$$

where: t is the time from the UAV entering the communication range of the RN to the communication range from the R; t_c is the time required for the UAV to enter the RN communication range to establish a process that can communicate with each other. The UAV speed is variable. When the UAV searches for a relay node along a set trajectory or in a dynamic random flight mode, the UAV cruises at a higher speed (usually 5 to 15 m/s) when the UAV enters the relay node communication range of the ground. In order to ensure good transmission quality and ensure that the data stored in the relay node can be completely transmitted to the UAV, the UAV flies at a lower speed and hovers in the air (usually 0-5 m/s), to perform data collection tasks. After the data transmission is completed, the UAV returns to the original cruise speed, continues to search for the next relay node, or returns to the base [15-17].

2.2. Design of Digital Aerial Photography System for UAV Based on Wireless Sensor Network

2.2.1. Composition of Wireless Sensor Networks

The wireless sensor network is composed of SN (sensor node), relay node (RN, relay node), unmanned aerial vehicle (UAV), data center (DC, data center) and other elements, as shown in Figure 2.

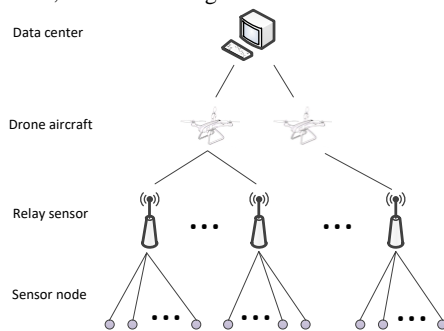


Figure 2. Wireless sensor network system

The nodes of the wireless sensor network have the characteristics of small size, low energy consumption, low price, and have the functions of sensing the external environment, performing wireless communication and computing. Such nodes can sense and collect data and information from a large number of environments. A large number of such wireless sensor nodes are deployed in a large geographic area that will form a dense wireless ad-hoc sensing network [18].

The most important function of the relay node is to connect the nodes of the wireless sensor network, the UAV communication, and the data transmission bridges and hubs. The relay node itself does not need to perceive the environmental information, and it acts as the data concentration node of the wireless sensor network. The sensor node in the area where it is located is notified to collect data, the data is stored in the buffer of the relay node, and the data is transmitted to the UAV within a

given communication time. The distance between each relay node can be very long and does not need to communicate with each other [19]. In general, the relay node has a relatively strong power supply and a long life period relative to the sensor node, and can provide a large communication range by means of antenna gain and others.

The UAV is a fixed-wing or rotary-wing unmanned aircraft with its own power, controllable and mobile communication equipment. It can be reused without a cockpit, but equipped with autopilot and flight attitude control. The mobile communication device carried by the UAV supports a variety of communication protocols and a variety of communication interfaces, and can communicate with the ground or air devices in a variety of communication modes. Since the UAV can provide power, the portable device has certain computing power and storage function, which can realize data compression and processing. When the communication quality is not good, the data received from the ground can be stored in the cache and recovered well. Data is transmitted to the data center when the communication quality is good [20].

The data center is composed of resources, such as servers, storage devices, databases, geographic information systems, and high-speed network bandwidth. The data center is responsible for receiving data transmitted by the UAV. In order to ensure the integrity and reliability of the data, the data center will perform statistical analysis and data mining on the collected information, and make decisions based on the results of the analysis or take corresponding actions (such as issuing instructions to the UAV, adjusting the path to collect data, etc.). Data in the data center can be accessed by users, computers or other devices, providing access to the service terminals via the Internet or mobile internet, and displaying the analyzed data information in a friendly and intuitive interface [21].

2.2.2. Architecture of Wireless Sensor Network

The architecture of wireless sensor network consists of the SN-RN data acquisition layer, the RN-UAV relay transport layer and the UAV-DC mobile aggregation layer, as shown in Figure 3.

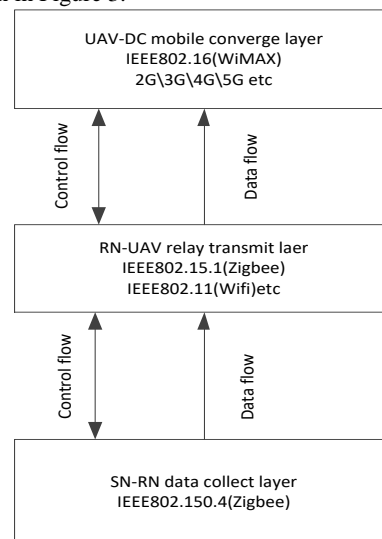


Figure 3. Wireless Sensor Network Architecture

1. SN-RN data acquisition layer

The data acquisition layer consists of a network established between the sensor node and the relay node. The data acquisition layer network has the following characteristics [22]:

- Limited hardware resources: therefore, the protocol layer of the operating system of the wireless sensor node needs to be simplified.
- Limited energy: since the wireless sensor node has less energy resources and cannot replenish energy at any time, once the energy is exhausted, the wireless sensor node will not continue to work normally.
- Distributed: multi-distributed structure is adopted, in which wireless sensor nodes can enter and leave the network at any time.
- Self-organization: through layered protocols and distributed algorithms, wireless sensor nodes can spontaneously schedule their work processes appropriately. When deployed to a specific area and activated, the corresponding network can be organized spontaneously.
- Dynamic topology: the system is a dynamic network, in which the wireless sensor nodes will exit the network due to running out of power or damage, and will be added to the current network because of the task, so the topology of the network is dynamically changed.
- Dense distribution: in order to enhance the task monitoring in the target information collection area, a large number of wireless sensor nodes will be deployed to this area.

Due to these characteristics of the data acquisition layer, this layer usually uses the IEEE 802.15.4 network communication protocol to achieve the above functions. A typical use of the IEEE 802.15.4 protocol is Zigbee. The transmission rate of the IEEE 802.15.4 protocol is generally less than 1 Mbps. IEEE 802.15.3 can also be used if the data transfer rate is required to increase. But high transmission rates also mean higher energy consumption. This layer is usually meshed by mesh, and the network hierarchy is usually a star structure or a tree hierarchy.

At the SN-RN layer, sensor nodes are dispersedly deployed in the aerial image area. When a star network hierarchy is adopted, each sensor node is centered on only one relay node, and the sensor nodes are only fixed with one at each monitoring cycle. The relay node communicates and monitors the data transmission. The sensor node and the sensor node are kept at a certain distance and do not communicate with each other. The data collected by all sensor nodes are directly aggregated to the designated relay node [23]; When adopting a tree-

like hierarchical structure, the sensor nodes at the outermost periphery are only responsible for the function of data collection and uploading data, the sensor nodes in the middle are responsible for data collection and data forwarding, and the sensor nodes communicate with each other. The data collected by all sensor nodes is directly or indirectly aggregated to the designated relay node, in order to minimize the energy consumed by the sensor nodes in the data transmission process, the level of the tree hierarchical structure cannot exceed 3 floors. In contrast, the star structure system has a longer life cycle, and the tree-level structure covers a larger monitoring area. Each relay node forms an autonomous sensor network area with a number of sensor nodes surrounding it [24].

2. RN-UAV relay transport layer

The relay transport layer consists of a network established between the relay node and the UAV mobile node. The relay transport layer network has the following characteristics:

1. Simple structure: direct communication between UAV and RN, that is, only one hop direct connection.
2. More energy: RN is generally powered by solar energy, and UAV can be powered by a rechargeable battery.
3. Stable and reliable: UAV communicates with the ground RN in the air, which may be less likely to be blocked by plants or houses, and the packet loss rate will be reduced.
4. Long communication distance: good communication quality, can provide antenna coverage with larger power.

From the perspective of compatibility, the relay transmission layer can use the IEEE 802.15.4 protocol for enhanced signals, or the IEEE 802.11 protocol with longer transmission distance. The network topology between the RNs of this layer is dominated by a linear structure or a grid structure. This topology facilitates the UAV to perform tasks in a straight line. For UAVs with single or multiple rotors, the UAV can enter the next straight line of data acquisition at the corner of the acquisition information area at a right angle.

In the RN-UAV layer, the relay nodes are deployed in a linear manner according to the rules. Many relay nodes are arranged in a row, and the adjacent two nodes are distributed in a distance of several hundred meters. There is no limit on the number of relay nodes in each row, and no communication and data transmission between any two relay nodes. The relay node is not responsible for the task of direct data collection. It is responsible for storing the monitoring data transmitted by the adjacent sensor nodes in its own buffer, waiting for the UAV to collect data.

5. UAV-DC mobile aggregation layer

The mobile aggregation layer consists of a network established between a single or multiple UAVs and a data center. A cellular data network is directly connected between the UAV and the DC. The mobile aggregation layer network has a very long communication distance, has error detection and packet loss retransmission function,

supports real-time or delayed data transmission, and has a simple structure.

2.3. UAV Aerial Photography System Based on Wireless Sensor Network

2.3.1. Composition of UAV Digital Aerial Photography System

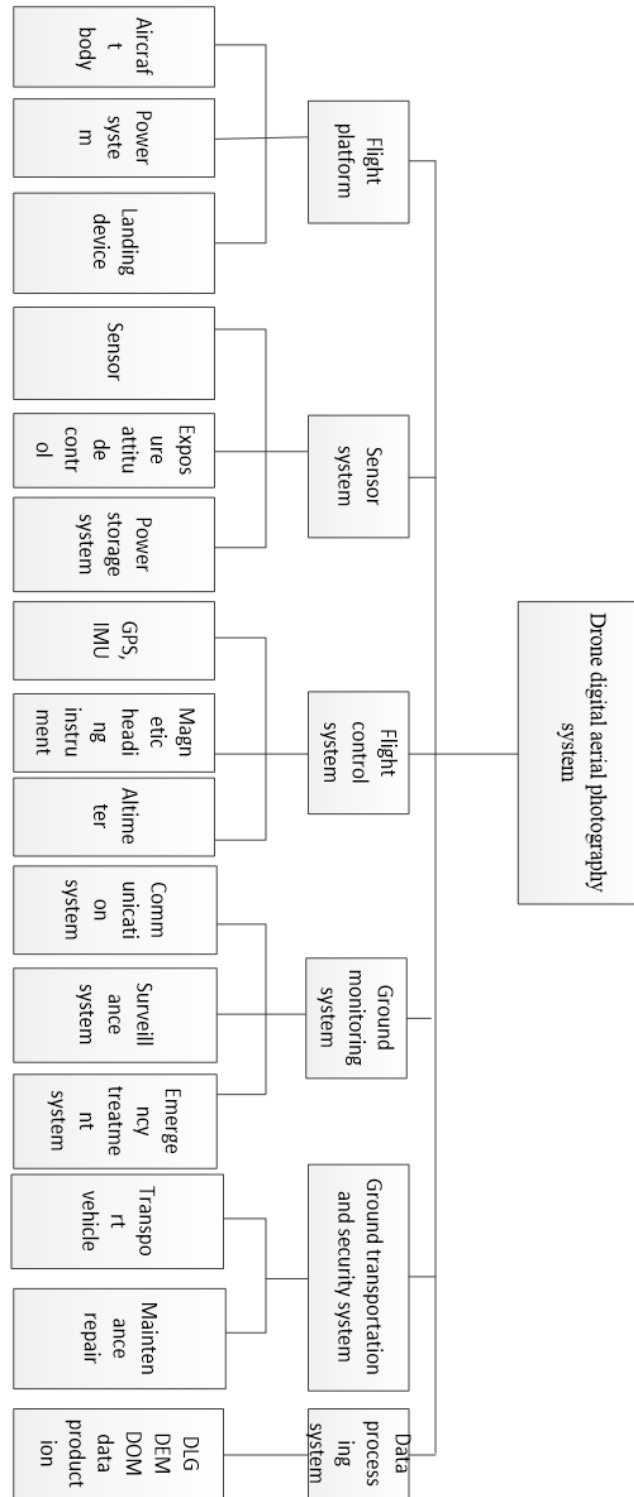


Figure 4. Composition of UAV low-altitude remote sensing aerial photography system

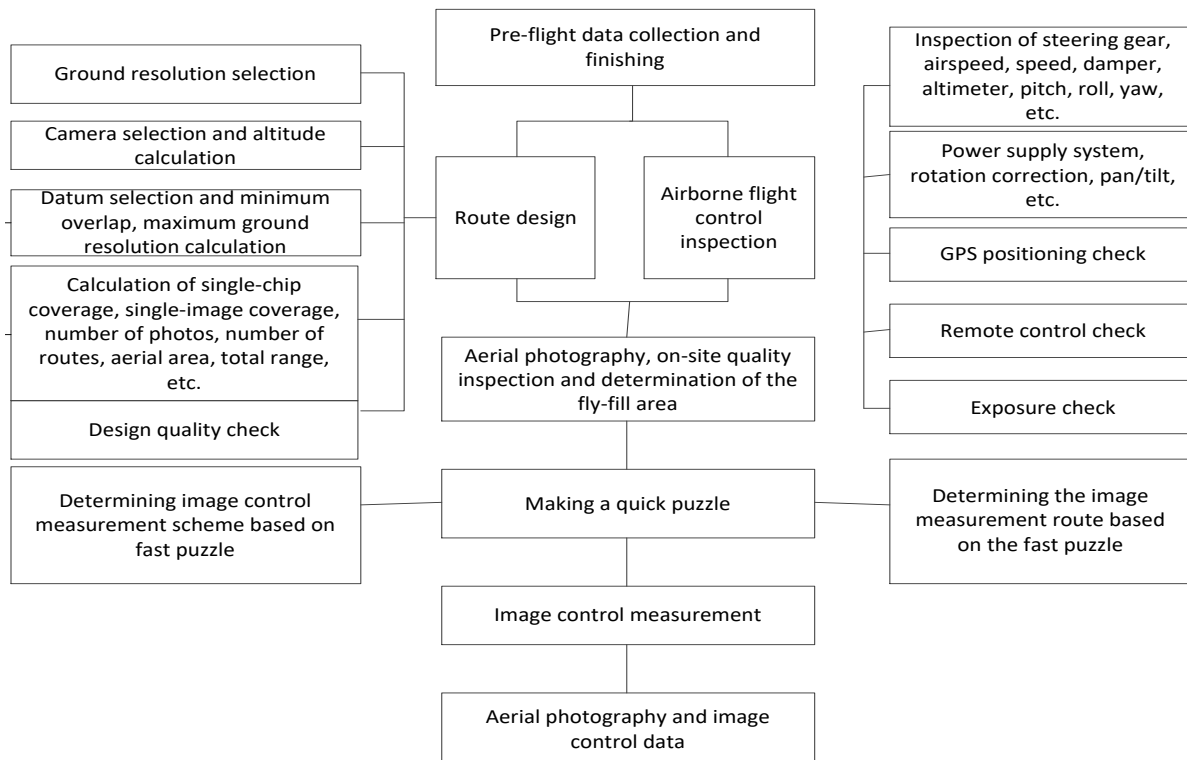


Figure 5. UAV aerial photography system technical process

2.3.2. Technical Process

Like traditional aerial photography, digital aerial photography of UAVs based on wireless sensor networks also requires steps, such as route design, aerial photography, quality inspection, fly-fill or fly-back, and image-controlled measurement. The difference is that the route design of the UAV aerial photography is small, so there is no need to consider the change of the curvature of the earth; the inspection of the aerial quality can be completed at the aerial scene without the need to print photos; Photographic measurement work under certain conditions must first create a full-area fast mosaic. The UAV aerial photography system technical process is shown as Figure 5.

1. Work permit and airspace coordination

At the first time after entering the photographic area, it should contact the local people's government or the competent department of surveying and mapping, timely inform the relevant projects, and coordinate the local personnel in traffic, accommodation, flight safety, guidance, medical treatment and other aspects to help, etc. If there is a confidential unit, military area or airport near the survey area, it is necessary to go to the air reference center under the jurisdiction of the survey area to handle airspace coordination procedures.

2. On-site survey

After coordinating local conditions and airspace, personnel should be organized to conduct on-site reconnaissance and collect relevant information. These materials include:

1. The weather conditions in the photography area in recent days.

2. Using the handheld GPS, the corners of the photography area is drilled and corresponding records are made. Google Earth can be used to verify the correctness of the four corners coordinate point of the survey area and confirm whether the photography area is correct.

Looking around the survey area, it is to see if there is a high mountain, and estimate whether the height of the mountain and height difference have an impact on flight safety, whether there is snow on the mountain, and whether the image affects the quality.

3. A suitable landing site is found according to the type of aircraft.

3. On-site route design

Digital photography of UAVs is generally performed on digital aerial photography in a small area. Unlike traditional aerial photography, there is no need to consider the curvature of the earth in the design of the route, and it is not necessary to know the elevation of the ground point very accurately. Traditional aerial photography has clear operating specifications and procedures. It is necessary to use a 1:10000 or 1:50000 topographic map or use the existing DEM for the design of the reference surface. If it is necessary (when the height difference is greater than 1/6 altitude), photographic partitioning is set. For digital aerial photography of UAVs based on wireless sensor networks, in general, the four-corner coordinates of the camera zone can be known for route design. Photographic partitioning is set under very special conditions [25].

1. According to the scale of the map, the approximate ground resolution is determined. The corresponding ground resolution should be selected before the relative altitude is determined.
2. Viewing the general situation of the photography area: the coordinates of the photography area or the

coordinates of the photography area required by Party A are entered into Google Earth in the computer to check whether the basic situation of the photography area is consistent with the mastery of the situation, whether there are an area of mountains, military facilities, airports, etc. that is not conducive to aerial photography.

3. Selection of the base plane of the photography area: according to the condition of photography area displayed in Google Earth, the highest and lowest elevations of the area are counted, and the datum of photography area is determined according to the maximum and minimum elevation values. The datum is generally the average of the maximum and minimum elevations in the photography area.
4. Selection of the appropriate heading and side overlap: the heading and side overlap required for the map are selected. For example, the target area of Longma Hotel in Cangzhou City, Hebei Province is to measure 1:2000 orthophotos, the heading overlap can be set to 65%, and the side overlap is set to 35%.
5. The heading and side overlap of the highest point, and the ground resolution at the lowest point in the area are calculated.

$$\text{Minimum ground resolution} = \frac{\text{Datum elevation} - \text{Lowest elevation} = \text{Relative altitude}}{\text{Focal length}} \times \text{Single cell size}$$

$$\text{Maximum overlap in the photo zone} = \frac{\text{Heading overlap} - \frac{\text{Highest elevation} - \text{Datum elevation}}{\text{Relative altitude}}}{1 - \frac{\text{Highest elevation} - \text{Datum elevation}}{\text{Relative altitude}}}$$

6. Adjusting the ground resolution and overlap for recalculation: when the minimum ground resolution of the photography area exceeds the resolution required by the map, or when the highest overlap of the photography area is less than the mapping requirement, the ground resolution must be changed. The relative altitude, the lowest point ground resolution, and the highest point overlap are recalculated until the requirements are met.
7. Coordinate transformation in route design: WGS84 latitude and longitude coordinates - used in UAV flight control
8. Plane coordinates must be used in the route design. If Party A has given a certain plane coordinate, it can be directly input into the route design software for calculation. If the four-corner coordinates are selected in Google Earth, it can be converted to WGS84 plane coordinates and then designed. Then it is converted into WGS84 latitude and longitude coordinate input flight control.
9. Calculating the coordinates of each exposure point: according to the set value, the route design software is entered and the coordinates of the exposure points are calculated. Statistics of the number of flights, number of photos, baseline length, side to side distance and total voyage of this aerial photograph are given.
10. Route design under special circumstances: When the elevation of the area is greater than 1/6 voyage, in principle, a photographic division should be established. For the aerial photography of UAVs, the elevation is broad. When the elevation of the

photography area is large, it is to try to increase the resolution and increase the overlap method to overcome. When this method still does not work, a photography partition must be set up.

4. Debugging of ground monitoring station

The ground monitoring station personnel designs the exposure point coordinates on the day before the flight or on the flight site, and introduces the coordinate points of exposure point into the ground monitoring software to confirm that there is no error before flying.

5. Take-off check

At the same time as the route design, in this time, the airborne flight control, camera, etc. are installed. This series must be checked after installation, or whenever the aircraft falls before entering the flight. There are mainly the following checks:

1. Yaw check: the gyro zero point is correct, and the right turn is positive. In UAV mode, when the PID value of running channel is not 0, the rudder deflects the damping yaw change in the corresponding direction.
2. Altimeter check: if there is a condition to get the air pressure value of the current control box, set the current air pressure value and the current altitude value on the ground station. The height of the aircraft is changed, and the height display value will be changed accordingly.
3. Speed check: if the aircraft is equipped with a speed sensor, the engine is turned by hand to see if there is a speed display on the ground station, and the speed division setting is corrected.
4. GPS positioning check: the time from power on to GPS3D positioning should be about 1 minute. If it is more than 5 minutes, it can't be positioned, and the GPS antenna connection or other interference are checked. After positioning, the number of satellites is generally more than 6 and the PDOP horizontal positioning quality data is as small as possible, generally between 1 and 2.
5. Vibration test: when the engine starting, the jitter of the sensor data at different speeds, and the beating of the control surface are observed, especially the attitude data shown by the attitude table (level meter). All beating must be in a small range, otherwise the damping measures should be improved.
6. Battery test: the effective working time of the battery is determined through the discharge test to ensure that the future flight is within a reliable and guaranteed power supply time. The alarm voltage of the ground station is set to: main power of 7V, servo power of 4.6 V.
7. Impact of digital transmission on the sensor: in UAV mode, if the impact is large, the actual value in the sensor data is checked to see if the gyro value is around zero; otherwise the transmitter antenna position must move. Other transmitters must also be tested this way.
8. Flight data check: if the flight path data has been uploaded for flight control check.

6. Aerial camera preparation

The camera first needs to adjust the focus to infinity, fix it with mechanical devices, and purchase a professional camera to place the equipment box for safe transportation.

The following preparations should be made before taking off:

1. Firstly, it is shoot on the ground, the purpose is to detect whether the image is illusory, and the aperture and shutter required for this flight are set.
2. When loading and unloading from the aircraft, it is handled gently to avoid touching the lens.
3. It is checked if the M file is used before the day, the lens cover is open, the camera is working properly, and there is power.
4. During the flight, a person is scheduled to record the exposure of each route, in order to compare with the final number of images.
5. After the flight is over, if the total quantity is correct is seen. The purpose is to stop the camera from working when the flight is halfway, and the total number is correct to download the image. Whether each piece can be opened is checked, a few images (urban, urban edge, mountain area) are selected to view the actual pixels in the PS.
6. One person is ready to record the flight situation, and whether there is any problem with the rise and fall. If there is any problem, it should specify the situation, process and result of the problem. In addition, basic information, such as weather, site conditions, and shooting conditions should be recorded.
7. The flight team should send the record (document) back to the technical person in charge every day. If the delay is caused by the lack of access to the Internet, etc., the delay should be notified by SMS.

7. UAV digital aerial photography

During the digital aerial photography of the UAV, attention should be paid to the monitoring of the flight state of the aircraft and the working state of the airborne sensor. There should be a response plan for various possible emergencies to ensure the safety of the flight process and the quality of the mission completion.

8. Field data finishing

After the UAV has landed, the image data should be downloaded in time, and some necessary basic checks should be performed on the acquired data.

1. Image overview check

Data is organized in such a way that each original image can be opened, each storage is complete, and the exposure is not moderate.

- It is checked whether the number of exposure points is consistent with the number of images. If it is inconsistent, the cause is found in time.
 - It is checked whether the recorded value of each route is consistent with the number of images actually flying. For example, if 20 images are recorded in the ground station of the first route and 005 is the first, it is checked whether 05-024 is the first route, especially the relationship between 024 and 025.
 - The images are loaded in folders according to the number of routes, and the number of images on each route should be the same.
2. The flight record form is filled in.
 3. Image naming rules

At present, the exposure point name of the flight control output starts with 1 and the serial number is

recorded. In order to ensure that the coordinate name of the exposure point is consistent with the image name, it is convenient to map the image to the exposure point when the exposure point is displayed, and the image name does not need to be changed. However, before the aerial photography is carried out, the original image in the camera should be deleted and set from 1 to ensure that the aerial photography image starts from 001. After the inspection is completed, the name of the image will be changed according to the requirements of the national basic aerial photography.

4. Packing and sending

All the images are packed by route folder, and it also includes the flight record table and the coordinate data of exposure point.

9. On-site quality inspection

1. Initial image inspection: the basic situation of the image is checked, including the number of images, the number of navigation belts, whether the image quality is clouded, foggy, snowy, whether the image is illusory, and whether the image is named correctly.
2. It is checked whether the data is complete: to check whether the flight record table, exposure point coordinate data, etc. are existed, and whether the completeness and specification are filled in.
3. Displaying the coordinates of the exposure point: it is checked whether the coordinates of the exposure point are consistent with the actual flight conditions. When exposure coordinates are clearly deviated from the route, it should make good records and check the images.
4. Image resampling: image resampling is performed in the PS, the purpose is to reduce the amount of image data, which is convenient for checking operations.
5. Image rotation: the image is rotated according to the method of filling in the flight record table, paying particular attention to whether the rotation of the odd-numbered and even-numbered navigation belts is the same.
6. Quality inspection: inspection records are output, and the unqualified images should be recorded accordingly.
7. Notice to make up and re-fly: if the image quality is found to not meet the design requirements, or there are relative loopholes or even absolute loopholes, it should be timely replenished or even re-flayed.

In addition, there are a few cases where the angle of the roll of the UAV is large, and the displacement of the adjacent headings between the heading and the sideways appears. When the elevation difference is large, some image pairs with small three-dimensional overlap will affect the turning point of the relative directional connection point in the later period, forming the so-called image island, which affects the construction of the free network, and must be supplemented.

When flying a certain route, it should not be re-float according to the original design. When the roll angle is large and the fly is made up, it is recommended that the first exposure of the fly-fill route be designed and flowed forward by adding half of the photographic baseline at the original first exposure point to ensure the heading and the adjacent airfoil. Correspondingly, it is also beneficial to insert the supplementary flying aerial film in a certain area

with a small degree of overlap, and the baseline between the inserted aerial film and the original flying aerial film is too short, which causes the intersection angle to be too small, and affects the construction of the free network; When the overlap is small and the fly is compensated, the reference plane of the area can be appropriately raised to increase the overlap on the premise that the ground resolution does not change greatly. After the calculation, the fly-fill reference plane is determined and the flight is carried out.

10. Image processing

The image that has passed the inspection must be pre-processed before calling the customer or the next process, including:

1. Format Transferring: different internal storage formats of camera may be different. Generally, all images need to be saved as TIF format.
2. Distortion error correction: correction of the distortion is performed by the pre-processing software according to the identified camera calibration parameters. The blackened edge of the corrected image indicates that the correction has been completed. When the parameters are input in the post-empty three measurements, all the distortion parameters are zero.
3. Submission of image results: the image results are organized, generally including the following:
 - original image of the submarine zone;
 - image after correction of the distortion of the submarine;
 - flight record table;
 - coordinate file of exposure point;
 - image inspection record;
 - data compilation record;
 - camera parameter file;
 - main point offset file after distortion correction.

3. Results

In order to test the validity of the paper, the design experiment is verified.

3.1. Experiment Setting

Flight platform setting: the flight platform is a hand-diver UAV, the production material is Elapor foam, and the length of wingspan is 163 cm.

The length of plane is 120 cm, the take-off weight is 2.7 kg and it has a lithium polymer battery (18.5 V, 5300 mAh). The suitable flying height is 59-750 m, the average wind speed of wind resistance is 50 km/h, the suitable temperature is -20°C-45°C, the maximum endurance time is 50 min, and the cruising speed is 65 km/h. The area covered by a single flight is shown in Table 1.

Table 1. Single flight coverage area of UAV system

Ground resolution/cm	Row height/m	Side overlap 65%	Side overlap 20%
		Side overlap 85%	Side overlap 80%
		Aerial area/km ²	Aerial area/km ²
1.6	59.4	0.7	1.62
2.6	96.5	1.13	2.65
3.2	119	1.42	3.20
5.0	186	2.25	5.12
10.0	371	4.54	9.97
20.0	743	8.67	18.20

Since the stability of the UAV's flight is easily affected by the airflow, in order to ensure that the aerial photography image does not have a loophole, the heading and the side overlap should be increased. Therefore, the design heading overlap is 70%, and the design side overlap is 50%.

3.2. Performance Testing

3.2.1. Aerial imaging effect

By using the method of this paper, the method of literature [7] and the method of literature [8], low-altitude aerial photography (70 frames in 1:2 000 frames) is carried out in a region of about 50 km², and the error in relative orientation is 4 μm (the pixel size is 6.4 micron m). The error plane in the encryption point is 0.5 m and the height is 0.5 m. The median error of DOM detection point is 0.63 m. The accuracy of aerial imaging results under different methods is shown in Table 2.

Table 2. Accuracy comparison of aerial imaging results

Method	Number of DOM checkpoints	Medium error/m	Maximum error/m	Medium error tolerance /m
The proposed method	30	0.63	1.07	1.2
Method of literature [7]	30	0.78	1.43	1.44
Method of literature [8]	30	0.92	1.32	1.48

Analysis of Table 2 shows that under the same number of detection points, the medium error, maximum error, and medium error tolerance of the digital aerial photography of the UAV by using the proposed method are 0.63 m, 1.07 m, and 1.2 m, respectively, which are lower than that of the method of literature [7] and the method of literature [8]. Therefore, the aerial imaging accuracy of the proposed method is higher and the imaging effect is better.

3.2.2. Comparison of system work efficiency

The experimental is set to test the work efficiency of system by using the proposed method, the method of literature [7] and the method of literature [8] method, a total of 4 sets of experiments are designed. The working time of the system is recorded as shown in Table 3.

Table 3. Comparison of system working hours under different methods

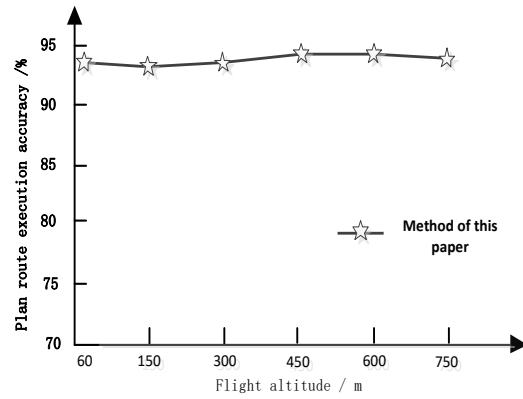
Number of trials	RN-UAV operation Adjust /s	Total working time of using the proposed method/s	Total working time of using the method of literature [7]/s	Total working time of using the method of literature [8]/s
1	723.114	6215.712	32417.991	29845.376
2	3892.231	78923.115	253241.988	395412.624
3	4231.892	81229.315	293134.221	264584.335
4	633.201	5332.633	27214.454	9478.560

Analysis of Table 3 shows that when the RN-UAV operation adjustment time is the same, the proposed method is used for aerial photography, the total working time of the system is 6215.712 s, 78923.115 s, 81229.315 s, and 5332.633 s, respectively, which are lower than the that of the method of literature [7] and the method of literature [8]. Therefore, the aerial photography work of the design method in this paper is short in time and the system works more efficiently.

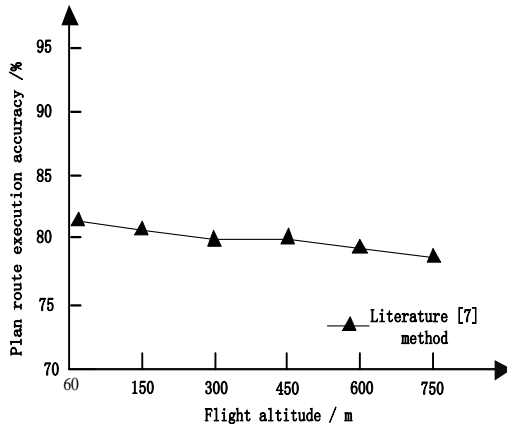
3.2.3. Comparison of planned route execution levels

The proposed method, the method of literature [7] and the method of literature [8] method for experimental testing is set to plan the route execution effect. According to the input aerial range and aerial camera parameters, the optimal route of the aerial camera area is solved, the coordinates of the aerial camera center point are solved, coordinate conversion is performed at the same time, and the flight route data is transmitted to the control center via the wireless sensor network. The accuracy of the flight path of the UAV under the three methods is counted. The result is shown in Figure 6.

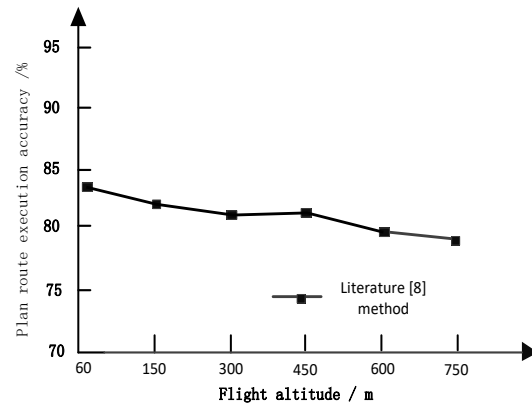
Analysis of Figure 6 shows that when the flight height of the UAV is 69-750 m, the accuracy of the UAV execution of the planned route flight by using the method of literature [7] is between 81% and 78%, and that of the method of literature [8] is maintained between 84% and 79%, and both of them show a trend of decreasing accuracy; while the accuracy of the proposed method is maintained at 93%-95%, and always stable. Therefore, the proposed method used for executing the UAV's planned flight route has high accuracy and better system control effect.



(a) This method plans route execution accuracy



(b) Document [7] method to plan route execution accuracy



(c) Document [8] method to plan route execution accuracy

Figure 6. Comparison of planned route execution accuracy under different methods

4. Discussion

4.1. Comparison of aerial imaging effect

According to the above experimental results, under the same number of detection points, the medium error, maximum error, and medium error tolerance of the digital aerial photography of the UAV by using the proposed method are 0.63 m, 1.07 m, and 1.2 m, respectively; medium error, maximum error, and medium error tolerance of the digital aerial photography of the UAV by

using the method of literature [7] are 0.78 m, 1.43 m and 1.44 m respectively, and those of the method of literature [8] are 0.92 m, 1.32 m, and 1.48 m, respectively. Therefore, the error values under the proposed method are lower than those in the literature [7] and the literature [8]. It proves that the aerial imaging of the proposed design method has higher precision and better imaging effect.

4.2. Comparison of system work efficiency

According to the above experimental results, when the RN-UAV operation adjustment time is the same, the proposed method is used for aerial photography. The total working time of the system is 6215.712 s, 78923.115 s, 81229.315 s, and 5332.633 s, respectively. When the method of literature [7] is used for aerial photography, the total working time of the system is 32417.991 s, 253241.988 s, 293134.221 s, and 27214.454 s respectively. When the method of literature [8] is used for aerial photography, the total working hours of the system are 29845.376 s, 395412.624 s, 264584.335 s, 9478.560 s respectively. Therefore, the system work time under the proposed method is lower than the system work time of the method in literature [7] and literature [8]. It proves that the aerial photography work of the design method in this paper is short in time and the system works more efficiently.

4.3. Comparison of execution levels of planned route

According to the above experimental results, when the flying height of the UAV is 69-750 m, the accuracy of the UAV's execution of the planned route flight under the proposed method is maintained between 93% and 95%, and it is always stable; The accuracy of the UAV's execution of the planned route flight under the method of literature [7] is between 81% and 78%; while that of the method of literature [8] is maintained between 84% and 79%, showing a downward trend. It is proved that the UAV execution of planned route of the proposed method has high accuracy and the system control effect is better.

In summary, according to the experimental results, the digital aerial photography system based on wireless sensor network designed in this paper has good accuracy of aerial imaging results, short aerial working time, and high accuracy of planned route execution. The imaging effect is better, the system works more efficiently, the system control effect is better, and it is more practical and advantageous.

5. Conclusions

Aiming at solving the problems of unclear imaging, low system efficiency and poor control effect of traditional aerial photography, a digital aerial photography system based on wireless sensor network is proposed. Based on the principle of aerial photography system, a wireless sensor network is established, and a large number of wireless sensor nodes are deployed in the interval time. Wireless communication and computing functions are completed by the nodes. The sn-rn data acquisition layer, rn-uav relay transmission layer and uav-dc mobile convergence layer are designed to constitute the wireless sensor network architecture. Combined with uav digital

aerial photography technology, a uav digital aerial photography system based on wireless sensor network is built. The experiment shows that the method has better overall imaging effect, higher system efficiency, better system control effect, stronger practicability and superiority. By reducing the transmission task of sensor nodes in WSN, the service life of sensor nodes can be extended. By increasing the function and power supply of the relay node, the resource consumption caused by the failure of the transmission node is reduced. The mobile nodes provide good network communication quality and improve the data acquisition efficiency and system life of UAV digital aerial photography system.

References

- [1] Jin, D.Y.; Chen, J.X. Application of wireless sensor network design on UAVs. *China Science and Technology Information* 2017, (8): 79-80.
- [2] Li, W. Research on data collection method based on UAV in wireless sensor network. Northwest University, 2016.
- [3] Yao, Z.M.; Jing, B.G.; Sun, C.P. Design and test of plant image monitoring system based on mobile wireless sensor network. *Journal of Agricultural Engineering* 2016, 32(11): 189-196.
- [4] Mou, S.; Yin, H.; Su, X. Wireless sensor network technology and application. China Water Conservancy and Hydropower Press 2016.
- [5] Liu, Q.K. Application of data fusion technology in wireless sensor networks. *Technology Outlook* 2016, 26(28): 14-21.
- [6] Zhou, X.M. Application of data fusion technology in wireless sensor network. *Digital Space* 2018, (1): 158-158.
- [7] Jin, D.Y.; Chen, J.X. Application of wireless sensor network design on UAVs. *China Science and Technology Information* 2017, 8(3): 254-261.
- [8] Chen, H.B.; Ma, S.Q.; Wang, G. et al. Remote sensing systems on board autonomous miniature aircraft. *Remote Sensing Technology and Application* 2001, 3(5): 18-23.
- [9] Yang, X.C.; Jia, X.F. Design and implementation of multi-rotor UAV route planning system. *Automation Application* 2018, 1(11): 45-50.
- [10] Pan, Y.; Ma, A.P. Discussion on rapid processing method of aerial photography measurement image data of UAV. *Architectural Engineering Technology and Design* 2016, (32):71-78.
- [11] Zhang, W.U. AV farmland information monitoring system based on wireless sensor network. *South Agricultural Machinery* 2017, 48(9): 36-37.
- [12] Wang, F.J.; Duan, H.L.; Guan, X. The production of 1:500 DLG using the UAV aerial system based on complex terrain. *Urban Geotechnical Investigation & Surveying* 2015, (5): 86-90.
- [13] Cao, F.H.; Song, Z.W.; Li, Y. et al. Determination of precise spatial position of aerial photography of UAV. *Bulletin of Surveying and Mapping* 2016, (6): 144-145.
- [14] Ding, L.; Wang, Z.S. Research and implementation of greenhouse monitoring system based on wireless sensor network. *Computing Technology and Automation* 2016, 35(3): 137-140.
- [15] Hu, H.F.; Ma, L. Research on security requirements of wireless sensor networks. *Practical Electronics* 2017, (21): 83-84.
- [16] Zong, J.L. Effective monitoring method for sensitive information of wireless sensor networks. *Electronic Technology & Software Engineering* 2017, (10): 14-14.
- [17] Guo, Y.; Chen, Y.; Hui, F. Research of laboratory remote monitoring and early warning system based on wireless

- sensor network. Research and Exploration in Laboratory 2016, 35(3): 105-109.
- [18] Zhang, B. Rapid mapping based on UAV digital aerial photography system. Research, 2016, (9): 20-20.
- [19] Zhao, D.W.; Tang, B.L. Zhang, C. Discussion on application of aerial photography based on UAV. Natural Science 2016, (9): 194-194.
- [20] Zhang, L.; Li, B.B. Application of STK in UAV route planning. Automation & Instrumentation 2016, (11): 151-153.
- [21] Qiu, G.Q.; Yang, Z.L.; Yang, L. et al. A network node design of wireless sensor based on ZigBee protocol. Automation & Instrumentation 2008, (3): 10-11+66.
- [22] Yu, Z.G.; Wan, S.Q.; Chen, Z.F. et al. Design of low power and multi-functional data acquisition system based on wireless sensor network. Journal of China Academy of Electronics and Information Technology 2012, 7(2): 124-128.
- [23] Wang, T.; Liu, S.; Ge, L.S. Design of High-speed wireless communication receiver in parallel DC/DC system. Journal of Power Supply 2018, 16(1): 166-170.
- [24] Bi, K.; Li, Y.C.; Ding, X.B. et al. Aerial photogrammetric technology of light small UAV: status and trend of development. Bulletin of Surveying and Mapping 2015, (3): 27-48.
- [25] Liu, P.; Peng, Y.P.; Zou, X.Q. et al. Present situation and prospect of unmanned aerial photogrammetric system in china. Geospatial Information 2010, 08(4): 4-6

The Application of Closed Hydraulic System of Hoisting Mechanism in Auto Crane

Duwei Nie*, Changxing Fu

Department of Mechanics Engineering, Huaihua Polytechnic College, Huaihua 418000, China

Received OCT 16 2019

Accepted JAN 5 2020

Abstract

At present, the hoisting mechanism of existing large-tonnage auto crane has mostly adopted open loop hydraulic system; for security reasons, the load loop tends to input larger load, causing unnecessary energy loss of engine. In order to solve this problem, the closed hydraulic system for the load loop carries on constant power control for load input power to ensure the constant control of optimal load rate of engine, which achieves the safety and energy saving of the auto crane. According to the principle that the power of hydraulic system is equal to the product of pressure and flow in the system, as long as carrying on constant control for the pressure and flow in hydraulic system, the closed loop control of hydraulic system can be realized.

© 2020 Jordan Journal of Mechanical and Industrial Engineering. All rights reserved

Keywords: Auto crane; Load input; Constant power control.

1. The working principle of Closed hydraulic system for lifting mechanism of autocrane

Because of the hydraulic transmission with large output force, small volume, light weight, simple structure, labor-saving transmission and operation, it is easy to realize stepless transmission and automatic control etc., hydraulic lifting mechanism widely applied. Especially in modern engineering crane, automobile crane and crawler crane widely use the hydraulic transmission mode [1].

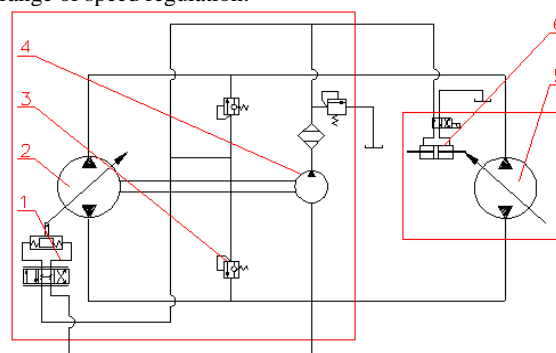
Auto crane hoisting mechanism has two main systems, namely the valve-controlled motor open-loop control system and the pump-controlled motor closed-loop control system.

The valve-controlled motor open-loop control system belongs to the restrictive-flow regulating system. Its biggest characteristic is simple system device, low costs and easy design as well as a large speed range, which is very beneficial to the micro-motion of auto crane [2]. However, due to the existing damper loss and low working efficiency, the system's calorific value is higher.

The pump-controlled motor closed-loop control system is a kind of volumetric speed control system. Because this kind of circuit does not have the throttling and overflow energy loss, the system is not easy to heat and its efficiency is high. It is widely used in high power hydraulic drive system, but due to the required high manufacture precision and the complicated structure, the cost of the hydraulic device is higher.

The schematic diagram of closed Hydraulic System for Hoisting mechanism of Auto crane is shown in Figure 1.

The oil inlet and outlet of the variable electro-hydraulic proportion pump 2 are connected with the oil inlet and outlet of variable motor 5 respectively to form a closed circuit, so that the ascending or descending of main windlass can be achieved. To supplement the internal leakage of the motor due to the volumetric efficiency, a charging pump (usually a dosing pump) is added to the system to charge the system. This charge pump also provides the system with a source of controlling oil. The variable electro-hydraulic proportion pump 2 can change its output through its variable servo. The electro-hydraulic proportion motor can also change its displacement through its variable servo so that the system can achieve a wide range of speed regulation.



1. variable servo; 2. variable electro-hydraulic proportion pump; 3. charging relief valve; 4. charging pump; 5. variable electro-hydraulic proportion motor; 6. variable servo

Figure 1. Schematic diagram of closed Hydraulic System for Hoisting mechanism of Auto crane

* Corresponding author e-mail: Dwnie2000@126.com.

When we operate a crane to make the weight drop, the weight's direction of gravity is the same as the movement direction, the weight drives the motor to rotate. At this moment, the motor and the pump change in function, the winding motor is no longer as executing components to absorb the power of the engine, but as a dynamic element to provide power to the engine, it will cause the load rate of engine lower than zero which leads to the rise of rotational speed, when it becomes serious that the engine will show "speed" phenomenon. In order to prevent the "speed" phenomenon of the engine, it is usually to load power and input circuit in the closed hydraulic system of automobile hoisting crane, to consume the power produced by the load drop of the lifting engine, in order to ensure that the engine load rate is greater than zero. The power consumed by the load loop is equal to the product of the pressure P and the flow Q [3].

$$P_i = PQ$$

The constant control of the input load power in the field of the existing large tonnage truck crane is mainly open loop control. Due to the shortcomings of low control precision, weak anti-interference ability and so on, it cannot meet the realistic needs. In practice, it will often input greater load for the safety of the crane itself and the crane operator, causing high load rate of engine, thus resulting in unnecessary energy loss of the engine.

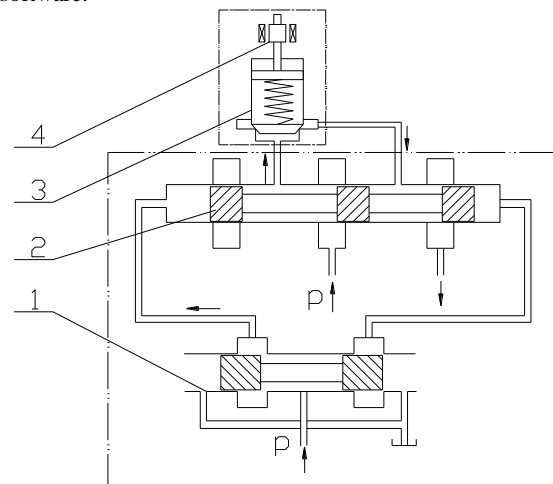
In order to solve this problem, we adopt the closed hydraulic system. When in condition of the main hoist down, due to the influence of the factors of wind load and inertia force and so on, the load rate of the engine is dynamic change. By taking closed control of the system pressure P and flow rate Q , it is to realize the optimal constant control of engine load rate, which can not only ensure the safety of the crane in the condition but also ensure the engine output power in the most energy state, to realize the constant control of the input load power.

2. The establishment of physical model of Closed Hydraulic System for Hoisting mechanism of Auto crane

Closed hydraulic system for hoisting mechanism of auto crane load input circuit mainly includes pilot-scale proportional servo flow valve and proportional relief valve. As shown in Figure 2 of physical model schematic diagram, pressure oil controlling oil passage enters into proportional servo console port through action of proportional electromagnet of pilot operation 1. It pushes valve core 2 of proportional flow servo valve to have respondent action. Pilot valve and main valve are slide valve structures. If we ignore the effect of flow force, force of fiction, valve core weight and spring force of pilot valve, then the control force of pilot reducing valve is in direct proportion to electromagnetic force. If we ignore the effect of flow force, valve core weight and force of fiction of pilot valve, control power is in direct proportional to main valve core displacement. By changing current of

input proportional electromagnet, we can control main valve displacement and aperture [4]. Hydraulic oil from main valve of proportional servo valve enters proportional relief valve 3. Proportional relief valve sets its pressure through current or voltage value of proportional electromagnet 4. Continuous overflow of proportional relief valve consumes power created by gravitational potential energy of carrying heavy things in over loads, to prevent galloping of the engine.

By comparing the mathematical modeling of the electromagnet, the mathematical modeling of the proportional relief valve and the mathematical modeling of the proportional servo flow valve, we can obtain the electro-hydraulic coupling model (not to be deduced here). Then we can build a simulation model of hydraulic circuit of Hoisting mechanism of Auto crane by using AMESim software.

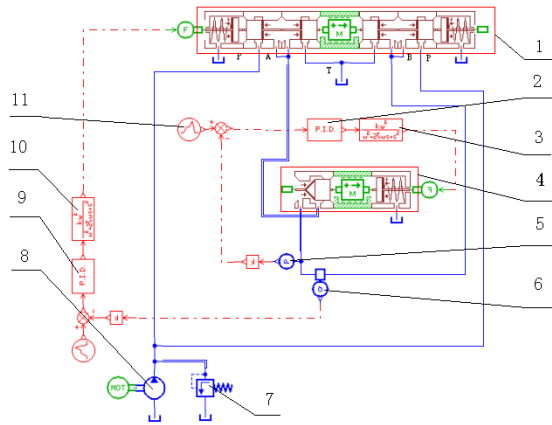


1 proportional servo valve pilot 2 main valve of proportional servo valve 3 proportional relief valve 4 proportional electromagnet.

Figure 2. Physical model schematic diagram

3. The Establishment of closed Hydraulic System Simulation Model for Hoisting mechanism of Auto crane

AMESim (Advanced Modeling and Simulation Environment for Systems Engineering) is the world famous engineering system and advanced modeling and simulation platform [5]. It provides a whole, full and systematic engineering design and simulation platform, which makes it possible for users to establish a complex and multidisciplinary electro-mechanical and hydraulic integrated system model on a single platform, and conduct the simulation calculation and deeper analysis on this basis. AMESim is growing rapidly. Its main product modules include four operation platforms^[6], one 3D animation front-back Processing Toolbox, 28 application model bases (A total of 3500 models), 5 Interface Tools, 1 optimal toolbox and 10 real-time simulation code generation function^[7].



1. Proportional flow valve 2. PID adjustable controller 3. Transfer function 4. Overflow valve 5. Pressure sensor 6. Flow sensor 7. Safety valve 8. Hydraulic pump 9. PID adjustable controller 10. Transfer function 11. Step-function signal

Figure 3. Closed-loop Control Simulation Model

By using AMESim signal control library, hydraulic library (including pipe model) and hydraulic component design library, we conduct modeling on investigative control system and hydraulic component, as shown in Figure 3. Meanwhile, it depends on its super strong computing power to carry out dynamic characteristics analysis on the system [8].

Pressure (flow) sensor transfers detective real-time pressure (flow) data to summator through proportional gain. Compared with step-input signal, with regard to the different values between them as input signal of PID adjustable controller. PID adjustable controller adjusts finished signal and acts on valve element of proportional overflow through transfer function and spring force sensor, so as to reach predicted pressure and flow value ultimately.

4. Dynamic characteristics of Closed Hydraulic System for Hoisting mechanism of Auto crane

For whatever reasons (external disturbance or system internal variation), as long as controlled variable deviates from specified value, closed-loop control system will generate corresponding control actions to eliminate deviations, have a thick skin on component characteristic variation and can improve visible response characteristics of system. Closed-loop control has stronger capacity of resisting disturbance, which can avoid from load rate's fluctuation of hoisting mechanism in suspended loading process. Even if it is impacted by dynamic factors of dynamic wind load, it also can eliminate interference rapidly.

Simulation parameters for closed-loop control simulation model of Hoisting mechanism of Auto crane are designed as shown in Table 1.

Table 1. simulation parameters

parameters names	parameters
motor speed	1000 r
pump emissions	45 ml/r
simulation time	10 s
simulation step	0.01s

The pressure dynamic curve for inlet of relief valve by simulation is shown in Figure 4.

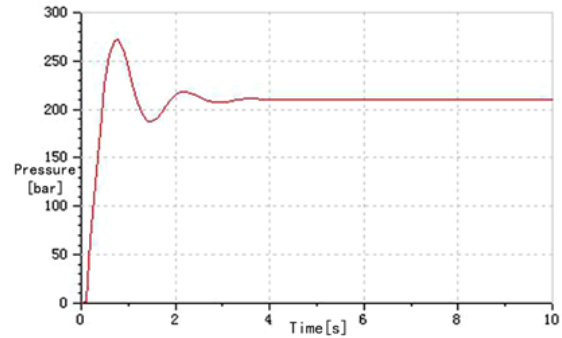


Figure 4. Curve of Closed-loop Control Pressure's Dynamic Characteristics

Dynamic response time of closed-loop control pressure can be controlled within 2 second with overshoot kept within 23% [9-11].

Dynamic characteristics for outlet flow of electro-hydraulic proportion multi-way valve are shown in Figure 5.

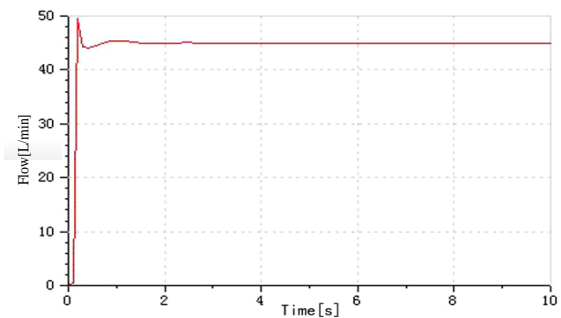
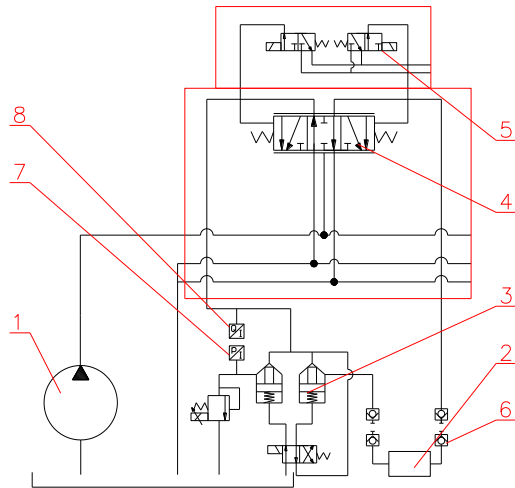


Figure 5. Closed-loop Control Flow's Dynamic Characteristics Curve

Dynamic response time of closed-loop control flow can be kept within 0.5 second with overshoot kept within 10%.

5. Experimental verification of Closed Hydraulic System for Hoisting mechanism of Auto crane

Taking the all terrain crane with the rated load of 400 tons that an enterprise produced as an example, a set of closed system is installed on the hoisting mechanism of the crane.



1. Hydraulic pump; 2. Idle executive component; 3. Cartridge reversing valve; 4. Electro-hydraulic proportional multi-way valve; 5. Pilot-operated reducing valve; 6. Quick-change connector; 7. Pressure transducer; 8. Flow transducer

Figure 6. Load input closed-loop control system and test system schematic diagram

As shown in Figure 6, Hydraulic pump 1 provides the hydraulic oil source to the system, Pilot-operated reducing valve 5 is placed in the right position to control the electro-hydraulic proportional multi-way valve 4. After passing the electro-hydraulic proportional multi-way valve, the hydraulic oil goes through the cartridge reversing valve into the relief valve. When the set relief valve pressure is reached, the hydraulic oil will overflow out through the relief valve and consume the produced engine power when the crane falls down. Therefore, it realizes the consumption of energy as heat. When the crane is affected by the factors of wind load and inertial force and leads to the changes in temperature and pressure, the pressure transducer 7 and the flow transducer 8 detect the real-time pressure and flow of the load input loop. Compared with the set pressure and flow value, it can quickly reach the set value through the closed-loop feedback.

Hydraulic system flow curves for open-loop and closed-loop control are collected as shown in Figure 7 and in Figure 8 when the main windlass is lifting 8 tons of weight.

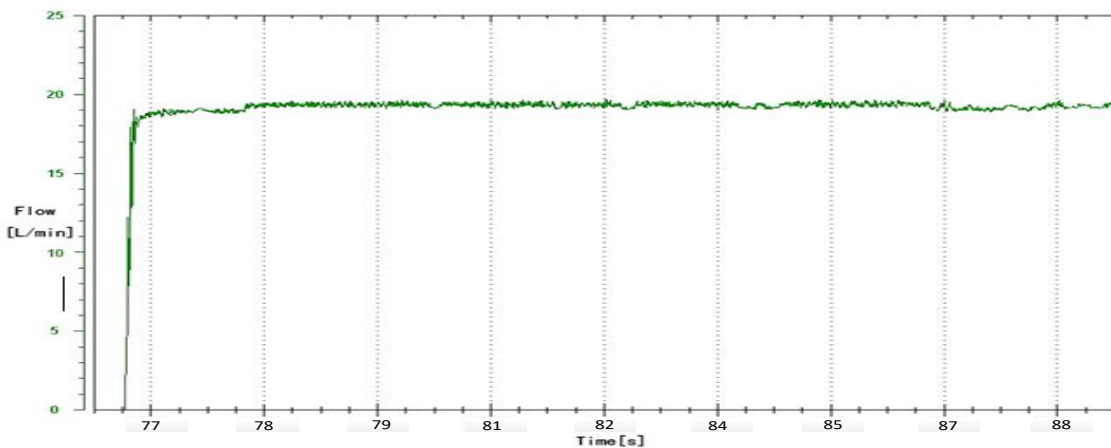


Figure 7. Hydraulic system flow curves for open-loop when the main windlass is lifting 8 tons of weight

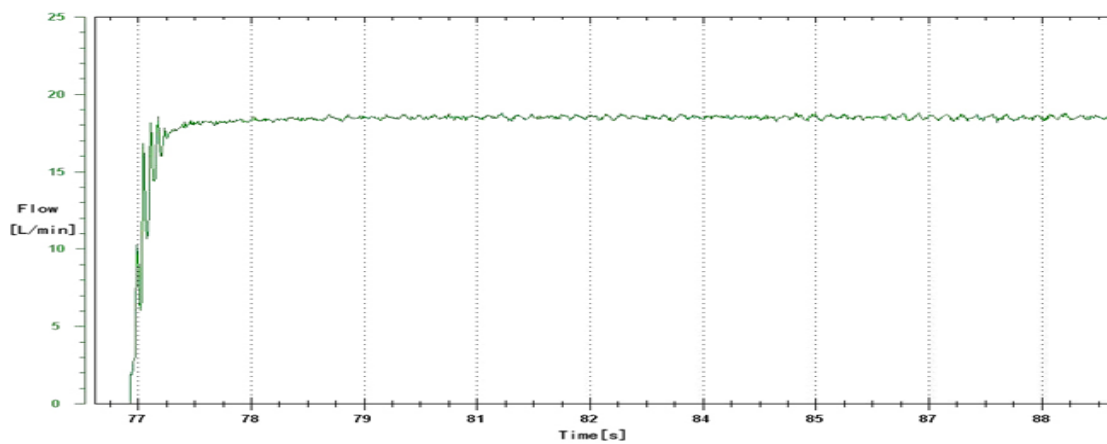


Figure 8. Hydraulic system flow curves for closed-loop when the main windlass is lifting 8 tons of weight

It can be seen from the figure that the open-loop control system has serious oscillations in the suspension process and is greatly affected by the wind load or other factors. When the flow rate is set to 18L, the static error exceeds 1.5 L, accounting for about 8%; The closed-loop control response time does not exceed 1s, the static difference can be controlled at 0.3L, accounting for about 1.5%, the oscillation is significantly reduced, indicating that its anti-interference ability is significantly better than the open-loop control system.

Pressure curve curves for hydraulic system of open-loop and closed-loop control are collected as shown in Figure 9 and in Figure 10.

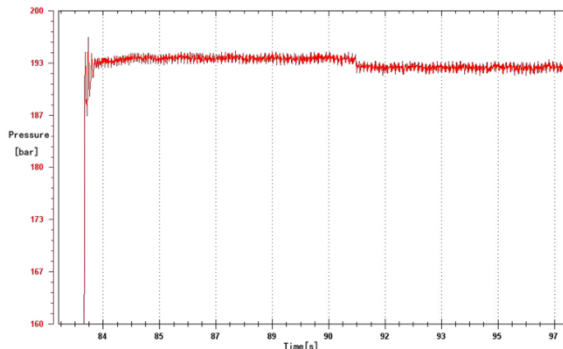


Figure 9. Pressure curve for open-loop control system when the main windlass is lifting 8 tons of weight.

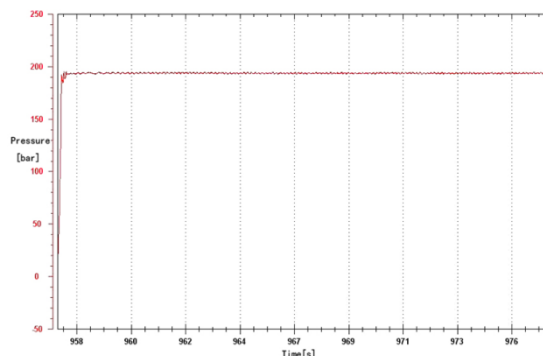


Figure 10. Pressure curve for closed-loop control system when the main windlass is lifting 8 tons of weight.

As can be seen from the figure, compared with the closed-loop control, the open-loop control system has no significant differences in the speed and oscillation of the response time without any other dynamic factors. However, when wind loads or other dynamic loads occur at 91 seconds in Figure 10, the open-loop control system shows obvious oscillations, static increase and can't be eliminated for a long time. In the closed-loop control system, the anti-interference ability is obviously better than that of open-loop control system.

We can draw a conclusion of analysis on pressure and flow dynamic characteristics that closed-loop control system has advantage in anti-jamming capability and eliminating offset capacity compared with open-loop control system. Therefore, with wind load capacity and

other strong dynamic load capacity of closed-loop control system, can be applied to loan input circuit of crane closed winch system in over loan situation. When loan rates of engine is reduced, the security of crane is guaranteed.

6. Conclusions

When the crane is influenced by wind loads, inertia force and other factors, through the closed-loop control of system pressure P and flow Q to the loading loop, closed hydraulic lifting mechanism changes from being disturbed by external dynamic load to the state with stable time within 1 second and not produce the "speed phenomenon" to the engine so as to ensure not only the safety of crane in this situation, but also the output power when the crane is in the most energy-saving state, realizing the constant control over input load power.

Acknowledgment

This research is supported by Hunan Provincial Department of Education Funding Project (17C1291).

References

- [1] Xiaoming Wang, Zhiqiang Lu. Research of Current Status and Development Trend of Large Cranes both at Home and from Abroad, Development and Innovation of Electromechanical Products. 2009, 12(3):6-8.
- [2] Aiwu Zhang. Design of Hydraulic System of Medium-and-Large Truck Cranes. 2007, 26(12):92-95.
- [3] Tai Zhang. Dynamic Study of Mechanism of Automobile Crane. Beijing: Mechanical Engineering, 1998, 34(6):8-10.
- [4] Wang Yilun. Hydraulic transmission, Harbin: Harbin Engineering University Press, April 21, 2005.
- [5] Yongling Fu, Haitao Qi. LMS Imagine. Lab AMESim system modeling and simulation example tutorial, Beijing: BEIHANG University Press, July 2011
- [6] Wilfrid Marquis-Favre, Eric Bideaux, Serge Scavarda. A planar mechanical library in the AMESim simulation software. Part I: Formulation of dynamics equations. Simulation Modeling Practice and Theory, 2005, 3-17.
- [7] Jiasheng Qin, Shanlan You. AMESim software characteristics and application, Construction Machinery, 2004, 47 (12).
- [8] Changzheng Huang, Jianping Tai. Current Status and Development Trend of Hydraulic System Modeling and Simulation Technology. Journal of Shaoguan University, 2009, 3:43-47.
- [9] Baligheid Sagarm, Krishnamurthy N, N Narendra. Development of an economic tensile and torsion testing machine for wires. Open Journal of Mechanical Engineering, 2016, 1(1):15-18.
- [10] Leonhard E. Benold, Simulation of Nonsteady Construction Processes, ASCE, 2009, 163-178.
- [11] Das Indrajit, Halder Arnab, Roy Sanjoy. Secure medical image sharing and storing (image encryption and hiding) in cloud environment. Advances in Industrial Engineering and Management, 2016, 5(2):208-213.

Monitoring Algorithm for Speed Information of Autonomous Vehicles Based on Magnetoresistive Sensor

Yu Tang

School of Intelligent Manufacturing, Panzhuhua University, Panzhuhua 617000, China

Received OCT 16 2019

Accepted FEB 9 2020

Abstract

Based on a magnetoresistive sensor, an algorithm for speed information monitoring of autonomous vehicles suitable for fewer target feature points is proposed. When using a magnetoresistive sensor on the road, the monitoring principle of the magnetoresistive sensor is that the magnetoresistive sensor generates a voltage signal and sends it to a signal processing module. In the signal processing module, the vehicles signal is compared with a threshold value to determine whether the vehicle is present. In the signal processing module, the vehicle signal is compared in the presence of the vehicle, and the node time synchronization technology is used to select the two-node autonomous vehicle speed information monitoring method. Then, the speed information of the autonomous vehicles in motion is monitored in real time. The vehicle speed information is sent to the upper node by using the single chip microcomputer. It is then sent to the coordinator module using ZigBee technology in the wireless sensor network. Finally, it is sent to the intelligent traffic monitoring center to achieve speed information monitoring of autonomous vehicles. The experimental results show that the accuracy rate of the autonomous vehicles' speed information monitored by the algorithm is above 97%, and the monitored energy consumption is only 13.5 J. This shows that the algorithm's monitoring accuracy and energy consumption have an advantage.

© 2020 Jordan Journal of Mechanical and Industrial Engineering. All rights reserved

Keywords: magnetoresistive sensor; autonomous; vehicles; speed; information; monitoring algorithm.

1. Introduction

Transportation is the urban arterial system, the link between the various social and economic activities of the city, and the fundamental condition for the economic development of the city and even the country. Properly solving the traffic problems will directly affect the development of the national economy and the living standards of the people. Throughout the history of global economic development, reasonable transportation layout and planning can promote the economic development of the entire society, and vice versa, which seriously restricts the pace of social and economic progress [1]. Intelligent transportation system, as the most direct and effective measure to alleviate urban traffic congestion and improve transportation efficiency, has become a hot spot in the field of transportation. Autonomous vehicles are a type of smart car, also known as a wheeled mobile robot, which relies mainly on the smart pilot (mainly computer system) in the car to achieve autonomous. Monitoring speed information is a prerequisite for obtaining traffic parameters [2], which provides real-time and reliable parameter basis for scientific dispatching and management of intelligent transportation system, and is the most basic and important part of the system. At present, the most widely used

monitoring and research methods for speed information of autonomous vehicles are toroidal coil monitoring, video monitoring, microwave monitoring and infrared monitoring. Among these monitoring technologies, there are generally disadvantages such as high installation and maintenance costs, environmental conditions affected by use conditions, and low monitoring accuracy. In order to make up for the shortage of the monitoring algorithm for the speed information of traditional vehicles, the focus of research has shifted to the magnetoresistive sensor monitoring technology (AMR) with characteristics of low cost, low power consumption, easy networking and micro-volume [3].

At present, the mainstream monitoring algorithms for vehicles based on magnetoresistive sensors include fixed threshold algorithm, adaptive threshold algorithm, state machine monitoring algorithm, artificial neural network algorithm and support vector machine algorithm. These algorithms generally have problems such as baseline drift, fixed thresholds leading to reduced accuracy, and inability to accurately discriminate the departure of vehicles [4]. The monitoring principle of magnetoresistive sensor: The distribution of the Earth's magnetic field is very limited in a very wide area (about several kilometers). A ferromagnetic object such as a car, whether it is moving or stationary, changes in the earth's magnetic field caused by

* Corresponding author e-mail: TANGYU041902@163.com.

its interference can be monitored by the magnetoresistive sensor.

There are two ways to monitor vehicles speed information. The first is a single-axis sensor that can be used to monitor the presence of vehicles. The other is to monitor the passage of vehicles [5]. Since different types of vehicles have different effects on the Earth's magnetic field when passing through, the output waveforms of the data acquisition system based on magnetoresistive sensors are also diverse. Accurate magnetic field information (intensity and direction of the magnetic field) can be obtained by using the appropriate magnetoresistive sensor and amplifier. The output waveform pattern of the data acquisition system is recognized by the single-chip microcomputer, which not only can judge the existence of the vehicles, but also can identify the vehicle type. That is, the presence of the vehicles, the direction and speed of the vehicles are determined by the two-axis sensor to obtain sufficient information.

The Earth's magnetic field strength is 500 to 600 m Gauss. When there is no large magnet object, the geomagnetic field in this area remains basically constant; when there is the large magnet object, the geomagnetic field of the area will change, and the magnetoresistive sensor can express the magnetic field changes before and after the disturbance in the form of voltage [6]. The autonomous vehicle is a large magnet object. Therefore, when the magnetoresistive sensor is placed in the lane, the output signal of the magnetoresistive sensor can be analyzed to obtain traffic parameters such as traffic volume and vehicle speed of the current section. The monitoring algorithm for speed information of the existing autonomous vehicles has various drawbacks [7]. Therefore, designing a monitoring algorithm for speed information of autonomous vehicles with high reliability, low cost, high precision and low power consumption has become the primary task of developing the intelligent transportation system.

In recent years, intelligent transportation has been a research hotspot at home and abroad, especially autonomous vehicles. At present, scholars at home and abroad have made some progress in the monitoring of vehicles speed information [8]. In 2012, AdiNurhadiyatna et al. proposed a new method for monitoring the speed of vehicles in real time from video. First, the principal components analysis method is used to identify the vehicles. The Kalman filter is used to track the past vehicles, and then the Euclidean distance method is used to estimate the speed of the vehicles. In 2012, Hou Liang et al. proposed an adaptive weighted average vehicle speed monitoring method based on a laser monitoring algorithm, which is processed according to the determined best performance monitor data to obtain the fusion value with the smallest error. The method has strong real-time performance and saves a large amount of data storage space, and has high practicability. In view of the target tracking algorithm based on SIFT and SURF features has the problems of poor real-time performance and large computational complexity, Meng Fanqing proposed an ORB-based moving target tracking method in 2015. The target is extracted from the ORB feature and matched between the frames, and then the extracted feature points are combined to complete the update and localization of

the target feature. However, when there are fewer matching features or fewer target feature points, the accuracy of the algorithm is significantly reduced. Aiming at the defects of the above algorithm, the monitoring algorithm for speed information of autonomous vehicles based on magnetoresistive sensor is proposed. The magnetoresistive sensor is applied to the speed monitoring of autonomous vehicles, and the algorithm is applied to the intelligent transportation system. The system is used to monitor the autonomous vehicles' speed information, which is helpful for the further development of autonomous vehicles and the improvement of transportation efficiency.

2. Materials and methods

2.1. Monitoring principle of magnetoresistive sensor

In the magnetoresistance effect, when the magnetization direction inside the nickel-iron magnetic alloy is parallel to the external magnetic field direction, the resistance value of the nickel-iron magnetic alloy reaches the maximum, which is independent of the applied magnetic field strength [9]. When there is a certain angle between the direction of the external magnetic field and the magnetization direction in the alloy, the resistance value of the nickel-iron magnetic alloy will decrease. When the direction of the external magnetic field is perpendicular to the magnetization direction in the alloy, the resistance value is the smallest, which is the well-known AMR anisotropic magnetoresistance effect. After a large number of experiments, the resistance value of the nickel-iron magnetic alloy is the angle function between the internal magnetization direction and the bias current direction [10], as shown in Figure 1 and formula (1).

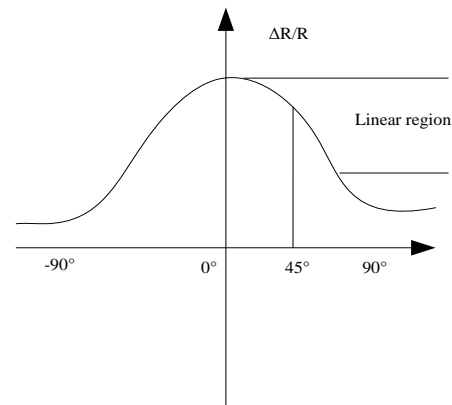


Figure 1. Principle of anisotropic magnetoresistance

It can be clearly seen from Fig. 1 that when the direction of the applied current is the same as the magnetization direction in the alloy ($\theta = 0^\circ$), the resistance change rate of the alloy strip is maximized; when $\theta = 45^\circ$, the resistance change rate of the alloy strip has a very good linear characteristic. Therefore, usually an internal bias magnetic field is applied so that the magnetoresistive sensor operates in the linear region.

$$R(\theta) = R_{\perp} \sin^2(\theta) + R_{\parallel} \cos^2(\theta) = R_{\min} \sin^2(\theta) + R_{\max} \cos^2(\theta) \quad (1)$$

Where, R_{\perp} is the resistance value when the bias current is perpendicular to the magnetization direction in the alloy, R_{\parallel} is the resistance value when the bias current is parallel to the magnetization direction in the alloy, and θ is the angle between the direction of the bias current and the magnetization direction in the alloy.

The nickel-iron alloy film is deposited on a silicon wafer using a modern semiconductor process to form a resistor strip, and then four such resistors are spliced into a Wheatstone bridge. When the applied magnetic field changes, the Wheatstone bridge can convert it to a differential voltage and output it [11]. After the output signal of the Wheatstone bridge is amplified, filtered, and digital-analog converted, the magnetic field strength in the direction of the sensitive axis of the sensor can be measured. The wheat stone bridge magneto-resistive sensor working diagram is shown in Figure 2 .

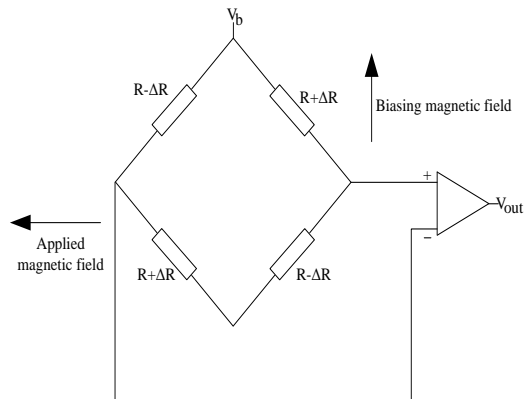


Figure 2. Wheatstone bridge magneto-resistive sensor works

In Figure 2, V_b is the power supply for the bridge. The magneto-resistive sensor is placed in a magnetic field. According to the anisotropic magnetoresistance effect, the resistance of the two resistors placed oppositely increases, while the resistance of the other two resistors decreases [12]. The differential voltage of the Wheatstone bridge is thus obtained. The Wheatstone bridge magneto-resistive sensor is shown in equation (2).

$$V_{out} = \frac{\Delta R}{R} g V_b \quad (2)$$

The output curve of the magneto-resistive sensor with the change of the external magnetic field is shown in Figure 3.

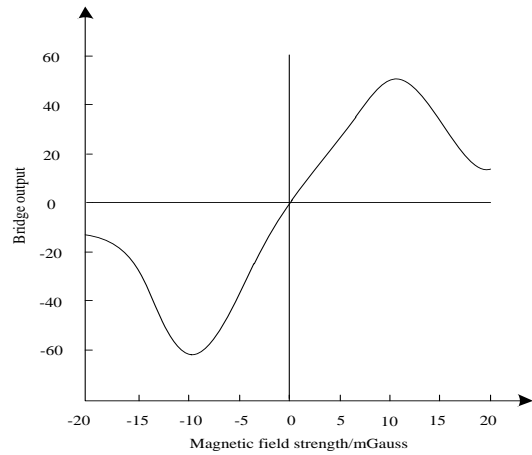


Figure 3. AMR magneto-resistive sensor changes with the change of the magnetic field

In a particular magnetic field, the bridge output is positively linearly related to the change in external magnetic field strength, and the Earth's magnetic field is just within this linearly correlated range. Therefore, the AMR magneto-resistive sensor is used to monitor changes in the local earth's magnetic field to obtain autonomous vehicles' speed information. This is very effective, and it is also an important basis for the use of magneto-resistive sensor.

The Earth is a natural magnet with a very weak magnetic field, about 0.5-0.6 Gauss. When a large magnet object enters the area covered by the Earth's magnetic field, the originally relatively stable geomagnetic field will be disturbed in a local range. These disturbances distort the magnetic field lines of the earth's magnetic field, and the disturbed earth's magnetic field is equivalent to the applied magnetic field that affects the resistance of the Wheatstone bridge [13]. The Wheatstone bridge can convert this change of magnetic field into the differential voltage. Autonomous vehicles are large magnet materials. During driving, it will locally disturb the stable earth's magnetic field and distort its magnetic lines of force. At this time, if the magneto-resistive sensor is buried below the road surface where the magnetic field lines are distorted, the influence caused by the autonomous vehicles (the strength, direction, time, and the like of the earth's magnetic field) can be expressed in the form of voltage. After the voltage signal is conditioned and analyzed, the speed information of the autonomous vehicles can be extracted. Finally, the traffic parameters such as the speed information of the autonomous vehicles are transmitted to the collection center of the traffic information in real time by using the wireless network. This is the basic principle of the magneto-resistive sensor to monitor the speed information of autonomous vehicles.

The flow chart for monitoring the speed of autonomous vehicles using the magneto-resistive sensor is shown in Figure 4.

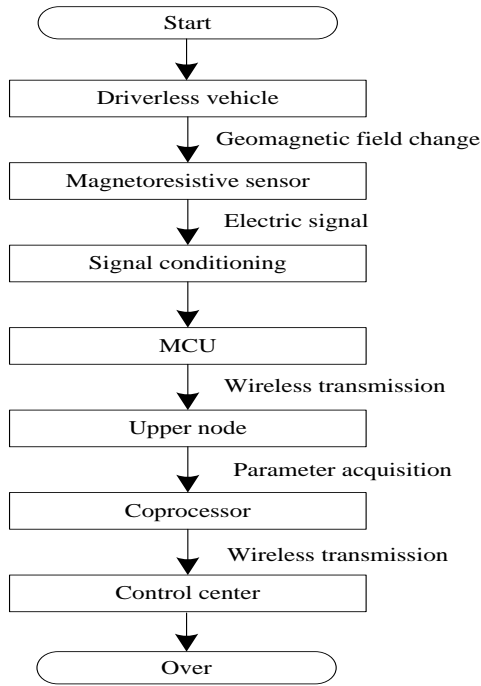


Figure 4. Magnetoresistive sensor monitoring speed information of driverless vehicles

As can be seen from Figure 4, when autonomous vehicles are driven on the road surface with the magnetoresistive sensors, the magnetoresistive sensor generates the voltage signal and sends it to the signal processing module. The vehicle speed information is sent to the upper node by using the single chip microcomputer. It is then sent to the coordinator module. Finally, it is sent to the intelligent traffic monitoring center to achieve speed information monitoring of autonomous vehicles.

When autonomous vehicles pass the road surface with the magnetoresistive sensor, the disturbance curve of the earth's magnetic field collected by the magnetoresistive sensor is shown in Figure 5. It can be seen from Figure 5 that autonomous vehicles have obvious regularity and variation characteristics on the earth's magnetic field during driving [14], so various parameters of road traffic can be obtained by analyzing the collected magnetic field curves.

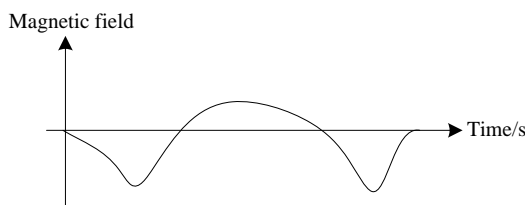


Figure 5. Earth's magnetic field curve disturbed by driverless vehicles

2.2. Monitoring algorithm for speed information

Currently, two intelligent resistive sensor nodes are generally used in intelligent transportation systems to estimate the speed information of autonomous vehicles. Assuming that the distance between two magnetoresistive sensors is S , and the times of autonomous vehicles passing through two magnetoresistive sensors are t_1 and t_2 , then

the speed formula of autonomous vehicles can be obtained as follows:

$$v = s / (t_2 - t_1) \quad (3)$$

However, because the distance between the two magnetoresistive sensors is very close, and the autonomous vehicles are very fast when passing through two magnetoresistive sensors, the estimated speed is far from the actual situation which included friction, inertia, acceleration and deceleration [15]. Therefore, a series of measures to improve the accuracy of the algorithm are implemented, such as further analysis of signals.

This article uses two nodes to obtain the speed information of autonomous vehicles. Assuming that the signal frequency is the same in the detection range of the magnetoresistive sensor, the vehicle runs at a constant speed between the two magnetoresistive sensor nodes. Through the hardware setting [16], the access point performs time synchronization to nodes A and B at intervals, which can offset the clock skew. The monitoring model of the speed information of autonomous vehicles is shown as Figure 6.

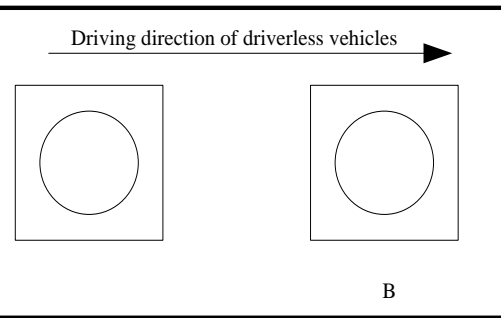


Figure 6. Unmanned vehicle speed information monitoring model

Assume that the length between the nodes of the magnetoresistive sensor is L_{AB} , the time of autonomous vehicles reaching the sensor nodes A and B is $t_{A,up}$ and $t_{B,up}$ respectively, and the time of autonomous vehicles leaving the nodes A and B respectively is $t_{A,down}$ and $t_{B,down}$, then the monitoring formula of the vehicle speed information v is as follows:

$$\Delta t_{up} = t_{B,up} - t_{A,up} \quad (4)$$

$$\Delta t_{down} = t_{B,down} - t_{A,down} \quad (5)$$

$$v_{up} = L_{AB} / \Delta t_{up} \quad (6)$$

$$v_{down} = L_{AB} / \Delta t_{down} \quad (7)$$

$$v = (v_{up} + v_{down}) / 2 \quad (8)$$

The accuracy of the vehicle speed information obtained by the above method is poor. Different magnetoresistive sensors have different sensitivities, and it is determined that the time of arrival or departure of autonomous vehicles may be delayed and varied [17]. Digital filtering can also cause delays in time monitoring, so the sensitivity of the magnetoresistive sensor is introduced. Assume that the correction parameter of the autonomous vehicles

arrival time is α , and the correction parameter of the departure time is β , then

$$\Delta t'_{up} = \Delta t_{up} - \alpha \tag{9}$$

$$\Delta t'_{down} = \Delta t_{down} - \beta \tag{10}$$

$$v'_{up} + v'_{down} = L_{AB} / \Delta t'_{up} + L_{AB} / \Delta t'_{down}$$

$$= \left[(\beta - \alpha) L_{AB} + (\Delta t_{up} - \Delta t_{down}) L_{AB} \right] / (\Delta t_{up} \Delta t_{down} + \beta \Delta t_{up} - \alpha \Delta t_{down} - \alpha \beta) \tag{11}$$

$$\approx v_{up} + v_{down}$$

The magnetoresistive sensor is different, and the correction parameters introduced should also be different. Here, the same correction parameters are used for the convenience of calculation, and α and β are extremely small. In order to reduce the complexity of the algorithm, an approximation method can be used, but the accuracy of the algorithm is also reduced. This algorithm is performed under the premise that the sensor nodes A and B receive signals at the same time. The introduction of node time synchronization technology makes the monitoring algorithm for speed information of autonomous vehicles more accurate.

The ZigBee technology is introduced into a wireless sensor network, which consists of the access points and nodes of the magnetoresistive sensor. All control commands can be communicated directly to each sensor node by the access point [18]. Time synchronization means that the access point adjusts the time of the sensor node to the standard time at intervals. Only two sensor nodes are time synchronized, and the collected signals of the sensors can be analyzed and calculated. During the process of sending a message to each sensor node by the access point, if the current time of the access point is t_{AP} , the time of each node can be synchronized to $t_{AP} + \Delta$. (Δ is the sum of the time that the message is transmitted at the access point and the time that the node receives the message. The time synchronization model of the wireless sensor is shown in Figure 7.

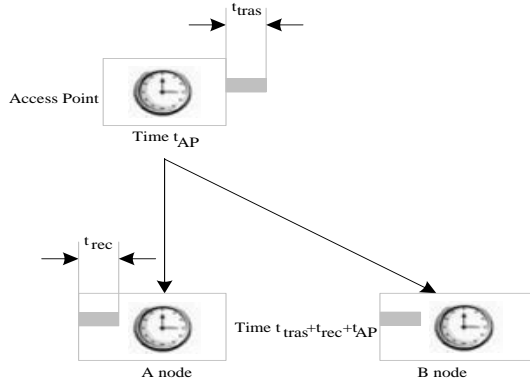


Figure 7. Wireless sensor time synchronization model

The vehicles signal is compared to a threshold to determine the presence of vehicles. The two-node monitoring method is selected to monitor the speed information of the autonomous vehicles [19], and the flowchart of the monitoring algorithm for speed information of autonomous vehicles based on magnetoresistive sensors is shown in Figure 8 and Figure 9. Figure 8 can determine the presence of autonomous vehicles and then monitor the speed information of autonomous vehicles by Figure 9.

As can be seen from Figure 8, the specific process for determining the existence of autonomous vehicles is as follows: After receiving the monitoring signal of the autonomous vehicles, the magnetoresistive sensor processes the signal through the moving average filtering process. Then, the threshold is updated and the threshold is initialized, and the signal to be monitored is divided into a vehicle state and a carless state by using a threshold. After the state is distinguished, the new threshold is calculated, and the new threshold is determined to be different from the current threshold. When the threshold difference is too large, the step of updating the threshold is returned; when the difference between the new threshold and the original threshold is sufficiently small, the state of the autonomous vehicles is judged by the state machine. When the current state is that there is a car, the result of the discrimination is output [20], and whether to continue monitoring is required. If it is necessary to continue monitoring, the new autonomous vehicles signal is read again, and if it is not necessary to continue monitoring, the process ends.

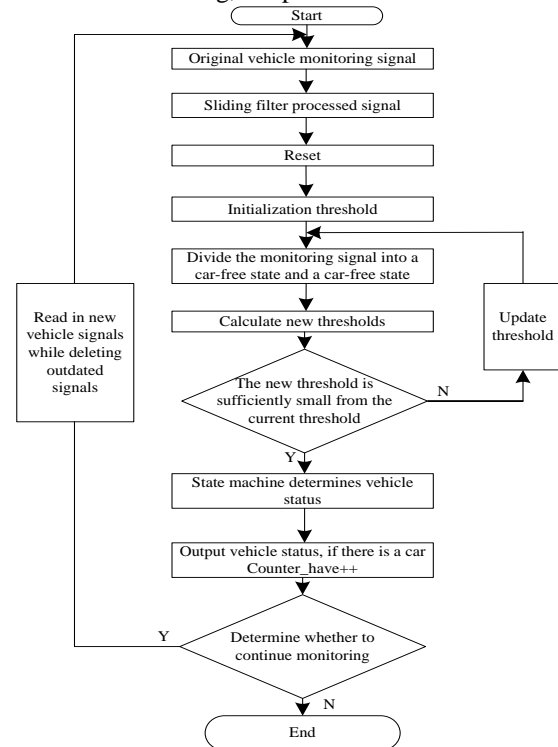


Figure 8. Unmanned vehicle presence algorithm

After determining the existence of autonomous vehicles, the vehicle speed information of the autonomous vehicles is monitored by Figure 9.

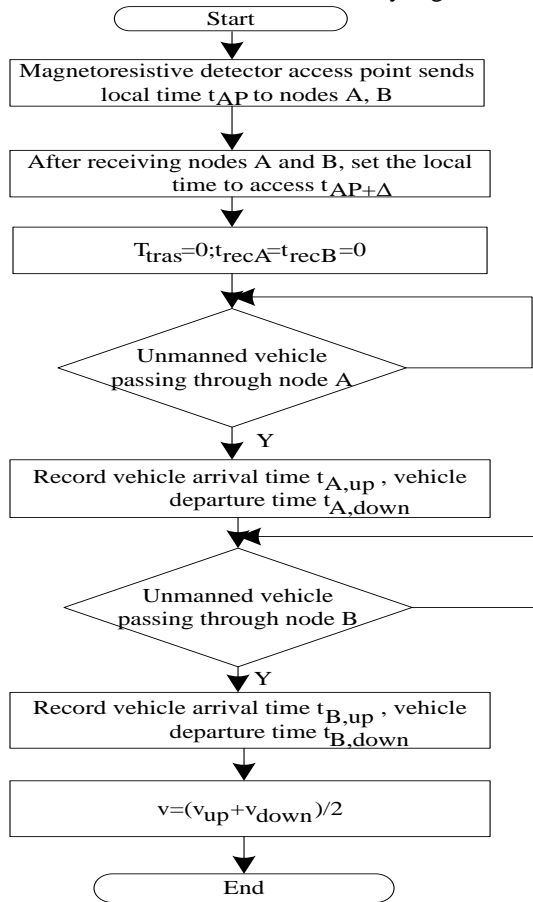


Figure 9. Sensor information monitoring algorithm for unmanned vehicles based on magnetoresistive sensor

As shown in Figure 9, after determining that autonomous vehicles exist, the access point sends the local time to the monitoring nodes A and B. After the nodes A and B receive the local time, the local time is set to access $t_{AP+\Delta}$. Let $T_{tras} = 0; t_{recA} = t_{recB} = 0$, when the vehicles pass the node A, record the arrival time and the departure time of the vehicles. When the autonomous vehicles pass the node B, the arrival time and the departure time of the vehicles are recorded. The speed information of the autonomous vehicles is obtained by the formula $v = (v_{up} + v_{down}) / 2$.

3. Results

In order to verify the effectiveness of the monitoring algorithm for speed information of autonomous vehicles based on magnetoresistive sensor, experiments were conducted on a two-way lane in a city. The algorithm is applied to the intelligent traffic monitoring system. The monitoring system includes two monitoring nodes, one upper node, one coordinator, one PC, and one 4G router.

In order to make the monitoring results more accurate, the buried depth, monitoring radius (sensitivity) and node spacing of the monitoring nodes are tested before the formal testing. When the parameters meet the best standards for system testing, the vehicle speed information monitoring of autonomous vehicles begins. The monitoring node sends the monitored speed information to the upper node of the roadside by wireless, and the data processed by the upper node is packaged by the coordinator and transmitted to the PC through the RS232 MCU.

The width of the city lane is generally 3.5-3.75 meters, and the monitoring node consisting of magnetoresistive sensors is buried in the center line position of the single lane. The monitoring node has a monitoring radius of 1.8 meters, which can just detect the geomagnetic signal after monitoring the vehicle's interference in the lane. The optimal buried depth and separation distance of the monitoring node are determined by monitoring the presence and the speed information of the autonomous vehicles.

100 autonomous vehicles will be monitored by two monitoring nodes on the road surface. When the monitoring nodes are buried at different depths, the monitoring results of autonomous vehicles are shown in Table 1.

Table 1. Statistics of buried depth monitoring results of monitoring nodes

Node burying depth/cm	Monitor vehicle passing quantity/n	Actual number of vehicles passing/n	Accuracy/%
0	105	100	95
10	103	100	97
20	100	100	100
30	98	100	98
40	94	100	94
50	92	100	92

The experimental data in Table 1 shows that when the buried depth of the monitoring node is 0 cm and 10 cm, the number of autonomous vehicles monitored by the algorithm is higher than the number of autonomous vehicles actually passed, and the traffic flow monitoring accuracy is low. The reason may be that the monitoring nodes are too exposed to the road surface under the sensitivity set before the experiment, and the passing vehicles of the adjacent lanes are also monitored. When the buried depth of the monitoring node is 40 cm and 50 cm, the number of autonomous vehicles monitored by the algorithm is lower than the number of autonomous vehicles actually passed, and the traffic flow monitoring accuracy is also low. The reason may be that the monitoring node is buried too deeply under the sensitivity set beforehand, and eventually the autonomous vehicles in the monitoring lane are missed. When the buried depth of the monitoring node is 20 cm and 30 cm, the autonomous traffic flow rate monitored by the algorithm is relatively high. It can be seen that the buried depth of the magnetoresistive monitoring node has the great relationship with the setting of its sensitivity. In order to make the monitoring node anti-theft function and easy to install, when the monitoring radius is set to 1.8 m, the optimal installation depth is 20 cm-30 cm.

Autonomous vehicles will pass at a speed of 60 km/h at different distances of the monitoring nodes. In this case, the speed information of autonomous vehicles is shown in Table 2.

Table 2. Monitoring results of distances of different monitoring nodes

Monitoring node spacing/m	Monitoring speed information results/km/h	Actual speed information result/km/h	Accuracy/%
2.5	55.18	60	91.96
3	56.05	60	93.42
3.5	57.18	60	95.3
4	58.31	60	97.18
4.5	57.35	60	95.58
5	56.81	60	94.68
5.5	55.04	60	91.73
6	54.18	60	90.3

It can be seen from Table 2 that when the distance between two monitoring nodes is 4 meters, the accuracy of the speed information monitored by the algorithm is the highest. Therefore, when using the algorithm of this paper to monitor the speed information of autonomous vehicles, the monitoring node is set to have the monitoring radius of 1.8 m, the buried depth of 20 cm, and the distance of 4 m between the two monitoring nodes.

The algorithm of this paper is used to monitor the speed information of autonomous vehicles. The test installation diagram is shown in Figure 10.

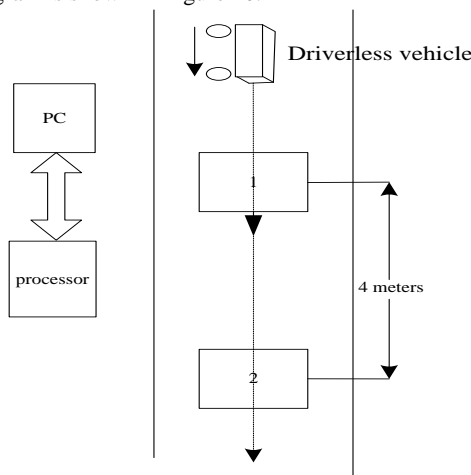


Figure 10. Experimental installation diagram

When the monitoring radius of the node is 1.8 m, the buried depth is 20 cm, and the distance between the two monitoring nodes is 4 m, the traffic parameters such as traffic flow, speed and time occupancy rate are counted, and the monitoring result is uploaded to the PC through the RS232 single-chip (once every minute).

In order to make the monitoring results accurate and reliable, the algorithm is used to carry out 5 tests in a number of time periods of the road. The monitored traffic flow is shown in Table 3.

Table 3. Traffic flow monitoring results

Number of experiments	Actual traffic flow/n	Monitor traffic/n	Accuracy/%
1	105	107	98.13
2	55	56	98.21
3	75	78	98.34
4	34	35	97.14
5	21	21	100

The time occupancy rate, also known as the lane occupancy rate, is an important parameter reflecting the traffic situation. The time occupancy rate refers to the ratio of the time taken by the vehicles through the cross section of the monitoring node to the statistical time during the statistical time (the experimental set time is 60 s). Traffic flow can reflect traffic conditions. The time occupancy rate reflects the intensity of the vehicles on the road from a microscopic perspective. It is the most direct response indicator of congestion. The time occupancy rate measured by the algorithm of this paper is shown in Table 4.

Table 4. Time occupancy monitoring results

Number of experiments	Actual time share/%	Monitoring time share results /%	Accuracy/%
1	73.5	74.8	98.26
2	52.1	53.4	97.57
3	66.8	64.5	96.43
4	25.9	26.7	97
5	32.4	31.5	97.14

Table 3 and Table 4 show that the accuracy of the algorithm can be as high as 97% when monitoring the traffic volume of autonomous vehicles. The algorithm of this paper is used to monitor the time occupation rate of autonomous vehicles, and the accuracy rate can be as high as 96% or more. It has very good dynamic monitoring effect, which shows that the algorithm can effectively reduce the complexity of the algorithm and improve the monitoring accuracy. It can be widely used in intelligent traffic monitoring systems.

In the traffic flow passed above, an autonomous vehicle is randomly selected. In the five experiments, the algorithm is used to monitor the speed information of the autonomous vehicles. The results are shown in Table 5.

Table 5. Vehicle speed monitoring results

Number of experiments	Actual speed of the vehicle/km/h	This algorithm monitors the speed/km/h	Accuracy/%
1	51.84	52.04	99.62
2	31.58	32.11	98.35
3	42.61	42.23	99.11
4	59.54	60.47	98.46
5	36.54	36.34	99.45

In the five experiments, the accuracy of the speed information of autonomous vehicles monitored by the algorithm is as high as 98%, which indicates that the speed information of the autonomous vehicles collected by the algorithm is more accurate.

If autonomous vehicles travel at a constant speed in the range of 0-80 km/h, the algorithm is used to monitor the situation of autonomous vehicles at different speeds. The monitoring results are shown in Table 6. The algorithm is compared to the video monitoring algorithm and the laser monitoring algorithm, and the results are listed in table 7 and table 8.

Table 6. Algorithm monitoring results

Serial number	Actual speed/km/h	Monitoring speed information/km/h	Accuracy /%
1	10	9.7	97
2	20	19.6	98
3	30	30.8	98.34
4	40	39.1	97.75
5	50	51.1	97.8
6	60	60.4	99.34
7	70	71.3	98.81
8	80	78.8	98.5

Table 7. the video monitoring algorithm monitoring results

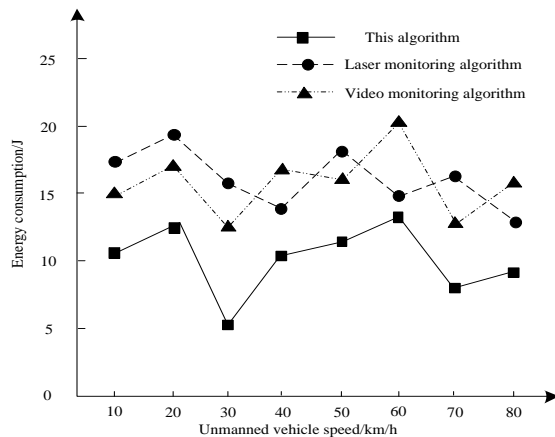
Serial number	Actual speed/km/h	Monitoring speed information/km/h	Accuracy /%
1	10	9.15	88.25
2	20	16.25	92.35
3	30	21.96	91.25
4	40	27.96	92.46
5	50	35.97	89.34
6	60	48.36	91.20
7	70	57.26	92.37
8	80	61.87	91.58

Table 8. the laser monitoring algorithm monitoring results

Serial number	Actual speed/km/h	Monitoring speed information/km/h	Accuracy /%
1	10	8.9	80.05
2	20	18.5	89.58
3	30	24.6	87.69
4	40	30.9	89.25
5	50	41.8	82.48
6	60	53.8	91.20
7	70	60.8	89.25
8	80	71.6	90.25

It can be seen from Table 6,7and 8 that when the driving speed of autonomous vehicles is 0-80 km/h, the accuracy of monitoring the speed information of autonomous vehicles is above 97%, and the accuracy of the video monitoring algorithm is above 88%, and the accuracy of the laser monitoring algorithm is above 80%, which indicates that the algorithm can meet the speed information monitoring of autonomous vehicles.

When the vehicle speed is 0-80 km/h, the energy consumption of the autonomous vehicles monitored by this algorithm, and the algorithm is compared to the video monitoring algorithm and the laser monitoring algorithm, and the result wereshown in Figure 11.

**Figure 11.** Comparison of energy consumption of three algorithms

It can be seen from Fig. 11 that when the vehicle speed is 0-80km/h, the energy consumption of the autonomous vehicles using the algorithm of this paper is only 13.5 J. The energy consumption of the video monitoring algorithm can reach up to 20.8 J, and the energy consumption of the laser monitoring algorithm can reach up to 19.7 J. It can be seen that the monitoring energy consumption using the algorithm of this paper is significantly lower than the energy consumption of the video monitoring algorithm and the laser monitoring algorithm. This verifies that the algorithm proposed in this paper has the advantage of low energy consumption when monitoring the speed information of autonomous vehicles.

Through the performance test of the monitoring algorithm for speed information of autonomous vehicles based on the magnetoresistive sensor, the algorithm can effectively monitor the traffic volume, time occupancy rate and speed information of autonomous vehicles. It can achieve accurate acquisition and transmission of speed information.

4. Discussion

There are widespread problems, such as urban traffic congestion, frequent traffic accidents, and exhaust pollution at home and abroad. Intelligent transportation systems can solve traffic problems such as traffic congestion, inconvenient traffic management, traffic accidents, and transportation. The intelligent traffic monitoring system can accurately provide traffic flow information to the traffic control department in real time, which provides a basis for the traffic control department to carry out work. The monitoring of speed information of autonomous vehicles is a core component of the intelligent traffic monitoring system. Through the intelligent traffic monitoring system, the vehicle information is collected and further processed, such as calculating autonomous vehicles density, judging the direction of vehicles, and monitoring vehicle speed information. In the end, the monitoring system for road restrictions and the road toll system are intelligent. Starting from China's basic national conditions with large traffic volume and complicated roads, the intelligent traffic monitoring system should have the advantages of energy saving, simple, practical, low cost and high monitoring accuracy. The AMR magnetoresistive sensor is small in size, low in cost, high in sensitivity, and long in use. Zigbee technology is a low-cost, simple, short-distance, low-energy wireless communication technology that can be applied to network data transmission. Therefore, this paper combines AMR magnetoresistive sensor monitoring technology and Zigbee technology to achieve speed information monitoring of autonomous vehicles. In the large environment of intelligent traffic monitoring system, the monitoring of speed information of autonomous vehicles is the front end of traffic parameter acquisition. Its stability and precision directly determine whether the intelligent traffic monitoring system can play the role of scientific management. The experiment proves that the algorithm has the advantages of high precision, low power consumption and low cost, and it has a good application prospect. The specific research contents and innovations of this paper are as follows:

1. By analyzing the advantages and disadvantages of the existing monitoring algorithm for the speed information of autonomous vehicles, the advantages of the monitoring algorithm for speed information of autonomous vehicles based on the magnetoresistive sensor are clarified, and the monitoring principle of the magnetoresistive sensor is elaborated.
2. The two-node monitoring algorithm for speed information of autonomous vehicles is proposed, which successfully solves the problem that the monitoring time is difficult to synchronize and the accuracy of the vehicle speed monitoring is low, and the high-precision monitoring of autonomous vehicles' speed information is realized.
3. When autonomous vehicles pass, the geomagnetic field is disturbed and produces a strong disturbance signal, which is completely different from the background signal. So set a threshold to monitor the presence of vehicles. Because the background signal drifts as a whole, the dynamic threshold algorithm is employed. The state machine algorithm is used in the specific judgment to improve the robustness of the algorithm and record the autonomous vehicles' arrival and departure time to estimate the vehicle speed. The clock synchronization two-node speed estimation algorithm is proposed to improve the accuracy of the algorithm and verify the feasibility of the algorithm.
4. The autonomous vehicles' speed monitoring algorithm is applied to the actual road section, and the monitoring performance and accuracy of the algorithm are tested repeatedly. Through a large number of experiments and data analysis, the optimal working environment of the monitoring algorithm for speed information of autonomous vehicles based on magnetoresistive sensors was determined. The experimental results also show that the algorithm has higher monitoring accuracy and lower power consumption, and achieves the expected goal.

During the monitoring of the AMR magnetoresistive sensor, the influence of the aging of the AMR magnetoresistive sensor on the monitoring accuracy was not considered. In the design of the monitoring algorithm for the autonomous vehicles' speed information, the signal characteristics are not used to obtain more traffic flow information, but the multi-node data is used to improve the monitoring accuracy of the algorithm. Further research work is as follows:

1. In the autonomous vehicles' monitoring algorithm, the autonomous vehicles have little disturbance to the earth's magnetic field when the slow speed passes, and the output signal of the magnetoresistive sensor does not fluctuate significantly. However, the algorithm designed now is based on the comparison between the strong fluctuation signal and the threshold signal, so it is likely to cause the leakage monitoring phenomenon. Autonomous vehicles have been passing the sensor for too long, and signal interruption may occur. It is easy to monitor into two cars, so further improvements to the algorithm are needed.
2. In the algorithm of autonomous vehicles' speed, it is difficult to achieve sensor node time synchronization. Because of various factors, such as filtering processing, sensor sensitivity, etc., it is also difficult to accurately

determine the arrival and departure time of autonomous vehicles, so the algorithm needs to be improved. The magnet material inside the autonomous vehicles determines the peak distribution. During the magnetoresistive sensor performance test, the vehicles pass the sensor from directly above. The time of the vehicles passing through the magnetoresistive sensor can be judged according to the position of the peak, and the speed of the autonomous vehicles can be further estimated. This algorithm can be implemented with a single node, and the signal processing requirements are improved.

3. Conduct large-scale, multi-lane monitoring research. The research in this paper is limited to a certain cross section of the road, and the intelligent traffic monitoring system collects traffic parameters from a wide range and grasps the traffic conditions. Therefore, the next step should be to arrange the monitoring nodes to multiple sections and intersections to realize networked information collection and processing.
4. Study a variety of monitoring techniques. Each monitoring technology of vehicles has its advantages and disadvantages. The development trend of intelligent traffic monitoring system is that multiple monitoring technologies are connected in parallel to realize the integration of monitoring data, in order to achieve all-weather, high-precision monitoring. In particular, the combination of video surveillance technology and magnetoresistive sensor enhances the monitoring efficiency of intelligent traffic monitoring systems.
5. Networking research on subsystems of intelligent transportation. The monitoring of autonomous vehicles speed information is only a subsystem of data acquisition in the intelligent traffic monitoring system. Its function is to provide the parameter basis for the intelligent traffic monitoring system, so that the control center of the intelligent traffic monitoring system issues corresponding instructions. Therefore, it needs to be networked with other subsystems of the intelligent traffic monitoring system to form the coordinated network, so as to truly reflect the value and advantages of the intelligent traffic monitoring system.

5. Conclusions

Monitoring algorithm for speed information of autonomous vehicles based on magnetoresistive sensor is proposed in this paper. The AMR magnetoresistive sensor is applied to the monitoring algorithm for the speed information of the autonomous vehicles. The algorithm is not affected by the weather, and has high monitoring accuracy, stable reliability and good scalability, which greatly prolongs the service life of the magnetoresistive sensor. The magnetoresistive sensor has the advantages of small size, convenient installation, small damage to the road surface, and easy maintenance. If the magnetoresistive sensor is installed on a large scale in practical applications, a large number of accurate autonomous vehicles speed information can be collected when monitoring by the algorithm proposed in this paper. This provides basic data support for the analysis of micro

and macro aspects of road traffic, the study of traffic flow characteristics, and the prevention of road traffic accidents.

Reference

- [1] Markevicius, V., Navikas, D., Zilyls, M., Andriukaitis, D., Valinevicius, A., Cepenas, M. 2016. Dynamic Vehicle Detection via the Use of Magnetic Field Sensors. *Sensors* 16, 78.
- [2] Daubaras A, Zilyls M. 2012. Vehicle Detection Based on Magneto-resistive Magnetic Field Sensor. *Elektronika ir Elektrotechnika* 118, 27-32.
- [3] Miao, J.J., Li, B.Y., Li, R.J. 2017. Monitoring and Evaluation Platform of DC Power Supply Based on Fuzzy Comprehensive Evaluation Model. *Chinese Journal of Power Sources* 41, 935-937.
- [4] Yu, Y., Guo, L., Deng, K. 2017. Design and Research of Big Data Analysis in Power Acquisition Data Analysis and Intelligent Monitoring System. *Automation & Instrumentation* 5, 162-163.
- [5] Zhang, H. 2017. Digital Image Watermarking Algorithm Based on Compressive Sensing and Discrete Cosine Transform. *Journal of Jilin University (Science Edition)* 55, 1504-1510.
- [6] Huang, J.H., Wei, K., Wu, B. 2017. Prevent Malicious Interference Signal Transmission Monitoring Vehicles Communication Network Simulation. *Computer Simulation* 34, 267-270.
- [7] Li, H., Li, X., Ding, W. 2017. Multi-sensor Based High-Precision Direct Georeferencing of Medium-Altitude Unmanned Aerial Vehicle Images. *International Journal of Remote Sensing* 38, 2577-2602.
- [8] Fang, X., Paynabar, K., Gebrael, N. 2017. Multistream Sensor Fusion-Based Prognostics Model for Systems with Single Failure Modes. *Reliability Engineering & System Safety* 159, 322-331.
- [9] Chen, S., Duan, H., Deng, Y., Li, C., Zhao, G., Xu, Y. 2017. Drogue Pose Estimation for Unmanned Aerial Vehicle Autonomous Aerial Refueling System Based on Infrared Vision Sensor. *Optical Engineering* 56(12): 124105.
- [10] Hossain, M.A., Elshafiey, I., Al-Sanie, A. 2019. Cooperative vehicle Positioning with Multi-Sensor Data Fusion and Vehicular Communications. *Wireless Networks* 25, 1403-1413.
- [11] Suhr, J.K., Jung, H.G. 2018. Sensor Fusion-Based Precise Obstacle Localisation for Automatic Parking Systems. *Electronics Letters* 54, 445-447.
- [12] Guo, L., Manglani, S., Liu, Y. 2018. Automatic Sensor Correction of Autonomous Vehicles by Human-Vehicle Teaching-and-Learning. *IEEE Transactions on Vehicular Technology* 67, 8085-8099.
- [13] Berntorp, K., Cairano, S.D. 2018. Tire-Stiffness and Vehicle-State Estimation Based on Noise-Adaptive Particle Filtering. *IEEE Transactions on Control Systems Technology* PP, 1-15.
- [14] Pirani, M., Hashemi, E., Khajepour, A. 2018. Resilient Corner-Based Vehicle Velocity Estimation. *IEEE Transactions on Control Systems Technology* 26, 452-462.
- [15] Ouyang, Z., Niu, J., Guizani, M. 2018. Improved Vehicle Steering Pattern Recognition by Using Selected Sensor Data. *IEEE Transactions on Mobile Computing* 17, 1383-1396.
- [16] Liu, Y.B., Xing, Y.L., Law, S.S. 2017. Internal Resonance Vibration Induced by Nonlinearity of Primary Suspension System in High-Speed Vehicle System. *Nonlinear Dynamics* 88, 2947-2956.
- [17] Liu, D.L., Li, X.P., Liu, Y.M. 2017. Attenuation of Low-Frequency Electromagnetic Wave in the Thin Sheath Enveloping a High-Speed Vehicle Upon Re-entry. *Journal of Applied Physics* 121, 074903.
- [18] Helak, K., Jehle, D., McNabb, D. 2017. Factors Influencing Injury Severity of Bicyclists Involved in Crashes with Motor Vehicles: Bike Lanes, Alcohol, Lighting, Speed, and Helmet Use. *Southern Medical Journal* 110, 441.
- [19] Yu, S., Gong, D., Zhou, J. 2017. Study on Vibration Reduction Design of Suspended Equipment of High Speed Railway Vehicles. *Mechatronics* 744, 012212.
- [20] Wang, D., Xin, P., Li, L. 2018. Risky Driver Recognition Based on Vehicle Speed Time Series. *IEEE Transactions on Human-Machine Systems* 48, 63-71

An Adaptive Scheduling Method for Resources in Used Automobile Parts Recycling

Pengfei Ning

Department of Logistics, Guangzhou College of Technology and Business, Guangzhou, 510850, China

Received OCT 16 2019

Accepted JAN10 2020

Abstract

When using the current method to schedule the resources in parts recycling, the resource scheduling delay is relatively long, which reduces the efficiency of parts resource scheduling, resulting in a low resource utilization rate. This paper proposes an adaptive scheduling method for parts recycling resources based on improved reverse particle swarm optimization. The current situation of waste vehicle recycling resource scheduling is analyzed, and the mathematical model of component recycling resource scheduling is constructed to consider time and cost. The reverse particle group is used to dispatch component recovery resources, and the inertia weight parameters are adjusted. The adaptation mechanism regards the degree of change of the particle function as the update factor of the inertia weight, avoiding the value according to the number of iterations; introducing the inverse learning operator, strengthening the ability of resource scheduling global search, and completing the recycling of used automobile parts and components Adaptive scheduling. The experimental results show that the proposed method has the highest recovery resource utilization rate, and the task time is about 200-400s, and the energy consumption is small. The proposed method can effectively schedule resources and improve the utilization of resources.

© 2020 Jordan Journal of Mechanical and Industrial Engineering. All rights reserved

Keywords: used automobiles; parts recycling; resource scheduling; reverse particle swarm optimization.

1. Introduction

In the process of rapid social development, automobile is the symbol of material civilization, which has brought changes to human life. But at the same time, with the rapid development of the automobile industry, the abandonment of used automobile machine parts has caused great negative pressure on the environment^[1]. In order to alleviate the shortage and used of resources and reduce the harm to the environment caused by used automobile parts, it is of great significance to reuse the parts of used automobiles to the maximum extent.

According to the latest statistics released by the China Automobile Industry Association on January 10, 2018, China's automobile production and sales exceeded 28 million vehicles in 2017, up 36.48% and 38.57% respectively from the same period last year, reaching a new high in production and sales and setting a new global historical record. At the same time, according to the analysis of professional experts in the world's first automobile market, China's automobile industry is still showing a good development trend in 2018, with an expected growth rate of between 20% and 25%. Data from the Traffic Administration Bureau of the Ministry of Public Security show that at the end of 2017, China's car ownership has reached 96.191.31 million vehicles, so according to the theoretical used rate of 6%, more than 577

vehicles are usedped each year. By 2020, China's car ownership is expected to exceed 150 million vehicles, and the used will exceed 9 million vehicles. Some people say that after becoming the world's largest parking lot, China is becoming the world's largest garbage dump.

In the recycling of used automobile parts and components, the amount of recycled resources is relatively large. Therefore, it is a hot issue in this field to allocate the recycled resources of automobile parts reasonably, schedule the tasks submitted, reduce the cost of execution and shorten the processing time^[2].

In-depth research on recycling resource scheduling of used automobile parts is the key content of the research in the field of used automobile resources, and its application is very extensive^[3]. In the use of used automobile parts recycling, spare parts resources are similar to water resources. After providing to users for use, users only need to use their own resources. As a result, the supplier of spare parts resources can manage the resources more conveniently and provide them to the users, while the users can use the spare parts resources at a lower price^[4]. However, there is a problem of poor resource utilization efficiency when the spare parts resources are dispatched at present. Therefore, the scheduling of recycling resources of used automobile parts is studied^[5].

In reference[6], resource scheduling model for automobile parts based on parallel resources and serial tasks is proposed using ant colony algorithm. The

* Corresponding author e-mail: npf561@163.com.

dynamic tasks submitted by users are divided into constrained sub-tasks, which are placed in the resource scheduling queue according to the running order. Aiming at the tasks in the same resource scheduling queue, the ant colony algorithm based on the shortest resource scheduling task is used to schedule the spare parts resources. Under the premise of fair scheduling, the delay time of resource tasks is shortened to maximize the satisfaction of users. The experimental results show that compared with other parts resource scheduling algorithms, this algorithm is fairer in scheduling, but because of the long delay of scheduling tasks, it reduces the utilization of parts resources. Reference[7] proposes a resource scheduling method for automobile parts recycling based on minimum cost with genetic algorithm. The problem of resource demand and supply of spare parts task is transformed into the problem of solving minimum cost. Choosing fairness, placement optimization and priority as entry points, from the mapping of automobile spare parts resources to graphs, the problem of construction is discussed. By changing the structure of the graph, the structure of the graph can be adjusted. Aiming at the high time complexity of resource scheduling, the incremental optimization of resource scheduling is realized. Finally, experiments on fairness, placement constraints and priority scheduling are carried out to verify the flexibility of the method in supporting multiple scheduling objectives. The simulation results show that the proposed method can effectively schedule spare parts resources, but the method has the problem of low resource utilization.

2. Material And Methods

2.1. Duality of Used Automobile Resources

The duality of used automobile resources is environmental pollution and resource. Used automobiles contain many kinds of different materials, such as metal materials, non-metallic materials and a small amount of organic materials. Some of the components will also cause harm to the environment^[8].

1. Metal materials, include steel plate, cast iron, aluminum and copper and their alloys, zinc, lead and so on. In order to prevent corrosion, the surface of steel plate is usually galvanized, tinned and aluminized, etc. Others, such as copper, are also used in automobile manufacturing. If used automobile cannot be recycled in time, some heavy metals will remain in the environment for a long time, which not only destroys the ecological environment, but also will enter the human body along with the food chain, causing health threats^[9].
2. Non-metallic materials, include plastics, glass, rubber, coatings, leather, fibers and so on. Among them, the "black pollution" caused by used tires is a serious problem. The long-term open-air stacking of used tires not only occupies land, but also easily breeds mosquitoes, spreads diseases and causes fires. On September 22, 1999, Stanislaus in Northern California, USA, 7 million used tires are spontaneously ignited, causing air pollution. Coatings are mainly used for anti-corrosion and beautifying the appearance of the car body, although the proportion is small, if improperly handled, it will pollute the environment. Air conditioning refrigerant, antifreeze and brake oil in

used cars are all serious pollution sources. Once they are leaked, they will cause environmental pollution and destroy the ozone layer in the atmosphere.

3. A small amount of organic matter in automobile parts not only pollutes the environment, but also seriously affects human health, as shown in Table 1. Some chemicals such as asbestos and ammonia nitrite contained in rubber can cause cancer.

Table 1. Chemicals in Automobiles Affecting Human Health

Chemical varieties	Site of use	Harmfulness
Asbestos	Brake pad and gasket	Carcinogenic
Ozone destroyers (CFC, trichloroethane, carbon tetrachloride)	Air conditioning, foaming agent, detergent	Ultraviolet irradiation
Polybutylphenol chloride (PCB)	Condenser	Harmful health
Polypropofol chloride (PCT)	Lubricating oil and insulating oil	Harmful health
Polychlorinated naphthalenes	Heat transfer agent	Harmful health
Cadmium (Cd)	Electric contact, anti-corrosion, electroplating	Harmful health
Mercury	Sensors and meters	Harmful health
Tribromopropionate and polybutylbromide	Combustion improver	Harmful health
2- naphthalene ammonia	Rubber antioxidant	Carcinogenic
4-amino-diphenyl	Cutting oil	Carcinogenic
Aromatic nitrite	Rubber	Carcinogenesis (nitrite ammonia)
Aliphatic grade two ammonia	Rubber	Carcinogenesis (nitrite ammonia)
Aliphatic secondary amines	Rubber	Carcinogenesis (nitrite ammonia)
Nitrite	Rubber	Carcinogenesis (nitrite ammonia)

From the above analysis, if not properly handled, used automobiles will not only harm the environment, but also cause a lot of used of resources. If, after the recycling and discarding of automobiles, reasonable disassembly and processing can make the second full use of its constituent materials, of which more than 60% of the steel can be recycled 100%; nonferrous metals, which account for 3%-4.7%, such as aluminum, magnesium and copper, can be broken and sorted, and a large part of them can also be recovered. Recycling, utilization and disposal of used automobiles have attracted great attention in developed countries. The recycling and reuse of used automobiles has become an important factor to make up for the shortage of natural resources. China's government has taken "taking

automobiles as the object, providing a set of recyclable and disassemble technologies, and combining them with enterprises, establishing demonstration sites” as one of the objectives and main research contents of the 11th Five-Year Plan. Therefore, developing advanced and efficient related technology research has become an important part of promoting the healthy development of automobile recycling and reuse industry^[10].

2.2. Significance and Function of Recycling and Utilization of Used Automobiles

Used automobiles are resource-intensive and high value-added products. In developed countries with market economy, great attention has been paid to the effective recycling of useful materials, such as used iron and steel, used non-ferrous metals and used plastics from used automobiles, moreover, the recycling management and recycling technology have been constantly improved. The significance and function of recycling used automobiles are mainly manifested in the following aspects:

1. The potential of resources is enormous. Some parts of used automobiles can be reused or remanufactured, such as engines, bumpers, etc. After testing and repairing, they can be reused. Not only can the performance meet the use requirements, but also the cost is relatively low. This fully demonstrates that recycling used automobiles can reduce the exploitation of primary resources, alleviate the pressure of resource scarcity per capita in China, and meet the needs of sustainable economic development^[11-13].
2. The effect of environmental protection is significant. The recycling of used automobiles can reduce the environmental pollution caused by mining and refining of original mineral deposits and manufacturing of new products, and can greatly save energy and reduce greenhouse gas emissions.
3. The stress of employment is alleviated. The implementation of the recycling of used automobiles will bring about a number of new industries, which can partly relieve the employment pressure^[14].
4. It can provide cheaper products. Through the development of remanufacturing as the main resource, we can fully extract the added value contained in the products and provide the products with good quality

and low price. The remanufacturing process restores the performance of parts and components according to the standards of new products through comprehensive disassembly and identification of products, so that the quality of remanufactured products can be equal to or even higher than that of new products.

2.3. Adaptive scheduling of resources in used automobile parts recycling

The resource recycling of used automobile parts is based on the used automobile parts as the object, through modern technology and process, under the standard market operation, to maximize the development and utilization of materials, energy and economic value-added wealth contained therein and make it a resource with high grade and usable, can achieve the purposes of energy saving, material saving and environmental protection^[15].

The establishment of recycling model of used automobile parts must be supported by perfect system and relevant laws and regulations. The developed countries in Europe and the United States, especially Germany and the United States, have formulated a relatively perfect recycling system for the reuse of abandoned vehicles and used products, as shown in Figure 1. The end-users of automobiles submit applications for used vehicles to the designated recycling points. After the recycling points are transferred to the designated used vehicle recycling units and disintegrated, the dismantled products are classified and sent to the used vehicle recycling plants and treatment plants in accordance with the recycling laws and regulations promulgated by the government departments, and then the relevant incentives and subsidies are used to promote the used vehicles recycling proceeds^[16].

This system, through market mechanism, combines users, government departments, recyclers and recycling funds, jointly carries out the work of resource recycling and reduction, and encourages the participation of the whole people by using the feedback mode. By drawing lessons from foreign experience in used automobiles recycling and combining with the current situation of China, this paper summarizes the process chart of used automobile parts recycling by studying the dismantling and recycling process of used automobiles, as shown in Figure 2.

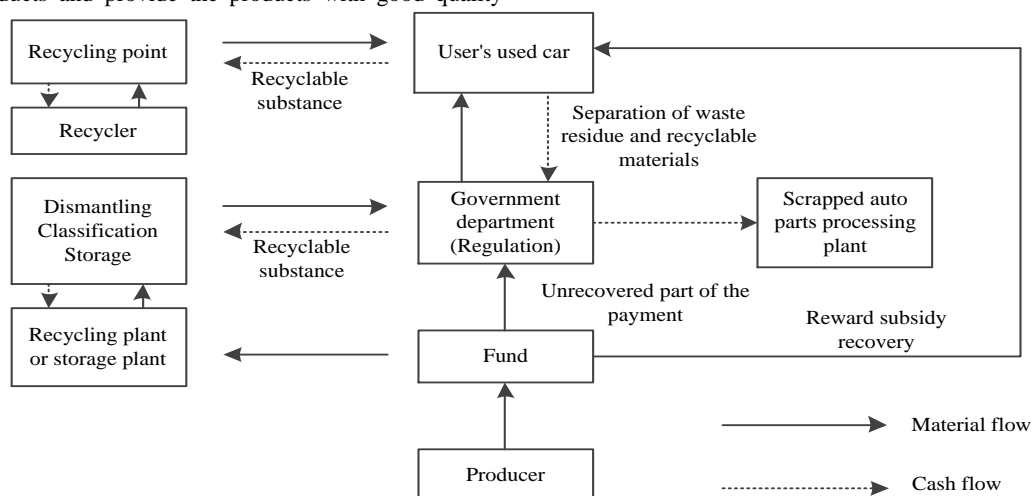


Figure 1. Automobile parts recycling system

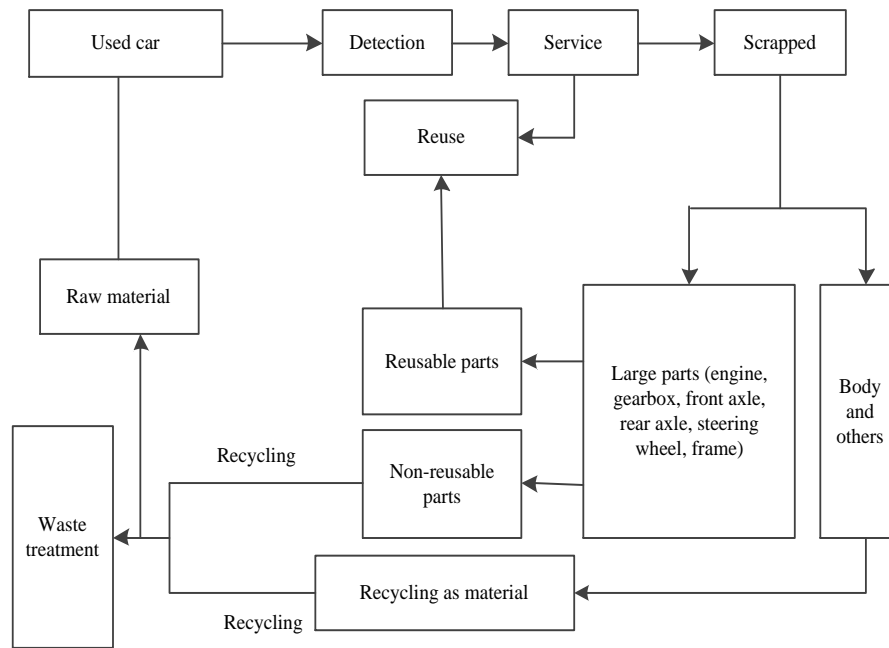


Figure 2. The process chart of automobile parts recycling

In the process of automobile parts recycling, the resource flow of used automobile parts is mainly reflected in the following four aspects [17-18]:

1. Reusable spare parts, used automobile parts cannot achieve equal life design, when the automobile is scrapped, there will always be a part of spare parts with good performance, which should be used directly after passing the test. It can be used as spare parts, and can also enter the product remanufacturing production line to produce remanufactured products.
2. Remanufacturable parts and components, it can absorb various new technologies and processes including advanced surface engineering technology, and implement remanufacturing or upgrading to produce remanufactured products with the same or higher performance than the original products;
3. Recyclable parts, which cannot be repaired or economically inexpensive at present, are recycled as parts for material recycling;
4. Waste disposal, some of which cannot recover their resources through reusing, remanufacturing and recycling procedures at present, can only be safely disposed of through landfills and other measures.

The recycling of used automobiles should realize the recycling of resources as much as possible. Used automobiles are recycled through the multi-level recycling ways of raw materials utilization layer, parts repair utilization layer and direct utilization layer to return to the manufacturing plant in the recycling system. The renewable and available resources are returned to the life cycle of automobiles or into various stages of the life cycle of other products, thus avoiding the waste of resources and reducing the pollution of the environment.

Based on the analysis of the present situation of the resource recycling scheduling for used automobile parts, this paper constructs a mathematical model for the resource recycling scheduling of parts, and considers the time and cost of the resource recycling scheduling of parts. Inverse particle swarm optimization (RPSO) is used to schedule the recovery resources of parts and components

and to adjust the inertia weight parameters. The degree of change of particle function is regarded as the update factor of inertia weight by adaptive mechanism, which avoids taking the value according to the number of iterations, so that the particle will not fall into the local optimum. By introducing the operator of reverse learning, the ability of global search for resource scheduling is strengthened, and the adaptive scheduling for recycling resources of used automobile parts is completed.

2.3.1. Establishment of Mathematical Model for Resource Scheduling of Automobile Parts

Before establishing the mathematical model for recycling resource scheduling of used automobile parts, the hypothesis is made:

1. Virtual machine performance can fulfill any task requirement;
2. All resources and tasks can be allocated;
3. Only one resource is allocated to a task;
4. Random allocation can be guaranteed.

There are m resources and n users in the recycling resources of used automobile parts. The mathematical model for the recycling resources scheduling of used automobile parts is described as follows:

$$M = \{U, V, F, \theta\} \quad (1)$$

In formula (1), U denotes the set of users, V denotes the set of parts recycling resources, F denotes the objective function, and θ denotes the algorithm for solving.

The specific characteristics of the mathematical model for the recycling resources scheduling of automobile parts are as follows:

1. The i th part resource (v_i) is divided according to its location and use, that is $v_i = \{\lambda_i, \mu_i, \phi_i\}$. Thus, the part recycling resource is expressed as $V = \{v_1, v_2, \dots, v_m\}$.

2. For a user has n tasks, different tasks are independent of each other. Therefore, all resource task sets are described as $T = \{t_1, t_2, \dots, t_n\}$, task execution time $S_{m \times n} = \{x_{ij}\}$, where x_{ij} is the time of task execution on component resource j [19].

3. The scheduling matrix E of spare parts resource is expressed as: $E_n = (e_i)$ is that spare parts recycling resource e_i performs task i , and the matrix used for resource utilization is $X_{m \times n} = \{X_{je_i}\}$, where X_{je_i} is that spare parts recycling resource e_i is used by task j .

In combination with the above, the time to complete the task of recovering parts and components resources v_i is as follows:

$$T_j = \max \{x_{ij}\}, i = 1, 2, \dots, n, j = 1, 2, \dots, m \quad (2)$$

For m used automobile parts recycling resources, the total time to complete the task is expressed as:

$$makespan = \sum_{j=1}^m \max \{x_{ij} \cdot x_{je_i}\} \quad (3)$$

In the process of scheduling spare parts recycling resources, the completion time of scheduling is an evaluation criterion in resource scheduling schemes, and the cost of scheduling should also be considered.

Assuming that the cost per unit time of parts recycling p_j is expressed as:

$$p_j = p_{i1} \times \alpha_i + p_{i2} \times \beta_i + p_{i3} \times \gamma_i \quad (4)$$

In formula (4), p_{ij} denotes the cost of recycling resources from components. α_i , β_i , γ_i represent the weight of the corresponding part at the time of recovery in the total build.

For a task, the cost P_i of parts recycling resources v_j is expressed as:

$$P_i = (p_{ij} \times \alpha_i + p_{i2} \times \beta_i + p_{i3} \times \gamma_i) \times \sum_{j=1}^m \max \{x_{ij} \cdot x_{je_i}\} \quad (5)$$

For all tasks, the total cost P of parts recycling resources is expressed as:

$$P = \sum_{j=1}^m p_j \times \max \{x_{ij} \cdot x_{je_i}\} \quad (6)$$

Thus, the total cost of scheduling can be minimized by using the spare parts recycling resource scheduling and objective optimization function [20].

2.3.2 Parts Recycling Resource Scheduling based on Improved Inverse Particle Swarm Optimization

It is assumed that the particle motion space is N -dimensional, the number of population is Z , and the number of iterations is t . In the search space, the position of the i th particle is $x_i = (x_{i1}, x_{i2}, \dots, x_{iN})$, $i = 1, 2, \dots, m$. The particle fitness is obtained by

introducing x_i into the particle the parameters. The local optimum position of the i th particle in the t th time of iteration search is $p_1 P_i(t) = (p_{i1}, p_{i2}, \dots, p_{iN})$, and the optimum position of the particle swarm search for parts recycling resources is $P_g(t) = (p_{g1}, p_{g2}, \dots, p_{gN})$, g is the particle subscript for the global optimum position.

Considering the completion time of spare parts recycling resource scheduling in Section 3.1 above, all completion time is defined as fitness function, which is expressed as:

$$T(X) = \max_{j=1}^m \sum_{i=1}^n x_{ij} \cdot time_{ij} \quad (7)$$

In the upper formula, $time_{ij}$ indicates the completion time of resource scheduling, x_{ij} indicates the task execution time on the build resource.

Aiming at the characteristics of resource scheduling for used automobile parts recycling, the coding method of task-to-computing node vector is adopted. a tasks are allocated to b computing resource nodes. Particle encoding method is $R = \{r_1, r_2, \dots, r_m\}$, where r_i is an integer, and $x_i \in [0, n-1]$ is the label of computing resource nodes. For example, $R = (2, 0, 3, 1, 4)$ means to assign five tasks to five computing resource nodes labeled 0, 1, 2, 3, 4. Among them, the first task is assigned to No. 2, the second task is assigned to No. 1, and so on.

The selection of particle inertia weight ζ has an important influence on the search ability and convergence of resource scheduling algorithm. If the fitness function of the current position and the function value of the last iteration position of a certain component resource particle are relatively small, it means that the scope of particle search is relatively small, and the search scope needs to be increased, so that the parts recycling resource particle can jump out of the local optimal interval, and reach the divergent state. When the difference between the fitness function of the current position and the function value of the last iteration position is large, the inertia weight is reduced, which makes the recovery of resource particles converge. When the resource particle falls into local optimum, the range of particle motion needs to be increased to realize the mutation operation of particle motion for parts recycling [21-23].

Based on the above considerations, a method for selecting the inertia weight ζ of adaptive mechanism is proposed.

$$\zeta(t+1) = 1 - 0.5f(t) \quad (8)$$

The $f(t)$ in formula (8) is determined by formula (9):

$$f(t) = \frac{F(x_g(t))}{F(x_g(t-1))} \quad (9)$$

In formula (9), $F(x_g(t))$ represents the function value of the global optimum fitness of current parts recycling resource particles. When the value of particle update factor $f(t)$ is between $[0, 1]$, when the value is 0, it means that

the distance from the optimal point is far, the value of ζ needs to be reduced, and when the value is 1, it means that the distance from the optimal point is close, and the value of ζ needs to be increased.

In order to expand the scope of particle search for parts recycling resources, an inverse learning operator is introduced to the particles. Based on the particle labeling method, the inverse learning operator is defined as $y_i = d - x_i$. d denotes the total number of recycled resource nodes, and the position of the particle motion obtained by reverse learning is $Y = (y_1, y_2, \dots, y_m)$. When the recycled resource particles fall into the local optimal solution, the reverse learning mechanism is used to realize the mutation operation of the particles, which can only adapt to the recycled resources scheduling of used automobile parts.

3. Results

In order to prove the effectiveness of the proposed resource adaptive scheduling method, practical experiments are carried out.

Setting of the experimental environment: a resource scheduling experiment is carried out under the Matlab simulation environment. The operating system is Windows 10, the processor is Core i4, and the memory is 4 G. By using the method, the particle swarm is used for reverse application, and the search range of the recovered resource particles is enlarged. The main parameters of PSO are represented in Table 2.

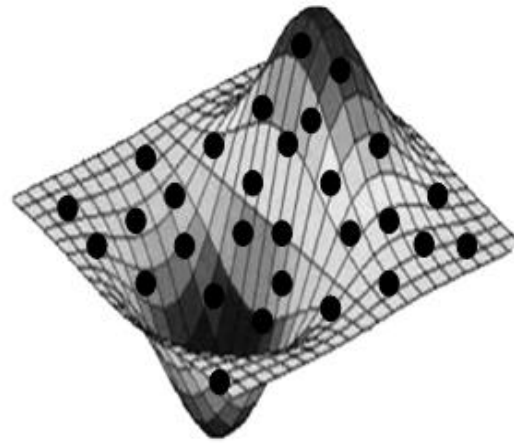
Table 2. Experimental parameters of particle swarm optimization

Parameters	Numerical value
Population size /m	200
Number of task resources/m	22
Number of computing resources/n	6
Learning factor 1	1
Learning factor 2	1
Size of external files	110

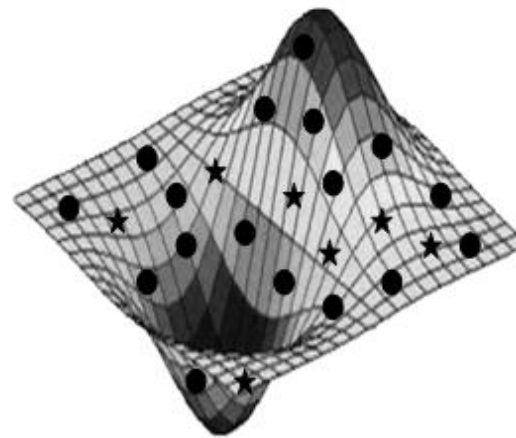
3.1. Testing of Utilization Rate of Recycling Resource

Figure 3 shows the comparison of the proposed method with ant colony algorithm and genetic algorithm. The following figure shows the resource utilization outside the plan in the Pentagon's three-dimensional coordinates the circle represents the recycled resources of the parts used, and the more the circles are, the higher the utilization rate of the recycled resources of the parts is.

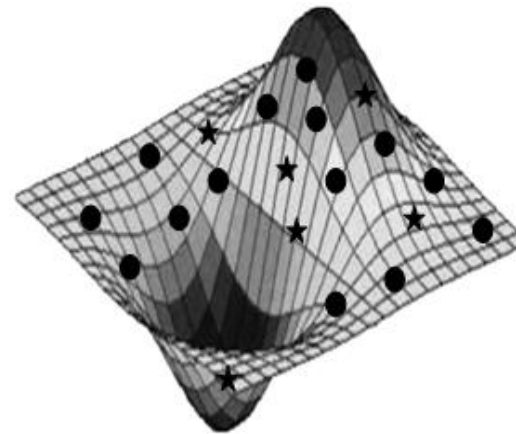
It can be seen from the analysis of Figure 3 that the number of circles in the result graph of this method is the largest, which proves that the utilization rate of parts recycling resources based on the improved reverse particle group component recycling resource method is higher than that of ant colony algorithm. The resource utilization of the genetic algorithm can effectively utilize the used resources.



(a) The method proposed in this paper



(b) Ant colony algorithm



(c) Genetic algorithm

Figure 3. Comparisons of resource utilization rate of spare parts recycling using different algorithms

3.2. Time-consuming Test for Completing Tasks

In the same environment, the completion time of resource scheduling tasks by using the proposed method is compared with that of ant colony algorithm and genetic algorithm, and the results are shown in Figure 4.

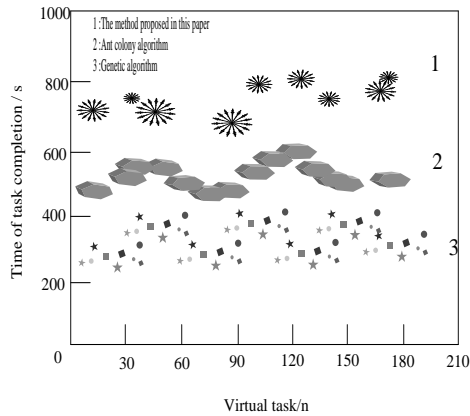


Figure 4. Comparisons of Completion Time of Resource Scheduling Tasks with Different Algorithms

The analysis of Figure 4 shows that the task completion time of the proposed method is significantly less than that of the ant colony algorithm and genetic algorithm. With the increase of resource tasks, the task completion time of the proposed method does not fluctuate greatly and is relatively stable. However, the task completion time of the existing ant colony algorithm and genetic algorithm fluctuates greatly with the increase of resource tasks.

The above experiments show that the method proposed in this paper can effectively reduce the completion time of recycling tasks and improve the scheduling efficiency of spare parts recycling resource .3.3 Energy Consumption Test for Resource

The energy consumption is used as an index for judging the scheduling effect. The energy consumption of the proposed method is compared with that of ant colony algorithm and genetic algorithm in resource scheduling. The energy consumption calculation formula is as formula (6):

The results are shown in Figure 5.

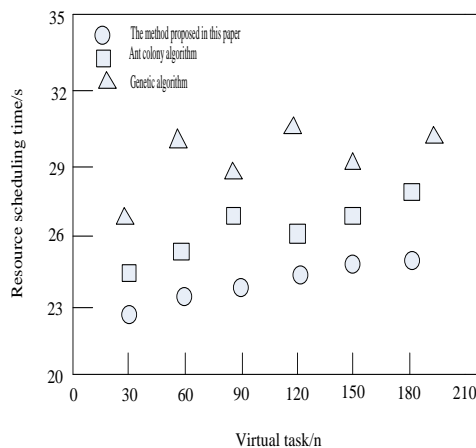


Figure 5. Comparison of Energy Consumption in Resource Scheduling with Different Algorithms

Analysis of Figure 5 shows that compared with ant colony algorithm and genetic algorithm, the energy consumption of the proposed algorithm is lower than that of the other two algorithms. With the increase of resource tasks, the energy consumption of the proposed algorithm is stable, while the energy consumption of the other two algorithms fluctuates greatly. The above experiments show

that the algorithm proposed in this paper can effectively improve the resource utilization rate of spare parts recycling .

4. Discussion

In the inspection of resource utilization, the resource utilization rate of parts recycling based on improved reverse particle swarm optimization is significantly higher than that of ant colony algorithm and genetic algorithm. This is mainly because this method adjusts the inertia weight parameters on the basis of the original particle swarm optimization. The introduction of inverse learning operator can improve the global search ability of particle swarm optimization, and promote parts recycling resource nodes to deal with more resource scheduling tasks quickly and accurately. Moreover, the existing ant colony algorithm and genetic algorithm do not schedule some of the resources when scheduling resources, because they neglect some of the resources, resulting in a reduction in the resource utilization of parts recycling.

In the test of the time-consuming task, as the resource task increases, the task completion time of the proposed method is relatively stable compared to the other two comparison algorithms.

In the test of energy consumption in the resource scheduling process, the proposed method is lower in energy consumption than the other two comparison algorithms. This is mainly because the proposed algorithm uses directional particle swarm optimization to prepare the resource pheromone, which can avoid falling into the local optimal cycle, and can obtain the global optimal solution more easily, thus effectively reducing energy consumption.

In summary, the method proposed in this paper has more advantages than the existing methods in the effective utilization of resources, the time-consuming to complete recycling tasks, and the energy consumption in the process of resource scheduling.

5. Conclusions

Nowadays, “Energy saving and environmental protection, green development and win-win” has become the consensus of all sectors of society. It is of great importance and long-term practical significance to study the recycling, reusing and rational scraping of used automobile parts for saving resources and protecting the environment, and promoting the harmonious development between the green manufacturing and operation of automobiles and human society and nature. Aiming at the low resource utilization of used automobile parts recycling, this paper proposes a resource scheduling method based on improved reverse particle swarm optimization (IPSO) for parts recycling. By using adaptive mechanism, the degree of change of particle function is regarded as the factor of inertia weight updating, which accelerates the convergence rate of parts recycling resource scheduling, introduces the factor of particle reverse learning, and strengthens the ability of particle global search for parts recycling resources. In the future, we need to do further research on the information and data security mode of the scheduling model.

6. Acknowledgement

Funded by the youth innovation talents project of the Guangdong provincial department of education (humanities and social sciences): Research on recycling inventory management of express packaging and remanufactured products (2016WQNCX162).

Reference

- [1] Xue, T.; Ma, T. Dynamic resource scheduling algorithm based on maximum resource utilization. *Application Research of Computers*, 2016, 33(5):1374-1378.
- [2] Xiong, Y.; Jiang, J.; Zhang, Z. Z.; et al. Hybrid Resource scheduling algorithm with traffic differentiation in TWDM-PON. *Acta Electronica Sinica*, 2017, 45(6):1490-1497.
- [3] Qiu, X. A. Novel scheduling algorithm based on utility function for LTE-A precoding system. *Science Technology and Engineering*, 2015, 15(6):215-219.
- [4] Li, T. C.; Li, S. Y. Resource scheduling in cloud computing based on improved bat algorithm. *Electronic Design Engineering*, 2017, 25(1):43-46.
- [5] Cui, J. M.; Liu, J. W.; Yang, C. Y. Resource scheduling algorithm based on priority queuing and network delay in cloud computation. *Journal of Guilin University of Technology*, 2017, 37(2):360-365.
- [6] Wei, Y.; Chen, Y. Y. Cloud computing task scheduling model based on improved ant colony algorithm. *Computer Engineering*, 2015, 41(2):12-16.
- [7] Chen, X. X.; Wu, H.; Wu, Y. W.; et al. Large-Scale resource scheduling based on minimum cost maximum flow. *Journal of Software*, 2017, 28(3):598-610.
- [8] Liu, F.; Peng, Z. Y.; Gao, X. Simulation of port resource equilibrium scheduling model in cloud computing environment. *Computer Simulation*, 2016, 33(8):297-300.
- [9] Ji, K. Cloud computing resource scheduling optimization based on ant colony algorithm with dynamic trend prediction. *Bulletin of Science and Technology*, 2016, 32(1):187-190.
- [10] Xv, Z. J.; Chen, S. X. Research of fusion algorithm based on membrane computing and ant colony algorithm in cloud computing resource scheduling. *Computer Measurement & Control*, 2017, 25(1):127-130.
- [11] Li, H. Y. Reverse supply chain coordination and incentive mechanism for automobile parts recycling and remanufacturing. Zhejiang University of Technology, 2016.
- [12] Zhang, W. D.; Wang, Y. J.; Qin Z. C. An RNTP based coordinated resource allocation scheme in lte indoor scenarios. *Journal of China Academy of Electronics and Information Technology*, 2017, 12(3):241-245.
- [13] Huang, H. Q.; Ye, X. M. Used auto parts recycling sorting process design. *Highways & Automotive Applications*, 2017, (3):13-16.
- [14] Tong, J. H.; Liu, W. H. Comparative study on remanufacturing and recycling channels of auto parts. *Machinery*, 2016, 54(11):54-56.
- [15] Meng, D.; Zhang, Q.; Luo, Y.; et al. An adaptive scheduling algorithm for ISAR imaging radar based on pulse interleaving. *Journal of Air Force Engineering University (Natural Science Edition)*, 2017, 18(2):25-31.
- [16] Wang, H. X.; Wang, Z. H.; Wen, G. F.; et al. Resource constrained multi-project scheduling based on adaptive particle swarm optimization algorithm. *Journal of Industrial Engineering and Engineering Management*, 2017, 31(4):220-225.
- [17] Hu, Y. Research on used automobile recycling industry from the perspective of circular economy. Zhejiang University of Technology, 2016.
- [18] Lei, M. N.; Huang, X.; Wu, Y. C.; et al. Application of Evaporative Air Conditioner in a Large Space Automobile Factory in Xi'an. *Journal of Xi'an Polytechnic University*, 2018, (01):72-76
- [19] Xia, C. L.; Yu, J. L. Study on Optimal Scheduling Modulation Control of Modular Multilevel Converter. *Journal of Power Supply*, 2015, 13(6):84-91.
- [20] Xue, J. Potentials of the renewable resource of usedped cars in China. *China's Population, Resources and Environment*, 2013, 23(2):169-176.
- [21] Upadhyay I.; Pandey G.N. Automated device for in-service monitoring of overhead pipes, burners and turbines in petrochemical plants. *Open Journal of Mechanical Engineering*, 2016, 1(1):1-7.
- [22] Zhang, Z.; Wang, J. L.; Ren, X. F. Design of standard parts recycling system based on machine vision. *Automation & Instrumentation*, 2017, (8):32-33.
- [23] Goswami S.; Choudhury A.; Das S., et al. Automated password protected door lock system. *Advances in Industrial Engineering and Management*, 2017, 6(1):48-52.

Intelligent Remote Monitoring System for Minor Faults of Intelligent Unmanned Vehicle

Jia Tao*, Yuchen Jia, Yuan Gao

Information Science and Technology, Hebei Agricultural University, Baoding 071000, China

Received OCT 16 2019

Accepted JAN 8 2020

Abstract

Monitoring the minor faults of an intelligent unmanned vehicle is the key means to ensure the successful completion of unmanned detection. Therefore, an intelligent remote monitoring system for the minor faults of an intelligent unmanned vehicle is designed. The system takes personal computer and digital signal processor as the control center. A/D conversion circuit converts the minor fault signals collected by the system into data information stored in SD storage module, and the clock reset module records the occurrence of minor faults. In the software part of the system, the fault data are acquired according to the data acquisition process and the signal sampling interruption service process, and the data eigenvalue of remote minor faults of the intelligent unmanned vehicle is monitored based on the variable statistical analysis method, so as to realize the effective monitoring of the minor faults of the intelligent unmanned vehicle. In order to verify the monitoring performance of the system, an experimental study is carried out. The results show that the system can remotely monitor the minor faults of the intelligent unmanned vehicle. Compared with the similar systems, the system has the advantages of efficiency and provides guarantee for the smooth detection of the unmanned vehicle.

© 2020 Jordan Journal of Mechanical and Industrial Engineering. All rights reserved

Keywords: Unmanned; Intelligent Vehicle; Minor Faults; A/D Conversion; Variable Statistical Analysis; Intelligent Monitoring.

1. Introduction

Intelligent unmanned vehicle is a new technology product. Intelligent unmanned vehicle usually refers to an unmanned, self-propelled vehicle (Li & Hu 2016; Dan et al. 2016) which is autonomously navigated by radio remote control or its own program control. Intelligent unmanned vehicles are usually used in scientific exploration, planet exploration, combat intelligence collection, and other fields. The main intelligent unmanned vehicles currently in service are MQ-1 Predator, MQ-9 Reaper, RQ-4 Global Hawk and so on. Intelligent unmanned vehicle is widely used in military and scientific research fields because of its low design cost, no casualty risk, strong survivability and good mobility. It is also the development direction of future automobile manufacturing industry (Zhou et al. 2015; Saska et al. 2017). Intelligent unmanned vehicle works in a harsh environment with abnormal temperature changes. For example, in the application fields of polar exploration and lunar exploration, the working environment temperature is below tens of degrees Celsius. The running state of the vehicle is greatly impacted by the ambient temperature, and it is prone to produce faults. The remarkable faults of the unmanned vehicle can be known through the alarm of the monitoring system, while the minor faults can not be

monitored by the monitoring system. It is difficult to detect. Often because of minor faults, the intelligent unmanned vehicle runs out of control and cannot complete the detection task (Hu & Seiler 2015; Liu et al. 2015). Therefore, it is of practical value and significance to study a remote monitoring system which can monitor the minor faults of an intelligent unmanned vehicle (Chi et al. 2015). This paper designs an intelligent remote monitoring system for minor faults of intelligent unmanned vehicle from both hardware and software aspects. The system uses A/D conversion circuit and storage module to acquire fault data and save them. The system has strong reliability. The time of minor faults is accurately recorded by clock reset module, which provides precise time basis for danger detection (Li & Ge 2015; Song et al. 2015). The fault monitoring method based on variable statistical analysis is one of the hotspots in recent years. It uses the correlation between process variables to diagnose faults. This method processes the historical data of process variables, decomposes the sample space by multi-projection method, projects the sample vectors to each subspace, calculates the corresponding statistics and statistical indicators, and applies them to process monitoring. Based on the data characteristics, this method is more suitable for complex and minor faults monitoring process, so it is applied in the field of minor faults monitoring of intelligent unmanned vehicle.

* Corresponding author e-mail: tj7890609@163.com.

2. MATERIALS AND METHODS

2.1. Overall structure of remote monitoring system for minor fault of intelligent unmanned vehicle

The whole monitoring system is based on PC + DSP (Personal computer and digital signal processor) as the control center. The system is mainly composed of data acquisition A/D(Converter) conversion of slave computer, minimum system of DSP, and the communication, data processing, display output and database call of host computer (Xiao et al. 2017). Among them, the data acquisition part of minor faults is driven by a multi-chip A/D converter controlled by a DSP for synchronous sampling. The minimum system of a DSP is centered on a DSP and consists of extended program memory, data memory, power supply circuit and reset circuit. Communication display module includes keyboard, LCD display, and serial communication module with host computer. Data processing module of host computer mainly realizes data filter design, time-frequency analysis, wavelet packet analysis and waveform display. In the process of fault diagnosis analysis, the call of database is

also an important part of signal analysis. The overall composition of the intelligent remote monitoring system for minor faults of an intelligent unmanned vehicle is shown in Figure 1.

Fig. 1 shows that the main working process of the minor faults monitoring system is as follows: firstly, the collected engine state parameter signal is put into the slave computer cache, then the slave computer packs the signal, and sets the data format. The serial communication module transmits the data to the host computer through the handshake protocol, and then the digital filter and the related signal time-frequency processing algorithm are used to process the various measured parameters, to make running state detection and call fault monitoring database for fault diagnosis (Goebel et al. 2015; Duan et al. 2016), and take further measures to identify, locate, isolate, alarm, and finally save the data to the host computer database. In the fault monitoring system, reasonable and reliable hardware system is very important, but the realization of monitoring tasks in the fault monitoring system, the fault diagnosis ultimately depends on the implementation of the program, the quality of the program directly affects the system performance.

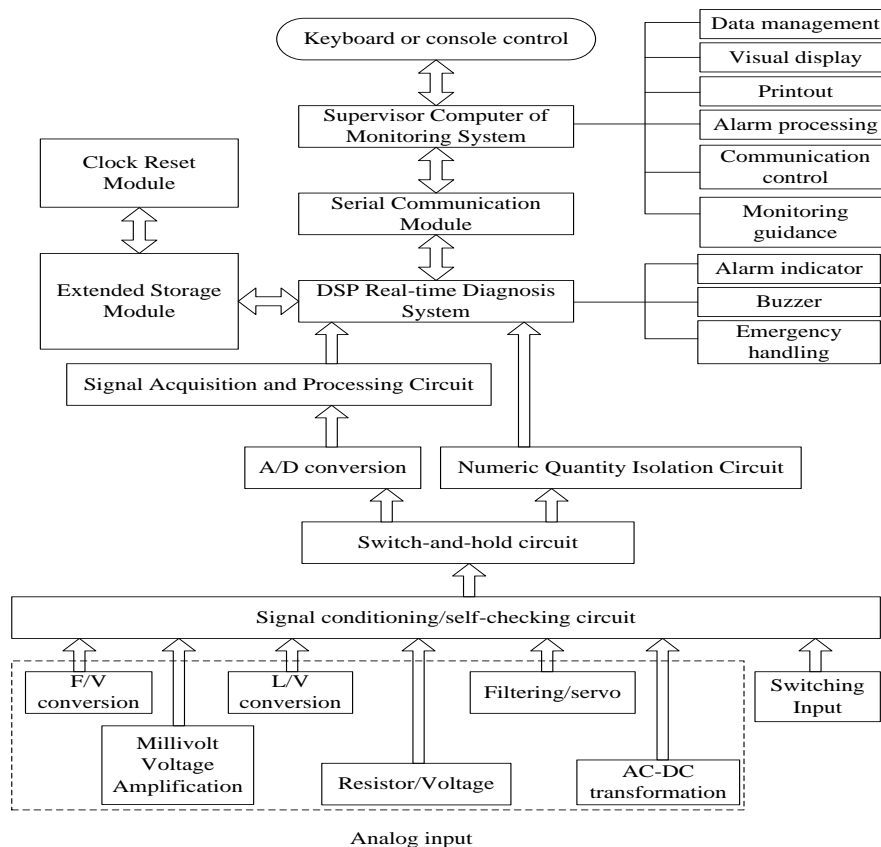


Figure 1. Overall structure of the system

2.2. Hardware design

2.2.1. A/D conversion circuit

The acquisition and analog-to-digital conversion of minor faults signal data in the system is accomplished by AD7874. It is a four-channel 12-path synchronous data acquisition device which can be developed by analog device company. The chip has built-in four-channel sampler-holder and 3 V reference power supply. It is made by LCO process with good linearity and has high accuracy and small relative delay time. The application of simultaneous sampling and time-sharing conversion technology makes that the four-channel special exchange results have phase similarity (Gu & Zhang 2016). Each A/D converter requires 8 us and four channels requires 32 us. Combined with other time expenditure, the sampling frequency of each circuit can reach 29 kHz (the period is about 34 us). Fig. 2 is the pin configuration of AD7874.

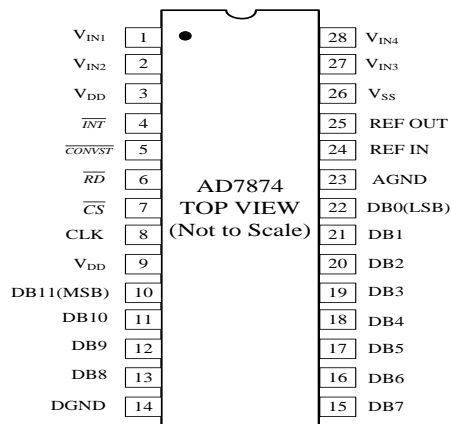


Figure 2. Diagram of AD7874 Pin configuration

As shown in Fig. 2, the internal structure of AD7874 is composed of sampling and holding device, data register, control logic circuit, comparator, reference power supply and internal clock. The working process is as follows: AD7874 receives an operation to make CONVST signal effective from DSP TWS32006713, then AD7874 converts four channels in turn. Indicating that the data conversion of minor faults has been completed, and sends an interrupt request signal to DSP (Bi et al. 2017; Wei et al. 2017). After the interruption of the response of TMS32006713, AD7874 is read four times in succession, and the data is read from channel 1 to channel 4 in turn, so the sampling values are obtained. When reading data from A/D converter, because AD7874 has a high-speed 12-bit data bus, the output signal level is TTL level, while the data bus of TWS32006713 works at 3.3 V level standard, it is necessary to add a level converter 74HC245 between them when designing the interface circuit. It is a driver powered by two voltages, with 3.3 V on one side and 5 V on the other side, playing the role of level conversion. Other signal lines such as INT and CONVST also need to be converted through 74HC245. Figure 3 is a schematic diagram of the interface between DSP and AD7874.

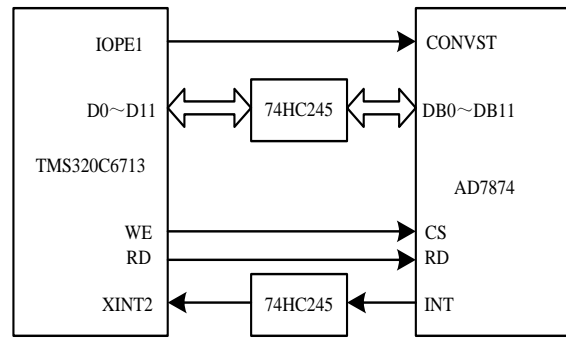


Figure 3. Interface schematic diagram of DSP and AD7874

The interface mode between A/D converter and DSP directly affects the transmission rate of sampled data, that is, the sampling rate. It is very important for real-time system to design a reasonable interface mode according to different needs. On the one hand, it can accurately sample and reasonably arrange the hardware resources of the DSP; on the other hand, it can make the software simple and efficient, and meet the real-time processing requirements.

2.2.2. Clock reset module

The clock reset module of the system is an important technology to record the occurrence time of minor faults of an intelligent unmanned vehicle. The clock circuit TMS320C6713 has a phase-locked loop (PLL) and an oscillator. The oscillator consists of five frequency dividers: D0, OSC, DIV1, D1, D2 and D3. PLL and oscillator can generate different clock signals to each part of the system, such as the DSP core, EMIF, McBSP and so on. The internal structures of PLL and oscillator are shown in Figure 4. Figure 4 shows that the external 3.3 V power supply is filtered and connected to PLDV to supply power to PL. The external 25 MHz crystal output terminal is connected to CLKIN foot. The CLKMODE0 should be raised so that the crystal frequency can pass through the rear frequency divider and phase-locked loop. CLKIN clock signal passes through D0 frequency division (range 1-32 frequency division) and PLL frequency multiplication (range 4-25 frequency multiplication), then inputs D1, D2, D3 three frequency dividers respectively, and outputs three clock signals to provide clock for chips and peripherals. If PLEN is 0, D0 and PLL will be bypassed. CLKIN outputs CLKOUT3 directly after OSC DIV1 frequency division, and the clock is reserved for users to use. All dividers and PLL divider frequencies can be set through the relevant registers, that is to say, the above output clock frequencies can be set by software.

Reset Circuit: For the TMS32006713, reset is an unshieldable external interrupt (interrupt vector address 0000H), which can be used at any time to put the chip in a known state. Reset is the highest priority interrupt, which is usually reset when the chip is in an unknown state after power-on (Okumus et al. 2017). Since the program memory in the reset signal operates and initializes the hardware state bits, the system should rerun the initialization program after each reset.

2.2.3. SD storage module

The system is designed based on STM32F107VCT6 microprocessor of ST company, which has the highest

execution speed of 72MIPS, nearly 30 universal I/O with freely defined functions, one USB2.0 host interface communication, read-write U disk, one USB2.0 slave interface communication, one SD card read-write interface, which can be used for video image and fault data storage, and the circuit design of SD storage module is shown in Figure 5, a 10/100 m adaptive Ethernet interface, in which independent watchdog is built-in to ensure that the system never crashes. The circuit consists of CMOS camera circuit, camera buffer control logic circuit, SRAM memory and 32-bit embedded system bus interface (Miao et al. 2017; Li 2015). The system camera buffer control

logic circuit is realized by programmable logic device EPM7128s. The design scheme is to connect IZ1 with MT9V011 by a programmable logic device, control image data to be cached in SRAM, and then notify the processor to read the data. The control logic circuit in CPLD chip reads image data and caches it into SRAM. The clock of CPLD in the system is 40 MHz, and the clock after 10 minutes is used as the clock of CMOS image sensor (Khorasani 2015). This can reduce the image output rate, and reduce the burden of STM32F107VCT6 on data processing, so that the processor has free time for other control operations.

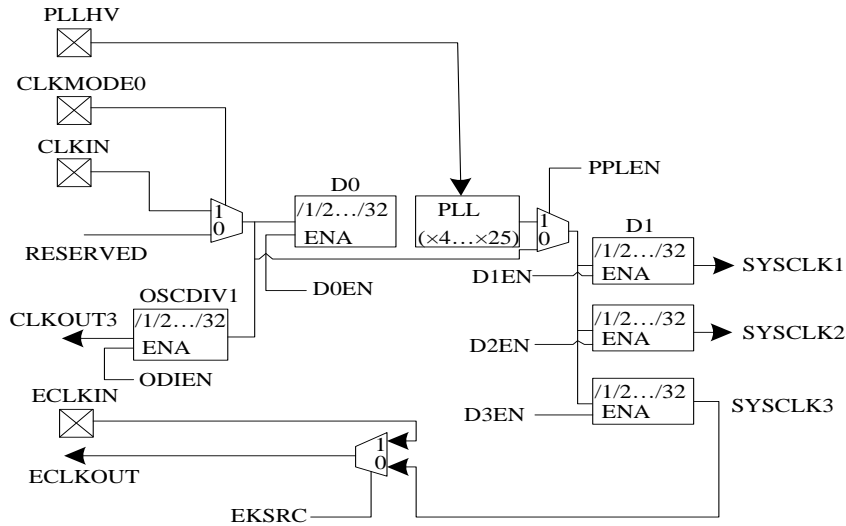


Figure 4. Diagram of clock generation circuit

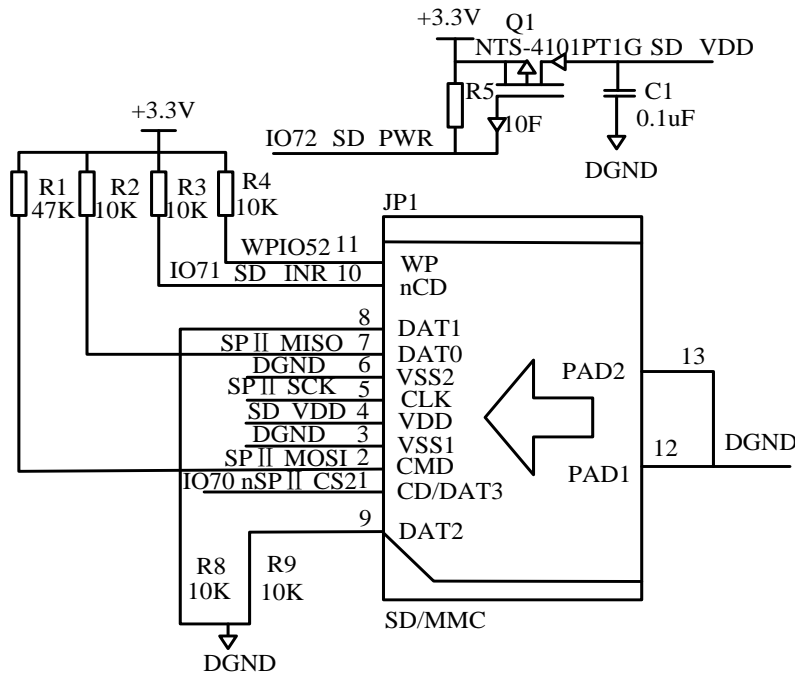


Figure 5. SD memory module circuit

2.3. Software design

2.3.1. Signal acquisition and conversion

A/D converter AD7874 is used as the main component of the acquisition module for minor faults signal acquisition. Procedure flow charts of fault data signal acquisition and interruption service flow chart of signal sampling are shown in Figs. 6 and 7. In the system, 1024-point vibration signal data of engine rotor are collected for processing and analysis, and 1024 data storage areas are set for the alarm signal. With ring queue storage, the address and length of the storage area remain unchanged (Yang et al. 2015). The first sampled data is stored in the first address of the storage area, and the latter data is stored back in turn. When the storage area is full, the last sampled data replaces the earliest data in the storage area, and saves the position of the last sampled point as a pointer for data reconstruction.

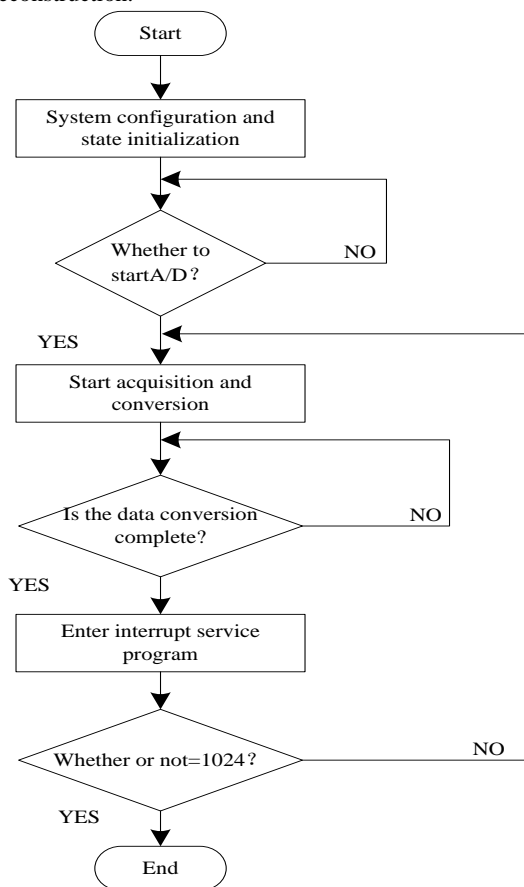


Figure 6. Flow chart of program for acquisition and conversion of minor faults signals

In Fig. 7, the timer 1 triggers the direct memory controller EDMA to control sampling. According to the requirement of the system, the core resources of the DSP are precious and need to complete a lot of calculation and communication control. Sampling time takes up a large part in running data sampling and other programs. Sampling module uses timer to trigger CPU to sample at a certain frequency, and EDMA to design sampling module can avoid CPU resources interfering with sampling module, so that CPU can use all resources to perform algorithm and other program operations. The process of data sampling using EDMA is described below.

Since the sampling is carried out at a certain frequency, a timer must be used to trigger an EDMA event, so that

EDMA can move the data from the A/D digital output to RAM. Before sampling, the timer 1 should be set to determine the sampling period, and then the EDMA and timer 1 should be correlated so that the timer 1 can trigger the EDMA event, and then the EDMA channel can be enabled.

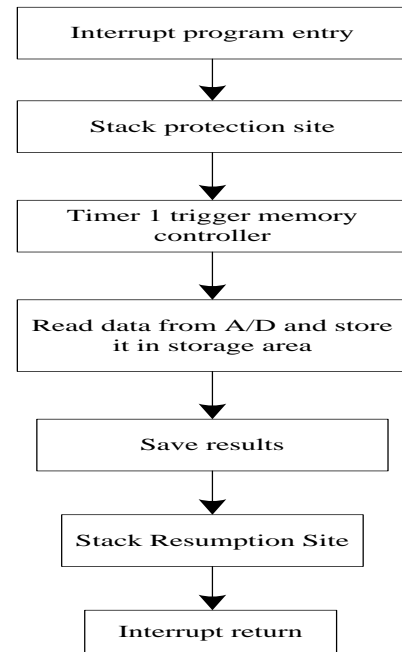


Figure 7. Flow chart of sampling interrupt service program for minor fault signal

2.3.2. Minor fault monitoring method based on variable statistical analysis

According to the collected monitoring data of the intelligent unmanned vehicle, the minor faults of the intelligent vehicle are monitored based on the statistical analysis of variables. Variables are transformed vectors of the original fault data matrix, and they are not correlated with each other. Their statistical characteristics reflect some points in the process. For example, the variance of variables is the eigenvalue of the covariance matrix of normalized data. Statistical characteristics of monitoring variables can reflect the change of working conditions.

Considering the original fault data matrix $X \in R^{n \times m}$, n represents the number of independent measurements and m represents the number of sensors. After standardizing the original process data (zero mean and unit standard deviation), the covariance of the sample of minor faults is calculated by the following formula:

$$S = \text{cov}(X) = \frac{1}{n-1} X^T X \quad (1)$$

By singular value decomposition of S , the load matrix P (matrix composed of eigenvalue vectors of S) can be obtained. Then the data matrix of minor faults in original process can be transformed as follows:

$$T = XP \quad (2)$$

In the formula, $P \in R^{m \times m}$ is the load matrix; $X \in R^{n \times m}$ is the score matrix (each column of T represents the corresponding TC).

Because TCSA is an algorithm based on sliding time window, it is necessary to calculate TC in each window and calculate its statistical characteristics. Let the length of the sliding time window be w , $X(k)$ is the process measurement value representing the length of a window:

$$X(k) = \begin{bmatrix} x_1 A_1 & x_2 A_1 & \cdots & x_m A_1 \\ x_1 A_2 & x_2 A_2 & \cdots & x_m A_2 \\ \vdots & \vdots & \ddots & \vdots \\ x_1(k) & x_2(k) & \cdots & x_m(k) \end{bmatrix} \quad (3)$$

In the formula, $A_1 = k - w + 1$, $A_2 = k - w + 2$.

A fault data matrix can be created:

$$X_{sum} = [X_{normal}; X_k] \quad (4)$$

In the formula, $X_{normal} \in R^{w \times m}$ is the measurement data matrix under normal working conditions. Then the normalized covariance matrix of X_{sum} is calculated, and the SVD decomposition is carried out to obtain the matrix T . The statistics (mean, variance, skewness, kurtosis) of the matrix are calculated, and the fault statistics matrix is constructed.

$$S(k) = [mean(k), var(k), skewness(k), kurtosis(k)] \quad (5)$$

The detection index can be calculated by the following formula:

$$DI(k) = \left\| S(k) - S^{(mean)} \left(diag \left(S^{(std)} \right) \right)^{-1} \right\|_p \quad (6)$$

It should be pointed out that, because the matrix T satisfies formula (7), when the statistics are only used differently and norm 2 is taken, the detection index degenerates as shown in formula (8):

$$\frac{1}{2w-1} T^T T = \begin{bmatrix} \lambda_1 & & \\ & \ddots & \\ & & \lambda_m \end{bmatrix} \quad (7)$$

$$DI(k) = \left\| \left(var(k) - var^{(mean)}(k) \right) \cdot \left(diag \left(var^{(std)}(k) \right) \right)^{-1} \right\|_2 \quad (8)$$

$$= \sum_{j=1}^m \left(\frac{\lambda_j(k) - \lambda_j^{(mean)}}{\lambda_j^{(std)}} \right)^2$$

The above operation is transformed into the monitoring of eigenvalues of covariance matrix. The monitoring eigenvalues are the fault data eigenvalues of unmanned vehicles. Based on these eigenvalues, the minor faults of intelligent unmanned vehicle can be monitored. The EDMA parameter code is set as follows:

```
EDMA Configfedma= {
EDMA_OPT_RMK (/ * EDMA_OPT)*/
EDMA_OPT_PRI_LOW, /* EDMA Event Priority*/
EDMA_OPT_ESIZEEs 32BIT, /* Unit length is 32 bits,
read data of two channels at a time*/
EDMA_OPTEs 2DS NO, /* One-dimensional transmission
of source data*/
EDMA_OPT_SUM_NONE, /* Source address is fixed
mode, because A/D address remains unchanged*/
EDMA_OPT_2DD_NO, /* One-dimensional transmission
of target data*/
EDMA_OPT_DUM_INC, /* Target address is self-
increasing mode*/
EDMA_OPT_TCINT_YES, /* Transmission completes
sending interruption*/
EDMAPT_TCC_OF (TCCINTNUM), /* Transmission
completion code*/
EDMA_OPT_LINK_YES, /* Connection enables*/
EDMA_OPT_FS_NO/* Synchronization of use unit */
)
EDMA_SRC_OF (0xA0300000), /* Setting source
address*/
EDMA_CNT_OF (sample count), /* Sampling points*/
EDMA_DST_OF (SAMPLE_DATA_ADDR), /* Target
data address*/
EDMA_IDX_OF (0x00000004), /* Set index, 4 bytes
increase by itself*/
EDMA_RLD_OF (sample count, 16 0x0) /* Count is reset
to sampling point*/
} ;
```

After starting the timer, the timer will trigger EDMA according to the sampling period. EDMA triggers an interrupt notification CPU after all sampling points are moved. Finally, the EDMA channel and timer are closed to complete the sampling process. In the engine monitoring system, the selection of various parameter filtering methods should be based on the characteristics of the monitored signal of the engine and its changing rules.

3. RESULTS

In this paper, BJUT-IV, an intelligent unmanned vehicle, is used as an experimental object to study the effectiveness of the intelligent monitoring system for minor faults in this paper. In the experiment, 10 minor faults occurred in the driving process of BJUT-IV, named AB-1, AB-2, AB-3-AB-10, and the complex environment of 80 m×80 m is selected as the driving section of the intelligent unmanned vehicle.

3.1. Fault data acquisition and analysis

In this paper, the system collects the minor faults characteristic data of the intelligent unmanned vehicle as shown in Fig. 8.

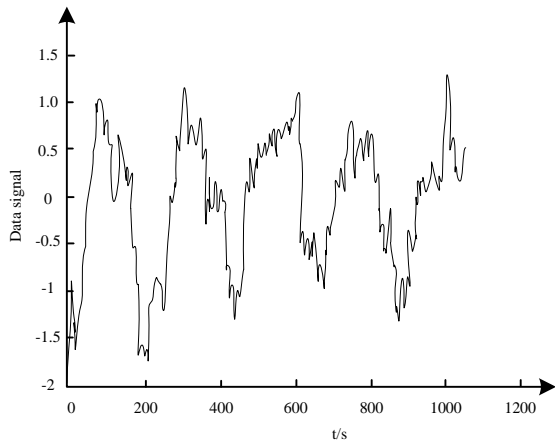


Figure 8. Data acquisition results of minor faults

Fig. 8 shows that the system can accurately collect the minor faults data of the intelligent unmanned vehicle, and then carry out fault analysis, which proves that the system is effective.

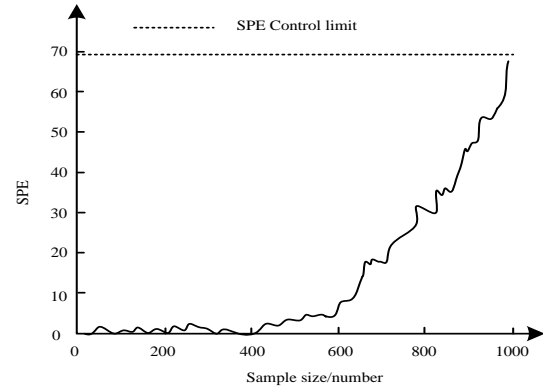
3.2 Comparison of system monitoring results

In order to highlight the advantages of this system in monitoring minor faults of intelligent unmanned vehicles, CUSUM-PCA monitoring system and DISSIM monitoring system are selected for comparative testing. Because the three systems all use statistical analysis methods to monitor minor faults of intelligent unmanned vehicles, the comparative effect is obvious. The usage time of the three systems for remote monitoring of the minor faults of the intelligent unmanned vehicle is shown in Table 1. The results of the three systems for monitoring the minor faults of the intelligent unmanned vehicle are analyzed from the perspective of statistical analysis variable SPE, as shown in Fig. 9, Fig. 10 and Fig. 11 (with limited space, only the first four minor faults are compared). When the monitoring curve is above the SPE control limit, the system can accurately monitor the minor faults of the unmanned vehicle, and the monitoring rate is higher. When the monitoring curve is below the SPE control limit, the system can not accurately monitor the minor faults of the unmanned vehicle, and the monitoring rate is lower.

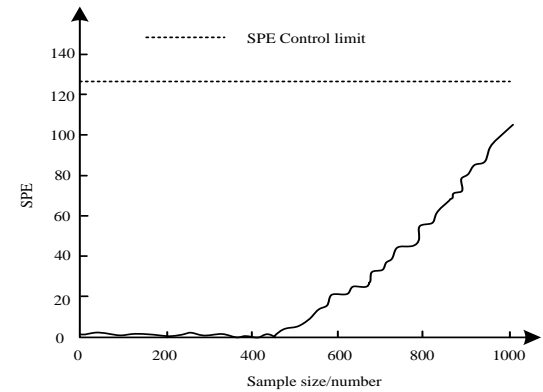
Table 1. Time-consuming for monitoring and controlling minor faults in three systems/s

Fault name	Paper system	CUSUM-PCA Monitoring System	DISSIM Monitoring System
AB-1	0.20	1.90	2.20
AB-2	0.10	1.70	2.10
AB-3	0.11	1.60	2.50
AB-4	0.21	1.50	1.90
AB-5	0.19	2.10	2.23
AB-6	0.18	1.85	2.19
AB-7	0.11	1.64	2.74
AB-8	0.15	1.73	2.11
AB-9	0.20	2.50	2.13
AB-10	0.13	2.46	1.98

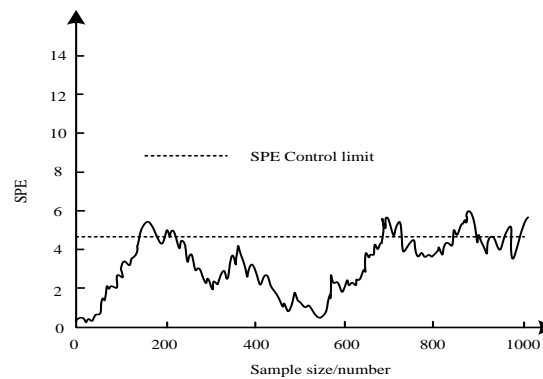
Table 1 shows that the system consumes about 0.10-0.21 seconds to monitor minor faults, 1.4-2.29 seconds less than that of CUSUM-PCA monitoring system and 1.8-2.53 seconds less than that of DISSIM monitoring system.



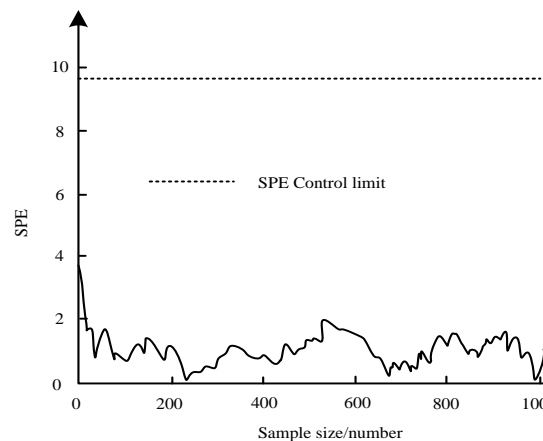
(a) Fault AB-1



(b) Fault AB-2

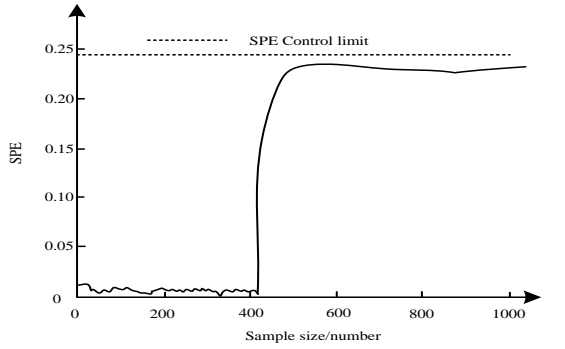


(c) Fault AB-3

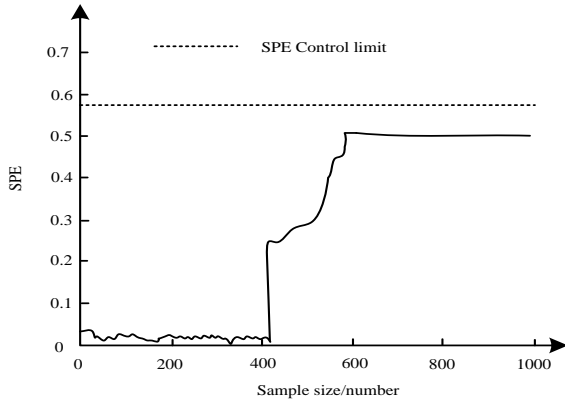


(d) Fault AB-4

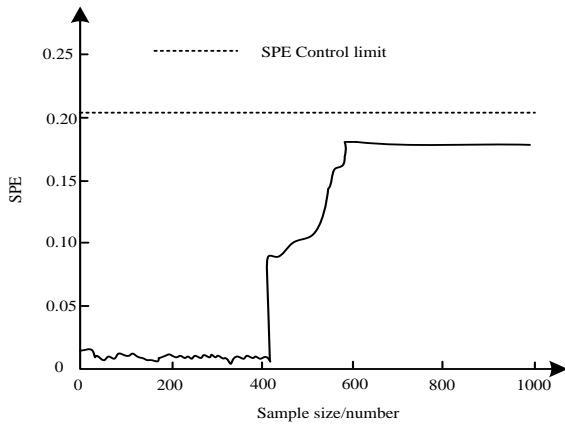
Figure 9. Fine fault recognition results of CUSUM-PCA monitoring system



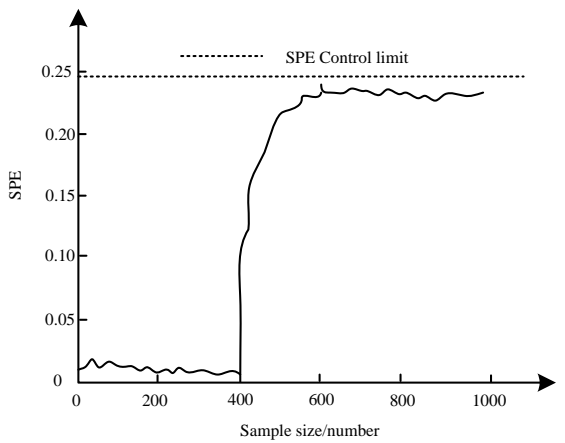
(a) Fault AB-1



(b) Fault AB-2

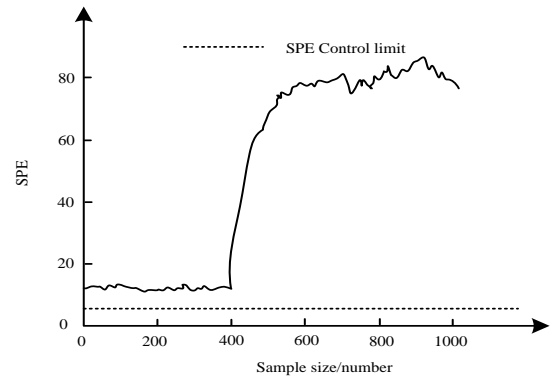


(c) Fault AB-3

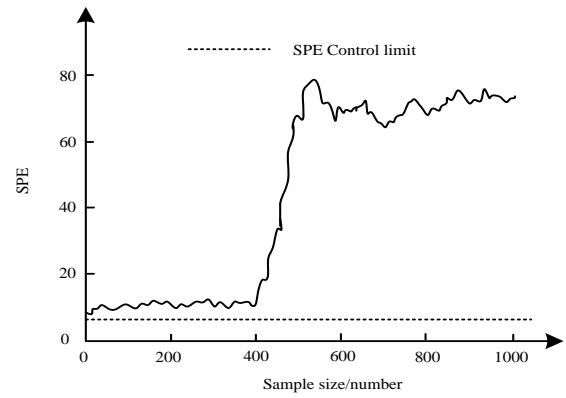


(d) Fault AB-4

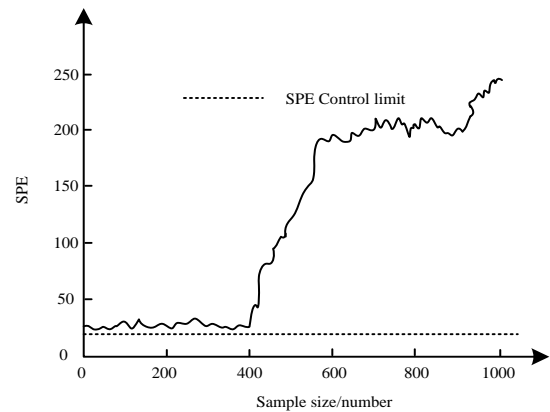
Figure 10. Fine fault recognition results of DISSIM monitoring system



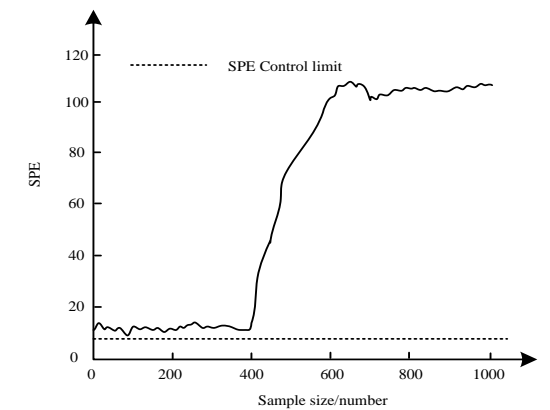
(a) Fault AB-1



(b) Fault AB-2



(c) Fault AB-3



(d) Fault AB-4

Figure 11. Fine fault identification results of the method in this paper

The above results show that the system can correctly monitor the minor faults of the intelligent unmanned vehicle, and achieve the purpose of remote monitoring the minor faults of the intelligent unmanned vehicle, while the CUSUM-PCA system and DISSIM system can not accurately monitor the minor faults of the intelligent unmanned vehicle.

4. DISCUSSION

The performance of this system is verified by unmanned driving test. Table 1 shows that the system consumes about 0.10-0.21 s to monitor minor faults, saves 1.4-2.29 s compared with CUSUM-PCA monitoring system and 1.8-2.53 s compared with DISSIM monitoring system. It can be seen that this system has a shorter time to monitor the minor faults of the intelligent unmanned vehicle, and improves the efficiency of the minor faults monitoring. Under the remote monitoring of this system, the minor faults of the intelligent unmanned vehicle are all within the scope of monitoring, which provides a reliable basis for the remote control and normal driving of the intelligent unmanned vehicle.

The results of Fig. 9 show that four kinds of minor faults curves of CUSUM-PCA monitoring system are under the SPE control limit, which shows that the system can not accurately monitor the minor faults of the intelligent unmanned vehicle, and the monitoring rate is low. The process of monitoring fault AB-1, AB-2 and AB-4 in CUSUM-PCA system is similar, and there is no junction between monitoring curve and SPE control limit, which indicates that the data collected by the system is not effective enough to correctly monitor minor faults of intelligent unmanned vehicles. When monitoring fault AB-3 in CUSUM-PCA system, there is a junction between monitoring curve and SPE control limit, which indicates that the data collected by the system is effective at this time, which increases the probability of system monitoring minor faults. But in general, the monitoring system cannot correctly monitor the minor faults of the intelligent unmanned vehicle. Similarly, from Figure 10, we can see that the DISSIM monitoring system cannot monitor four kinds of minor faults of the intelligent vehicle.

The results of Fig. 11 show that the monitoring curves of the system in this paper are above the SPE control limit, which shows that the system can accurately monitor the minor faults of the intelligent unmanned vehicle, and provide an effective basis for solving the faults of the intelligent vehicle and reducing the probability of the unmanned accident. This system has strong ability to monitor minor faults, which is mainly embodied in the following aspects: (1) This system takes PC+DSP as the control center, and is driven by DSP to synchronously sample multiple A/D converters to complete the fault data acquisition of intelligent unmanned vehicle; PC+DSP combination has excellent performance and wide application scope, which provides an excellent component for minor faults monitoring system, and DSP control A/D converter to complete data acquisition, improving the accuracy of minor faults data to a certain extent, and improving the accuracy probability of monitoring minor faults. (2) The fault monitoring method adopted in this system has a strong ability in monitoring minor faults. The data collected by the hardware of the system are analyzed by variable statistics. Variables are transformed vectors from the original minor faults data matrix, and they are not related to each other. Variable statistical analysis method

first calculates the covariance of minor fault samples, and decomposes the singular value of variance results to get the load matrix, then calculates the process measurements in the length of sliding time window, creates the data matrix and constructs the statistical matrix, which is transformed into the monitoring of the eigenvalues of the covariance matrix, and the monitoring eigenvalues are the fault data eigenvalues of the unmanned vehicle. It can control the minor faults of the intelligent unmanned vehicle and improve the ability of the system to monitor the faults.

5. CONCLUSIONS

Intelligent unmanned vehicle started late, but it has broad application prospects. It is mainly used to detect complex environment and unknown areas. However, the navigation control system of unmanned vehicle is often threatened by complex environment, resulting in uncontrollable faults, while minor faults are not easy to detect, easy to lose direction, seriously affecting the detection effect of unmanned vehicle. Therefore, this paper designs a remote monitoring system for minor faults of intelligent unmanned vehicle. Monitoring minor faults of intelligent unmanned vehicle mainly uses variable statistical analysis method to monitor minor faults from the data point of view, with higher accuracy and better effect. In order to verify the effectiveness of the system in monitoring the minor faults of the intelligent unmanned vehicle, the experimental study shows that the system has strong ability and high efficiency in monitoring the minor faults of the intelligent unmanned vehicle. It provides a new means for monitoring the minor faults of the intelligent unmanned vehicle, and shows a high application value.

ACKNOWLEDGEMENT

This research was supported by Project of Scientific Research Youth Fund for Higher Education Institutions in Hebei Province in 2019. Item number: QN2019211.

REFERENCES

- [1] Bi, H., Zheng, W. & Ren, Z. 2017. Using an unmanned aerial vehicle for topography mapping of the fault zone based on structure from motion photogrammetry. *International Journal of Remote Sensing* 38 (8-10): 2495-2510.
- [2] Chi, Y., Zhang, Y. & Liu, Z. 2015. A survey on technologies for automatic forest fire monitoring, detection, and fighting using unmanned aerial vehicles and remote sensing techniques. *Canadian Journal of Forest Research* 45 (7): 150312143318009.
- [3] Dan, L., Duan, J. & Hui, S. 2016. A Strong Tracking Square Root Central Difference FastSLAM for Intelligent unmanned Vehicle With Adaptive Partial Systematic Resampling. *IEEE Transactions on Intelligent Transportation Systems* 17 (11): 3110-3120.
- [4] Duan, J.M., Shi, H. & Liu, D. 2016. Research of Navigation Control System for Intelligent unmanned Vehicles. *Computer Simulation* 33 (2): 198-203.
- [5] Goebel, M.E., Perryman, W.L. & Hinke, J.T. 2015. A small unmanned aerial system for estimating abundance and size of Antarctic predators. *Polar Biology* 38 (5): 619-630.
- [6] Gu, A., Zhang, X.X. 2016. Fault diagnosis system for power battery based on RBF neural network. *Chinese Journal of Power Sources* 40 (10): 1943-1945.

- [7] Hu, B., Seiler, P. 2015. Pivotal decomposition for reliability analysis of fault tolerant control systems on unmanned aerial vehicles. *Reliability Engineering & System Safety* 140 (4): 130-141.
- [8] Khorasani, K. 2015. A hybrid fault detection and isolation strategy for a team of cooperating unmanned vehicles. *International Journal of Control* 88 (1): 90-103.
- [9] Li, L., Hu, D. 2016. Introduction to the Special Issue on Intelligent unmanned Vehicles in China. *IEEE Transactions on Intelligent Transportation Systems* 17 (7): 2020-2021.
- [10] Li, Y.H. 2015. Temperature remote monitoring system design and GSM-based STM32. *Automation & Instrumentation* (1): 56-59.
- [11] Li, Y.X., Ge, X.L. 2015. Characteristic Performance Analysis of Traction Motor on EMU with Broken Bars Using FEM. *Journal of Power Supply* 13 (1): 41-47.
- [12] Liu, X.M., Zhu, J.L. & Zhang, L. 2015. The model of WDM optical network for Unified Avionics Network. *Journal of China Academy of Electronics and Information Technology* 10 (2): 138-143.
- [13] Miao, Y., Yu, H. & Zhou, J. 2017. Modeling of landslide topography based on micro-unmanned aerial vehicle photography and structure-from-motion. *Environmental Earth Sciences* 76 (15): 520.
- [14] Okumus, E., San, F.G.B. & Okur, O. 2017. Development of boron-based hydrogen and fuel cell system for small unmanned aerial vehicle. *International Journal of Hydrogen Energy* 42 (4): 2691-2697.
- [15] Saska, M., Baca, T. & Thomas, J. 2017. System for deployment of groups of unmanned micro aerial vehicles in GPS-denied environments using onboard visual relative localization. *Autonomous Robots* 41 (4): 1-26.
- [16] Song, Y., Weng, X. W. & Guo, X. 2015. Small UAV Attitude Estimation Based on the Algorithm of Quaternion Extended Kalman Filter. *Journal of Jilin University (Science Edition)* 53 (3): 511-518.
- [17] Wei, W., Tischler, M.B. & Cohen, K. 2017. System Identification and Controller Optimization of a Quadrotor Unmanned Aerial Vehicle in Hover. *Journal of the American Helicopter Society* 62 (4): 1-9.
- [18] Xiao, W., Chen, Y.G. & Yang, Y.P. 2017. The impact of intelligent vehicle on the two-route system with a work zone. *International Journal of Modern Physics C* 28 (8): 1750106.
- [19] Yang, P., Tang, K. & Lozano, J.A. 2015. Path Planning for Single Unmanned Aerial Vehicle by Separately Evolving Waypoints. *IEEE Transactions on Robotics* 31 (5): 1130-1146.
- [20] Zhou, H., Kong, H. & Wei, L. 2015. Efficient Road Detection and Tracking for Unmanned Aerial Vehicle. *IEEE Transactions on Intelligent Transportation Systems* 16 (1): 297-309.

Review Study of Physical and Mechanical Characteristics on Mixed Soil with Scrap Tire Rubber Particles

Jianguang Bai, Yan Zhang*, Shuzheng Wu

College of Energy and Transportation Engineering, Inner Mongolia Agricultural University, Hohhot 010018, China

Received OCT 16 2019

Accepted JAN 8 2020

Abstract

When the sand is mixed with rubber particles, the cohesion and the internal friction angle can be increased, whereas the dynamic shear modulus can be reduced and the damping ratio and the liquefaction resistance can be increased. The addition of rubber particles affects the skeleton structure of mixed sand, and affects its stress-strain relationship. The compressibility of mixed sand can be increased and the Poisson's ratio can be changed. When the clay is mixed with rubber particle, the shear strength can be increased. The compression coefficient of mixed clay can be reduced and compression modulus can be increased, and the removal rate of phenol can be improved. It can improve the strength, deformation and physical characteristics of mixed clay. When loess is mixed with rubber particle, its dynamic characteristics and compaction characteristics can be changed. When expansive soil is mixed with rubber particle, its swelling and shrinkage characteristics and compressive strength can be improved, and its shear strength can be changed. When fly ash soil is mixed with rubber particle, its dynamic characteristics and shear strength can be affected. In order to further ascertain the effect of rubber particles on soil, the following aspects should be further studied: comprehensive effect of rubber particle content and size on the skeleton structure and stress-strain relationship of mixed sand; mechanism of dynamic characteristics of mixed sand; rubber particle content and size meeting the needs of engineering in the aspects of strength and deformation; effect of rubber particles on physical and mechanical characteristics of silt and silty clay; effect of rubber particles on permeability of clay; effect of rubber particles on collapsibility and strength of loess; effect of rubber particles on compaction and dynamic characteristics of expansive soil; effect of rubber particles on deformation, compressive strength and compaction characteristics of fly ash soil; durability and environmental influence on strength and deformation characteristics. It provides a direction for the rational utilization of scrap tire because of its effect of rubber particles on improvement of the characteristics of soil.

In the paper, the physical and mechanical characteristics on mixed soil with rubber particles are reviewed, and the problems existing in the improvement of soil characteristics by rubber particles are analyzed and the prospects are forecasted. It is a reference for the utilization of scrap tire and the improvement of soil characteristics.

© 2020 Jordan Journal of Mechanical and Industrial Engineering. All rights reserved

Keywords: rubber particle, mixed soil, scrap tire, strength and deformation.

1. Introduction

In recent years, with the rise of global automobile industry, the number of scrap tires is increasing day by day. The number of scrap tires in China has exceeded 300 million by 2015, and it is growing at an annual rate of 8%-10%. Tire rubber belongs to the refractory or non-fusible polymer materials, it has strong corrosion resistance and hard to degradation. Under the influence of natural force, it would not disappear for decades or even centuries. Scrap tires are hazardous industrial solid waste, which would seriously pollute the ecological environment and affect human health [1, 2]. Therefore, the rational use of scrap tires has become a hot topic to solve environmental problems and promote economic development.

The application of scrap tires in civil engineering is a good way to solve this problem. And it is also one of the development directions of circular economy [3]. Scrap tires can be used in concrete to improve the seismic performance [4], resilience [5], toughness [6, 7], ductility [8], durability [9], workability [10], and strength characteristics of concrete [11, 12]. It can also be widely used to improve soil characteristics [13, 14] as seismic backfill material for slope, retaining wall, bridge and other geological structures [15]. Mixed soil formed by mixing scrap tire rubber particles into soil does not pollute the soil [16]. It is environmentally friendly [17, 18]. Scrap tires become valuable material resources [19]. In this paper, the strength, deformation, dynamic characteristics and physical characteristics of mixed soil formed by mixing scrap tire rubber particles into the soil are studied.

* Corresponding author e-mail: zhanyanli@imau.edu.cn.

2. Rubber particle sand mixed soil

2.1. Shear strength

There are many factors affecting the shear strength of rubber particle sand mixed soil, including rubber particle content, size, size ratio of rubber particles to sand, temperature and so on. Different size ratio and rubber particle content can increase or decrease the shear strength of the mixed soil [20].

Studies by Zhang Yongfu et al. [21], with the increase of rubber particle content, the cohesion and internal friction angle of mixed soil are increased first and then decreased. The internal friction angle reaches the maximum when the rubber particle content is 10%. The cohesion reaches its maximum when the rubber particle content is 20%, as indicated in Table 1. The cohesion and internal friction angle of rubber particle sand mixed soil are affected not only by rubber particle content, but also by rubber particle size [22]. With the increase of rubber particle size, the role of rubber particles in the internal structure is weakened, and the stress transfer mainly through sand-sand [23]. Rubber particles with 6 mm size can provide the maximum shear strength at 30% rubber particles content. Compared with pure sand, the addition of rubber particles can improve the shear strength of soil.

The main reason is that the addition of rubber particles makes the contact and occlusion between particles more sufficient in rubber particle sand mixed soil. When shear occurs, rubber particles undergo continuous extrusion and deformation. It fills the entire interface voids. It enhances the ability to resist deformation of the specimen. At the same time, the sliding and rolling of particles are limited to a certain degree. Rubber particles can inhibit the buckling of bearing capacity chain. Therefore, the shear strength of rubber particle sand mixed soil can be improved [24].

Some studies showed that the addition of rubber particles would slightly reduce the internal friction angle of sand [25]. The higher content of rubber particle it has, the lower the strength is [26]. It has differences with the former [21, 22] in the form of research results. Actually, both of them have coincidence. As Table 1 [21], when the content of rubber particles is less than 30%, the internal friction angle of sand can be increased by adding rubber particles, but it is opposite when the content of rubber particles is more than 30%. The more amount of doping, the more obvious the reduction of internal friction angle. Size Ratio of Particles to Sand decides the mixture behavior of rigid sand and soft rubber particles [27]. It is also an important reason for differences in result due to the different size ratio. Therefore, the mechanical behavior of rubber particles in sand is closely related to content, particle size and size ratio. There are differences between the two research conditions, so the results are not contradictory.

Table 1. Tested values of shear strength parameters of rubber particle sand mixed soil under different proportions [21]

Proportion/%	Cohesion/kPa	Internal friction angle/(°)
0	7.5	36.02
10	14.7	42.27
20	18.9	38.34
30	18.2	34.42
40	15	31.95
50	12.4	27.4

Rubber particle content and confining pressure can influence shear characteristics of mixed soil. When the

content of rubber particles is not more than 20%, it is similar to pure sand and has the characteristics of first shear shrinkage and then shear dilation. When it is above 20%, it shows monotonous shear shrinkage characteristics [21]. The higher the content of rubber particles, the more obvious the shear shrinkage. And its strain-stress curve ($\varepsilon_c - p$ curve) is hyperbolic, as shown in Fig. 1 [28]. The extended Duncan-Chang Hyperbolic Model Parameter can also be used for simulation [29]. With the increase of rubber particle content, mixed soil gradually changes from sand skeleton to rubber particle skeleton which generates different contact systems [30]. The stress-strain characteristics of rubber particle sand mixed soil changes from brittle to ductile [31]. Different confining pressure and different types of contacts have different influence on deviating stress of system. When the confining pressure is 300-400 kPa, peak deviating stress decreases with the increase of rubber particle content [32]. When the confining pressure is less than 200 kPa, it is basically unchanged [33].

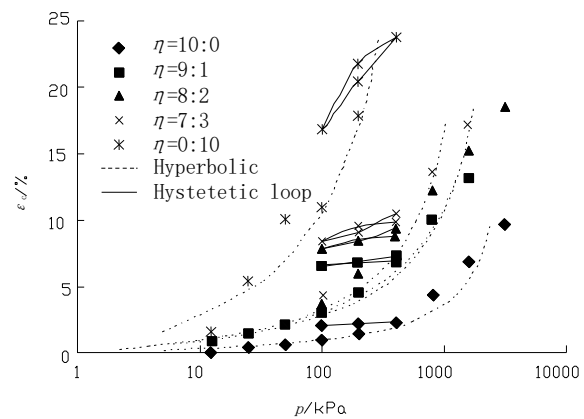


Figure 1. $\varepsilon_c - p$ curves (η is proportion) [28]

2.2. Dynamic characteristics

Rubber particle sand mixed soil can be used as light fill material for slope, pavement base and retaining wall. It may bear dynamic load. Dynamic shear modulus, damping factor and liquefaction resistance are important indexes for evaluating the dynamic characteristics of rubber particle mixed soil [34]. The size and content of rubber particles can influence dynamic shear modulus and damping ratio of mixed soil [35, 36].

According to the curves of dynamic shear modulus and shear stress ($G - \gamma$ curves), as shown in Fig. 2 [37], the dynamic shear modulus of rubber particle sand mixed soil would decrease with the increase of rubber particle content and shear-strain. The attenuation coefficient decreases with the increase of rubber content. The attenuation coefficient increases with increase of consolidation pressure. And consolidation pressure has nonlinear influence on the dynamic shear modulus-dynamic shear strain curve, the rubber particle content increases but it decreases [38]. The dynamic shear modulus can be forecasted by considering confining pressure and rubber particle content [39].

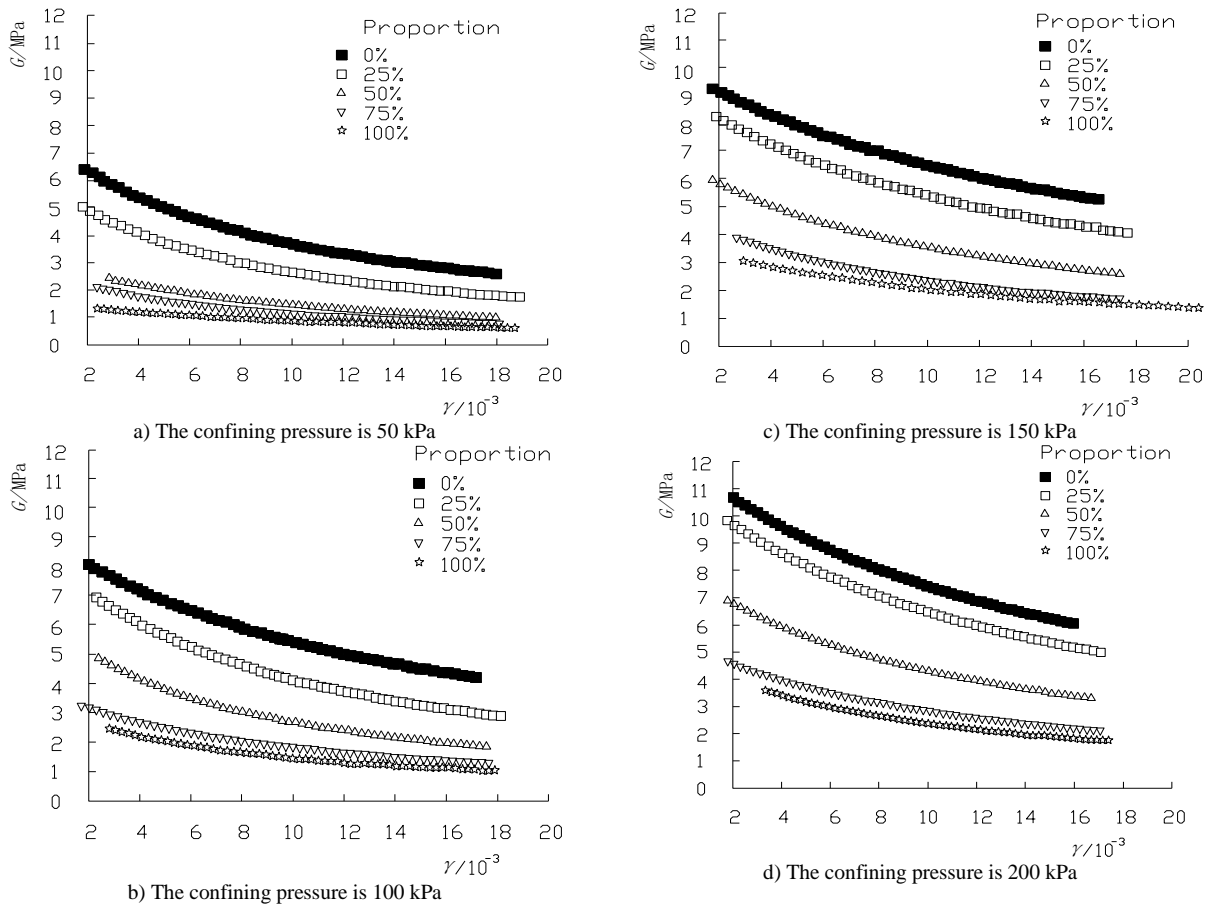


Figure 2. $G - \gamma$ curves of composite soil with rubber and sand with different contents [37]

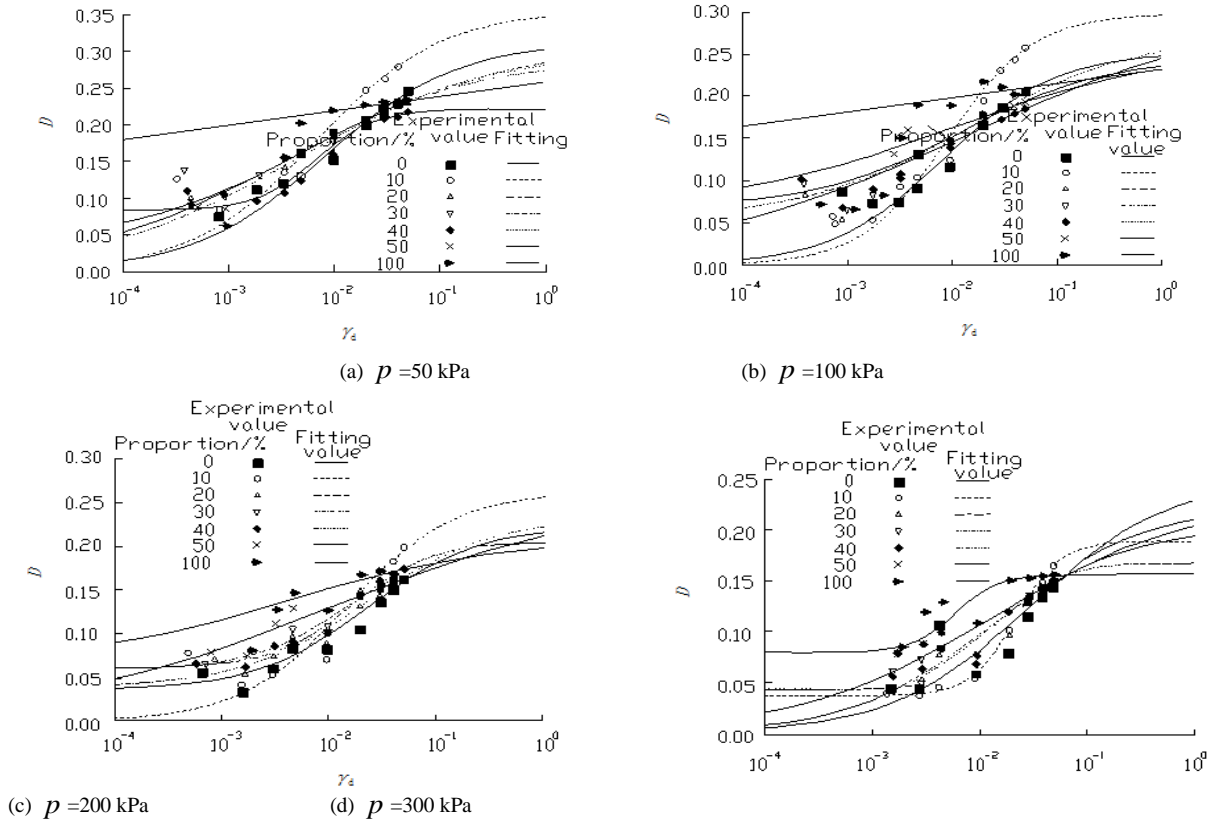


Figure 3. $D - \gamma_d$ curves of composite soil with rubber and sand with different contents (p is confining pressure) [41]

The damping ratio of rubber particle sand mixed soil is not only related to rubber particle content, but also related to shear strain size, confining pressure and average effective stress. At small strain, the damping ratio of rubber particle sand mixed soil increases with the increase of rubber particle content [40]. According to the curves of damping ratio and shear stress ($D - \gamma_d$ curves), as shown in Fig. 3 [41] at large strain (10^{-2} - 10^{-1}), the damping ratio of 10% rubber particle content is greater than that of pure sand and mixed soil of other rubber particle content. The greater the confining pressure is, the higher the damping ratio of rubber sand is [42]. The ratio is a power function of the average effective stress [43].

The sand mixed by rubber particles performs well in dynamic characteristic. No matter how big the particle size is, the more the content of rubber particles is, the more obvious the anti-liquefaction performance of sand is improved [44].

Because of the improvement on dynamic shear modulus, damping ratio and liquefaction resistance of rubber particle sand mixed soil, it can be used as base cushion for seismic isolation. The acceleration reduction coefficient is 0.212-0.592 and the displacement coefficient is 1.01-1.39 for rubber particle is added to sand for seismic isolation [45]. And the dynamic characteristics of the superstructure are improved and the isolation effect is obvious.

With the content of rubber particles increasing, the maximum acceleration of mixed soil cushion decreases. When the volume fraction of rubber particles is 45%, the maximum acceleration is the best [46]. When the volume fraction of rubber particles is 10%, mixed soil can isolate low-rise buildings [47]. For tall buildings, isolation cushion can reduce basal shear by 40% [48]. Therefore, when rubber particle sand mixed soil worked as isolation cushion, the maximum acceleration and building size must be considered to determine the optimum content of rubber particle.

2.3. Deformation

Rubber particles have a positive effect on deformation in mixed soil [49]. Rubber particle content is the decisive factor to control the deformation of rubber particle sand mixed soil. With the increase of the content of rubber particles, the residual strain of mixed soil increased, oedometric modulus decreases, compression increases. Mixed soil behaves natures similar to rubber particles [50]. The pure sand and rubber-sand with 10% rubber content, its e - $\log(p)$ curves has linear regression characteristic. Rubber-sand with 20%-25% rubber content and pure rubber particles, its e - $\log(p)$ curves has approximate linear characteristics. And its linear fitting slope increases with the rubber particle content increasing. When rubber particle content is less than 30%, it is medium compression material; When rubber particle content is 40% and 50% or 100%, it is high compression material [51]. The rubber particle size also influences the deformation of the mixed soil, and the rubber particle size of 4-9 mm has the greatest influence on reducing the settlement of fine sand [52].

The Poisson's Ratio of rubber particle sand mixed soil mainly is effected by relative compactness and rubber particle content. Poisson's Ratio increases with the relative compactness increasing. However, with the increase of rubber particle content, the effect of relative compactness on Poisson's ratio decreases [53]. The initial Poisson's

Ratio curve of mixed soil varies in V-shape with rubber content, decrease first and increase second. And the critical rubber content ranges from 35% to 40%. The Poisson's Ratio tend to 0.5 in failure stage. Rubber particles and sand in mixed soil form different force skeleton which causes this change [54]. Poisson's Ratio under triaxial stress can be calculated by formula (1) [55].

$$\mu = \frac{1}{2} \cdot \frac{(\sigma_z + 2\sigma_x)\varepsilon_z - \sigma_z\varepsilon_y}{(\sigma_z + 2\sigma_x)\varepsilon_z - \sigma_x\varepsilon_y} \quad (1)$$

In the formula: μ is Poisson's Ratio; σ_x is confining pressure; σ_z is axial pressure; ε_y is radial strain in direction y ; ε_z is axial strain.

The size, content, and size ratio of rubber particle determine the type of force skeleton and stress ratio of rubber particles to rubber particle sand mixed soil. Strain and confining pressure influence the action behavior of mixed soil. The interaction of them make rubber particle sand mixed soil shows different natures in strength and deformation.

3. Rubber particle clay mixed soil

3.1. Strength characteristics

The shear strength of rubber particle clay mixed soil is affected by the content and size of rubber particles. It tends to increase first and then decrease with the increase of rubber particle content. When rubber particle content is 40%, the shear strength is maximum. And its strength is 20-40% higher than that of clay. When rubber particle content is less than 20%, increasing the size of rubber particles can significantly improve the shear strength of mixed soil. The internal friction angle decreases first and then increases with the increase of rubber particle content. As shown in Fig. 4(a) [56]. And the trend of cohesion is the same as that of shear strength, which increases first and then decreases, as shown in Fig. 4(b) [56]. After the shear displacement reaches 3-5 mm, the shear strength remains basically unchanged [57]. The samples exhibit the characteristics of first shear shrinkage and then dilation.

Rubber particles can also be mixed with clay and a certain amount of cement to form light mixed soil. Cement content, rubber particle content and water content has remarkable influence on strength and engineering characteristics of mixed soil. The increase of cement content can obviously strengthen the material unconfined compressive strength and Shear strength. When the cement content is small (10%), rubber particle content has little effect on the unconfined compressive strength of mixed soil; When the cement content is small (13%, 15%), unconfined compressive strength decreases obviously as the rubber particle content increases [58]. With the increase of the content of rubber particle, the cohesion of mixed soil increases, and its internal friction angle reduces [59]. The stress-strain relationship of mixed soil transits from strain softening to strain hardening [60]. Rubber particles change the brittle failure behavior of cemented clay and reduce the expansive force of clay [61]. The workability and fluidity of mixed soil become better as water content increases. But after forming, its strength reduces.

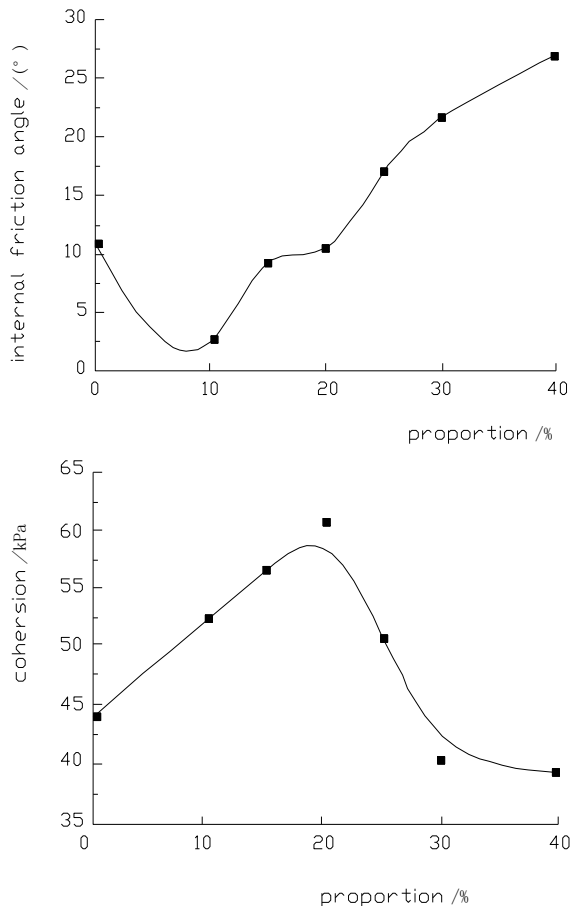


Figure 4. Effect of scrap tire particles on (a) internal friction angle and (b) cohesion for soft dredger fill [56]

3.2. Deformation

The compressibility of rubber particle clay mixed soil is between clay and pure rubber particles. It shows low compressibility at low dosage and high compressibility at high dosage. With the increase of rubber particle content, the void ratio and compressibility coefficient decrease first and then increase, and compression modulus increases first and then decreases. When the content is 30%, the void ratio and compressibility coefficient are minimum, and compression modulus is maximum. Moreover, the consolidation rate of cohesive soil can be increased by 400% with the addition of rubber particles [62]. The main reason is that rubber particles fill the voids between clay particles to reduce the void volume and compressibility of soil. With the increase of rubber particle content, the soil skeleton is gradually transformed into rubber particle skeleton, which leads to the increase of void ratio. The formation mechanism is similar to that of rubber particle sand. However, this change occurs only when the size of rubber particles and clay is relatively small. If the size of rubber particles and clay is big, the skeleton structure of mixed soil can change. Besides, the compressibility of mixed soils should consider the influence of the compressibility of rubber particles themselves.

Effect of rubber particles on optimum water content of rubber particle clay mixed soil is mainly influenced by rebound effect and specific surface area of rubber particles in compaction process. When the rubber particle size is 30 mesh and 12 mesh, with the increase of rubber particle content, optimum water content of rubber particles-kaolin

increases, optimum water content of rubber particles-red clay decreases, and the maximum dry density of mixed soil decreases. The effect of rubber particle size on the optimum water content and maximum dry density of mixed soil is not significant [63]. Different types of clay minerals, such as kaolin, montmorillonite and illite, have different water absorption ability because of their own structure and composition. However, after adding rubber particles, there are differences in interaction mode and interaction strength between soil and rubber particles which leads to different trends of optimum water content.

3.3 Physics

The removal rate of phenol from clay can be improved by adding rubber particles into clay. The adsorption effect of rubber particles is better than that of clay. The removal rate of phenol decreases with the increase of concentration of phenol. The adsorption of phenol by rubber particles, bentonite and kaolin conforms to Langmuir and Freundlich adsorption—isortherm, and it has good linear correlation [64]. However, the influence of rubber particle size and its size ratio to clay was not considered.

Clay generally has small void and bad water permeability, which leads to many engineering geology problems. When rubber particle size and size ratio between rubber particles and soil are big, the addition of rubber particles can cause the changes of pore size and connectivity of soil. Therefore, the permeability of soil is affected by rubber particle, and the specific change law needs to be further studied.

4. Rubber particle special soil mixed soil

4.1. Loess

Dynamic characteristics are improved after adding rubber particles into loess. The change law is affected by rubber particle content and dynamic shear strain. The maximum dynamic elastic modulus and dynamic shear modulus of mixed soil decrease significantly with the increase of rubber particle content. The maximum damping ratio increases with the increase of rubber particle content. When dynamic shear strain ranges from 0-0.002, the content of rubber particles has little effect on dynamic shear modulus ratio; When dynamic shear strain is bigger than 0.002, the dynamic shear modulus ratio increases with the increase of the rubber particle content. When dynamic shear strain ranges from 0-0.01, damping ratio varies greatly. When dynamic shear strain is bigger than 0.01, damping ratio tends to be stable [65]. In the study of dynamic elastic modulus, dynamic shear modulus and damping ratio, the influence of confining pressure and rubber particle size on them needs to be considered.

The compactibility of rubber particle loess mixed soil has closely relation with rubber particle content. When rubber particle content is less than 20%, compactibility characteristics of mixed soil are similar to loess; when rubber particle content is higher than 40%, compactibility characteristics of mixed soil are similar to non-cohesive soil. There is a power function relationship between the maximum dry density and the optimum water content of mixed soils with different rubber particle content, as shown formulas (2) and (4). There is a functional relationship between rubber particle content and the optimum water content of mixed soil under different compaction energy, as shown formulas (3) and (5). Under light and heavy compaction energy conditions, the optimum content of compaction of mixed soil is 30% and 40% respectively.

The recommended values of compaction index for mixed soils with different rubber particle content are shown in Table 2 [66].

Rubber particles can be mixed with baryta powder and added to loess. The internal friction angle of mixed soil increases with the increase of Barites and rubber particle content and it increases almost linearly with the increase of rubber particles content. However, the cohesion decreases with the increase of Barytes and rubber particle content [67]. Effect on shear strength of mixed soil caused by rubber particles and barytes powder also is determined by comprehensive effect of internal friction angle and cohesion. At the same time, the influence of rubber particles and baryte particles size needs to be considered.

Table 2. Compaction parameters of mixtures [66]

Light compaction			Heavy compaction		
Proportion (%)	Optimum water content (%)	Maximum dry density (g/cm ³)	Proportion (%)	Optimum water content (%)	Maximum dry density (g/cm ³)
20	14.5	1.48	20	12.0	1.58
30	14.0	1.43	30	11.7	1.47

Note: Formula (2)-Formula (5) can be used to calculate other content.

Light compaction:

$$\rho_{dmax} = 6.57 - 1.10w_{opt} + 0.057w_{opt}^2 \quad (2)$$

$$w_{opt} = 12.66 - 0.016x - 5.71x^2 \times 10^{-4} \quad (3)$$

Heavy compaction:

$$\rho_{dmax} = -14.40 + 2.06w_{opt} - 0.067w_{opt}^2 \quad (4)$$

$$w_{opt} = 17.66 - 0.185x + 1.93x^2 \times 10^{-4} \quad (5)$$

In the formula: ρ_{dmax} is the maximum dry density; w_{opt} is the optimum water content; x is rubber particle content.

4.2. Expansive soil

Expansive soil has typical characteristics of swelling in water absorption and shrinkage in water loss. It always causes unfavorable engineering geological problems such as settlement of ground and slope collapse. Therefore, engineering geological characteristics of expansive soil generally needs to be improved to meet engineering requirements.

Property improvement of expansive soil can be achieved by mixing coal gangue, lime and chemical solution. By adding a certain amount of coal gangue, the compression strength [68], shear strength [69] and CBR value [70] of expansive soil can be improved. Besides, coal gangue can control the attenuation of internal friction angle and cohesion of pure expansive soil caused by dry-wet cycling [71]. By adding a certain amount of coal gangue and lime in expansive soil, it can improve its compaction characteristics [72, 73]. Expansive soil mixed with NaCl solution or other solutions can be improved chemically to reduce the deformation of expansive soil [74].

The effect of rubber particles on improving expansive soil in the aspects of swelling and shrinkage characteristics

and compressive strength is better. Rubber particles in expansive soil can weaken the interaction of expansive soil and water [75]. At the same time, it can reduce the content of hydrophilic minerals and swelling and shrinkage characteristics [76]. Rubber particles in expansive soil can improve its compression strength [77, 78] and decrease its stiffness. Freeze-thaw cycling can affect the compression strength of improved expansive soil. Under the same number of freeze-thaw cycling, the unconfined compression strength of improved expansive soil tends to increase first and then decrease with the increase of rubber particle content. When rubber particle content is 3%, the unconfined compression strength of improved expansive soil is maximum. Compression strength decreases as the number of freeze-thaw cycles increases. When water content is 20%, under the same condition of freeze-thaw cycles, it shows frozen shrinkage and thawed expansion in low rubber particle content; and it's opposite in high rubber particle content because of influence of ice-water interaction [79].

When the content of rubber particles in expansive soil is less than 23%, the cohesion of improved expansive soil is generally lower than that of pure expansive soil, which results in significant decrease in shear strength [76]. The content of rubber particles used in this study ranged from 15% to 25%. The shear strength in the range of 0-15% has not been tested. Therefore, the overall change trend of shear strength of expansive soil with rubber particles needs to be further studied.

The swelling and shrinkage characteristics of improved soil is lower than that of pure expansive soil, which is the main purpose of improving expansive soil. However, the idea that the shear strength and dynamic characteristics of the improved expansive soil may meet the needs of practical engineering still needs to be studied.

4.3. Fly ash soil

The dynamic strength of fly ash soil mixed with rubber particles decreases with the increase of the cycle number of failure under the same confining pressure. At the same number of failure, the dynamic strength decreases with the increase of the confining pressure. The initial tangential modulus and average dynamic modulus of fly ash soil mixed with rubber particles are reduced, while the cohesion and internal friction angles are improved [80].

Recent years, fly ash soil is gradually widely used in engineering. If adding rubber particles into fly ash soil, the improved effect of its compression strength, deformation, compaction characteristics and other aspects need a lot of further research.

5. Conclusions

1. The strength, deformation, dynamic characteristics of the soil and the poor engineering characteristics of the special soil can be changed when the rubber particles of scrap tires are mixed into sand, clay, loess, expansive soil and fly ash soil. The influence on characteristics of soils mixed with rubber resulted by different rubber particle content, size, size ratio, strain and confining pressure is different.
2. When the sand is mixed with rubber particles, the cohesion of mixed soil can be improved. And the cohesion of mixed soil can reach its peak under the certain rubber particle content and size conditions. The

internal friction angle of the mixed soil may increase or decrease, which is related to the size ratio of rubber particles and sand.

3. Rubber particles can improve the shear strength of rubber particle sand mixed soil, but the variation of unconfined compressive strength and CBR of mixed soils with rubber particle content and size has not been studied in details. The rubber particle content affects the skeleton structure of mixed soil and the stress-strain relationship of mixed soil. At the same content of rubber particle, the skeleton structure of mixed soil is different when the size of rubber particle is different. The comprehensive influence of content and size on skeleton structure and stress-strain relationship of mixed soil is worth further study. When the sand is mixed with rubber particles, the dynamic shear modulus can be reduced and the damping ratio can be increased, and the liquefaction resistance can be increased. It can be used in a seismic engineering. However, the study on the dynamic characteristics mechanism of rubber particle sand mixed soil is insufficient. Whether it is still related to the skeleton structure of mixed soil remains to be discussed. The rubber particles in rubber particle sand mixed soil also affects its deformation characteristics. In order to meet the engineering requirements to the utmost in terms of various characteristics, it is necessary to find suitable rubber particle content and size.
4. When the clay is mixed with rubber particles, the shear strength and compression modulus can be increased and the compression coefficient can be reduced to a certain extent. Rubber particles play a significant role in improving the strength and deformation characteristics of mixed soil.

The study of rubber particle clay mixed soil mainly focuses on some low liquid limit clay and different clay minerals such as kaolinite and montmorillonite. At present, there is no detailed study on the characteristics of silt and silty clay. Clay usually has small pores and poor water permeability. Rubber particles in mixed soil can cause changes of their pores, which affects the water permeability of clay. The specific law of change needs further study.

Loess is widely distributed in northwest China, and most loess has collapsibility. It is of great significance to have a further study on the effect of rubber particles on collapsibility of loess. The addition of rubber particles can improve the dynamic characteristics of loess to a certain extent. However, attention should be paid to the influence of confining pressure and rubber particle size on it. When loess is mixed with rubber particles, the changes of compressive strength, shear strength and CBR are lack of in-depth studies. The influence of rubber particles and barite powder on shear strength of loess should also consider the factors such as the size of rubber particle and barite particle. When the expansive soil is mixed with rubber particles, its swelling and shrinkage characteristics and compression strength can be improved. And its shear strength is also affected to some extent. However the influence of rubber particles on the compaction and dynamic characteristics of expansive soils and its mechanism are not well studied. It needs a further study on the improvement effect of rubber particles on deformation, compressive strength and compaction characteristics of fly ash soil.

(5) The durability of rubber particle mixed soil and its environmental influence on strength and deformation characteristics are not study in detail.

Acknowledgements

The authors would like to thank the National Natural Science Foundation of China (51669025) for their support for this study.

References

- [1] Kong, D. S., Jia, T., Wang, X. M., Zhang, W. W. & Wu, Y. K.: Test on unconfined compressive strength of lightweight soil mixed with rubber chips of scrap tires. *Journal of Central South University (Science and Technology)*. 47(1): 225-231(2016).
- [2] Ding, L. Q. & Li, Y. Z.: Application and research status of scrap tire rubber particles. *Sichuan Cement*. 299: 85(2017).
- [3] Anvari, Seyed, M. & Shooshpasha, I.: Influence of size of granulated rubber on bearing capacity of fine-grained sand. *Arabian Journal of Geosciences*. 9(18): (2016).
- [4] Liu, J. H. & Song, S. M.: Effects of rubber particles treated surface on concrete damping capacity. *Journal of Beijing University and Technology*. 35(12): 1619-1623(2009).
- [5] Fu, C. Q., Fan, S. F., Deng, X. B., Zhang, G. G., Li, J. & Lu, C. Y.: Experimental study on mechanical properties of rubber concrete with different curing age. *Concrete*. 324(10): 64-68(2016).
- [6] Wang, J. J., Zhang, Y. H., Qin, W. X., Wang, S. J. & Zhang, H. B.: Mechanical properties of rubber concrete. *Bulletin of Chinese Ceramic Society*. 35(7): 2219-2223(2016).
- [7] Ma, N. Z.: Experimental research on mechanical property of rubber concrete. *Subgrade Engineering*. 186(3): 79-82(2016).
- [8] Ismail M. K. & Sherir, M. A. A.: Siad Hocine. Properties of self-consolidating engineered cementitious composite modified with rubber. *Journal of Materials in Civil Engineering*. 30(4): (2018).
- [9] Liu, Y. R., Ge, S. G. & Han, Y.: Research progress of scrap rubber powder modified cement-based composites. *Material Herald*. 28(24): 422-426(2014).
- [10] Ma, K. L., Long, G. C., Xie, Y. J., Chen, X. B., Qian, Z. M. & Tan, W. Y.: Effect of rubber particles on properties of self-compacting concrete. *Bulletin of Chinese Ceramic Society*. 42(8): 966-973(2014).
- [11] Zhang, H. B., Guan, X. M., Liu, X. X. & Li, F.: Study on compressive strength and interface of rubberized concrete. *Material Herald*. 23(4): 65-67(2009).
- [12] Huang, S. W., Xu, Y. H. & Luo, Q.: Research progress in rubber particles modified portland cement concrete. *Material Herald*. 23(1): 101-105(2019).
- [13] Fu, R., Coop, M. R. & Li, X. Q.: Influence of particle type on the mechanics of sand-rubber mixtures. *Journal of Geotechnical and Geoenvironmental Engineering*. 143(9): 1-15(2017).
- [14] Wei, H. B., Jiao, Y. B. & Liu, H. B.: Effect of freeze-thaw cycles on mechanical property of silty clay modified by fly ash and crumb rubber. *Cold Regions Science and Technology*. 116: 70-77(2015).
- [15] Wang, Z. Y., Zhang, N. & Li, Q.: Dynamic response of bridge abutment to sand-rubber mixtures backfill under seismic loading conditions. *Journal of Vibroengineering*. 19(1): 434-446(2017).
- [16] Dong, C., Li, D. Y. & Li, S. S.: Effects of scrap tire crumb size on shear strength of sand. *Journal of Guangxi University (Science and Technology)*. 42(4): 1392-1398(2017).
- [17] Liu, F. C., Ren, D. B., Liu, N. & Zhao, C. Q.: Numerical simulation on the isolation effect of geocell reinforced

- rubber-sand mixture cushion earthquake base isolator. *China Civil Engineering Journal*. 48(S1): 109-118(2015).
- [18] Wang, Z. Y., Zhang, N. & Jin, Y.: Experimental study on dynamic properties of sand-rubber mixtures in a small range of shearing strain amplitudes. *Journal of Vibroengineering*. 19(6): 4378-4393(2017).
- [19] Zhang, T., Cai, G. J., Liu, S. Y., Duan, W. H. & Wang, P. C.: Experimental study on strength characteristics and micromechanism of rubber-sand mixtures. *Chinese Journal of Geotechnical Engineering*. 39(6): 1082-1088(2017).
- [20] Perez, J. C., Lopera, Kwok, C. Y. & Senetakis, K.: Micromechanical analyses of the effect of rubber size and content on sand-rubber mixtures at the critical state. *Geotextiles and Geomembranes*. 45(2): 81-97(2017).
- [21] Zhang, Y. F., Liu, F. C. & Ren, D. B.: Study on shear characteristics of rubber-sand mixtures by triaxial CD tests. *Journal of Hunan University of Technology*. 29(1): 17-23(2015).
- [22] Anbazhagan, Panjamani, Manohar, D. R., Rohit & Divyesh.: Influence of size of granulated rubber and type chips on the shear strength characteristics of sand-rubber mix. *Geomechanics and Geoengineering*. 12(4): 266-278(2017).
- [23] Perez, J. C. & Lopera, Kwok, C. Y.: Senetakis K. Effect of rubber size on the behaviour of sand-rubber mixtures: A numerical investigation. *Computers and Geotechnics*. 80(11): 199-214(2016).
- [24] Liu, F. C. & Wu, M. T.: Micromechanics simulation of direct shear test of rubber-sand mixture with discrete element method. *Journal of Hefei University of Technology (Science and Technology)*. 40(7): 944-951(2017).
- [25] Ali, F. C.: Direct shear tests on waste tires-sand mixtures. *Geotechnical and Geological Engineering*. 29(4): 411-418(2011).
- [26] Martin, C. & Jun-Boum, P.: Laboratory determination of strength properties of frozen rubber-sand mixtures. *Cold Regions Science and Technology*. 60(2): 183-192(2010).
- [27] Changho, L. Q., Hung, T. & Woojin, L.: Characteristics of rubber-sand particle mixtures according to size ratio. *Journal of Materials in Civil Engineering*. 22(4): 323-331(2010).
- [28] Deng, A. & Feng, J. R.: Experimental study on sand-shredded tire light fills. *Journal of Building Materials*. 13(1): 116-120(2010).
- [29] Liu, F. C., Zhang, Y. F. & Ren, D. B.: Stress-strain characteristics of rubber-sand mixtures in uniaxial shear and simple shear tests. *Rock and Soil Mechanics*. 37(10): 2769-2779(2016).
- [30] Kim, H. K. & Santamarina, J.: Sand-rubber mixtures (large rubber chips). *Canadian Geotechnical Journal*. 45(10): 1457-1466(2008).
- [31] Zhang, T., Cai, G. J. & Duan, W. H.: Strength and microstructure characteristics of the recycled rubber tire-sand mixtures as lightweight backfill. *Environmental Science and Pollution Research*. 25(4): 3872-3883(2018).
- [32] Perez, J. C., Lopera & Kwok, C. Y.: Senetakis K. Investigation of the micro-mechanics of sand-rubber mixtures at very small strains. *Geosynthetics*. 24(1): 30-44(2017).
- [33] Deng, A. & Feng, J. R.: Effect of scrap tire bead addition on shear behavior of sand. *Journal of PLA University of Science and Technology (Natural science Edition)*. 10(5): 483-487(2009).
- [34] Li, B., Huang, M. S. & Zeng, X. W.: Dynamic behavior and liquefaction analysis of recycled-rubber sand mixtures. *Journal of Materials in Civil Engineering*. 28(11): 1356-1365(2016).
- [35] Kostas, S., Anastasios, A. & Kyriazis, P.: Dynamic properties of dry sand/rubber (SRM) and gravel/rubber (GRM) mixtures in a wide range of shearing strain amplitudes. *Soil Dynamics and Earthquake Engineering*. 33(1): 38-53(2012).
- [36] Anastasios, A., Kostas, S. & Kyriazis, P.: Small-strain shear modulus and damping ratio of sand-rubber and gravel-rubber mixtures. *Geotechnical and Geological Engineering*. 30(2): 363-382(2012).
- [37] Shang, S. P., Sui, X. X., Zhou, Z. J., Liu, F. X. & Xiong, W.: Study of dynamic shear modulus of granulated rubber-sand mixture. *Rock and Soil Mechanics*. 31(2): 377-381(2010).
- [38] Liu, F. C., Yan, J. & Wang, H. D.: Experimental study on dynamic characteristics of dry rubber-sand mixture at large strains. *Chinese Journal of Rock Mechanics and Engineering*. 35(2): 4265-4278(2016).
- [39] Wang, Z. Y., Zhang, N. & Jin, Y.: Experimental study on dynamic properties of sand-rubber mixtures in a small range of shearing strain amplitudes. *Journal of Vibroengineering*. 19(6): 4378-4393(2017).
- [40] Senetakis, K. & Anastasiadis, A.: Effects of state of test sample, specimen geometry and sample preparation on dynamic properties of rubber-sand mixtures. *Geosynthetics International*. 22(4): 301-310(2015).
- [41] Liu, F. C., Chen, L. & Wang, H. D.: Evaluation of dynamic shear modulus and damping ratio of rubber-sand mixture based on cyclic simple shear tests. *Rock and Soil Mechanics*. 37(7): 1903-1913(2016).
- [42] Zhou, J.: Study on dynamic properties of composite soil mixing soil and scrap tire rubber particles. *Hunan Communication Science and Technology*. 44(3): 65-69(2018).
- [43] Brara, A., Brara, A. & Daouadji, A.: Dynamic properties of dense sand-rubber mixtures with small particles size ratio. *European Journal of Environmental and Civil Engineering*. 21(9): 1065-1079(2017).
- [44] Li, B. & Huang, M. S.: Dynamic triaxial tests on liquefaction characteristics of rubber-sand mixture. *Rock and Soil Mechanics*. 38(5): 1343-1349(2017).
- [45] Xu, D., Li, Y. R. & Huang, X. X.: Research on isolation properties of sand-rubber vibration isolation cushion. *Journal of Anhui University of Science and Technology (Natural Edition)*. 37(3): 17-22(2017).
- [46] Wang, Q. Q., Zheng, W., Shi, J. B.: Study on the optimal of sand and rubber for isolation cushion. *Journal of Anhui University of Science and Technology (Natural Edition)*. 35(1): 16-18(2015).
- [47] Madhusudhan, B. R., Boominathan, A. & Banerjee, S.: Static and large-strain dynamic properties of sand-rubber tire shred mixtures. *Journal of Materials in Civil Engineering*. 29(10): (2017).
- [48] Pitilakis, K., Karapetrou, S. & Tsagdi, K.: Numerical investigation of the seismic response of RC buildings on soil replaced with rubber-sand mixtures. *Soil Dynamics and Earthquake Engineering*. 79(11): 237-252(2015).
- [49] Changho, L., Hosung, S. & Jong-Sub, L.: Behavior of sand-rubber particle mixtures: Experimental observations and numerical simulations. *International Journal for Numerical and Analytical Methods in Geomechanics*. 38(16): 1651-1663(2014).
- [50] Duan, W. H., Zhang, T. & Cai, G. J.: Experimental study on compressibility characteristic of rubber-sands mixture. *Journal of Engineering Geology*. 23(suppl.): 200-204(2015).
- [51] Zhang, Y. F., Liu, F. C., Yue, H. T. & Gan, L.: Study on laterally confined compression test of rubber-sand mixture. *Journal of Hunan University of Technology*. 29(3): 1-9(2015).
- [52] Anvari, Seyed, M., Shooshpasha & Issa.: Influence of size of granulated rubber on bearing capacity of fine-grained sand. *Arabian Journal of Geosciences*. 9(18): 1899-1911(2016).
- [53] Liu, F. C., Zheng, Y. F., Liu, N. & Zhang, Y. F.: Influence of proportioning and relative density on static parameters of rubber-sand. *Journal of Hunan University of Technology*. 31(5): 24 -31(2017).

- [54] Liu, F. C., Wu, M. T., Liu, N., Zhang, Y. F. & Chen, J. L.: Experimental study on poisson's ratio of rubber-sand mixtures. *Chinese Journal of Rock Mechanics and Engineering*. 36(1): 3596-3606(2017).
- [55] Liu, N., Liu, F. C., Zhang, X. Q., Ren, D. B. & Zhang, Y. F.: Study of poisson's ratio of calculation method for mixture under the triaxial test. *Journal of Hunan University of Technology*. 29(6): 16-22(2015).
- [56] Li, S. S. & Li, D. Y.: Shearing properties of composite soil mixing clay with rubber particle of scrap tire. *Journal of Yangtze River Scientific Research Institute*. 34(7): 99-105(2017).
- [57] Zhang, L., Li, D. Y., Li, S. S. & Huang, T.: Effects of scrap tire chips on shear strength of soft dredger fill. *Journal of PLA University of Science and Technology (Natural science Edition)*. 34(4): 102-106(2015).
- [58] Xin, L., Liu, H. L., Shen, Y. & He, J.: Unconfined compressive test of light weight soil mixed with rubber chips of scrap tires. *Journal of PLA University of Science and Technology (Natural science Edition)*. 11(1): 79-83(2010).
- [59] Xin, L., Gao, D. Q. & He, J.: Engineering characteristics of lightweight soil mixed with rubber chips of scrap tires (paper presented at 11th National Symposium on Rock Mechanics and Engineering, Wuhan, Peoples R. China. Oct19-24)(2010).
- [60] Xin, L., Liu, H. L., Shen, Y. & He, J.: Consolidated undrained triaxial compression tests on light weight soil mixed with rubber chips of scrap tires. *Chinese Journal of Geotechnical Engineering*. 32(3): 428-433(2010).
- [61] Yadav, J. S. & Tiwar, S. K.: Effect of waste rubber fibres on the geotechnical properties of clay stabilized with cement. *Applied Clay Science*. 149: 97-110(2017).
- [62] Li, S. S., Li, D. Y. & Zhang, Y. S.: Effects of scrap tire crumbs on compression behavior of clay. *Journal of Shandong University of Science and Technology*. 35(5): 55-62(2016).
- [63] He, J., Li, Y., Ruan, X. C. & Hu, X. J.: Compaction performance of ground rubber and clay mixtures. *Journal of Engineering Geology*. 23(5): 1013-1019(2015).
- [64] Li, Y., He, J., Ruan, X. C. & Hu, X. J.: Adsorption performance of phenol by waste tire rubber particles and clay. *Journal of Hubei University of Technology*. 30(5): 113-116(2015).
- [65] Hu, Z. P., Liu, Z. H., Zhang, Z. Q. & Xu, J. W. & Yan, X. B.: Test on influence of rubber power on dynamic mechanic properties of manipulated loess. *Journal of Chang'an University (Natural Science Edition)*. 33(4): 62-67(2013).
- [66] Li, Z. H. & Zhang, H. Y.: Compaction properties of granulated rubber and loess. *Rock and Soil Mechanics*. 31(12): 3715-3726(2010).
- [67] Xu, J. W., Hu, Z. P., Ma, S. L., Yan, X. B. & Liu, Z. H.: Effect of barite powder and rubber powder on the shear strength of manipulated loess. *Journal of Xi'an University of Science and Technology*. 33(5): 565-570(2013).
- [68] Guo, L. Y., Zhang, Y., Zhou, T. P., Yang, X. Y. & Han, C.: Experiment study on expansive soil improved by coal gangue powder. *Journal of Inner Mongolia Agricultural University*. 34(4): 127-130(2013).
- [69] Yang, X. Y. & Zhang, Y.: Mechanism analysis of coal gangue powder improving shear strength of expansive soil. *Coal Engineering*. 46(9): 123-125(2014).
- [70] Zhang, Y., Liu, B. B., Kang, X. C., Guo, L. Y., Yu, G. P., Dong, W. & Liang, J.: Research on CBR of expansive soil improved by coal gangue. *Journal of Inner Mongolia Agricultural University*. 36(2): 77-81(2015).
- [71] Zhang, Y., Yin, X. X. & Liu, T.: Strength properties of solidified expansive soil with coal gangue and its pore structure characterization under condition of optimum dosage. *Transactions of the Chinese Society of Agricultural Engineering*. 34(22): 267-274(2018).
- [72] Li, W. S., Zhang, Y., Guo, L. Y., Meng, F. F. & Yu, X. H.: Research on mechanism of compaction expansive soil with coal gangue. *Journal of Inner Mongolia Agricultural University (Natural Science Edition)*. 35(4): 107-110(2014).
- [73] Zhang, Y., Kang, X. C. & Guo, L. Y.: Engineering properties of expansive soil improved by lime and coal gangue. *Bulletin of the Chinese Ceramic Society*. 34(9): 2720-2724, 2730(2015).
- [74] Li, W. S., Zhang, Y., Zhao, R. & Feng, X. B.: Effect of pore solution on deformation of chemical modified expansive soil. *Non-Metallic Mines*. 41(5): 92-95(2018).
- [75] Zuo, C. Y. & Zhou, J. Deng W.: A evaluate summarizing on reform effect of expansion soil admix rubber particles. *Shanxi Architecture*. 36(25): 83-84(2010).
- [76] Zhou, W. L., Xie, P., Ma, Q., Yang, Y. & Zuo, C. Y.: Experiment on characteristics of expansive soil modified with waste tire rubber particles. *Journal of Sichuan University (Engineering Science Edition)*. 43(3): 44-48(2011).
- [77] Yang, Q. G. & Wang, Y. F.: Study on road performance of waste rubber tire particles mixed expansive soil. *Shanxi Architecture*. 43(36): 99-101(2017).
- [78] Shen, Z., Wang, Y. F., Kang, X. C., Fu, H., Wang, Z. Q., Guan, S. S., Wang, C. & Wu, Z. Z.: A Study of road performance on soil mixed with waste rubber tire particles. *Journal of Nanjing Institute of Technology (Natural Science Edition)*. 16(2): 44-50(2018).
- [79] Zong, J. M., Song, Y. J., Lu, Y., Xu, L. & Zhang, Y. Z.: Unconfined compressive strength test on expansive soil improved by waste tire rubber particles under freeze-thaw cycles. *Journal of Yangtze River Scientific Research Institute*. 34(9): 110-114(2017).
- [80] Li, C. Y., Liu, H. B. & Wei, H. B.: Experimental research on dynamic characteristics of fly ash soil improved by rubber particles. *Rock and Soil Mechanics*. 32(7): 2025-2028, 2033(2011).

Design of Intelligent Obstacle Avoidance System for Fully Automated Unmanned Vehicle Based on Laser Ranging

Chunyuan Li *

Institute of Mathematics and Statistics, Baicheng Normal University, Baicheng 137000, China

Received OCT 16 2019

Accepted FEB 4 2020

Abstract

The vehicle obstacle avoidance system based on fuzzy neural network uses the fuzzy neural network to extract the road obstacle information, and has not designed the obstacle avoidance path, which has the disadvantage of low correct rate of obstacle avoidance results. An intelligent obstacle avoidance system for fully automated unmanned vehicle based on laser ranging is designed. The system consists of three parts: information acquisition, information processing and information control. The hardware consists of laser rangefinder, controller module, motor module and GPS positioning system. The laser rangefinder obtains obstacle information by using pulsed infrared laser beam and transmits measurement information in real time. The main engine of fully automated unmanned vehicle is given information processing to realize effective obstacle detection. The system adopts obstacle avoidance path and obstacle avoidance process based on grid-ant colony algorithm to realize intelligent obstacle avoidance of fully automated unmanned vehicle. The correct rate of obstacle avoidance to static and dynamic obstacles in the designed system is 100%. The system is an intelligent obstacle avoidance system for fully automated unmanned vehicle with high precision and high application value.

© 2020 Jordan Journal of Mechanical and Industrial Engineering. All rights reserved

Keywords laser ranging; automated; unmanned vehicle; intelligent obstacle avoidance; system design; grid-ant colony.

1. Introduction

Fully automated unmanned vehicle is a kind of intelligent vehicle which does not need to be driven by human, and it can also be regarded as a four-wheeled robot. It consists of three systems: sensor system, main control computer system and automatic driving system. It relies on a variety of precise sensors, laser rangefinders and acoustic radar before and after the vehicle to collect information about the surrounding environment. Then the collected information is transported to the main controller system through processing and transformation, and the main controller issues commands to make the driving system drive safely and correctly, so as to realize unmanned driving [1]. Nowadays, the main problem of fully automated unmanned driving is the simplicity of driving, that is, there are too few kinds of assumptions about the road condition to control the whole road condition like human beings. The unmanned driving on the highway is more mature, because the highway road conditions are relatively easy to achieve automatic control. Secondly, the collection of all kinds of information on the road is not complete, only the specific and simple road information can be used, and the handling of unexpected situations lacks great adaptability.

Obstacle avoidance is a basic function of autonomous mobile robots. Many scholars have done a lot of research on it. The basic idea of potential field method is that the mobile space of robots is a virtual force field [2]. The target point generates gravity, the obstacle generates repulsion, and the robot moves under the resultant force of gravity and repulsion. The information is simplified to a single resultant force, and the details of local obstacles are lost [3-5]. The Vector Field Histogram (VFH) takes the mobile robot as the center to establish a 1-D polar histogram to represent the environment. The linear and angular velocities are controlled separately. The curvature velocity method can better solve the problem of losing the details of the environment by a single resultant force of the potential field method. Curvature-velocity method and dynamic window transform obstacle avoidance problem into the constrained optimization problem of linear-angular velocity space.

Laser range finder is a kind of active imaging laser sensor, which is not affected by the change of illumination. It has short wave length, fast scanning speed and easy installation. It is widely used in automobile anti-collision and line-patrolling robot. In order to accurately acquire the obstacle information of fully automated unmanned vehicle on the moving path, an intelligent obstacle avoidance system of fully automatic unmanned vehicle based on laser

* Corresponding author e-mail: chunyuanyuanli0410@163.com.

ranging is designed by using laser rangefinder to collect obstacle information.

2. Materials and Methods

2.1. Intelligent Obstacle Avoidance System of Fully Automated Unmanned Vehicle based on Laser Ranging

The system consists of three parts: information acquisition, information processing and information control. The acquisition information system ascertains the fixed obstacles from the GIS investigation of the regional environment, and then uses the grid-ant colony algorithm to plan the path and get the obstacle avoidance parameters. It is introduced into the LabVIEW software system and runs the collision avoidance algorithm to complete the obstacle avoidance design of the fixed obstacles. The measurement of random obstacles is to transmit the information measured by laser rangefinder to the data processor of software. During the operation of the information processing system, the automated unmanned vehicle uses the method of automatic staying to judge the movement form of random obstacles and to plan the next forward path so as to enable the information control system to have the functions of autonomous navigation and obstacle avoidance and complete the task of intelligent obstacle avoidance [6]. Finally, it forms the circulation, coherence and integrity of information collection, information processing and information control. The overall design of the system is shown in Figure 1.

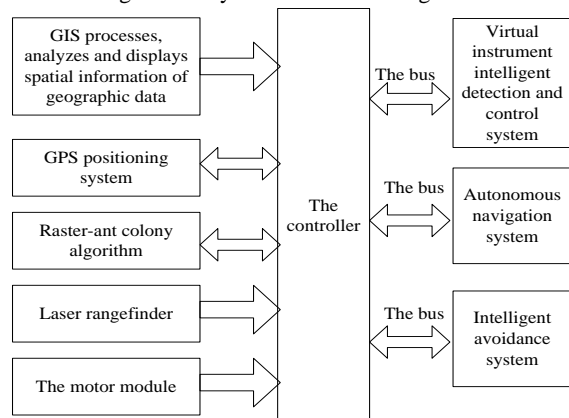


Figure 1. Overall structure of the system.

2.2. System Hardware Design

2.2.1. Laser Range Finder

Laser range finder is a high precision and high resolution external sensor based on TOF (Time of Flight) principle. The laser rangefinder has an operating temperature of -10°C to $+50^{\circ}\text{C}$, a detection frequency of $1/6$ to $1/3\text{HZ}$, and a field of view of 6.5° .

Taking LMS 200 of SICK Company in Germany as an example, its scanning area is 180° , the scanning direction is counterclockwise, the maximum limited distance is 8 m, and the resolution of distance and angle is 15 mm and 1° , respectively. It has the advantages of fast scanning (scanning cycle is 13.3 ms), dense data points and high measurement accuracy. In order to reduce the adverse effects caused by the uneven intensity of reflected light, LMS200 uses the binary method to deal with the intensity

of reflected light [7], which is insensitive to environmental light, mainly affected by obstacle materials and surface smoothness.

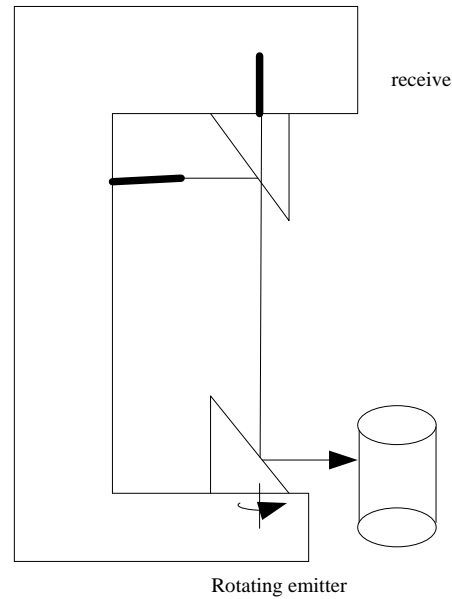


Figure 2. of laser rangefinder.

LMS200 laser range finder is a non-contact active ranging system, which does not need preset transmitter and location mark. Its working principle is based on the measurement of laser beam's flight time, as shown in Figure 2. Pulsed infrared laser beams are emitted and reflected back when they encounter objects, and recorded by the receiver of the range finder. The time of laser pulse transmitting and receiving is proportional to the distance between the distance meter and the measured object. The pulsed laser beam is deflected by a rotating light mirror (rotating speed is 75 rps) inside the range finder to form a sector scanning area for the surrounding environment. The contour of the target object is determined from a series of pulses received. Through high-speed serial interface (500 kbit/s RS422), real-time measurement data can be transmitted to the main engine of fully automated unmanned vehicle for further data processing [8-11]. The scanning data coordinates of the laser rangefinder are shown as follows:

$$G_n = (d_n, \phi_n)^T, n = 1, \dots, N \quad (1)$$

Where, d_n represents the amount of data transmission, ϕ_n represents the measurement angle of an object, T represents measurement time.

Cartesian coordinate can be expressed as:

$$H_n = (x_n, y_n)^T, n = 1, \dots, N \quad (2)$$

Where $x_n = d_n \cos \phi_n$, $y_n = d_n \sin \phi_n$, N is the number of scanned data.

2.2.2. Controller Module Design

The hardware of the intelligent obstacle avoidance system of fully automated unmanned vehicle based on laser ranging mainly adopts the controller to realize the obstacle avoidance of the vehicle. The controller mainly includes two parts: the host computer and the slave computer. The host computer and the slave computer exchange data mainly through RS232 serial communication cable, and realize the embedded connection. The controller structure is shown in Figure 3.

The host computer refers to the module that controls the mobile robot directly [12-14], including the data collection module, the direct control module and the touch screen display module of the laser range finder. The slave computer refers to the indirect control module of the laser range finder, including the camera, the embedded control chip and the motor drive circuit. The slave computer is mainly responsible for collecting the signal of the laser range finder and the external environment information [15-18], and make the control plan according to the intelligent control algorithm. The host computer is responsible for displaying the data in the slave computer and making management through analysis and judgment. It can also directly issue control commands to the slave computer.

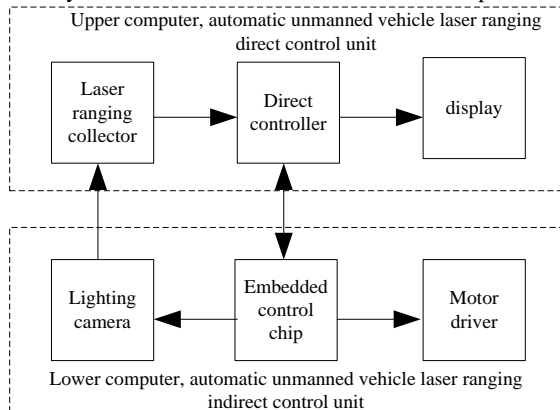


Figure 3. Structure diagram of the controller.

2.2.2. Motor Module Design

The obstacle avoidance system of fully automated unmanned vehicle adopts DC motor drive mode, which controls the forward, backward or left-right steering of the vehicle by controlling left and right DC current. As shown in figure 4, DC motor adopts DC motor driver chip L298N, and double-bridge motor driver chip L298 has maximum output current of 4 amperes, which has over-temperature protection function and high noise suppression ratio. The output just meets the driving requirements of the left and right DC motor of the vehicle. The operation state of the motor can be controlled by the level input of three L298N input ports. The working state of the motor is shown in Table 1.

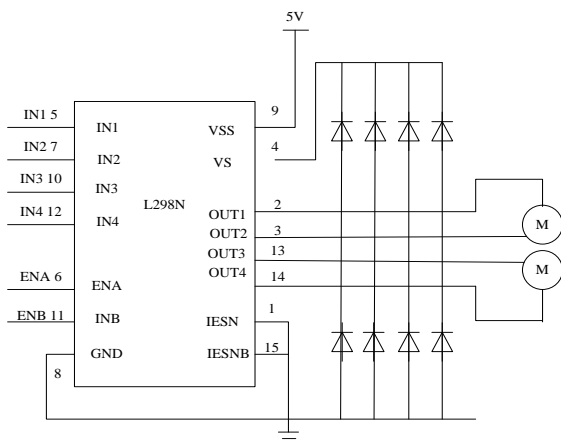


Figure 4. Motor module.

Table 1. DC motor operating status.

ENA	IN1	IN2	Running condition
0	X	X	Stop
1	1	0	Forward
1	0	1	Reverse
1	1	1	Brake
1	0	0	Stop

2.3. System Implementation

2.3.1. Obstacle Avoidance Path based on Grid-Ant Colony Algorithm

The system adopts the principle of avoiding collision based on grid-ant colony algorithm. The grid method is a kind of approximate discrete data which is approximated by a finite grid. Its row array is easy to store, operate, display and maintain for computer. The size of the grid determines the accuracy of the geographic data in the coverage area, and they are inversely proportional, so the finer the grid element is, the more accurate the grid data is. The grid method is the preferred method for system path planning: firstly, the space of a known region is made into a grid network model, including the location and size of the fixed obstacles in the region [19]; secondly, the size of the grid is determined by the accuracy of the path. Because the vehicle and obstacle cannot be in the same grid when avoiding obstacles, the safe distance between the vehicle and obstacle is at least twice the grid edge length. Finally, the grid of the region and the fixed obstacle is coded. Ant colony algorithm (ACA) is a probabilistic algorithm used to find the optimal path in the graph. Ant colony algorithm has been successfully applied in several fields. The proposed algorithm is applied to vehicle intelligent obstacle avoidance system to ensure the accuracy of autonomous obstacle avoidance [20]. The system adopts the principle of avoidance based on raster-ant colony algorithm, and does not take constant as the initial pheromone, so as to reduce the number of times that ants fail to find the path, and to ensure the accuracy of intelligent obstacle avoidance. The whole process is shown in Figure 5: white grid represents feasible grid, black grid represents infeasible grid, starting point is S , target point is O .

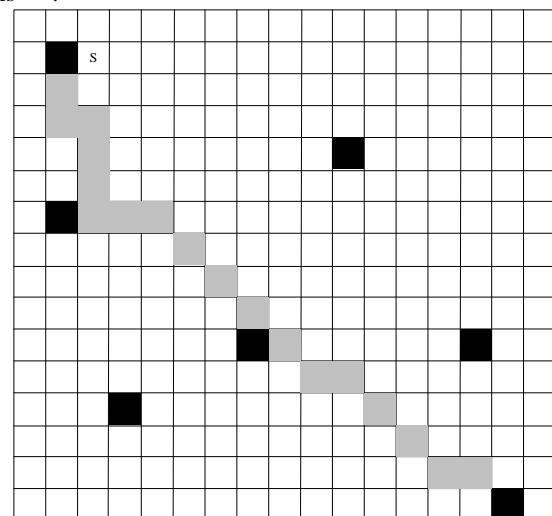


Figure 5. Grid - ant algorithm design drawing.

Assuming that there are K ants searching for the target O from the starting point S , the ant can only walk one step to the adjacent non-obstacle grid around it. Assuming that the k -th ant is in the first square, the probability that it chooses the next square j is:

$$P_{ij}^k = \frac{(\tau_j)^\alpha (\eta_{ij})^\beta}{\sum_j (\tau_j)^\alpha (\eta_{ij})^\beta} \quad (3)$$

Where: τ_j denotes the content of pheromones in the grid j ; $\eta_{ij} = 1/d_{ij}$ denotes the reciprocal of the distance between the grid i and j ; α and β are constants, usually $1 \leq \alpha \leq 2.2 \leq \beta \leq 5$. Each ant sprays a certain pheromone in the square it passes after it has completed its journey.

$$\Delta\tau_k = Q/L_k \quad (4)$$

Where L_k denotes the length of the path taken by the k -th ant; Q is a constant. If an ant fails to find the target O , it searches again until it finds a feasible route [21-23]. After all the ants have found the target O , the pheromones in each square is updated with the following formula:

$$\tau_{n+1} = \rho\tau_n + \sum_{k=1}^K \Delta\tau_k \quad (5)$$

Where ρ is the degree of retention of pheromones.

The path planning of system obstacle avoidance design is as follows:

Step 1: Let the planned path be a directed polygon with X points.

Step 2: Run along the original planning path.

Step 3: Automated unmanned vehicles will have random obstacles when they drive on the set route independently.

Step 4: When a random obstacle is measured by a laser rangefinder, the coordinates of the current vehicle are obtained, and the size of D and L is compared (where D is the distance between the vehicle and the obstacle and L is the distance between the vehicle and the next sub-target).

Step 5: in first comparison, if $D > L$, it thinks there is no obstacle, continue to move forward, laser detector has been used to measure. Return the comparison of D and L to step 4.

Step 6: in the initial comparison, if $D < L$, it proves that there is an obstacle. At this time, the vehicle will wait for the set time t in situ. When there is no obstacle at time t , it will follow the original path.

Step 7: When there is an obstacle in Time t measurement, the vehicle stays and regards the random obstacle as a fixed obstacle to use the system to re-plan the path; or when the volume of the obstacle is relatively small, the vehicle steers to the feasible grid adjacent to the obstacle to avoid the obstacle. In order to achieve the optimal path planning for obstacle avoidance, the system compares the results of partial re-planning with the results of back-to-the-original path movement after corner, and chooses the best path.

Step 8: If it encounters another obstacle, go back to step 4 and recycle. If there is no random obstacle, run directly to the final target point.

2.3.2. Implementation Process of Obstacle Avoidance

The system controller is based on ARM (Advanced RISC Machines) embedded platform and S3C2440 microprocessor chip. It supports SD card slot and 256M memory configuration. The interface is relatively rich. It can transmit and store pictures, videos and multi-dimensional data. It can reasonably reduce the control delay. Receiving the teaching information of the instructor, kinematics calculation and trajectory planning are carried out based on it, and communication is realized by RS485 bus to ensure the coordinated movement of all links [24]. The microprocessor chip S3C2440 controls the direct controller with the host computer and the camera and servo driver of the slave computer. The chip is the core of the whole control system. It can accurately control the driving frequency and pulse number of the motor and directly decode, encode and compress the data in the controller. The embedded technology greatly simplifies the design cost and the complexity of implementation [25-27]. As shown in Figure 6, the intelligent obstacle avoidance process of fully automated unmanned vehicle is controlled by laser rangefinder.

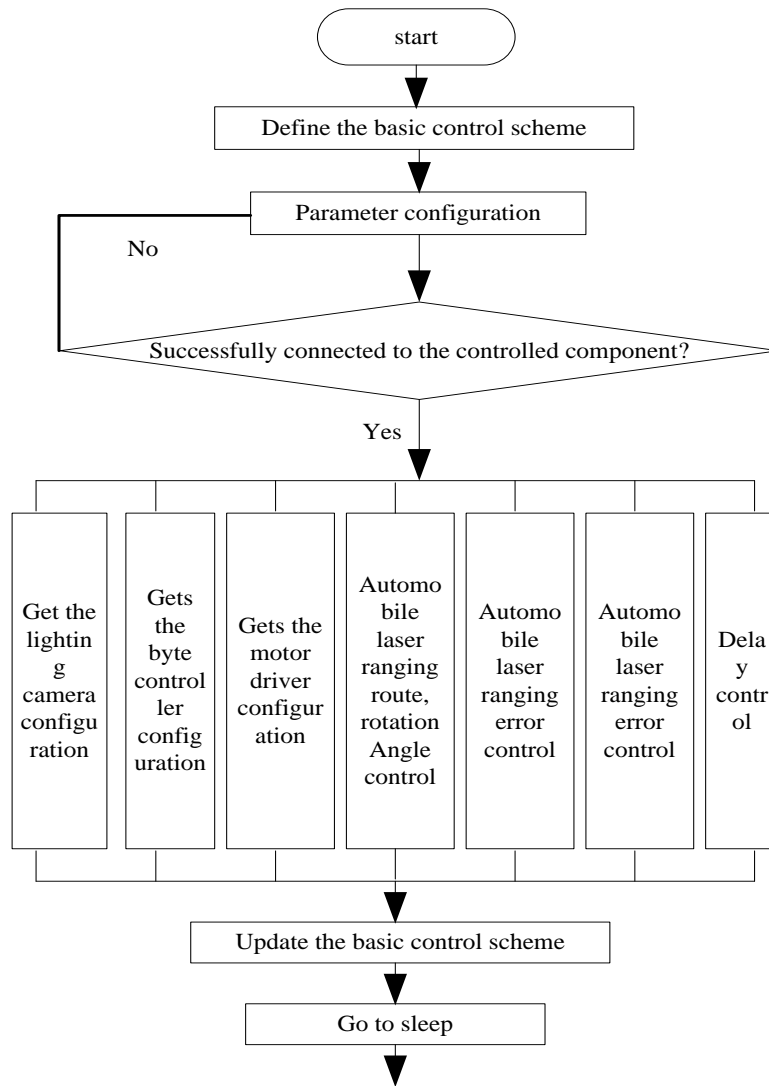


Figure 6. Obstacle avoidance control flow of fully automatic unmanned vehicle with laser rangefinder.

3. 3. Results

3.1. Analysis of Obstacle Avoidance Effect

In order to verify the feasibility and effectiveness of the designed system, the unmanned vehicle shown in Figure 7 is simulated in the obstacle avoidance test chart of Figure 8. Static obstacle avoidance test and dynamic obstacle avoidance test are carried out respectively. Figure 9 shows that the obstacle avoidance system designed in this paper can completely avoid static obstacles and effectively avoid collision with static obstacles during vehicle movement.

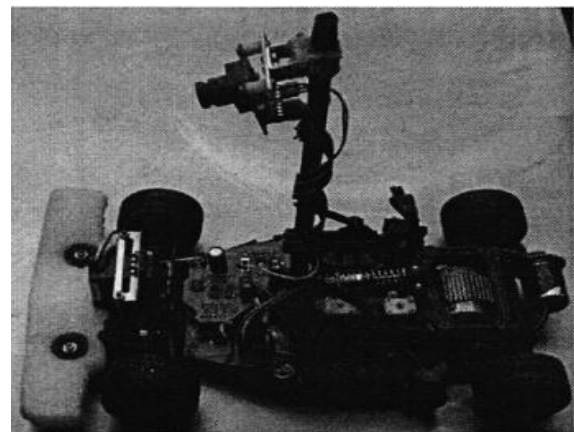


Figure 7. Physical drawing of fully automatic unmanned car.



Figure 8. Obstacle avoidance test route.

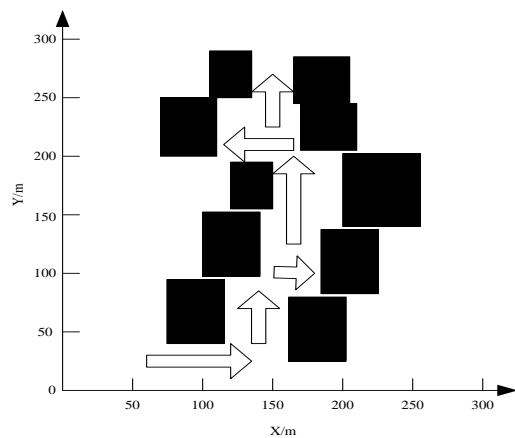


Figure 9. The movement track of the intelligent obstacle avoidance static obstacle driven by an automatic uav.

In the course of driving a fully automated UAV (Unmanned Aerial Vehicle), the obstacles in the path of motion are always in the state of motion, that is, they have dynamic characteristics. Therefore, the robot must have self-adaptability and adjustability when moving. Figure 10 is the path of the robot in the environment with dynamic obstacles. As can be seen from Figure 10, the system designed in this paper is also applicable to obstacle avoidance. The vehicle can adjust its motion path adaptively to avoid path obstacles effectively, which proves that the system in this paper has strong flexibility and adaptability.

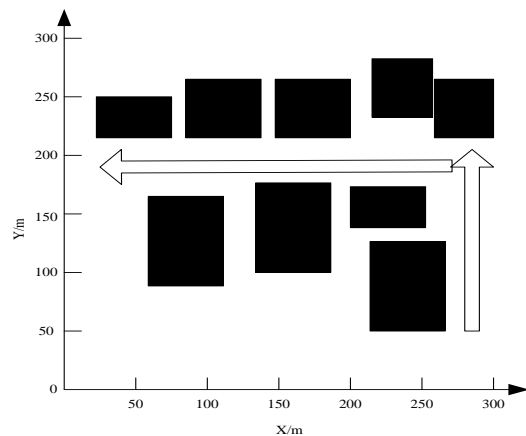


Figure 10. Trajectory of intelligent obstacle avoidance and dynamic obstacle avoidance in a fully automatic uav driving vehicle.

3.2. Correct Analysis of Obstacle Avoidance Results

On the basis of the above experimental results, the experiment further verifies the accuracy of the intelligent obstacle avoidance results of this system. In order to highlight the high accuracy of obstacle avoidance in practical application of the designed system, 14 static obstacles with different distances are set up in the laboratory, and the obstacle avoidance results of the vehicle obstacle avoidance system based on fuzzy neural network and visual positioning are taken as experimental reference. The accuracy of obstacle avoidance of the three systems at different distances from obstacles is compared and analyzed. The experimental results of the three systems are described in Tables 2, 3 and 4, respectively.

Table 2. The static obstacle avoidance results of the proposed system.

The standard distance/cm	Car travel distance /cm	Distance from obstacles /cm	Successful obstacle avoidance
20	19.8	0.2	Yes
40	36.5	3.5	yes
60	58.6	1.4	yes
80	76.5	3.5	yes
100	98.6	1.4	yes
150	147.5	2.5	yes
200	195.6	4.4	yes
250	245.6	4.4	yes
300	282.6	7.4	yes
400	396.4	3.6	yes
500	418.9	1.1	yes
600	596.2	3.8	yes
700	616.5	3.5	yes
800	795.4	4.6	yes

The results of Table 2 show that the system has a good effect on avoiding static obstacles. Detailed analysis of the data in the table shows that all fully automated unmanned vehicles can stop at a certain distance from the obstacles in the test and avoid collision with the obstacles. From the third column of the table, it can be concluded that when the system detects obstacles in a certain position in front of the vehicle, at the same time, the system can give instructions to the vehicle according to the distance of the obstacle, effectively avoiding the collision between the vehicle and the obstacle. It shows that the system has a good application in intelligent avoidance of collision between fully automatic unmanned vehicle and obstacles.

Table 3. Static obstacle avoidance based on fuzzy neural network and obstacle avoidance system.

The standard distance/cm	Car travel distance /cm	Distance from obstacles /cm	Successful obstacle avoidance
20	26.5	-6.5	no
40	48.6	-8.6	no
60	75.6	-15.6	no
80	66.2	13.8	yes
100	105.5	-5.5	no
150	174.2	-24.2	no
200	224.3	-24.3	no
250	162.4	87.6	yes
300	312.5	-12.5	no
400	416.2	-16.2	no
500	472.3	27.7	yes
600	623.1	-23.1	no
700	706.3	-6.3	no
800	817.4	-17.4	no

The result of data analysis in Table 3 shows that when using the vehicle obstacle avoidance system based on Fuzzy Neural Network to avoid static obstacles, there are

11 experimental tests in which fully automated unmanned vehicles cannot brake within a safe distance, but collide with obstacles, and a certain distance of movement will occur after the collision, which shows that the system is ineffective in avoiding static obstacles and prone to collision accident.

Table 4. Based on the results of visual positioning and static obstacle avoidance system.

The standard distance/cm	Car travel distance /cm	Distance from obstacles /cm	Successful obstacle avoidance
20	23.5	-3.5	no
40	38.6	1.4	yes
60	57.5	2.5	yes
80	75.1	4.9	yes
100	123.1	-23.1	no
150	146.2	3.8	yes
200	223.2	-23.2	no
250	246.5	3.5	yes
300	326.1	-26.1	no
400	367.5	32.5	yes
500	485.2	14.8	yes
600	574.2	25.8	yes
700	736.2	-36.2	no
800	826.7	-26.7	no

From the experimental results in Table 4, it can be seen that the vehicle obstacle avoidance system based on visual positioning has failed six times in many tests, and the number of failures is lower than that of the vehicle obstacle avoidance system based on fuzzy neural network, and lower than that of the system in this paper.

According to the same test method, the correct rate of avoiding dynamic obstacles in three systems is tested. Limited by the limitation of the length of the article, the experiment will arrange 15 different dynamic obstacles in one road plane, and describe the results of avoiding obstacles in three systems with Table 5.

Table 5. Dynamic obstacle avoidance results of the three systems.

Dynamic Obstacle Number	System in this paper	Obstacle Avoidance System based on Fuzzy Neural Network	Obstacle Avoidance System based on Visual Positioning
1	yes	No	no
2	yes	No	yes
3	yes	Yes	no
4	yes	No	no
5	yes	Yes	yes
6	yes	Yes	no
7	yes	No	no
8	yes	Yes	yes
9	yes	No	no
10	yes	Yes	no
11	yes	No	no
12	yes	Yes	no
13	yes	No	yes
14	yes	No	no
15	yes	Yes	yes
Deviation/cm	0.1	2.3	1.2

The results of Table 5 show that the proposed system has a good effect on obstacle avoidance of dynamic obstacles. In the experiment, the system can effectively avoid obstacles every time, and 100% of obstacle avoidance is successful. The deviation value of the proposed system is the smallest, which indicates that the higher the measurement accuracy of the proposed system is. In the experimental test, the success times of the vehicle obstacle avoidance system based on fuzzy neural network and the vehicle obstacle avoidance system based on visual positioning are 7 and 5 times, respectively. The correct rate

of obstacle avoidance is 47% and 33%, respectively. The correct rate of obstacle avoidance for dynamic obstacles is low.

The comprehensive implementation results show that the proposed system has a higher correct rate of obstacle avoidance results for static and dynamic obstacles, and has a better application value in practical applications.

4. Discussion

In this paper, the intelligent obstacle avoidance system of fully automated unmanned vehicle based on laser ranging is designed effectively, but the obstacle avoidance system of fully automated unmanned vehicle is a complex system with human and environment. It is still in the exploratory stage. The future large-scale and wide application of obstacle avoidance system needs further research.

(1) In local obstacle avoidance path planning, virtual obstacles are constructed in straight line segments. In practical applications, fully automated unmanned vehicles often face environments with curved sections or even unstructured roads, which needs to carry out more adaptable obstacle avoidance path planning. This problem can be solved by increasing the number of laser rangefinders or installing panoramic radar.

(2) There is a coupling relationship between longitudinal and lateral motion of fully automated unmanned vehicle. In this paper, the lateral control of the target path tracking control is carried out under the condition of keeping the longitudinal speed stable. By controlling the vehicle chassis to achieve the comprehensive control of the vehicle movement direction, the performance of the automated unmanned vehicle's path tracking control will be further improved.

(3) Because the obstacle avoidance system has good expansibility in both hardware and software resources, it can effectively unify the algorithms of target path tracking control, road and obstacle detection, and apply the results of vehicle condition monitoring to lane maintenance system, adaptive cruise control and vehicle anti-collision system, so as to develop practical vehicle-assisted driving products.

5. Conclusions

In this paper, an intelligent obstacle avoidance system of fully automated unmanned vehicle based on laser ranging is designed. The obstacle information is acquired by laser ranging instrument. The reason why the intelligent obstacle avoidance system of fully automated unmanned vehicle can be accomplished with high quality is as follows:

(1) Laser rangefinder is not affected by the change of illumination. Its wavelength is short, scanning speed is fast, and installation is convenient. It is widely used in automobile collision avoidance and line-patrolling robot.

(2) Using grid-ant colony algorithm for obstacle avoidance path planning can solve the drawbacks of slow speed and easy to fall into local optimum in the process of ant colony algorithm construction. Aiming at the problem that ant colony algorithm is easy to fall into deadlock in the face of concave obstacles, a generalized pheromone updating rule is proposed, which can effectively avoid concave obstacles for fully automated UAV.

Reference

- [1] Guo, J.; Hu, P.; Wang, R. Nonlinear Coordinated Steering and Braking Control of Vision-Based Autonomous Vehicles in Emergency Obstacle Avoidance. *IEEE Transactions on Intelligent Transportation Systems* 2016, 17(11):3230-3240.
- [2] Liu, J.; Jayakumar, P.; Stein, J. L. Combined Speed and Steering Control in High-Speed Autonomous Ground Vehicles for Obstacle Avoidance Using Model Predictive Control. *IEEE Transactions on Vehicular Technology* 2017, 66(10):8746-8763.
- [3] Rosolia, U.; Bruyne, S. D.; Alleyne, A. G. Autonomous Vehicle Control: A Nonconvex Approach for Obstacle Avoidance. *IEEE Transactions on Control Systems Technology* 2017, 25(2):469-484.
- [4] Schaub, A.; Baumgartner, D.; Burschka, D. Reactive Obstacle Avoidance for Highly Maneuverable Vehicles Based on a Two-Stage Optical Flow Clustering. *IEEE Transactions on Intelligent Transportation Systems* 2017, 18(8):2137-2152.
- [5] Graf, P. M.; Bernardini, D.; Esen, H. Spatial-based predictive control and geometric corridor planning for adaptive cruise control coupled with obstacle avoidance. *IEEE Transactions on Control Systems Technology* 2017, (99):1-13.
- [6] Beckmann, H.; Hering, L.; Henze, M. J. Spectral sensitivity in *Onychophora* (velvet worms) revealed by electroretinograms, phototactic behaviour and opsin gene expression. *Journal of Experimental Biology* 2015, 218(Pt 6):915-922.
- [7] Braginsky, B.; Guterma, H. Obstacle Avoidance Approaches for Autonomous Underwater Vehicle: Simulation and Experimental Results. *IEEE Journal of Oceanic Engineering* 2016, 41(4):882-892.
- [8] Erlien, S. M.; Fujita, S.; Gerdes, J. C. Shared Steering Control Using Safe Envelopes for Obstacle Avoidance and Vehicle Stability. *IEEE Transactions on Intelligent Transportation Systems* 2016, 17(2):441-451.
- [9] Shah, B. C.; Švec, P.; Bertaska, I. R. Resolution-adaptive risk-aware trajectory planning for surface vehicles operating in congested civilian traffic. *Autonomous Robots* 2016, 40(7):1139-1163.
- [10] Ali, F.; Kim, E. K.; Kim, Y. G. Type-2 fuzzy ontology-based semantic knowledge for collision avoidance of autonomous underwater vehicles. *Information Sciences* 2015, 295(C):441-464.
- [11] Tang, P.; Zhang, R.; Liu, D. Local reactive obstacle avoidance approach for high-speed unmanned surface vehicle. *Ocean Engineering* 2015, 106:128-140.
- [12] Persiani, F.; Crescenzo, F. D.; Miranda, G. Three-Dimensional Obstacle Avoidance Strategies for Uninhabited Aerial Systems Mission Planning and Replanning. *Journal of Aircraft* 2015, 46(3):832-846.
- [13] Zhang, X.; Zhang, X.; Wang, Y. Extended social force model-based mean shift for pedestrian tracking under obstacle avoidance. *Iet Computer Vision* 2017, 11(1):1-9.
- [14] Guerra, M.; Efimov, D.; Zheng, G. Finite-time obstacle avoidance for unicycle-like robot subject to additive input disturbances. *Autonomous Robots* 2017, 41(1):1-12.
- [15] Viering, D. H. H. M.; Baaij, J. H. F. D.; Walsh, S. B. Genetic causes of hypomagnesemia, a clinical overview. *Pediatric Nephrology* 2017, 32(7):1123-1135.
- [16] Reynard, F.; Terrier, P. Role of visual input in the control of dynamic balance: variability and instability of gait in treadmill walking while blindfolded. *Experimental Brain Research* 2015, 233(4):1031-1040.
- [17] Mariëlle, W.; Van, O.; Heeren, A.; Smulders, K. Improved gait adjustments after gait adaptability training are associated with reduced attentional demands in persons with stroke. *Experimental Brain Research* 2015, 233(3):1007-1018.
- [18] Ghosh, S.; Panigrahi, P. K.; Parhi, D. R. Analysis of FPA and BA meta-heuristic controllers for optimal path planning of mobile robot in cluttered environment. *Iet Science Measurement & Technology* 2017, 11(7):817-828.
- [19] Lee, B. H.; Jeon, J. D.; Oh, J. H. Velocity obstacle based local collision avoidance for a holonomic elliptic robot. *Autonomous Robots* 2016, 41(6):1-17.
- [20] Maclellan, M. J.; Richards, C. L.; Fung, J. Comparison of kinetic strategies for avoidance of an obstacle with either the paretic or non-paretic as leading limb in persons post stroke. *Gait & Posture* 2015, 42(3):329-334.
- [21] Rauh, N.; Franke, T.; Krems, J. F. Understanding the Impact of Electric Vehicle Driving Experience on Range Anxiety. *Human Factors* 2015, 57(1):177-187.
- [22] Rodrigues, J. A.; Lussi, A.; Seemann, R. Prevention of crown and root caries in adults. *Periodontology* 2015, 55(1):231-249.
- [23] Braña, F. Morphological correlates of burst speed and field movement patterns: the behavioural adjustment of locomotion in wall lizards (*Podarcismuralis*). *Biological Journal of the Linnean Society* 2015, 80(1):135-146.
- [24] Jung, J.; Shin, K.; Sael, L. Random Walk with Restart on Large Graphs Using Block Elimination. *Acm Transactions on Database Systems* 2016, 41(2):1-43.
- [25] Chakraborty A.; Bairagya S.; Sarkar A. Analytical model of surface potential of double surrounding gate mosfet. *Advances in Industrial Engineering and Management*, 2016, 5(1):93-97.
- [26] Yin, L. F.; Yang, B. J.; Wang, C. S. A Multi-Agent Algorithm of Obstacle Avoidance Based on Vectorial Artificial Potential Field. *Computer Simulation* 2016, 41(2):1-43.
- [27] Meng X. B.; Sun S. R. A product conceptual design process model integrating semantics and its support system. *Journal of Mechanical Engineering Research and Developments*, 2016, 39(3):772-781.

Distributed Multi-level Inventory Algorithms for Automotive Maintenance Spare Parts Based on Centralized Control Model

Jiangang Li*

Automotive Engineering Department, Zibo Vocational Institute, Zibo 255314, China

Received OCT 16 2019

Accepted JAN 15 2020

Abstract

In order to increase the inventory of automotive maintenance spare parts, this article takes automobile maintenance spare parts as the research object, and proposes a distributed multi-level spare parts inventory algorithm based on centralized control to address the problems of low satisfaction of the automotive maintenance spare parts warehouse and poor effectiveness of spare parts inventory control. . The characteristics of automobile maintenance spare parts supply, vehicle maintenance spare parts supply and vehicle maintenance spare parts inventory management are introduced, and the current status of automobile maintenance spare parts inventory management is analyzed. Using the conditions of centralized ordering and mutual allocation, the functions of inventory cost and estimated inventory cost were calculated. A mathematical model for centralized ordering and mutual spare parts inventory was established. Through the establishment of a model, the research of distributed multi-level inventory algorithm for automobile maintenance spare parts is completed to realize inventory optimization. The experimental results show that the algorithm not only has the advantage of high satisfaction rate of automobile maintenance spare parts library, but also improves the efficiency and control ability of spare parts inventory turnover.

© 2020 Jordan Journal of Mechanical and Industrial Engineering. All rights reserved

Keywords: centralized control; automobile maintenance spare parts; distributed; multi-level inventory.

1. Introduction

The concept of spare parts begins with modular design of products. Spare parts are parts and components that can replace the vulnerable parts in machine equipment. According to different uses, spare parts can be roughly divided into two categories: one is that in order to maintain the normal operation of production equipment and promote the continuity of production process, enterprises must reserve a certain number of spare parts of production equipment, which is called maintenance spare parts; the other is that after the sale of their own products, in order to ensure the normal operation of such products after sale, it is necessary to maintain a certain number of spare parts to provide maintenance or replacement services for users. Such spare parts are called service spare parts. Maintenance spare parts inventory in service spare parts of automobile service enterprises is selected as the research object[1-2].

With the continuous development of Internet technology, many related scholars have proposed a variety of distributed multi-level inventory algorithms for vehicle maintenance spare parts. Reference [3] proposed a distributed multi-level inventory algorithm for automobile maintenance spare parts based on industry chain cloud service platform. Aiming at the cooperative demand of spare parts business of chain cooperative service platform

in manufacturing industry, a cross-node inventory cooperative solution was proposed and a near-term demand forecasting calculation model was established. Combining the application of real-time collection and processing of historical transaction data and inventory data of distributed node enterprises, the effectiveness of inventory control scheme was guaranteed. MapReduce framework was used to optimize the calculation process of model parameters and improve the operation speed. The genetic algorithm was used to obtain the optimal solution of the model, the results of the model were pushed to the downstream dealer enterprise group, and the dynamic generation of orders was controlled by feedback information. The model was applied to the cloud service platform of the automobile industry chain, which reduced the response time of the industry chain, but the algorithm had high inventory and high cost of spare parts. Reference [4] proposed a distributed multi-level inventory algorithm for automobile maintenance spare parts based on virtual center. In automobile spare parts maintenance and support, the inventory control of automobile maintenance spare parts was one of the effective ways to improve the efficiency of automobile equipment support. A two-level inventory model was established to optimize the cost of inventory management, and a distributed multi-level inventory control strategy for automobile maintenance spare parts was given. Reference [5] proposed a distributed multi-level inventory algorithm for automobile maintenance spare

* Corresponding author e-mail: hjgsk23021@163.com.

parts based on non-preemptive maintenance priority. Considering the influence of non-preemptive maintenance priority on the maintenance process of faulty parts, the availability evaluation model and initial inventory optimization model of automobile maintenance spare parts under non-preemptive maintenance priority were established. The objective function of non-preemptive priority allocation scheme in multi-level support system was constructed, and the genetic algorithm was used to optimize the priority allocation scheme. Finally, the distributed multi-level inventory of automobile maintenance spare parts was optimized. The above two algorithms had the problem of low satisfaction rate of spare parts warehouse, which reduced the efficiency of support. Reference [6] presented a distributed multi-level inventory algorithm for automobile maintenance spare parts based on system dynamics. A dynamic model of multi-level inventory cooperative management system composed of suppliers, distribution centers and stores was constructed from the point of view of dynamic system. Through sensitivity analysis, the inventory adjustment cycle, demand forecasting weight and safety of automobile maintenance spare parts were determined. By improving the parameters such as full inventory days, an optimized multi-level inventory system dynamics model of automobile maintenance spare parts was finally obtained. The algorithm had the problem of low turnover efficiency of spare parts inventory.

In summary, a distributed multi-level inventory algorithm for automobile maintenance spare parts based on centralized control is proposed. The overall research framework of the algorithm is:

- (1) The characteristics of automobile service spare parts inventory are analyzed;
- (2) The current situation of inventory management of automobile service spare parts is analyzed;
- (3) The mathematic models of spare parts inventory in centralized ordering and mutual allocation are constructed respectively, and the research on distributed multi-level inventory of automobile maintenance spare parts is completed.
- (4) The experimental results and analysis. The validity of the distributed multi-level inventory algorithm for automobile maintenance spare parts based on centralized control through the test of spare parts inventory and spare parts warehouse satisfaction rate is verified, and the turnover rate of spare parts inventory of the proposed algorithm is discussed.
- (5) Conclusions.

2. Materials and methods

2.1. Inventory Characteristics of Automotive Service Spare Parts

2.1.1. Demand for automotive service spare parts

When repairing a certain equipment, parts used to replace aging or worn parts are called spare parts. In order to shorten the repairing time, a certain number of spare parts are usually kept in the warehouse. These preserved parts are called spare parts. As the most important link in the sales supply chain of automobile manufacturing enterprises, the service of 4S automobile shops brings huge profits to automobile enterprises. The flow direction of service spare parts is from 4S shops to customers. From the perspective of 4S shops, there are three main demands for

automobile service spare parts: the first is that customers need to carry out vehicle repair and daily maintenance, cosmetology and so on every fixed cycle or journey; the second is that after a traffic accident, the corresponding vehicles need to be repaired. A certain number of accident spare parts are required. Thirdly, the owners with special requirements need certain spare parts. Some customers will require 4S shops to refit the automobile or customers themselves to carry out refitting and daily simple maintenance. Generally speaking, there is no big difference between the spare parts for the first type of demand and the general products. The number of customers' car purchases is known, and the frequency of daily maintenance is relatively stable. Therefore, it is easy to predict. While the spare parts for the second type of demand are very uncertain, because the occurrence of accidents is discontinuous and uncertain. This brings great difficulties to spare parts prediction. This uncertainty will be transmitted along the upstream and downstream of the supply chain [7], thus increasing the difficulty of spare parts control in automobile manufacturers and 4S shops. Generally, statistical methods are more accurate in demand analysis.

2.1.2. Supply of automobile service spare parts

Usually, a car contains at least 6,000 kinds of parts and components. With the development of science and technology, the models of cars are changing with each passing day, and new models are constantly introduced. All parts and components cannot be produced by the whole car factory. Many automobile manufacturers mainly produce automobile engines and pay attention to the research and development of car bodies, for example, Japan's Toyota, Germany's Volkswagen, etc., other parts are mainly supplied by suppliers.

According to the types of suppliers, there are two main types: one is the factory entrusted by the automobile manufacturing enterprises; the other is the long-term supplier of spare parts, such as Bosch, Wanxiang, Delphi and so on. According to the geographical location of spare parts supply, there are three main categories: the first category is imported parts, although domestic automobile development is faster, the development capacity of new products in a real sense is less, so more than half of the spare parts need to be imported from abroad, the logistics route of imported parts is more complex, and the cycle is relatively long; The second category is self-made parts, automobile manufacturing enterprises with core R&D capabilities will manufacture relevant core components by specialized departments to improve core competitiveness and reduce costs; the third category is domestic parts supplied by domestic suppliers, the order lead time is shorter and the logistics cost is relatively low..

2.1.3. Characteristics of inventory management of automobile service spare parts

Above all, we can see from the demand and supply of automobile service spare parts that the demand of spare parts is uncertain and the supply mode is diverse. In addition, the inventory of automobile service spare parts has the following outstanding characteristics:

- (1) Spare parts have a wide variety of inventory and different prices.

Because there are many kinds of spare parts that make up automobiles, there are also many kinds of service spare parts that need to be provided by 4S shops. The price difference is massive. The price of more valuable spare

parts can reach more than 90,000 yuan, while the price of cheap spare parts is only a few yuan.

(2) Long life cycle

Compared with general products, the life cycle of auto repair spare parts is much longer. The life cycle of a typical product is its duration, from the launch of a new product to the exit of the market, it is a life cycle. The life cycle of a car is the life cycle of the car plus the life cycle of the parts it uses. For example, after an automobile is launched into the market, it will exit the market after about 10 years. If the life of the vehicle is 15 years, the duration of the automobile is 25 years.

(3) Service spare parts need to meet a higher level of service

Service spare parts are mainly to provide services to customers. The important sign of judging service level is to look at the response time of customers' needs, to make the fastest response in the shortest time, solve the customer's problems, not only to obtain profits but also to win customers' trust, so as to establish the brand image of the company [8]. Generally speaking, if a private car is repaired, it will affect the daily travel of customers and bring inconvenience to personal life during the repair period; if the vehicle of logistics company needs to be repaired, it will affect the operation of the whole company; if it is repaired for medical, fire and other emergency vehicles, it may also affect life and property safety. Therefore, the automobile service spare parts should have a faster response speed, and then meet the higher level of service.

(4) Long inventory turnover time

The demand for service spare parts is not only the daily maintenance, but also the failure of the automobile product. With the development of science and technology, the quality of automobiles is getting better and better. The probability of failure is also reduced. The inventory turnover rate of service spare parts is lower than that of general consumables. At present, Shanghai General Motors is the best after-sales service in China. Its annual inventory turnover is three times, while that of automobile companies like Huachen is only 2 times.

(5) Reverse Logistics

For expensive and repairable automotive service spare parts, spare parts suppliers will provide maintenance services. For these spare parts, first of all, they will be repaired in 4S shops. If they are not repaired properly, they will be repaired in regional maintenance center. At the same time, they will replace spare parts for customers. If the repair of the regional repair center is not good, it will be returned to the factory for repair, and the repair will be

completed as local stock. This reverse logistics process is more complex, mainly for expensive repairable automotive service spare parts, the inventory management of these spare parts is also very important.

(6) Low selectivity of inventory content

For the whole automobile factory, there are as many as 20,000 kinds of automobile spare parts, while the inventory of automobile service spare parts for after-sales service is relatively less selective. After fixed spare parts are selected in production, the spare parts needed in service are determined. For example, in production, five of the 20 types of spare parts that meet the requirements are selected, and the types of spare parts for after-sales service are five. The selectivity of the inventory contents is relatively small.

2.2. Current Situation of Inventory Management of Automotive Service Spare Parts

Audi, BMW, Chery three automobile brands are chosen to understand the operation of their service spare parts, and make a specific description[9,10], as shown in Table 1. CDC refers to the central distribution center, RDC refers to the regional distribution center, where the retail only lists 4S shops, not including maintenance stations.

Table 1. Logistics Status of Service Spare Parts for Four Automobiles

Automobile brand	Audi	BMW	Chery	
Inventory structure	Layer number	3	2	3
	Number of CDC	1	1	1
	Number of RDC	7	3	15
	Number of 4S shops	150	70	310
Inventory control method	Fixed order quantity	Fixed order quantity	Fixed order quantity	
Is spare parts classified management?	ABC classification	ABC classification	ABC classification	
Vehicle factory procurement lead time	Imported CKD parts	Three months	Three months	Three months
	Domestic parts	Two months	Two months	Two months
4S shop's lead time	One week	One week	One week	

In order to shorten the demand response time, the main distribution mode is from the central distribution center to the regional distribution center and then to 4S shops, as shown in Figure 1.

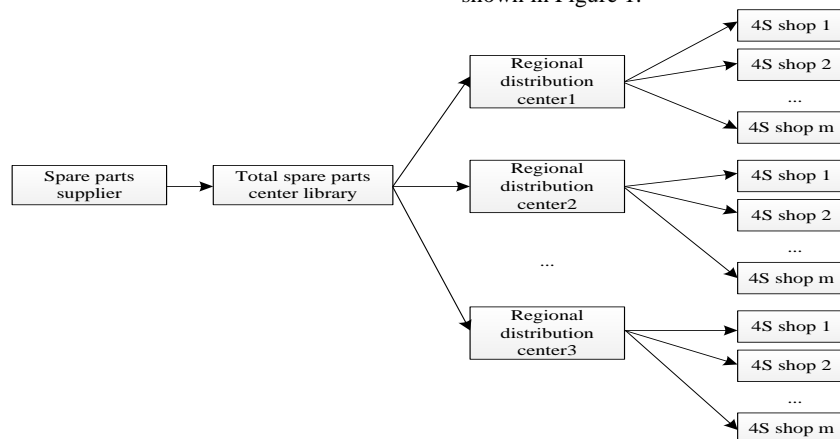


Figure 1. Existing supply mode of automobile service spare parts

As can be seen from Figure 1, the automobile manufacturing enterprises have a general central distribution center throughout the country. At the same time, they are divided into several regional distribution centers according to the region. Each regional distribution center serves 4S shops within its service scope. This method has faster demand response speed, and the specific process is as follows:

- (1) 4S shops in a certain area draw up orders according to their market forecast and their own stock situation, and submit the orders to the regional distribution center serving them. If the stock of automobile service spare parts in the regional distribution center is sufficient, it will be distributed to 4S shops. If it is not enough, it is necessary to submit the order to the central distribution center in conjunction with the order of each 4S shop and its own inventory.
- (2) If the total quantity of service spare parts in the central distribution center of the automobile manufacturing enterprise is sufficient, it will be distributed to the regional distribution center. If the spare parts are insufficient, the procurement plan will be formulated according to the actual situation of the headquarters [11,12], and the order will be submitted to the supplier to order, and the supplier supplies to the central distribution center.
- (3) The central distribution center distributes the goods through sorting, packing and other procedures according to the order requirements of the Regional Distribution Center. After receiving spare parts, the Regional Distribution Center distributes the goods according to the order requirements of the 4S shop it serves.

2.3. Research on Distributed Multi-level Inventory of Automotive Maintenance Spare Parts Based on Centralized Control

2.3.1. Core ideas

The core idea of the centralized control strategy is to set up an inventory coordination center in the spare parts management department of the headquarters of automobile manufacturing enterprises. Based on the real-time centralized storage of spare parts demand and inventory information in each region, the centralized control of the inventory in each sub-warehouse is carried out by the coordination center, or the ordering from external suppliers is unified, or inventory is transferred between different regions within the company. Each regional warehouse is responsible for the spare parts supply of service stations

nationwide under the unified dispatch of the headquarters coordination center. This inventory coordination center enables the entire company to physically disperse distributed inventory, forming a virtual centralized inventory.

2.3.2. Mode of operation

Under the guidance of the above ideas, the centralized control strategy operates in the following ways. An inventory coordination center has been set up in the spare parts management department of automobile manufacturer headquarters. Instead of sending spare parts demand information to the major regional warehouses, the regional service stations order spare parts directly from the headquarters [13]. The headquarters coordination center inquires the company's real-time inventory database immediately after receiving the orders from the service stations. The geographic location of the service station and the inventory situation of the major regional warehouses designate the corresponding large regional warehouses to supply them. The Headquarters Inventory Coordination Center should monitor the inventory situation of each regional warehouse in real time, coordinate the order business with the spare parts suppliers when the total stock of the company has dropped to the company's general order point, take charge of the inventory replenishment of the downstream major regional warehouses, and the spare parts suppliers will send the spare parts directly to the regional sub-warehouse under the coordination of the Headquarters Coordination Center: When some large-scale sub-warehouses need to replenish and the existing total inventory of the entire company has not yet fallen to the company's total order point, it should compare the expected inventory costs under the order situation with the expected inventory costs under the transfer situation, if the former is smaller than the latter, then for centralized ordering, if the latter is smaller than the former, the stocks are reasonably allocated between the major sub-warehouses to avoid the company's overall inventory backlog and partial shortages. At this time, the original spare parts central warehouse of headquarters no longer undertakes the replenishment business to the subordinate major sub-warehouses. Its responsibilities are similar to those of other large sub-warehouses. It is responsible for the spare parts supply of its peripheral service stations under the dispatch of the headquarters inventory coordination center. The improved supply mode and supply process are shown in Figure 2 and 3.

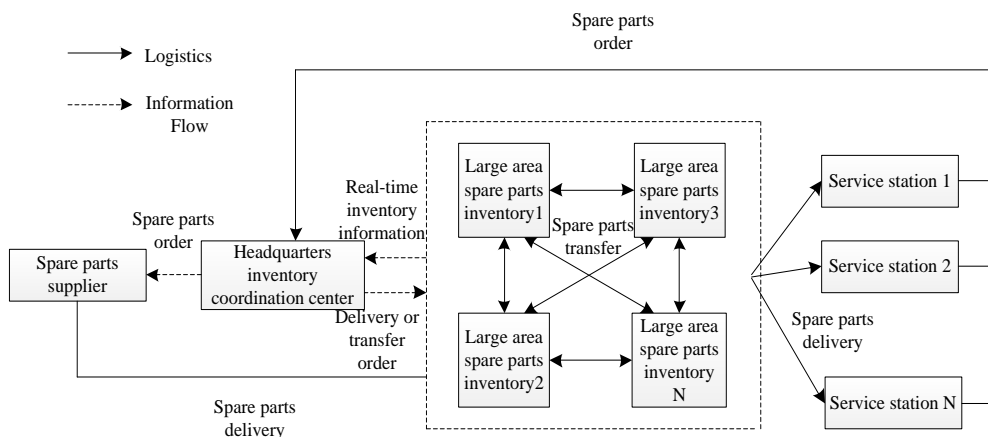


Figure 2. The improved supply mode of automobile spare parts

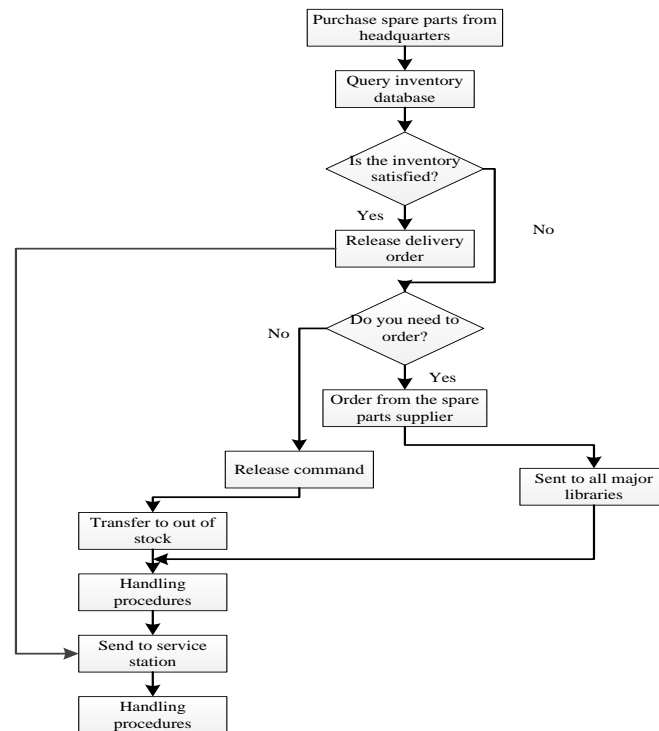


Figure 3. Improved Supply Process of Automobile Spare Parts

The spare parts inventory coordination center company's headquarters plays a very important role. Its main functions include: collecting spare parts purchase orders from service stations nationwide, assigning corresponding large-scale warehouses to supply spare parts to service stations; purchasing spare parts from suppliers when the company's overall inventory is insufficient; processing the information and control parameters needed in order together with spare parts suppliers and establishing the standard mode and business process of order processing, assisting spare parts suppliers in real-time understanding of the inventory and consumption of major downstream sub-warehouses, and making preparations for production; consulting with each sub-warehouse to determine the relevant parameters of inventory control, such as regular or continuous replenishment strategy of major sub-warehouses, safe inventory, order point, order quantity and allocation amount, etc. [14]; real-time monitoring of spare parts consumption and inventory in each region, dynamic automatic replenishing according to the spare parts consumption and inventory situation in each region; ordering the spare parts supplier and assisting to deliver the goods to the warehouse on time; when the company's overall inventory is insufficient, it is necessary to transfer the inventory among the regions, carrying out the inventory allocation between regions.

The above centralized control strategy breaks the situation of independent decision-making and self-governing of each regional warehouse in the management of its own inventory, strengthens coordination and cooperation among various regions, and then links physical distributed inventory into a virtual centralized inventory, effectively resolving various problems in existing modes of automobile spare parts supply.

2.3.3. Advantages of centralized control strategy

(1) Effective control of bullwhip effect in spare parts supply chain

In order to ensure the smooth implementation of the centralized control strategy, it is necessary to collect the data information of the spare parts supply chain into the Headquarters Inventory Coordination Center in real time. Through the real-time aggregation of data information, the company headquarters can grasp the demand and current inventory information of its downstream regions in real time, and can make decisions according to the demand and inventory situation of downstream regions in time. Ordering spare parts suppliers or allocating inventory among different sub-warehouses is the way to deal with this problem. It can reduce the fluctuation caused by the transmission of data information in the spare parts supply chain [15]. With the centralized storage of historical information, and through scientific analysis methods, we can more accurately predict the future demand of some spare parts and reduce the error of demand forecasting. In this way, the bullwhip effect caused by the non-sharing of demand information and the independent operation of inventory in spare parts supply chain system can be effectively controlled.

(2) Exerting the Scale Advantage of Centralized Inventory Management

In order to meet the requirements of rapid response to customer demand, it is difficult for automobile manufacturers to achieve centralized physical management of service spare parts inventory, which makes the advantages of centralized inventory management difficult to play. But centralized control strategy makes physically dispersed distributed inventory become virtual centralized inventory, and centralized inventory management can be realized through information sharing. Setting up the headquarters' spare parts inventory coordination center, consulting with the major sub-warehouses to formulate inventory control strategies, and implementing replenishment and allocation of the sub-warehouses by the coordination center, can give full play to the scale advantage of centralized inventory management[16].

(3) Strengthening coordination and cooperation among nodes

In the implementation of centralized control strategy, supply chain-based business process reengineering is a key link, which can solve the multi-organizational collaboration problems involved in multi-level inventory management. Through business process reengineering among spare parts supply chain nodes, coordination and cooperation among nodes are strengthened, seamless connection between nodes is effectively realized, so as to achieve the goal of optimizing spare parts inventory control.

(4) Reducing the uncertainty of suppliers

Spare parts suppliers can timely understand the inventory and consumption of the latter according to the spare parts demand and inventory information centralized in the headquarters of automobile manufacturing enterprises, timely replenishment of raw materials, shorten the lead time of supply, and then improve the ability of supplying for automobile manufacturing enterprises. And automobile manufacturers can also track the implementation of spare parts suppliers' orders, get timely feedback from suppliers, and reduce the loss of shortage. At the same time, the management level and competitiveness of spare parts suppliers have been improved correspondingly.

2.3.4. Model construction

(1) Model description

Supposing an automobile manufacturer has a regional spare parts warehouse in the whole country (the original headquarters spare parts central warehouse is regarded as one of these warehouses), which is responsible for the spare parts supply of service stations throughout the country. With continuous inventory replenishment strategy, the headquarters coordination center monitors the whole company's spare parts database in real time. When the inventory of some large-scale warehouses drops to the ordering point, and the existing total inventory of the whole company also drops to the company's total ordering point, the headquarters coordination center adopts centralized ordering strategy, and the headquarters coordination center provides spare parts suppliers with the strategy of centralized ordering. In order, the supplier delivers the spare parts directly to the different warehouses; when the stock of some large warehouses falls to the order point, and the total stock of the whole company has not yet fallen to the company's total order point, it is necessary to calculate the expected inventory cost in the case of ordering and allocation separately. If the former is less than the latter, the set is adopted. If the latter is smaller than the former, the mutual allocation strategy will be adopted, and the other regions will allocate to the regions requiring orders under the dispatch of the headquarters coordination center.

For an automobile repair spare part, the following assumptions are made:

The demand of differentiated warehouse k is D_k in every week, which obeys the normal distribution of $N(\mu_k, \sigma_k^2)$, and the demand is independent and identical distribution every week. So if the time period t is taken into account, the demand D_k of t period obeys the $N(\mu_k, \sigma_k^2)$ normal distribution, $k = 1, 2, 3, \dots, N$; the lead time of spare parts supplier supplying to differentiated

warehouse k is L_k . For the reason of warehouse capacity, regional warehouse k allows the maximum warehouse capacity of the spare parts to be V_k , and the company sets the service level of spare parts to be P , that is, the probability that the demand can be met directly from the local warehouse. and the service level of spare parts set by the company is $p1$, that is, the probability that the demand can be met directly from the local warehouse. The objective of inventory optimization is to determine the inventory control parameters, i.e. the total order point of the company and the order point, and order quantity or allocation quantity of the different warehouses, so as to make the expected inventory costs of the spare parts of the whole company are minimal in the time period T under the condition of given spare parts service level P and given the system time period T to be considered[17].

(2) Symbol definition

Firstly, the symbols in the model and their meanings are listed.

I_{kT} is the initial inventory of the spare parts of regional warehouse k in period T , D_k denotes the weekly demand of the spare parts in regional warehouse k in period T , which obeys the $N(\mu_k, \sigma_k^2)$ normal distribution, D_{kT} denotes the demand of the spare parts in regional warehouse k in period T , which obeys the $N(\mu_k, \sigma_k^2)$ normal distribution, and $P_{kT}(x)$ denotes the probability that the demand of the spare parts in regional warehouse k in period T is x . L_k represents the lead time from supplier to regional warehouse k . D_{Lk} represents the demand of regional warehouse k for the spare parts within the lead time L_k , which obeys the $N(L_k \mu_k, L_k \sigma_k^2)$ normal distribution. r_k represents the order point of regional warehouse k , Q_k represents the order quantity from regional warehouse k to supplier. $Q1$ indicates the order quantity of regional warehouse k to suppliers, and the allocation quantity between regional warehouse k and other regionals when allocating to each other. P indicates the unit purchase price of the spare parts when the company orders to suppliers. CO indicates the transaction costs of that headquarters coordination center orders to the spare parts suppliers on behalf of the regional warehouses that need to order, including telecommunications, contract notarization and travel expenses at the time of ordering. CT indicates that the business processing costs of that the headquarters coordination center handles the transfer business in each time when transferring to each other. Cin_k means that the business processing expenses of that regional warehouse k handles the spare parts storage in each time. $Cout_k$ means that the business processing expenses of that regional warehouse k handles the spare parts out of the warehouse in each time. CH_k indicates the storage

expenses of the spare parts in unit time in regional warehouse k , including warehouse usage fee, warehouse keeper's salary, insurance premium, tax, interest on occupied funds, etc. CS_k states the loss fee of unit spare parts in the case of shortage of warehouse k , including penalty for breach of contract, loss to users, loss of sales opportunity profit, etc., due to company's shortage during the three guarantees period. Ct represents the transportation cost of bit spare parts and unit distance, d_{kj} represents the transportation distance from k to regional warehouse j , Q_{kj} represents the allocation amount between k and regional warehouse j , CO_{kT} and CD_{kT} respectively represents the expected inventory cost of k in period T under centralized order and mutual allocation, TCO_T and TCT_T respectively represents the expected inventory cost of the whole company in period T when centralized orders and mutual transfers are made.

(3) Model establishment

A mathematical model for centralized inventory control of regional spare parts warehouses under the unified management of headquarters coordination center is established. When establishing the inventory model, the following costs are considered: transaction cost of order, purchase cost, warehouse storage cost of maintaining spare parts inventory, loss cost of shortage caused by shortage, business processing cost allocated between different warehouses and transportation cost of spare parts when allocating. There are two cases: one is the situation of centralized ordering to spare parts suppliers through the headquarters coordination center in each region requiring ordering; the other is the situation of inventory allocation to regions requiring replenishment under the scheduling of the headquarters coordination center.

In the case of centralized ordering, it is necessary to determine the optimal order quantity of different warehouses so as to minimize the expected inventory cost of the whole company during the period T . Inventory costs include transaction costs, purchase costs, warehousing business processing costs, storage costs, as well as out-of-stock loss costs. Because of the centralized order of the whole company, transaction costs and purchase costs can be considered from the perspective of the whole company, while warehousing business

processing costs, warehousing and storage costs and out-of-stock loss costs vary with the different regional warehouses, so it is necessary to calculate the regional warehouses as a unit, and then aggregate and count them into the whole company. Transaction cost and purchase cost are the inventory cost under the condition of centralized order of the whole company.

Inventory costs related to regional warehouses are calculated using the following formulas (1).

So in the case of centralized order, the total expected inventory cost function of the whole company in period T is as follows:

$$TCO_T = CO + P \sum_{k=1}^N Q_k + \sum_{k=1}^N CO_{kT} \tag{2}$$

Considering the constraints of centralized ordering, the maximum storage capacity of spare parts in each region is allowed to be V_k , and the following constraints are obtained:

$$I_{kT} + Q_k \leq V_k \tag{3}$$

The mathematical model of spare parts inventory in centralized ordering is as follows:

$$MinTCO_T = CO + P \sum_{k=1}^N Q_k + \sum_{k=1}^N CO_{kT} \tag{4}$$

$$s.t. I_{kT} + Q_k \leq V_k$$

In the case of mutual allocation, it is necessary to determine the optimal allocation amount of different warehouses so as to minimize the expected inventory cost of the whole company during the period T . Here, the inventory cost includes the disposal cost of allocation business, the disposal cost of inward and outward warehousing business, the transportation cost of spare parts when allocating each other, and the storage cost and the loss cost of shortage. Because it is allocated by the company's headquarters coordination center, the allocation of business processing costs can be considered from the perspective of the whole company, while the processing costs, storage costs, shortage loss costs and transportation costs vary with the different regional warehouses, so it is necessary to calculate the regional warehouses as a unit. Then, the inventory cost under the whole company's allocation can be obtained by summarizing and counting the disposal cost of the whole company's allocation business.

$$CO_{kT} = \delta(Q_k) \times Cin_k + CH_k \times T \times \sum_{D_{kT} \leq I_{kT} + Q_k} [(I_{kT} + Q_k - D_{kT}) \times P_{kT}(D_{kT})] + CS_k \times \sum_{D_{kT} \leq I_{kT} + Q_k} [(D_{kT} - I_{kT} - Q_k) \times P_{kT}(D_{kT})] = \delta(Q_k) \times Cin_k CH_k \times T \times \int_0^{I_{kT} + Q_k} (I_{kT} + Q_k - x) \times \frac{1}{\sqrt{2\pi T \sigma_k}} + CS_k \times \int_{I_{kT} + Q_k}^{\infty} (x - I_{kT} - Q_k) \times \frac{1}{\sqrt{2\pi T \sigma_k}} \tag{1}$$

Where, $\delta(x) = \begin{cases} 1, & x > 0 \\ 0, & x \leq 0 \end{cases}$, then, the inventory cost of the whole company in period T is calculated, and the inventory cost of each regional warehouse is added into the transaction cost and purchase cost of the whole company.

The inventory costs associated with the regional sub-repositories can be calculated as formulas :

$$\begin{aligned}
 CT_{kT} = & \sum_{j=1}^N [\eta(Q_{kj} \times Cout_k) + \sum_{j=1}^N \delta(Q_k) \times Cin_k] + \sum_{j=1}^N (\delta(Q_k) \times Q_{kj} \times Ct \times d_{kj}) + CH_k \times T \times \\
 & \sum_{D_{kT} \leq I_{kT} + Q_k} [(I_{kT} + Q_k - D_{kT}) \times P_{kT}(D_{kT})] + CS_k \times \sum_{D_{kT} \leq I_{kT} + Q_k} [(D_{kT} - I_{kT} - Q_k) \times P_{kT}(D_{kT})] = \\
 & \sum_{j=1}^N [\eta(Q_{kj} \times Cout_k) + \sum_{j=1}^N \delta(Q_k) \times Cin_k] + \sum_{j=1}^N (\delta(Q_k) \times Q_{kj} \times Ct \times d_{kj}) + CH_k \times T \times \\
 & \int_0^{I_{kT} + Q_k} (I_{kT} + Q_k - x) \times \frac{1}{\sqrt{2\pi T \sigma_k}} + CS_k \times \int_{I_{kT} + Q_k}^{\infty} (x - I_{kT} - Q_k) \times \frac{1}{\sqrt{2\pi T \sigma_k}}
 \end{aligned} \tag{5}$$

Where, $\eta(x) = \begin{cases} 1, & x < 0 \\ 0, & x \geq 0 \end{cases}$. Next, the expected inventory cost of the whole company in the period T is calculated, and the inventory cost of each regional warehouse is summed up and included in the allocation business processing cost of the whole company.

Therefore, in the case of allocation, the total expected inventory cost function of the whole company in period T is as follows:

$$TCT_T = CD + \sum_{k=1}^N CT_{kT} \tag{6}$$

Considering the constraints of allocation, the maximum storage capacity of spare parts is allowed to be

V_k by the sub-storage of spare parts in each region, so that the import amount of warehouse k can be satisfied:

$$0 < I_{kT} + Q_k \leq V_k \tag{7}$$

The inventory transferred from the warehouse shall not be lower than its ordering point after deducting the amount transferred, and the amount transferred from the warehouse k shall be satisfied:

$$-(I_{kT} - r_k) < Q_k < 0 \tag{8}$$

The mathematical model of spare parts inventory allocated to each other is as follows:

$$\begin{aligned}
 MinTCT_T = & CT + \sum_{k=1}^N CT_{kT} \\
 s.t. & \begin{cases} 0 < I_{kT} + Q_k \leq V_k \\ -(I_{kT} - r_k) < Q_k < 0 \end{cases}
 \end{aligned} \tag{9}$$

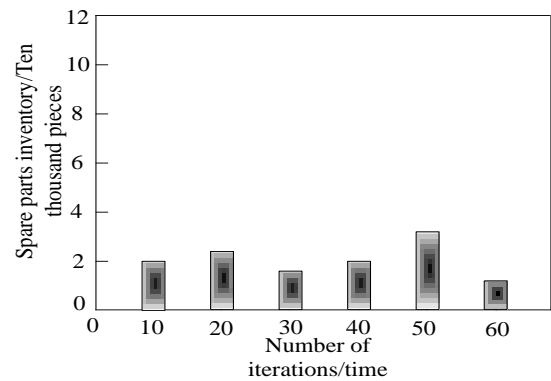
Based on the constructed data model, the spare parts inventory optimization algorithm is obtained as:

$$P(t) = \frac{\sum_{k=1}^N CT_{kT}}{V_k} \tag{10}$$

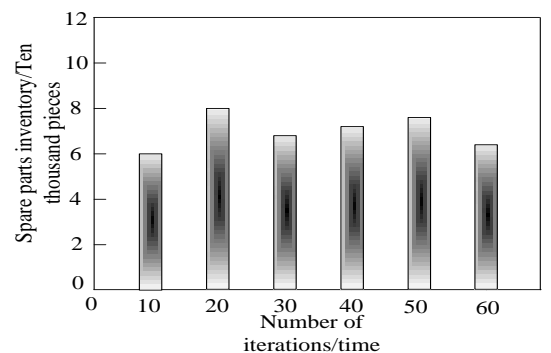
By deriving formula (14), the research of distributed multi-level inventory algorithm for automobile maintenance spare parts is realized.

3. Results

In the experiment, CPU with memory of 3G is selected, the running system is Windows 7, and the running software is MATLAB. In order to verify the validity of the proposed method, the stock of automobile maintenance spare parts is tested. The higher the inventory of automobile maintenance spare parts is, the more the cost is. The test results are shown in Figure 4.



(a) Test results of inventory of automobile maintenance spare parts based on the proposed algorithm



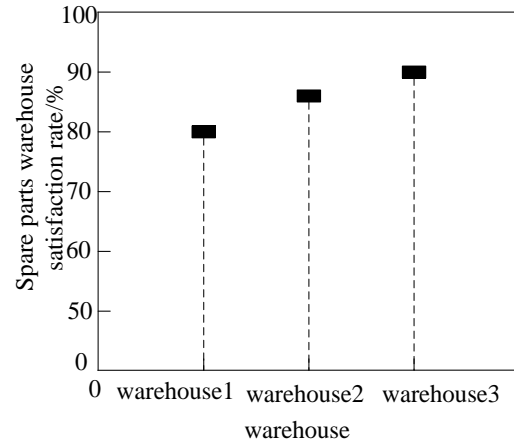
(b) Test results of inventory of automobile maintenance spare parts based on the algorithm in reference [3]

Figure 4. Contrast results of inventory of automobile maintenance spare parts.

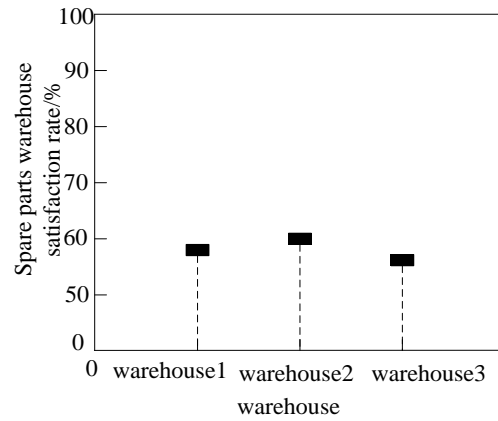
Analysis of Figure 4 shows that in the 60 iterations, the inventory of automobile maintenance spare parts controlled by the proposed algorithm is between 20,000 and 40,000 pieces. In the 30th and 60th iterations, the inventory of spare parts is less than 20,000 pieces. In the 60 iterations by using the algorithm in reference [3], the total inventory of spare parts is between 60,000 and 80,000 pieces. In the 20th iteration, the inventory of spare parts is the largest, which is 80,000 pieces. By contrast, when the proposed algorithm is used to control the inventory of spare parts, the inventory is smaller and the cost is lower, which can accurately guarantee the inventory control of spare parts and improve the control ability.

On the basis of inventory measurement of automobile maintenance spare parts, three warehouses are designed, which are warehouse 1, warehouse 2 and warehouse 3. Satisfaction rate of spare parts warehouse is tested. The test results are shown in Figure 5.

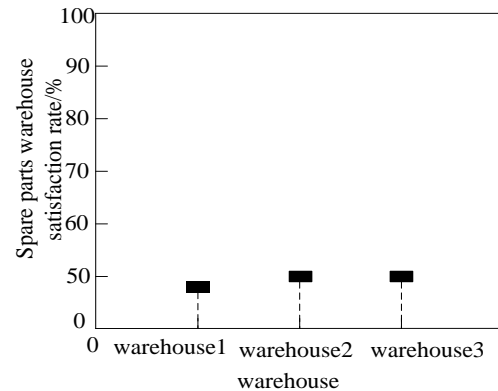
Figure 5 shows that in the proposed algorithm, the warehouse satisfaction rate of spare parts in warehouse 1 and warehouse 3 is 80% and 90%. In the algorithm of reference [4], the satisfaction rate of spare parts in warehouse 1 and warehouse 3 is lower than 60%, and the satisfaction rate of spare parts in warehouse 2 is 60%. In the algorithm of reference [5], the satisfaction rate of spare parts in warehouse 1 and warehouse 3 is lower than 50%, and the satisfaction rate of spare parts in warehouse 2 is 50%. By comparison, the proposed algorithm has a higher satisfaction rate of automobile maintenance spare parts in warehouse and improves the efficiency of support. The above two experiments verify the effectiveness of the proposed algorithm.



(a) Test results of the satisfaction rate of spare parts warehouse based on the proposed algorithm



(b) Test results of the satisfaction rate of spare parts warehouse based on the algorithm in reference [4]

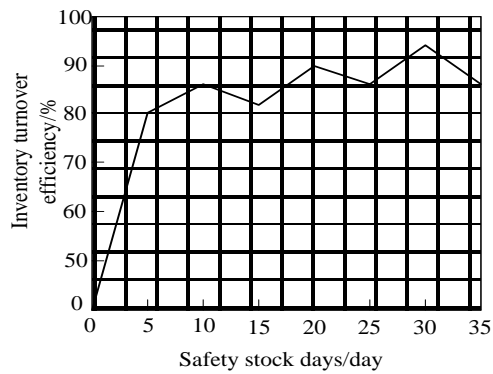


(c) Test results of the satisfaction rate of spare parts warehouse based on the algorithm in reference [5]

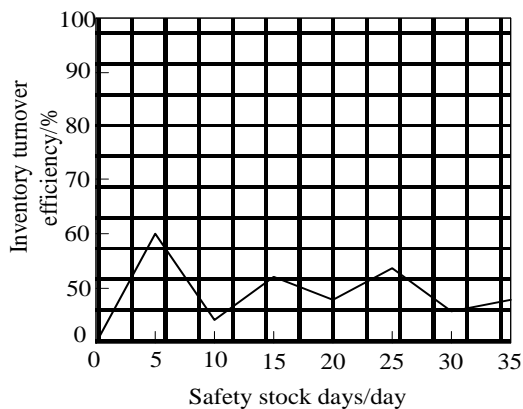
Figure 5. Contrast results of Satisfaction Rate of Spare Parts Warehouse with Different Algorithms

4. Discussion

On the basis of the above experiments, the validity of the proposed algorithm is further discussed. The safety inventory days and inventory turnover efficiency of automobile maintenance spare parts are discussed. The discussion results are shown in Figure 6.



(a) Inventory turnover efficiency of automotive maintenance spare parts based on the proposed algorithm



(b) Inventory turnover efficiency of automotive maintenance spare parts based on the algorithm in reference [6]

Figure 6. The discussion results of inventory turnover efficiency of automobile maintenance spare parts based on different algorithms

Analysis of Figure 6 shows that in the proposed algorithm, the inventory turnover efficiency of spare part is 80% when the safe inventory days of automobile maintenance spare parts are five days; the inventory turnover efficiency of spare part is 90% when the safe inventory days are 20 days; the inventory turnover efficiency of spare part exceeds 90% when the safe inventory days are 30 days, indicating that the average inventory turnover efficiency of spare parts between 80%

and 100%. In the algorithm of reference [6], the inventory turnover efficiency is 60% when the safe inventory days of automobile maintenance spare parts are five days, and it is the lowest. The overall inventory turnover efficiency of spare parts is between 0% and 60%. By comparison, the proposed algorithm has higher inventory turnover efficiency of automobile maintenance spare parts and greatly reduces the storage cost.

5. Conclusions

With the expansion of automobile service business, the scale of automobile service companies has developed fast from several initial regions to national automobile service enterprises. With the intensification of competition in the industry, the selling price of automobiles has gradually become transparent, the price has been declining, and the profit margin of the whole automobile sales of automobile enterprises has gradually decreased. The automotive industry as a whole has gradually paid attention to the automotive after-sales service market, which is the third barrel of gold in the automotive industry. On the other hand, as consumers' rational consumption consciousness gradually strengthens, in order to occupy the market, vehicle manufacturers have to put forward higher requirements on the quality of after-sales service. Maintenance service is an important part of automobile after-sales service, and service spare parts are the material guarantee of maintenance service. In order to supply the service stations all over the country with repair spare parts quickly, the automotive service enterprises have to pay more attention to it. Aiming at the above problems, the inventory of automobile maintenance spare parts and the satisfaction rate of spare parts warehouse are tested respectively, and good experimental results are obtained. The inventory turnover efficiency of automobile maintenance spare parts is further discussed. The experimental results and discussion results verify the effectiveness of the proposed method as a whole, and at the same time improve the control capability of spare parts inventory.

Reference

- [1] Shi, X. Aircraft Maintenance Information Management System Design. *Automation & Instrumentation* 2017, 25(8):47-49.
- [2] Wang, Y. F.; Li, W. Three-phase High-power and Zero-current-switching OBC for Plug-in Electric Vehicles. *Journal of power supply* 2017, 15(2):85-93.
- [3] Lv, R.; Sun, L. F. An overall scheme and a software tool of coordination and control of accessories stock for cloud service platform of industrial chain. *Computer Engineering and Science* 2017, 39(10):1812-1818.
- [4] Ge, H. Y.; Shi, Q.; Xia, W. Research on Simulation of Inventory Optimization Control of Equipment Maintenance Spare Parts. *Computer Simulation* 2017, 34(7):386-390.
- [5] Xu, L.; Li, Q. M.; Li, H.; et al. Optimization of spare parts inventory for multi-level support system under non-preemptive priorities. *Journal of Naval University of Engineering* 2016, 28(2):92-97.
- [6] Zhao, C.; Zhang, H. Research on Optimization and Simulation of Multi-level Inventory of Chain Retail based on System Dynamic. *China Business and Market* 2017, 31(10):73-80.
- [7] Dong, X. J.; Han, W. J. Application Research of Ant Colony Algorithm in Traffic Management. *Journal of China Academy of Electronics and Information Technology* 2016, 11(6):663-666.
- [8] Mo, D. Y.; Tseng, M. M.; Wang, Y. Mass Customizing Spare Parts Support Services Based on Response Time With Inventory Pooling Strategies. *IEEE Transactions on Engineering Management* 2016, 63(3):305-315.
- [9] Li, Y.; Jia, G.; Cheng, Y.; et al. Additive manufacturing technology in spare parts supply chain: a comparative study. *International Journal of Production Research* 2016, 55(5):1498-1515.
- [10] Liao, G. L. Optimal economic production quantity policy for a parallel system with repair, rework, free-repair warranty and maintenance. *International Journal of Production Research* 2016, 54(20):1-16.
- [11] Thorsen, A.; Yao, T. Robust inventory control under demand and lead time uncertainty. *Annals of Operations Research* 2017, 257(1-2):207-236.
- [12] Tao, F.; Fan, T.; Lai, K. K.; et al. Impact of RFID technology on inventory control policy. *Journal of the Operational Research Society* 2016, 68(2):1-14.
- [13] Halman, N.; Klabjan, D.; Mostagir, M.; et al. A Fully Polynomial-Time Approximation Scheme for Single-Item Stochastic Inventory Control with Discrete Demand. *Mathematics of Operations Research* 2016, 34(3):674-685.
- [14] Chen, W.; Dong, M. Joint inventory control across products with supply uncertainty and responsive pricing. *Journal of the Operational Research Society* 2018, 69(8):1215-1226.
- [15] Dighewar A.B. Performance and emission characteristics of diesel engine with egr for various biodiesel blends: a review. *Open Journal of Mechanical Engineering*, 2016, 1(2):1-4.
- [16] Gutierrez-Alcoba, A.; Rossi, R.; Martin-Barragan, B.; et al. A simple heuristic for perishable item inventory control under non-stationary stochastic demand. *International Journal of Production Research* 2017, 55(7):1885-1897.
- [17] Sarkar D.; Deyasi A. Comparative analysis of absorption coefficient for parabolic and gaussian quantum wells for photodetector application. *Advances in Industrial Engineering and Management*, 2016, 2:5.

Design of Path Tracking Control System for UAV Based on Adaptive Preview Method

Yiping Li*

Institute of Railway Locomotive and Vehicle, Wuhan Railway Vocational College of Technology, Wuhan 430000, China

Received OCT 16 2019

Accepted FEB 7 2020

Abstract

Because the simple preview tracking method cannot meet the requirements of UAV dynamic path tracking, a path tracking control system based on adaptive preview is designed. Firstly, the image information collected by the camera is sent through the monitoring module of the system, and the road information, such as obstacles is judged according to the TCP network communication protocol. Then, the corresponding operation instructions are sent to the bottom control module according to the monitoring information, and the image information collected by the camera is sent to the sensor through the monitoring module to build the line to judge the UAV kinematics Sex tracking error model. Finally, the future driving behavior of UAV is analyzed, and the adaptive preview time model is constructed to complete the trajectory tracking of UAV. Experiments show that the system is correct, adaptive preview has obvious advantages, and can accurately control the vehicle tracking the preset path.

© 2020 Jordan Journal of Mechanical and Industrial Engineering. All rights reserved

Keywords: Adaptive preview; Unmanned vehicle; Path; Tracking control; Monitoring; Vehicle kinematics model;

1. Introduction

With the rapid development of China's economy, the scale of automobile production and marketing has shown an explosive growth, which has brought many practical problems: the number of deaths caused by traffic accidents in China is close to 200,000 every year, ranking the first in the world, while causing casualties, but also causing great social and economic losses, most of which are caused by the driver's misjudgment and uncivilized driving. As a result, serious traffic congestion has occurred in major cities in China, and major cities such as Beijing, Shanghai and Hangzhou have begun to limit the total number of cars. In addition, the long-term idling condition of the automobile engine severely reduces the engine's emission performance and causes serious pollution to the atmosphere (Zhang et al. 2017). These problems are not only caused by the lagging construction of traffic facilities, but also related to the unreasonable path planning and immature driving technology of drivers. The increasingly severe traffic problems force the government to strengthen the enforcement of traffic regulations, and at the same time promote the development of unmanned vehicles (Islam et al. 2017).

Unmanned vehicles were first born in the United States. In the early 1980s, the experimental prototype of the Autonomous Land Vehicle, which was funded by the U.S. Department of Defense, was born (Maeng et al. 2017). Limited to the backward sensor technology and control technology at that time, its driving speed was only

4.8 km/h, and it could not run in complex environment. As a technical verification vehicle, it demonstrated the autonomous environment recognition and obstacle avoidance of unmanned vehicle, and achieved the results of stage research (Dan et al. 2016). China's first unmanned vehicle was born in the early 1990s, limited to the technical level at that time, the vehicle still needs human intervention in the process of driving, cannot achieve full autonomous driving, and cannot drive in complex traffic environment (Guo et al. 2017). In 2000, the fourth generation of unmanned vehicle was born in Changsha, which adopted the latest electronic sensor technology at that time. The speed of the new car reached 76 km/h, and the performance of the unmanned vehicle was greatly improved (Ofodile et al. 2016). In 2011, based on the Red Flag car HQ3 of The Chinese FAW group, a new experimental prototype car with unmanned driving system developed by National Defense University of Science and Technology was assembled. The vehicle was tested at Changsha-Wuhan section of Beijing-Zhuhai Expressway. Along the road, it passed through the complicated sections of uphill and downhill, tunnel, wet and slippery road. The vehicle achieved complete autonomous driving in more than 96% of the time. It shows that China has entered the ranks of advanced countries in driverless technology (Tong 2016).

As the name implies, the unmanned vehicle is the vehicle that can perceive the driving environment and perform automatic acceleration, braking, steering, parking and tracking operations, while reaching its destination safely. These operations are based on a variety of on-board sensors and control algorithms (Fresk et al. 2016). In this

* Corresponding author e-mail: yipingemail@sohu.com.

paper, a path tracking control system for unmanned vehicle based on adaptive preview is designed to achieve high-precision path tracking control for unmanned vehicle.

2. Module description of system design

2.1. Design of system hardware

Unmanned vehicle can drive independently. The core of its system structure is “intelligence”. It not only has conventional vehicle functions, such as acceleration, deceleration and steering, but also integrates intelligent monitoring (environment perception), behavior decision-making and path planning, vehicle control and other system functions. It can synthesize environment and self-driving information to achieve similar human driving behavior (Liu et al. 2016). This paper designs the structure of the path tracking control system for unmanned vehicle based on adaptive preview as shown in Figure 1, which is divided into three parts: monitoring module, planning decision module and bottom control module.

The monitoring module transmits the image information collected by the camera and the information of the sensor judging obstacles, roadsides and batteries to the monitoring terminal and the planning decision module through the TCP network communication protocol. The planning decision module transmits the corresponding operation instructions to the bottom control module according to the monitoring information (Xie et al. 2016).

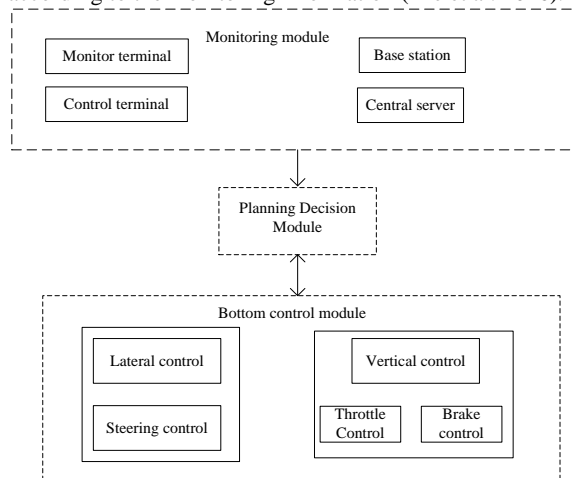


Figure 1. The overall structure of an unmanned vehicle path tracking control system based on adaptive preview

(1) Monitoring module

The module is mainly composed of an unmanned intelligent vehicle (data terminal), a server, a control terminal and a monitoring terminal, using the server and a client mode (Wen 2016). The working principle is that the unmanned vehicle transmits the information of the vehicle to the server through TCP network communication protocol. At the same time, the server transmits the information of the unmanned vehicle through TCP network communication protocol to the monitoring end and the planning decision module. The planning decision module transmits the corresponding operation instructions to the bottom control module according to the information. Figure 2 shows the principle and structure of remote monitoring system.

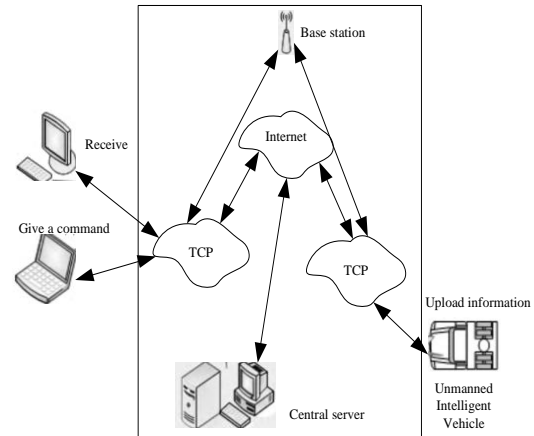


Figure 2. Principle and structure of remote monitoring system

In the remote monitoring module, the information of the unmanned vehicle is mainly positioned by the inertial navigation system (GPS). The encoder on the steering wheel collects the deflection angle of the direction of the vehicle. The camera of the unmanned vehicle collects image information and the information of sensor judging obstacles, road edges and battery (Gang et al. 2018).

(2) Planning decision module

The decision-making and planning module integrates the environment and self-driving information to produce safe and reasonable driving behavior and guide the motion control system to control the vehicle. The sub-module of behavior decision-making is a narrow decision-making module. It reasonably decides the current vehicle behavior according to the information output from the monitoring module, and determines the constraints of trajectory planning according to different behaviors. It guides the trajectory planning module to plan the appropriate path, speed and other information, and sends it to the bottom control module for tracking control. Figure 3 shows the structure of the planning decision module.

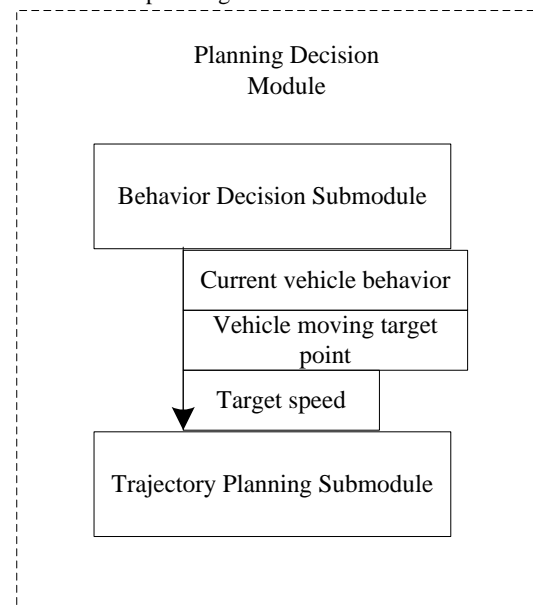


Figure 3. Structural diagram of planning and decision module

(3) Bottom control module

The structure of the underlying control module is shown in Figure 4. The core processor consists of two DSP

boards. Control board 1 is responsible for vehicle steering motor control and steering lane change control (Guo 2017). Control board 2 is responsible for driving motor control, relay control, lamp and horn control (Asl & Yoon 2016). The bottom control module receives the instructions of the planning decision module and controls the vehicle response to ensure the control accuracy and track the target speed and path (Yu et al. 2016).

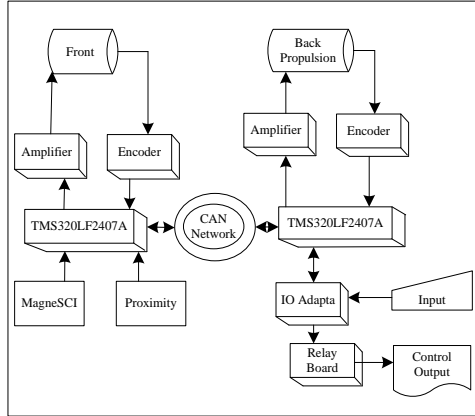


Figure 4. The overall structure of the bottom control module

2.2. Design of system software

2.2.1. Vehicle kinematics model

Firstly, the system software constructs the vehicle kinematics model, and then linearizes the vehicle kinematics model to obtain the linear tracking error model of vehicle kinematics, which can be used to predict the future behavior of the vehicle (Klinger et al. 2017).

(1) Vehicle kinematics model

A vehicle model is defined on the two-dimensional plane of Cartesian world coordinate system. As shown in Figure 5, in order to simplify the design of the controller, this paper assumes that the wheel is in point contact with the ground, and that the contact point is pure rolling without relative sliding. This ideal constraint is essentially a non-holonomic constraint (Baizid et al. 2017).

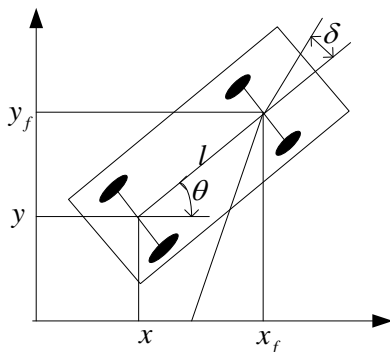


Figure 5. Generalized coordinates of vehicle

Assuming that the vehicle moves only on the plane, the nonholonomic constraint equation of the front and rear wheels is as follows:

$$\dot{x}_f \sin(\theta + \delta) - \dot{y}_f \cos(\theta + \delta) = 0 \tag{1}$$

$$\dot{x} \sin \theta - \dot{y} \cos \theta = 0 \tag{2}$$

where, \dot{x} represents the abscissa of vehicle's rear wheel center in nonholonomic constraint equation; \dot{y} represents the center coordinate of vehicle's rear wheel in nonholonomic constraint equation; x_f represents the center abscissa of the front wheel of a vehicle; y_f represents the longitudinal coordinate of the center of the front wheel of a vehicle; θ represents the yaw angle of the vehicle; δ represents the steering angle of the front wheel of the vehicle.

Many types of kinematics models for wheeled mobile robot can be transformed into Unicycle models. Unmanned vehicle is a typical wheeled mobile robot. The vehicle kinematics model can be written as follows:

$$\begin{bmatrix} \dot{x} \\ \dot{y} \\ \dot{\theta} \end{bmatrix} = \begin{bmatrix} \cos \theta \\ \sin \theta \\ \frac{\tan \delta}{l} \end{bmatrix} v \tag{3}$$

where: l represents the distance between the front wheel center and the rear wheel center; v represents the speed of the rear wheel center of a vehicle.

Vehicle's input variables are defined as $u = \begin{bmatrix} v & \delta \end{bmatrix}^T$, and vehicle's current coordinates are defined as $x = \begin{bmatrix} x & y & \theta \end{bmatrix}^T$.

Formula (3) can also be written as follows:

$$\dot{x} = f(x, u) \tag{4}$$

(2) Error model of vehicle kinematics

Generally speaking, in the problem of trajectory tracking, the method of tracking reference vehicle is generally adopted. The reference trajectory is assumed to be generated by a virtual reference vehicle, and the reference value is expressed by r . Therefore, the reference trajectory of a vehicle can be written as follows:

$$\dot{x}_r = f(x_r, u_r) \tag{5}$$

where, $x_r = \begin{bmatrix} x_r & y_r & \theta_r \end{bmatrix}^T$, $u_r = \begin{bmatrix} v_r & \delta_r \end{bmatrix}^T$.

The right side of Formula (5) is expanded by Taylor around point (x_r, u_r) , and the higher order part is removed to obtain.

$$\dot{x} = f(x_r, u_r) + \left. \frac{\partial f(x, u)}{\partial x} \right|_{\substack{x=x_r \\ u=u_r}} \leq \tag{6}$$

$$(x - x_r) + \left. \frac{\partial f(x, u)}{\partial u} \right|_{\substack{x=x_r \\ u=u_r}} \leq (u - u_r)$$

It can also be written as follows:

$$\dot{x} = f(x_r, u_r) + f_{x,r}(x - x_r) + f_{u,r}(u - u_r) \quad (7)$$

where: $f_{x,r} - f$ is the Jacobian matrix relative to x ;
 $f_{u,r} - f$ is the Jacobian matrix relative to u .

Combining Formula (6) and Formula (7), the error model of vehicle kinematics can be obtained.

$$\dot{\tilde{x}} = f_{x,r}\tilde{x} + f_{u,r}\tilde{u} \quad (8)$$

$$\tilde{x} = x - x_r, \tilde{u} = u - u_r \quad (9)$$

where: \tilde{x} represents the deviation between the current position and the reference position of the vehicle; \tilde{u} represents the deviation of the control variables.

The discrete linear time-varying model of vehicle kinematics is obtained by using Euler method to make discretization of Formula (7):

$$\tilde{x}(k+1) = A(k)\tilde{x}(k) + B(k)\tilde{u}(k) \quad (10)$$

Among them,

$$A(k) = \begin{bmatrix} 1 & 0 & -v_r(k)\sin\theta_r(k)T \\ 0 & 1 & v_r(k)\cos\theta_r(k)T \\ 0 & 0 & v_r(k)\cos\theta_r(k)T \end{bmatrix},$$

$$B(k) = \begin{bmatrix} \cos\theta_r(k)T & 0 \\ \sin\theta_r(k)T & 0 \\ \frac{\tan\delta_r(k)T}{l} & \frac{v_r(k)T}{l\cos^2\delta_r(k)} \end{bmatrix}.$$

k represents the sampling time, T represents the sampling period and A and B are the discrete linear function.

2.2.2. Adaptive preview time model

After linearizing the vehicle kinematics model in the preceding section and obtaining the linear tracking error model of vehicle kinematics to predict the future behavior of vehicle, this paper establishes an adaptive preview time model to realize the path tracking control of unmanned vehicle (Okumus et al. 2017).

(1) Primary planning path

The ‘‘taboo double line shifting’’ experiment stipulated in ISO standard was used for analysis (Bi et al. 2017). At present, the experimental road refers to the ISO/3888 technical report of the double lane-changing driving test procedure and considers the adaptability design when the speed changes (Saska et al. 2017). The schematic diagram of the test route is shown in Figure 6.

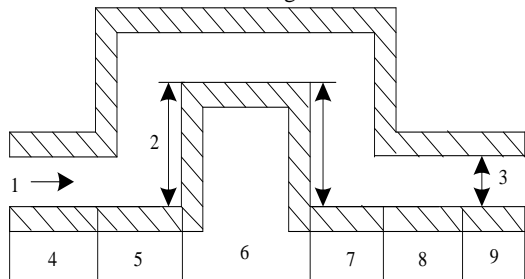


Figure 6. Test Route Diagram

In Figure 6, 1 represents the direction of the vehicle, 2 represents the drift of the lane, 3 represents the width of the road, 4 represents the section 1, 5 represents the section 2, 6 represents the section 3, 7 represents the section 4, 8 represents the section 5, and 9 represents the section 6. The sizes of roads in ISO/3888-1:2016 are shown in Table 1.

Table 1. ISO/3888-1:2016 Path Dimensions

Road section	Length	Lane departure	Road width
1	15	-	1.1 * Vehicle width + 0.25
2	30	-	-
3	25	3.5	1.2 * Vehicle width + 0.25
4	25	-	-
5	15	-	1.3 * Vehicle width + 0.25
6	15	-	1.3 * Vehicle width + 0.25

In this paper, 6-power polynomial is used to design section 2 and section 4. The formula is as follows:

$$f(x) = p_1x^6 + p_2x^5 + p_3x^4 + p_4x^3 + p_5x^2 + p_6x + p_7 \quad (11)$$

This ensures that the curve part and the straight line part are continuously differentiable (Jin et al. 2017).

The schematic diagram of the target path is shown in Figure 7.

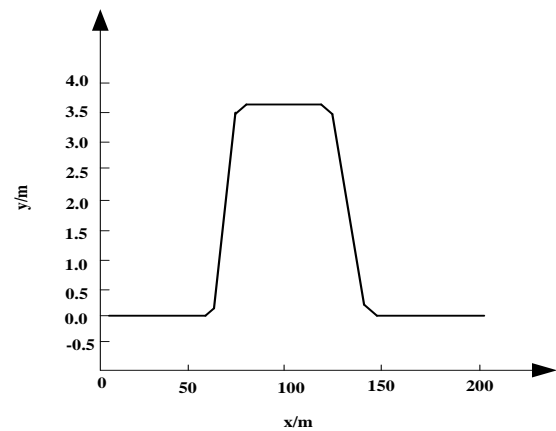


Figure 7. Target path diagram

(2) Optimal model design of fixed preview time

Generally, select a certain preview time value, or manually collect data at different road curves and speeds. This will result in a great waste of time, and there is the possibility of lateral deviation divergence when there is no data collected (Pei et al. 2017). Fixed preview time generally ranges from 0.3 s to 1.5 s. At low speeds, such preview time can meet the requirement of lateral deviation (Ding et al. 2017). When the speed is fast, the same preview time may not meet the boundary conditions of lane width. As shown in Figure 8, the vehicle track effect is better in straight road, the error is larger in bend road, and the maximum lateral deviation can reach 50 m.

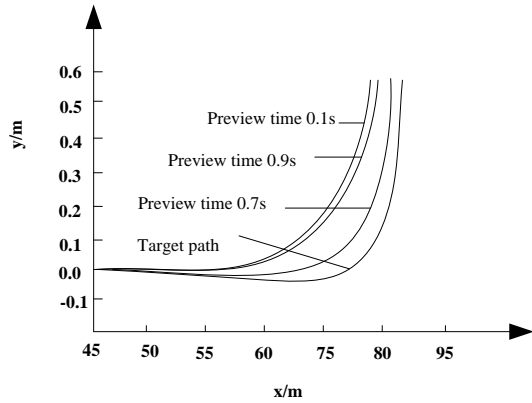


Figure 8. Corresponding trajectories of different preview times

In order to improve the adaptive ability of preview model, the model needs to adopt adaptive preview time.

(3) Adaptive preview time

In the current position of the vehicle, the lateral deviation, heading angle deviation and lateral acceleration of the actual trajectory and the primary planned path within the current traveling time t are calculated according to different preview time t_p . According to these three factors and the estimated preview time t_p , the corresponding optimization function is designed, and the steering control is carried out according to the preview time in time t (Abou donia et al. 2017). The optimization function J_1 of lateral deviation is designed as follows:

$$J_1 = \int_0^t (Y_L - Y_p)^2 dt \tag{12}$$

where, Y_L is a primary planning path, Y_p is a preview path, dt is a derivative function and \int_0^t is a steering control vector. The formula for deviation J_2 of vehicle heading angle is as follows:

$$J_2 = (\psi_L - \psi_p)^2 \tag{13}$$

where, ψ_L is the heading angle of the corresponding points on a primary planning path and ψ_p is the heading angle when it reaches the preview point.

The effect of lateral acceleration on vehicle speed is obvious and widely accepted. From the rollover hazard index, the effect of longitudinal acceleration should also be fully considered in longitudinal control (Chen et al. 2016).

$$J_3 = \int_0^t \left(\frac{a_t}{a_s} \right)^2 dt \tag{14}$$

where, J_3 is the optimization function of vehicle lateral acceleration, a_t is the lateral acceleration vector of unmanned vehicle, and a_s is the standard threshold of the lateral acceleration of unmanned vehicle.

The comprehensive optimization function is as follows:
 $J = \min (w_1 J_1 + w_2 J_2 + w_3 J_3)$ (15)

where, the weight coefficients of each sub-optimal function are w_1 , w_2 and w_3 . The choice of the three factors determines the different driving styles. If the value of w_1 is increased, it means to reduce the lateral deviation; if the value of w_2 is increased, it means to emphasize the consistency of the heading angle of the vehicle and increase the stability of the vehicle; if the value of w_3 is increased, it represents to emphasize the consistency of vehicle heading angles. The appropriate preview time t can be obtained by iterative optimization method. The schematic diagram of adaptive preview time acquisition is shown in Figure 9.

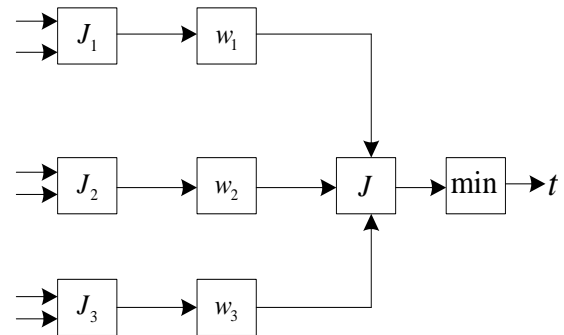
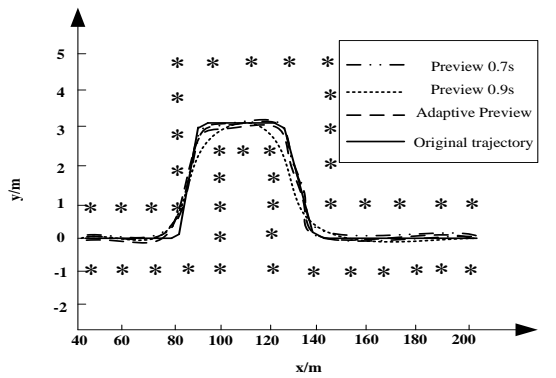


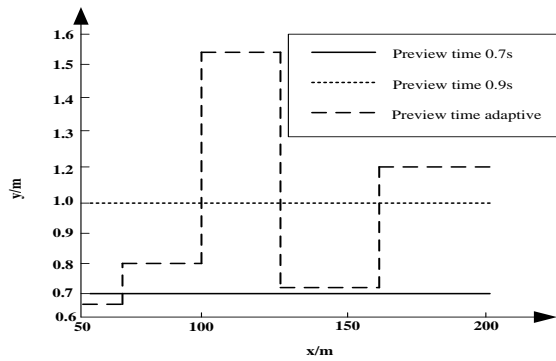
Figure 9. A schematic diagram of adaptive preview time acquisition

3. RESULTS

According to ISO3888-1:2016, double line-shifting experiment is carried out. With no brake and automatic lifting, the peak adhesion coefficient of road surface is 0.8. The simulation experiments at different speeds are carried out with this system. Figure 10 shows the trajectory at 80 km/h. Fixed preview time of 0.9 s, 0.7 s and adaptive preview are adopted respectively.



(a) 80 km/h trajectory

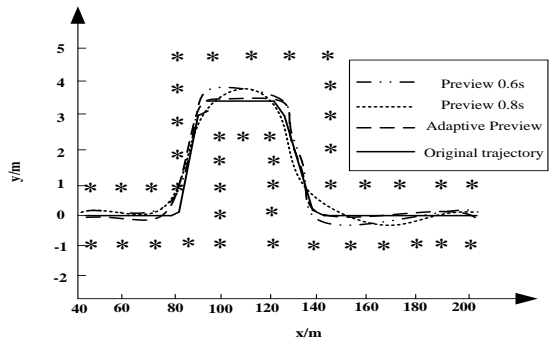


(b) Preview time at 80 km/h

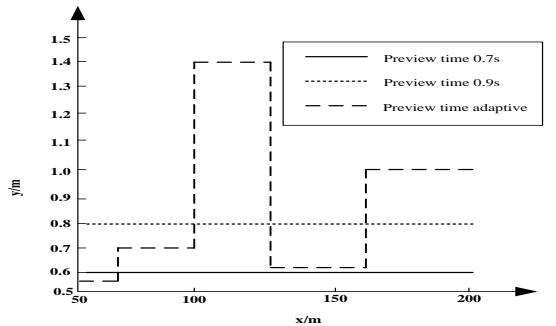
Figure 10. Simulation at 80 km/h

Figure 10 shows that the trajectory deviation is the largest when the preview time is 0.9 s, followed by 0.7 s, and the adaptive preview time is the best when the preview speed is 80 km/h.

Figure 11 is the simulation result at 90 km/h:



(a) Trajectory at 90 km/h

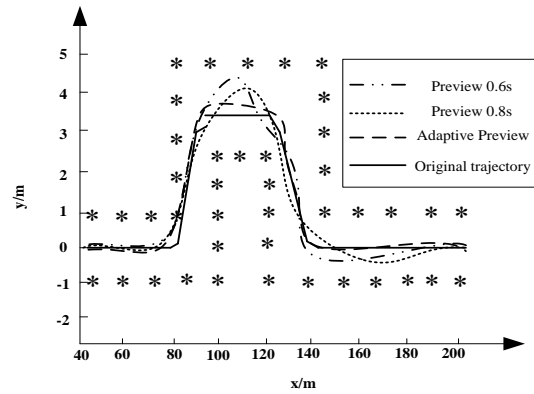


(b) Preview time at 90 km/h

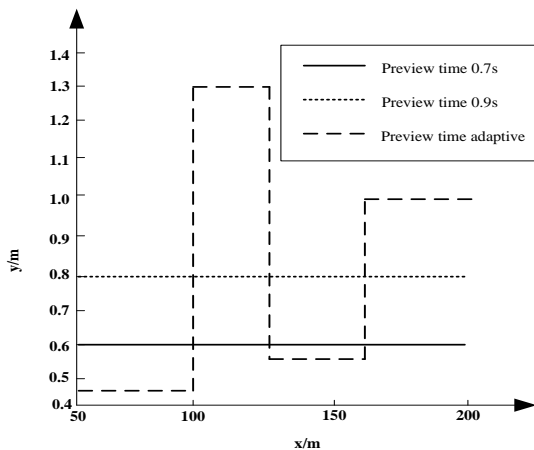
Figure 11. Simulation at 90 km/h

In Figure 11, when using fixed time of 0.6 s to preview, a large lateral deviation occurs at 100 m and a peak value of 0.5 m at 154 m; when using 0.8 s preview time, the error is 0.24 m at 110 m and the peak value of the whole trajectory occurs at 160 m. At this time, the error is 0.5 m. With the prolongation of preview time, the adjustment time after the end of the bend is prolonged correspondingly. When adapting to preview time, the lateral error can be guaranteed within 0.2 m, and the adjustment time is the shortest. The lateral error has been controlled within 0.1 m at 146 m.

Figure 12 shows the simulation results at 100 km/h:



(a) Trajectory at 100 km/h



(b) Preview time at 100 km/h

Figure 12. Simulation at 100 km/h

In Figure 12, it is obvious that the closer the speed is to the limit condition, the more obvious the advantage of adaptive preview is. The maximum error of 0.6 s preview time is 1.0 m. If the width of the vehicle is taken into account at this time, the vehicle has deviated from the road in Section 3 of double-shift line, and is close to the road edge in 0.8 s preview time, and the performance of adaptive preview time is the best. This is because the fixed preview time is equivalent to not considering the current speed and road attribute characteristics in front, and it always keeps a fixed visual angle in front, which obviously cannot adapt to the changing road conditions. Adaptive preview can make corresponding judgments according to the current vehicle speed and road characteristics ahead, and accurately track the preset path. Therefore, it can achieve better results than fixed preview time.

Figure 13 shows the path tracking using the designed system in this paper:

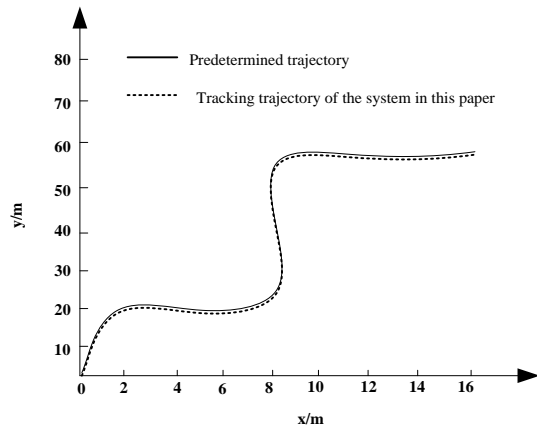


Figure 13. Path tracking of the system in this paper

The analysis of Figure 13 shows that the tracking trajectory of the unmanned vehicle is almost the same as the experimental predetermined trajectory, and the deviation is not greater than 1 m when the system is used to control the unmanned vehicle to track under the setting of adaptive preview. It shows that the tracking control accuracy of the system in this paper is high.

4. DISCUSSION

Based on the research content of this paper, the challenges faced by the future development of unmanned vehicles are discussed. Unmanned vehicle is a new thing which integrates multi-disciplines organically. Its development is a process of continuous exploration and gradual progress. There are still many challenges for real batch road operation. It is not only the maturity of technology, but also the social problems such as license, liability determination, insurance and so on. The first step to solve the problem is to acknowledge the existence of the problem, rather than to hide one's troubles and take no remedial measures. The difficulties and challenges faced by unmanned vehicles mainly include the following aspects.

(1) Safety and reliability. Safety and reliability are always the barriers that cannot be bypassed in the promotion of unmanned vehicles. The self-safety of unmanned vehicle mainly includes hardware security, software security and network security. If we recognize the concept of active safety and passive safety, the safety of unmanned vehicles is more related to active safety. Firstly, there is a risk of failure of the environmental sensor of the unmanned vehicle. Vehicle-borne high-definition camera based on the principle of visible light reflection is vulnerable to strong light interference, which makes it impossible to obtain real and clear images; ultrasonic probe based on the principle of ultrasonic reflection is vulnerable to noise and the influence of ultrasonic adsorbent material, which makes it impossible to accurately measure the distance of obstacles; millimeter-wave radar based on the principle of electromagnetic reflection may also suffer noise and deception attack under the support of specific equipment; 64-line laser rangefinder with the highest accuracy attenuates sharply in severe weather such as heavy rain and fog, which seriously affects the accuracy of three-dimensional map generation. Secondly, unmanned algorithms do not allow security vulnerabilities, which requires a lot of test data. At present,

only Google has conducted seven years of closed testing, while the testing time of other manufacturers is much shorter. It is irresponsible to promote the application of unmanned driving algorithm without long-term practical verification. Finally, the access of unmanned vehicles to the Internet is bound to face network security problems. In the absence of reliable firewall strategies, network hackers can invade the core brain of unmanned vehicles through the Internet, tamper with code to remotely control unmanned vehicles, maliciously manipulate steering or braking systems, and create targeted safety incidents.

(2) The imperfection of technical evaluation standard system. How to evaluate the technical indicators of Intelligent Network Unified Vehicle needs to formulate corresponding technical standards to measure. The technical standards must be based on a large number of experimental data. China clearly divides the development stage of Intelligent Network Unified Vehicle into five stages. The technical requirements of different stages are different, and the technical parameters are different. At present, the technical standard system of Intelligent Network Unified Vehicle in China is not perfect, which cannot provide evaluation basis for different stages of Intelligent Network Unified Vehicle, especially the maturity of high-level unmanned driving technology cannot be defined and judged.

5. CONCLUSIONS

This paper designs a path tracking control system for unmanned vehicle based on adaptive preview. The system consists of monitoring module, planning decision module and bottom control module, which can realize the three functions of monitoring, decision-making and control of unmanned vehicle. The system software linearizes the vehicle kinematics model, obtains the linear tracking error model of vehicle kinematics to predict the future behavior of the vehicle, and constructs the adaptive preview time model to complete the trajectory tracking of the unmanned vehicle. After applying this system to actual operation, the tracking deviation is less than 1 m, and the effect is ideal. The adaptive preview system in this paper can make corresponding judgment according to the current vehicle speed and road characteristics in front, and accurately track the preset path, which can meet the requirements of trajectory tracking control of unmanned vehicles.

Based on the research content of this paper, the following suggestions are put forward for the future development challenges of unmanned vehicles:

(1) To reduce the application cost on the basis of guaranteeing performance. Unmanned vehicle is a sunrise industry, which will drive the development of a large number of related industries, such as sensors, cameras, vehicle-borne radar, high-precision positioning and navigation system, wireless communication network system, vehicle-borne processors, and man-machine interactive system, etc. At the same time, it will also bring many conveniences to the development of human and society, such as greatly reducing traffic accidents caused by human factors, carbon emissions, and road congestion, sharing traffic resources and improving travel efficiency. The economic and social benefits brought by the unmanned vehicle industry are considerable, but the application cost at this stage is unacceptable, and it has become a roadblock to promote the road. In view of this problem, it is suggested to draw lessons from the mature experience of the promotion of new energy vehicles:

firstly, a demonstration park is established to gradually radiate the promotion point-to-area, and reduce costs by increasing the number of applications; secondly, targeted financial subsidies, etc. are carried out, and after the technology matures, the industry is stimulated to actively reduce manufacturing costs by subsidizing the mechanism of slope reduction.

(2) To strengthen the research of networking technology among people, vehicles, roads and backgrounds. Network is a platform for integrating social information and resources. The development of unmanned vehicles in the future cannot be separated from the progress of network technology. Many real-time information related to unmanned driving needs to be obtained from Internet platform, such as the accuracy of GPS positioning system, the smooth condition of roads and bridges, the weather condition, the change of driving destination, etc. The quality of the network and the real-time nature of the network information determine whether the unmanned vehicle can advance according to the set destination. In addition, OTA (Over-the-air, air download) is the future trend of the development of the upgraded vehicle program for unmanned vehicles. Owners need not go to 4S stores to complete the upgrade of the unmanned system, so as to obtain the latest driving experience. The upgrade of OTA system also needs the support of high-speed network. Improving the download speed, coverage and signal stability of the network is another important precondition for the promotion of unmanned vehicles. At the same time, it is necessary to strengthen the research of network security technology to reduce the risk of hackers intruding into the network of unmanned vehicles.

REFERENCES

- [1] Aboudonia, A., El-Badawy, A. & Rashad, R. 2017. Active Anti-Disturbance Control of a Quadrotor Unmanned Aerial Vehicle Using the Command-Filtering Backstepping Approach. *Nonlinear Dynamics* 90(9): 1-17.
- [2] Asl, H.J. and Yoon, J. 2016. Robust Image-Based Control of the Quadrotor Unmanned Aerial Vehicle. *Nonlinear Dynamics* 85(3): 2035-2048.
- [3] Baizid, K., Giglio, G. & Trujillo, M.A. 2017. Behavioral Control of Unmanned Aerial Vehicle Manipulator Systems. *Autonomous Robots* 41(5): 1203-1220.
- [4] Bi, H., Zheng, W. & Ren, Z. 2017. Using an Unmanned Aerial Vehicle for Topography Mapping of the Fault Zone Based on Structure from Motion Photogrammetry. *International Journal of Remote Sensing* 38(8-10): 2495-2510.
- [5] Chen, F., Wen, L. & Zhang, K. 2016. A Novel Nonlinear Resilient Control for a Quadrotor UAV via Backstepping Control and Nonlinear Disturbance Observer. *Nonlinear Dynamics* 85(2): 1281-1295.
- [6] Dan, L., Duan, J. & Hui, S. 2016. A Strong Tracking Square Root Central Difference FastSLAM for Unmanned Intelligent Vehicle with Adaptive Partial Systematic Resampling. *IEEE Transactions on Intelligent Transportation Systems* 17(11): 3110-3120.
- [7] Ding, W., Ding, W. & Ding, W. 2017. Multi-Sensor Based on High-Precision Direct Georeferencing of Medium-Altitude Unmanned Aerial Vehicle Images. *International Journal of Remote Sensing* 38(8-10): 2577-2602.
- [8] Fresk, E., Nikolakopoulos, G. & Gustafsson, T. 2016. A Generalized Reduced-Complexity Inertial Navigation System for Unmanned Aerial Vehicles. *IEEE Transactions on Control Systems Technology* 25(1): 192-207.
- [9] Gang, B.G. & Kwon, S. 2018. Design of an Energy Management Technology for High Endurance Unmanned Aerial Vehicles Powered by Fuel and Solar Cell Systems. *International Journal of Hydrogen Energy* 43(20): 9787-9796.
- [10] Guo, J., Luo, Y. & Li, K. 2017. Adaptive Neural-Network Sliding Mode Cascade Architecture of Longitudinal Tracking Control for Unmanned Vehicles. *Nonlinear Dynamics* 87(4): 2497-2510.
- [11] Guo, K. 2017. Research and Design of Remote Monitoring of Communication Power Supply Based on Web. *Chinese Journal of Power Sources* 41(4): 633-634.
- [12] Islam, S., Liu, P.X. & Saddik, A.E. 2017. Observer-Based Adaptive Output Feedback Control for Miniature Aerial Vehicle. *IEEE Transactions on Industrial Electronics* (99): 1-1.
- [13] Jin, H., Sun, Y.H. & Wang, M.Y. 2017. Juvenile Tree Classification Based on Hyperspectral Image Acquired from an Unmanned Aerial Vehicle. *International Journal of Remote Sensing* 38(8-10): 2273-2295.
- [14] Klinger, W.B., Bertaska, I.R. & Ellenrieder, K.D.V. 2017. Control of an Unmanned Surface Vehicle With Uncertain Displacement and Drag. *IEEE Journal of Oceanic Engineering* 42(2): 458-476.
- [15] Liu, J.D., Zhang, J.C. & Li, H.N. 2016. A Novel Strategy of Neutral Point Potential Balancing for T-NPC Three-level Three-phase Four-leg Inverters. *Journal of Power Supply* 14(1): 68-73.
- [16] Maeng, S.J., Park, H.I. & Yong, S.C. 2017. Preamble Design Technology for GMSK-Based Beamforming System with Multiple Unmanned Aircraft Vehicles. *IEEE Transactions on Vehicular Technology* 66(8): 7098-7113.
- [17] Ofodile, N.A. & Turner, M.C. 2016. Decentralized Approaches to Antiwindup Design With Application to Quadrotor Unmanned Aerial Vehicles. *IEEE Transactions on Control Systems Technology* 24(6): 1980-1992.
- [18] Okumus, E., San, F.G.B. & Okur, O. 2017. Development of Boron-Based Hydrogen and Fuel Cell System for Small Unmanned Aerial Vehicle. *International Journal of Hydrogen Energy* 42(4): 2691-2697.
- [19] Pei, Y., Liu, B. & Hua, Q. 2017. An Aeromagnetic Survey System Based on an Unmanned Autonomous Helicopter: Development, Experiment, and Analysis. *International Journal of Remote Sensing* 38(8-10): 3068-3083.
- [20] Saska, M., Baca, T. & Thomas, J. 2017. System for Deployment of Groups of Unmanned Micro Aerial Vehicles in GPS-denied Environments Using Onboard Visual Relative Localization. *Autonomous Robots* 41(4): 1-26.
- [21] Tong, Y. 2016. The Exploration and Research of Software Development Architecture Based on ASP. NET MVC Pattern. *Journal of China Academy of Electronics and Information Technology* 11(6): 599-602.
- [22] Wen, W.H. 2016. Application of Artificial Intelligence Technology in Mechanical and Electronic Engineering. *Automation & Instrumentation* (2): 96-97.
- [23] Xie, H. & Lynch, A.F. 2016. State Transformation-Based Dynamic Visual Servoing for an Unmanned Aerial Vehicle. *International Journal of Control* 89(5): 892-908.
- [24] Yu, M.J., Li, X. & Lv, F. 2016. Design of Hardware-in-Loop Simulation System for Radio Frequency Target Tracking. *Computer Simulation* 33(5): 100-104.
- [25] Zhang, D., Chen, Z. & Xi, L. 2017. Transitional Flight of Tail-Sitter Unmanned Aerial Vehicle Based on Multiple-Model Adaptive Control. *Journal of Aircraft* 55(9): 1-6.

Optimization of Clutchless AMT Shift Control Strategy for Electric Vehicles

Jingpu Li, Pengcheng Sheng^{*}, Kaikai Shao

Automotive Engineering Department, Xingtai Polytechnic College, Xingtai 054000, China

Received OCT 16 2019

Accepted FEB 9 2020

Abstract

With the development of the economy, the number of cars in China is rapidly expanding, which has caused a certain degree of pollution to the environment. The emergence of electric vehicles has the good evasive effect on this issue. In order to shorten the shifting time of the electric clutchless automatic mechanical transmission (AMT) and reduce the shifting shock, the DC brushless drive motor, the clutchless and synchronizer-free AMT and the final drive are combined to establish the electric vehicle power transmission model of the drive motor and AMT controlled by the power transmission integrated controller. And the dynamic analysis of the picking phase, the shift process, and the torque reduction and torque recovery phases are carried out. Based on the dynamics of the shifting process, the implementation flow of the coordinated control of the shifting process is created. The classical PD control algorithm is used to optimize its control strategy and realize the optimal shift control of the clutchless AMT of electric vehicles. The experimental results show that the electric vehicle with the shift control strategy has a shifting time of 720 ms-750 ms in the static, low speed, medium speed and high speed state, and the impact degree is inside $\pm 10 \text{ m}\cdot\text{s}^{-3}$ during the shifting process. This shows that the electric vehicle using the proposed shift control strategy has less time for shifting, high shifting quality, and smooth shifting process.

© 2020 Jordan Journal of Mechanical and Industrial Engineering. All rights reserved

Keywords: Electric vehicle; Clutchless; AMT; Shift control; Strategy; Optimization.

1. Introduction

In the face of increasingly severe energy and environmental problems, more and more countries regard the development of new energy vehicles as a national development strategy (Yang et al. 2017a). Under the trend of the country to vigorously develop green, energy-saving and environmentally friendly new energy vehicles, the in-depth study of the integrated drive technology of pure electric vehicle power system and the coordinated control of automatic shifting, and the development of automotive electric drive system are conducive to China's environmental protection and energy security. This provides the basis for the sustainable development of people, resources and the environment in the automotive industry.

The automated mechanical transmission (AMT) has the simple structure, low cost, and high transmission efficiency. It has the good application prospect in electric vehicles (Yang et al. 2017b). However, the shifting process relies on the sliding friction of the synchronizing ring, so the noise impact is large and the shifting time is long, which seriously affects the smoothness and ride comfort of the vehicle shifting and limits its application (Kang et al. 2017). In order to improve the efficiency of the electric

drive system and meet the power requirements, the drive motor of the pure electric vehicle or the series hybrid electric vehicle usually matches the transmission (Wang et al. 2016a). Compared to automatic transmission (AT), continuously variable transmission (CVT) and dual clutch transmission (DCT), electronically controlled electric AMT does not require hydraulic or pneumatic power (Ren et al. 2017). AMT also has many shortcomings, such as the wear of the clutch friction disc, the power interruption during shifting, the contradiction between shifting time and shifting shock, but these problems do not affect its application performance on electric vehicles. Domestic and foreign scholars have done a lot of research on this (Zhou et al. 2016). Existing research can be divided into three categories depending on the structure of the AMT. In order to reduce the shift shock, the first type retains both the traditional AMT clutch and the synchronizer. Scholars have studied the two-speed rear mechanical automatic transmission (I-AMT). Through the feedback control of the clutch and the motor, shifting without power interruption is achieved (Su et al. 2016). In the I-AMT, the dry clutch is placed behind the AMT to eliminate power interruptions, but it inevitably causes energy loss (Izadkhast et al. 2016). In order to reduce the friction loss of the clutch, the control method of the jaw clutch is proposed. There is less research on the use of a synchronizer AMT for the pure

* Corresponding author e-mail: spcamt18@163.com.

electric vehicle because the AMT of this structure is complicated in structure and control, and it is not easy to achieve good results (Pelletier et al. 2016). The second type of study retained the synchronizer of the traditional AMT, but the clutch is removed. The reasons are: 1. the motor has the characteristics of low speed and large torque, so the vehicle can be started directly by the motor drive. 2. The motor can be quickly switched between torque mode, free mode and speed mode to meet the shifting requirements. 3. Eliminating the clutch helps increase efficiency and reduces the weight and cost of the electric car. 4. The shifting power interruption caused by canceling the clutch can be compensated by shortening the shifting time (Hu et al. 2016a). The clutch is eliminated and the coordinated control of the drive motor and the shifting motor in the shifting process control becomes very important (Sarker et al. 2016). There are many studies on AMTs without clutches and synchronizers. Scholars have explored the feasibility of clutchless AMT for electric vehicle applications and proposed corresponding control methods. In order to shorten the synchronization time of the synchronizer and improve the service life of the synchronizer, scholars have proposed the constraint control method for the lock loop synchronizer. To improve the life of the synchronizer, the scholars designed the multivariable robust H-negative controller to evaluate the effect of closed-loop control based on noise and disturbance (Hannan et al. 2017). In order to improve the composite optimal control strategy for electric vehicle transmissions, a powertrain test rig including a high-performance electric dynamometer is established. The linear secondary regulator is used to actively compensate the torque of the driving motor, and the nonlinear time optimal control is used to track the execution Rotor position. The proposed control strategy can analyze the shift process and effectively improve the shift quality (CHAI Benben et al. 2018).

The control method of the drive motor in the shift process control is proposed by coordinating the control of the drive motor and the shifting motor to improve the shifting effect. These studies have proved that it is feasible to cancel the clutch in AMT, but the feasibility of canceling the synchronizer has not been further studied. In the third type of study, the synchronizer in the AMT was cancelled. Because the target gear is directly connected to the motor after the clutch is removed, the clutch is connected to the vehicle through the output shaft. The inertia of these two parts is relatively large. If AMT relies on the synchronizer to complete the synchronization, the synchronization time is longer and the synchronizer wears out faster (Moon & Moon 2016). The shifting of the clutchless, synchronizer-free AMT requires the drive motor to have precise and fast speed regulation. At present, there are few studies on the control of the AMT shifting process of the clutchless synchronizer in pure electric vehicles. The existing research proves the feasibility of clutchless and synchronizer-free AMT, and proposes corresponding control strategies. However, the shifting time of the clutchless synchronizer AMT is relatively long compared to other types of transmissions. How to shorten the shift time under the premise of ensuring a small impact is still worth studying. In this paper, the optimization of the shift control strategy for the clutchless AMT of electric

vehicles is studied. These include the synchronous control of the speed of the drive motor before the gear shift, the control of the shift actuator and the coordinated control of the two to shorten the shift time and improve the vehicle dynamics.

2. MATERIALS AND METHODS

2.1. Power transmission model of electric vehicle

The electric vehicle power transmission system studied in this paper adopts the combination of DC brushless drive motor, AMT without clutch and synchronizer, and main decelerator. The drive motor and AMT are controlled by the power transmission integrated controller (Hu et al. 2016b). The biggest advantage of the integrated controller is that it uses a control core, which saves the communication time between the drive motor controller and the AMT controller, thus shortening the shift time. The structure of the power transmission system is schematically shown in Figure 1.

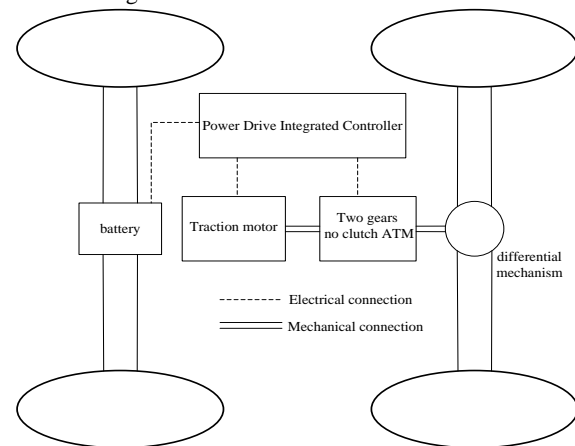


Figure 1. Structure diagram of power transmission system

The composition of the power transmission integrated controller of the pure electric vehicle is shown in Figure 2. The integrated controller calculates the appropriate target gear according to the accelerator pedal position, brake signal and vehicle speed, and completes the shift by coordinating the control of the drive motor and the shifting motor (Wang et al. 2016b). In the shifting process, the drive motor needs to perform multiple mode switching, and adjust the speed and torque in time to ensure that the shifting is smooth.

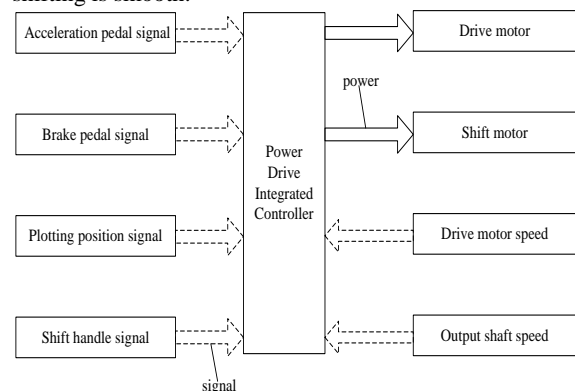


Figure 2. Integrated controller of electric vehicle power drive

2.2. Dynamic analysis of the shifting process

Figure 3 is the schematic diagram of the structure of the AMT. The shift actuator is a motor-drive mechanism that does not require hydraulic power, which improves the efficiency of the AMT. Figure 4 shows the dynamics of the entire vehicle transmission system.

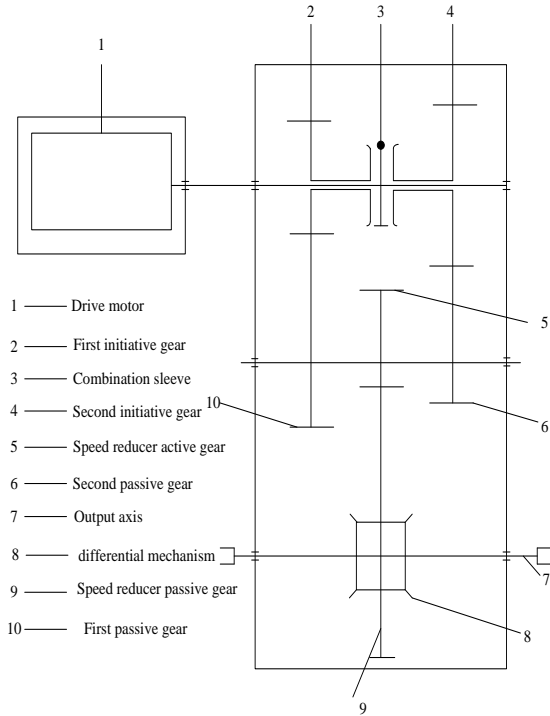


Figure 3. AMT structure diagram

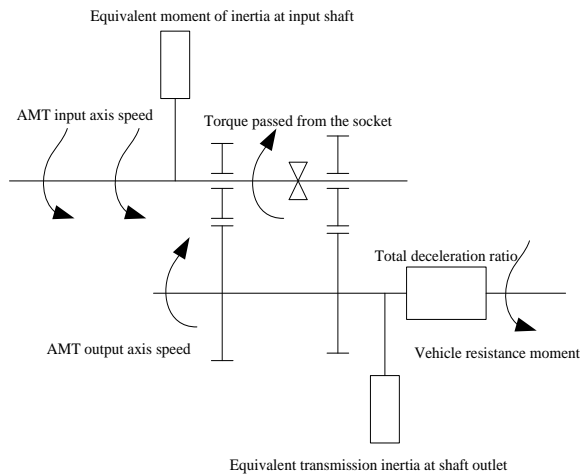


Figure 4. Dynamic model of vehicle transmission system

2.2.1. Force analysis during the picking stage

During the picking phase, the force analysis of the meshing teeth is shown in Figure 5.

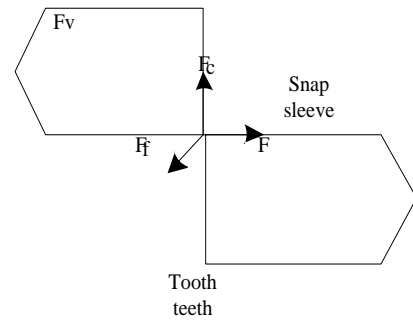


Figure 5. Stress analysis of meshing teeth in extraction stage

When picking up the gear, the resistance F mainly comes from the friction F_f between the engaging ring gear and the joint sleeve. The expression is

$$F_f = \mu F_v = \mu T_c / R \quad (1)$$

where μ is the tooth surface friction factor; F_v is the contact surface positive pressure; T_c is the torque transmitted by the joint sleeve; R is the joint sleeve indexing circle radius.

The torque T_c transmitted by the sleeve is:

$$\begin{cases} T_c = (T_m - J_m \alpha_m - c_{in} \omega_m) i_g \\ T_v = (T_c - J_v \alpha_{out} - c_{out} \omega_{out}) i_0 \end{cases} \quad (2)$$

where T_m is the traction motor torque; J_m is the equivalent moment of inertia of the AMT input; ω_m is the angular velocity of the input shaft. c_{in} is the rotational damping coefficient of the input shaft; i_g is the current gear ratio; T_v is the equivalent resistance torque of the whole vehicle. J_v is the equivalent moment of inertia of the AMT output; ω_{out} is the angular velocity of the AMT output shaft; c_{out} is the rotational damping coefficient of the output shaft; i_0 is the main reduction ratio.

When AMT is not in neutral, ω_m and ω_{out} satisfy the following equation:

$$\omega_m = i_g \omega_{out} \quad (3)$$

From the Equations (1), (2) and (3):

$$F = \frac{\mu (i_g i_0 J_v T_m + i_g^2 J_m T_v)}{R (i_0 i_g^2 J_m + i_0 J_v)} \quad (4)$$

In the Equation (2), c_{in} and c_{out} are relatively small, and they are ignored in the derivation of the Equation (4).

When the actual output torque T_m of the motor is 0, F_f is the smallest, and the pick is the lightest. Therefore, it is necessary to reduce the output torque T_m of the drive

motor to 0 before the lift, that is, to switch the drive motor from the torque mode to the free mode.

2.2.2. Force analysis of the gear shift process

In the gear stage, the force analysis of the meshing teeth is shown in Figure 6, and in Figure 6, F_h is the longitudinal force of the contact surface.

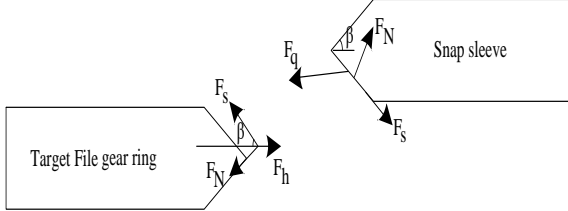


Figure 6. Stress analysis of meshing teeth when hanging

At the beginning of the gear, the engaging teeth are in contact with the end of the target gear, and the resistance F_q of the fork is as follows.

$$F_q = F_N \sin(\beta) + F_s \cos(\beta) \quad (5)$$

where F_N is the contact surface positive pressure; β is the tooth end chamfer angle; F_s is the contact surface friction.

F_N and F_s meet the following equation:

$$\begin{cases} F_s = \mu_2 F_N \\ F_c + F_s \sin(\beta) = F_N \cos(\beta) \end{cases} \quad (6)$$

$$F_c = T_c / R \quad (7)$$

where μ_2 is the frictional contact coefficient of the tooth end contact surface; F_c is the force transmitted by the joint sleeve.

From (5), (6) and (7):

$$F_q = \frac{T_c [\sin(\beta) + \mu_2 \cos(\beta)]}{R [\cos(\beta) - \mu_2 \sin(\beta)]} \quad (8)$$

In order to ensure that the target gear is successfully engaged, the resistance F_q of the fork is as small as possible, that is, T_c is as small as possible. It can be seen from Equation (2) that T_c depends on the output torque T_m of the drive motor and the difference in rotational speed between the sleeve and the engagement ring gear. The smaller the speed difference and T_m are, the smaller the T_c is. Therefore, when the gear is engaged, the drive motor should stop the torque output and control the difference in rotational speed between the clutch sleeve and the engagement ring gear as small as possible.

According to the above description, that is, the clutch output torque at the synchronization point is driven by the friction torque. The transition to static friction torque is prone to sudden changes in torque. This results in a large longitudinal impact of the vehicle and affects the smooth start.

2.2.3. Dynamics analysis of the torque reduction and recovery phases

From the force analysis in the picking stage, it can be seen that the drive motor should be switched from the torque mode to the free mode before the picking. After the gear is completed, the drive motor needs to be restored from free mode to torque mode. Switching between torque mode and free mode should establish appropriate control strategies to avoid large shocks.

The impact j of a pure electric vehicle can be expressed as:

$$j = \frac{da}{dt} = \frac{d^2 u_a}{dt^2} \quad (9)$$

where a is the acceleration; u_a is the vehicle speed. The longitudinal acceleration of the vehicle is

$$a = \frac{T_m i_g i_0 \eta_T - T_V}{\delta m r} \quad (10)$$

where η_T is the transmission efficiency; δ is the rotation mass conversion factor; m is the vehicle mass; r is the wheel radius.

From (9) and (10):

$$j = \frac{1}{\delta m r} \frac{d(T_m i_g i_0 \eta_T - T_V)}{dt} \quad (11)$$

Since the shifting time is very short, it can be assumed that the running resistance torque of the vehicle remains unchanged during the shifting process, and then Equation (11) can be simplified as:

$$j = \frac{i_g i_0 \eta_T}{\delta m r} \frac{dT_m}{dt} \quad (12)$$

It can be known from Equation (12) that the impact degree of the pure electric vehicle is proportional to the first derivative of the motor output torque. The more intense the output torque of the motor changes, the greater the impact will be. The impact is inversely proportional to the height of the AMT gear. In order to ensure that the impact of the torque reduction and recovery phases is as small as possible, sudden changes in the motor output torque should be avoided. In the low gear, the motor torque drops and the recovery rate should be less than that in the high gear.

2.3. Optimizing the control method of the shifting process

2.3.1. Shift coordination control

During the shifting process of the electric vehicle, a series of dynamic changes have occurred in the transmission system, such as the alternation of the motor load condition and the no-load condition, and the transmission gear shift. For the clutchless AMT electric drive system, the key to shifting is the coordinated control of the drive motor, transmission and shift actuator.

According to the specific control method in the automatic shifting process, the shifting process can be divided into three stages: unloading, synchronous gearing and loading.

During the driving process of the car, the integrated controller continuously collects the driving status information of the car. Combined with the driver's operating intention, the shifting module analyzes and judges that when the shifting condition is reached, the integrated controller issues the shift signal, and the control system enters the shifting process.

In the unloading phase, the motor controller controls the drive motor to operate in the torque mode to unload the drive motor. When the output torque of the motor to be driven reaches the unloading target torque TE1*, the motor controller controls the driving motor to be switched from the torque mode to the free mode, so that the shifting actuator performs the lifting operation without any impact under the condition of no load. In the synchronous gearing phase, the motor controller controls the drive motor to switch from free mode to speed mode. The drive motor is regulated to reduce the difference in rotational speed between the main and driven parts of the synchronizer. When the driving motor speed reaches the target speed n*, the motor controller controls the driving motor to switch from the speed mode to the free mode, so that the shifting actuator completes the gearing operation smoothly and without impact under no load conditions. During the loading drive phase, the motor controller controls the drive motor to switch from free mode to torque mode. The output torque of the drive motor is loaded to the target torque TE2* required by the power system. At this time, the shift actuator is maintained at the current position, the vehicle is normally driven according to the driver's operation intention, and the entire shifting process ends. Based on the dynamics of the shifting process, the coordinated control implementation process of the shifting process is shown in Figure 7.

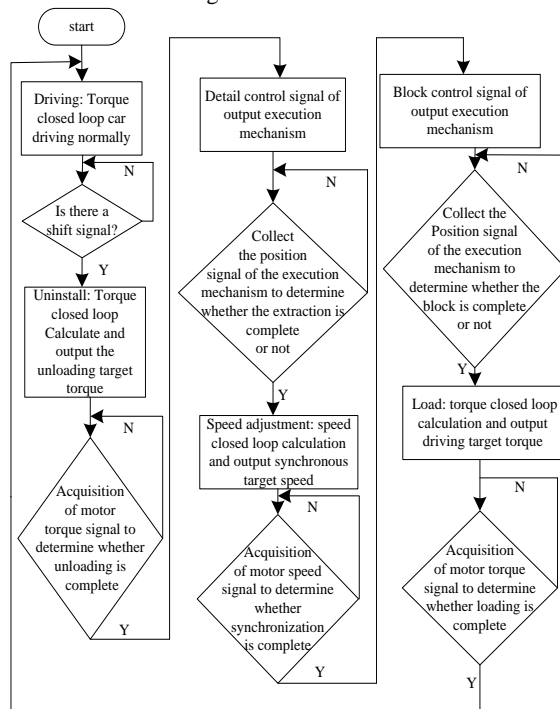


Figure 7. Coordinated control flow of gear shifting process

Analysis of the shifting process shows that the shifting coordinated control system compensates for the effect of clutchless in the power transmission system by accurately controlling the speed and torque of the drive motor, and smoothly completes the shifting. Therefore, in the entire shift coordination control system, the control of the drive motor is extremely important. The adjustment level of motor speed and torque determines the speed and smoothness of the shifting process. Therefore, on the basis of the integrated electric drive of the motor-transmission, the corresponding control strategy is established for the speed and torque of the drive motor at each stage, and the reliability of the system automatic shift coordination

control strategy and the shift quality of the whole vehicle are improved.

2.3.2. Optimization of shift control strategy

In the automatic shifting process of AMT without clutch, for the adjustment of the output characteristics of the drive motors in each stage, when the normal driving, unloading and loading phases of the vehicle are the torque adjustment of the motor, the speed adjustment is in the synchronization phase.

In the whole shifting process, not only the torque and the rotational speed of the drive motor are precisely adjusted, but also the drive motor needs to be switched between the torque adjustment and the rotational speed adjustment. The entire control link is automatically coordinated by the integrated controller. The output characteristics of the drive motor are temporarily not controlled by the accelerator pedal.

The shifting process of the electric vehicle AMT without clutch is realized by using the working mode of the electric vehicle power motor and the control shifting actuator. There are three main types of actuators, namely, electronically controlled hydraulic, electronically controlled pneumatic and electronically controlled. The electric control electric type is selected as the DC motor drive of the electric vehicle. This type of DC motor drive uses the master chip to generate PWM to control the speed and matrix of the motor. It can use the sensor to adjust the PWM wave according to the position change of the shift selector to control this.

The shifting quality of the clutchless two-speed AMT system is to change the transmission ratio of the transmission to meet the purpose of changing the transmission speed and torque of the vehicle. The evaluation of its quality mainly depends on two aspects. One is the time to shift gears. How to achieve fast and smooth shifting needs to take into account the ECU operating rate, actuator response, shifting speed, coordinated control of the power motor and the efficiency of the transmission. The second is the impact of shifting. The vehicle's longitudinal acceleration rate of change can be used to identify it.

First, the maximum change rate $(dT / dt)_{max}$ of the power motor matrix needs to be confirmed. When the real-time rate of change is less than this premise, its state value is reduced to 0, which can switch between the torque mode and the free mode. In the speed regulation of the power motor, if n_1 is the target speed value after the speed regulation, n_2 is the mechanical automatic transmission intermediate shaft speed, and Δn is the speed correction amount, then the following equation can be given.

$$n_1 = i_g n_2 + \Delta n \tag{13}$$

Since the speed before and after synchronization are increased, correction is required. It is found that adjusting the value of the axial force change rate can achieve the effect of reducing the synchronous impact.

In order to ensure the control of the selection action and shifting, the classical PD control algorithm can be adopted. Within this algorithm, the shift position sensor's deviation from the current position value and the target position value is $e(t)$. The shift actuator motor drive voltage $U(t)$ and its relationship are as follows,

$$U_{(t)} = K_p e(k) + K_d [e(k) - e(k-1)] \quad (14)$$

After the end of the gear, the driver's purpose will be automatically recognized by the controller, and then the target torque of the power motor will be completed, so that it will take the least time to increase the target torque, and the free mode to torque mode can be changed.

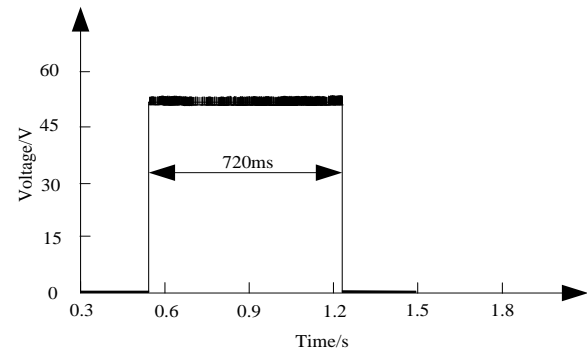
3. RESULTS

In order to verify the effect of the shift control method in this paper, the actual vehicle test under typical working conditions was carried out. The shifting quality is mainly measured by the shifting time and the difference in rotational speed between the AMT output shaft and the target gear when the target gear is engaged. According to the previous theoretical and experimental data analysis, we know that the point that is prone to impact during the starting process is the clutch synchronization point. Before the synchronization point is the second stage of the starting process, and after the synchronization point is the third stage of the starting process. In the second stage, the dynamic friction torque transmitted by the clutch is determined by the pressing force between the clutch master and driven parts. In the third stage, the static friction torque transmitted by the clutch is equivalent to the motive torque. To ensure that the vehicle starts smoothly, the dynamic friction torque output by the clutch should be equal to the engine output torque before the synchronization point. Therefore, the control of the second stage can be divided into two stages before and after: increasing the coupling speed of the clutch in the first half to shorten the start time as the goal; reducing the torque transmitted by the clutch in the second half to suppress the impact at the synchronization point.

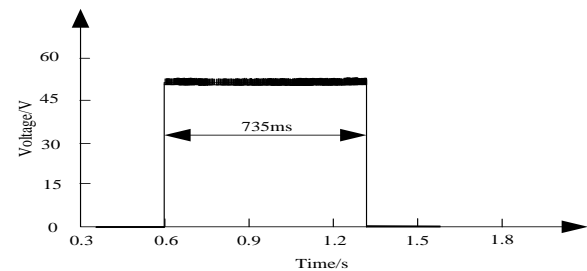
CRUISE software is developed by AVL List. Its modular modeling ideas and graphical modules make it easy to build a complete vehicle model. Its complete solver ensures the accuracy and speed of calculation of the entire vehicle model. Improve more advanced control modules such as the transmission program (GB Program) module, transmission control (GB Control) module and calculation optimization functions such as automatic transmission shift law optimization (GSP), DOE functions, etc. to optimize the automatic transmission simulation. The field has played a greater role. The use of CRUISE software to build a commercial vehicle AMT vehicle model and the use of GSP function modules to optimize its shifting rules are of great significance for accelerating vehicle development and speeding up transmission calibration.

3.1. Static shift

The static shift time is mainly determined by the AMT shift motor speed, the gear ratio of the shift actuator and the stroke between the high and low gears. The static shift time reflects the shortest shift time determined by the AMT mechanical structure. The shift time can be obtained by measuring the terminal voltage of the shifting motor. The shift time at rest is shown in Figure 8.



(a) Low block to high block



(b) High block to Low block

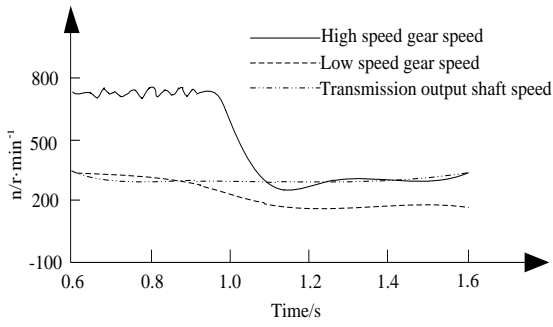
Figure 8. Voltage waveform at the end of the shift motor during parking shift

It can be seen from Figure 8 that in the static situation, when the electric vehicle is changed from the low speed gear to the high speed gear, the voltage changes at 0.5 s, and the voltage value is 0 at 1.22 s. The entire shifting process time is 720 ms. In the static situation, when the electric vehicle is changed from the high speed gear to the low speed gear, the voltage changes at 0.6 s, and the voltage value is 0 at 1.35 s. The entire shifting process time is 735 ms.

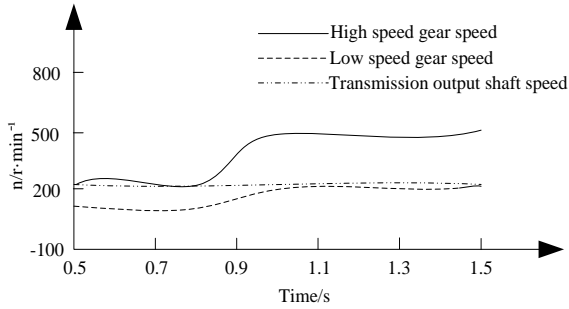
3.2. Shifting during driving

In the first stage, the clutch is quickly combined to eliminate the gap between the master and the driven parts within a short time; in the second stage, the clutch's coupling speed is controlled to make the clutch smoothly enter the combined state; in the third stage, the clutch continues to slowly couple, which can be pursued High vehicle acceleration, shortening the start time. In the fourth stage, when the speed difference between the clutch master and driven parts is reduced to Δn , the combination of clutches is controlled according to the change in engine speed: if the engine speed is increased or maintained.

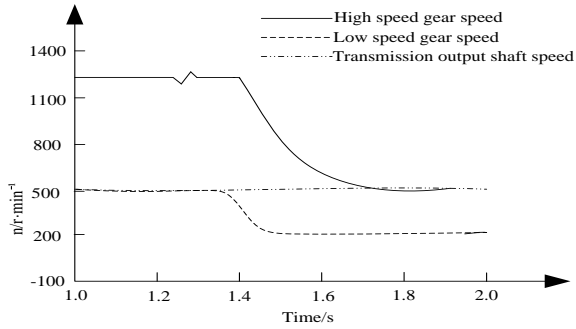
Keep the same, and the throttle opening of the engine increases, continue to engage the clutch or maintain its current position; otherwise, slowly release the clutch to the semi-engagement point position; Phase 5, after synchronization, the clutch is quickly engaged until the end. Figure 9 shows the rotational speed of each part of the AMT when shifting at low, medium and high vehicle speeds. The shift time depends mainly on the speed of the car. The higher the speed is, the greater the difference in rotational speed between the sleeve and the target gear is, and the longer it takes to match the speed is. Therefore, shifting at different speeds can reflect the effect of the shift control strategy.



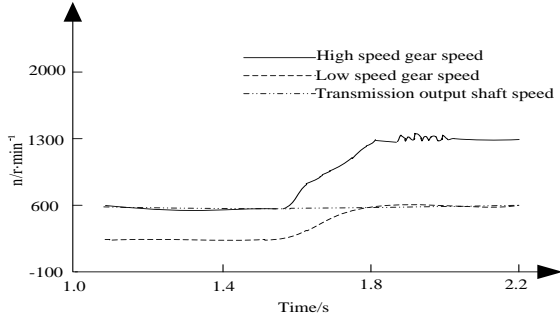
(a) At low speed Low block to high block



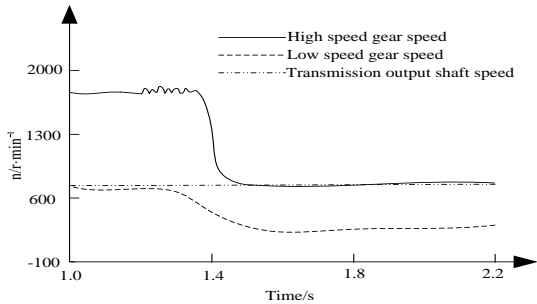
(b) At low speed high block to Low block



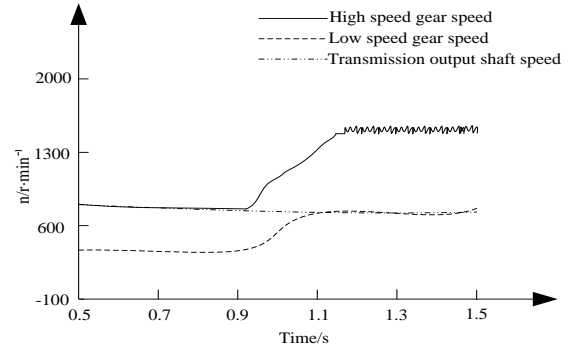
(c) Medium speed Low block to high block



(d) Medium speed high block to Low block



(e) At high speed Low block to high block

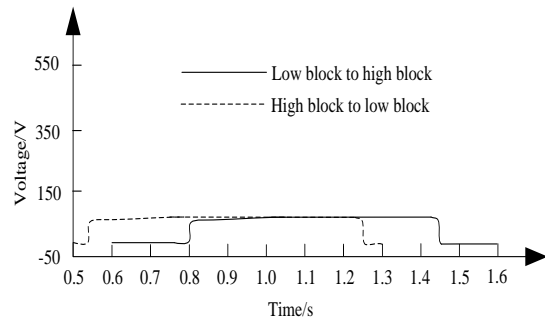


(f) At high speed high block to Low block

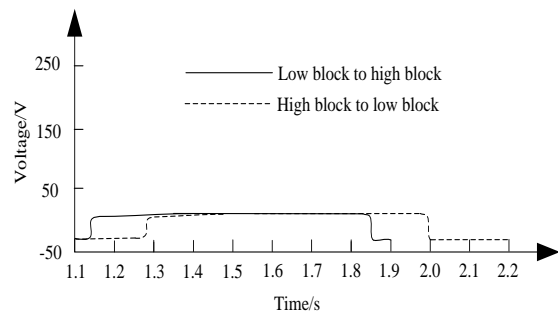
Figure 9 . Shift speed curve at different speeds

As can be seen from Figure 9, the shift motor does not stop during the shifting process, whether it is low speed, medium speed or high speed. This shows that the drive has been completed before the clutch reaches the neutral cut-off point. The effectiveness of the shifting of the clutchless AMT control strategy is verified.

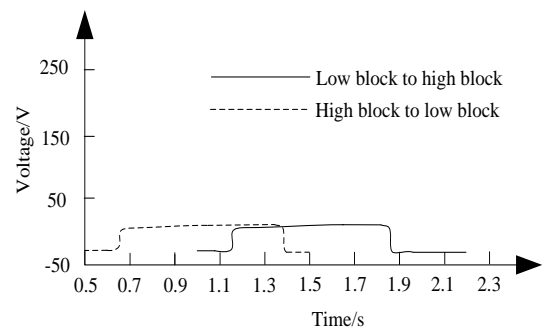
Figure 10 shows the shifting time for low, high and low gears at low, medium and high speeds.



(a) Shift time at low speed



(b) Shift time at medium speed



(c) Shift time at high speed

Figure 10. Shift time at different speeds

The low gear shifts of low, medium and high speeds are 723 ms, 725 ms and 729 ms, respectively, and the shift times of high gears and low gears are 742 ms, 749 ms and 751 ms respectively. This shows that the clutchless AMT shift control strategy studied in this paper can significantly shorten the shift time of electric vehicles.

The impact degree is the rate of change of the longitudinal acceleration of the vehicle, which is an important indicator reflecting the smoothness of the shifting process. According to the subjective feelings of passengers, countries have set corresponding standards for the impact value, and the German recommended value is $10 \text{ m}\cdot\text{s}^{-3}$. The impact value of electric vehicles at different speeds is shown in Table 1.

Table 1. Impact value of electric vehicles at different speeds

Time/s	At low speed/ $\text{m}\cdot\text{s}^{-3}$		Medium speed/ $\text{m}\cdot\text{s}^{-3}$		At high speed/ $\text{m}\cdot\text{s}^{-3}$	
	Low block to high block	high block to Low block	Low block to high block	high block to Low block	Low block to high block	high block to Low block
0.5						
0.6						8.9
0.7	-3.6	0				2.5
0.8						1.7
0.9						3.5
1.0		-0.5			2.4	-2.8
1.1	-0.7		-0.3	-9	3.5	-0.8
1.2			-4.9		-1.8	3.2
1.3		0		-8.7	2.9	1.9
1.4				5.1	-3.4	2.5
1.5			0	-4.2	2.8	-3.5
1.6	0.3			3.4	-3.4	
1.7				-2.8	6.7	
1.8				4.2	0.5	
1.9			3.1	7.6	-2.4	
2.0				5.4	3.4	
2.1				-1.9	-5.6	
2.2				2.6		

It can be seen from Table 1 that the electric vehicle using the clutchless AMT control strategy proposed in this paper has the shock degree of $\pm 10 \text{ m}\cdot\text{s}^{-3}$ during shifting with low speed, medium speed and high speed. This shows that the clutchless AMT control strategy can meet the requirements of shift smoothness.

The test results show that, in the static situation, the whole process time of the electric vehicle from the low speed to the high speed is 720 ms, and the process time from the high speed to the low speed is 735 ms. At low, medium and high speeds, the time required for the low gear to shift to the high gear is 723, 725, 729 ms, and the time for the high gear to the low gear is 742, 749, 751 ms. Whether it is low speed, medium speed or high speed, the shifting motor does not stop during the shifting process. The electric vehicle using the clutchless AMT control strategy proposed in this paper has the shock degree of $\pm 10 \text{ m}\cdot\text{s}^{-3}$ during shifting with low speed, medium speed and high speed. This shows that the shift control strategy of this paper has a good effect in shortening the shift time and

reducing the shift impact. At the same time, it verifies the effectiveness of the clutchless AMT control strategy proposed in this paper.

4. DISCUSSION

(1) For the shifting process control of the electric vehicle without clutch AMT, the DC brushless drive motor, the AMT without the clutch and the synchronizer, and main decelerator are combined to establish the power transmission model of the electric vehicle controlled by the power transmission integrated controller. The integrated controller of the power traditional model has only one control core, which can save the communication time between the drive motor controller and the AMT controller, thereby shortening the shift time.

(2) Through the process of shifting coordinated control, the shifting coordinated control strategy compensates for the effect of no clutch in the power transmission by accurately controlling the speed and torque of the drive motor, and smoothly completes the shift. Therefore, the control of the drive motor is extremely important in the entire shift coordination control system. The adjustment of the speed and torque of the motor determines the speed and smoothness of the shifting process. On the basis of the integrated electric drive system of the motor-transmission, the speed and torque of the drive motor at each stage are given corresponding control strategies in order to improve the reliability of the coordinated control strategy of the system automatic shift and the shift quality of the whole vehicle.

5. CONCLUSIONS

In this paper, based on the dynamic model of the integrated electric drive system of the motor-transmission, the automatic shifting principle of the clutchless AMT electric drive system is analyzed, and an automatic shift control strategy based on the classical PD control algorithm is developed. The effectiveness of the strategy is verified by experiments. The experimental results show that the automatic shift coordination control strategy developed in this paper can accurately control the speed and torque of the drive motor. The shifting mechanism can be coordinated, and the absolute value of the shifting impact is within the range of $\pm 10 \text{ m}\cdot\text{s}^{-3}$, which is in line with the standard. It can smoothly complete the automatic shifting of the clutchless AMT drive system. The shift time is short, about 730ms. It is the effective strategy which improves shift performance.

ACKNOWLEDGEMENT

Foundation item: Self-financing project of Hebei Provincial Department of Science and Technology - Shifting Control Strategy Optimization of non-Clutch AMT for Electric Vehicle (No. 18212221).

REFERENCES

- [1] Hannan, M.A., Hoque, M.M.&Mohamed, A. 2017. Review of Energy Storage Systems for Electric Vehicle Applications: Issues and Challenges. *Renewable & Sustainable Energy Reviews* 69(2017): 771-789.
- [2] CHAIBenben;WU Shaofang;ZHANG Jianwu;LIN Lianhua;XU Haigang;National Engineering Laboratory of

- Automotive Electronic Control Technology, Limited; S C . Optimal Control Strategy of Two Speed Automatic Mechanical Transmission in Shift Process[J]. Journal of Shanghai Jiaotong University, 06(2018):791-805.
- [3] Hu, X.,Jiang, J. &Cao, D. 2016b. Battery Health Prognosis for Electric Vehicles Using Sample Entropy and Sparse Bayesian Predictive Modeling. *IEEE Transactions on Industrial Electronics* 63(4): 2645-2656.
- [4] Hu, X.,Moura, S.J. &Murgovski, N. 2016a. Integrated Optimization of Battery Sizing, Charging, and Power Management in Plug-In Hybrid Electric Vehicles. *IEEE Transactions on Control Systems Technology* 24(3): 1036-1043.
- [5] Izadkhast, S., Garcia-Gonzalez, P. &Frias, P. 2016. An Aggregate Model of Plug-in Electric Vehicles Including Distribution Network Characteristics for Primary Frequency Control. *IEEE Transactions on Power Systems* 31(4): 2987-2998.
- [6] Kang B.,Tan X.J. &Chen,W.J. 2017. Comparative Research on Hierarchical Equalized Charging Schemes for Electric Vehicle Battery. *Chinese Journal of Power Sources* 41(9): 1338-1340.
- [7] Moon, S.C.& Moon, G.W. 2016. Wireless Power Transfer System with an Asymmetric Four-Coil Resonator for Electric Vehicle Battery Chargers. *IEEE Transactions on Power Electronics* 31(10): 6844-6854.
- [8] Pelletier, S.,Jabali, O. &Laporte, G. 2016. 50th Anniversary Invited Article-Goods Distribution with Electric Vehicles: Review and Research Perspectives. *Transportation Science*50(1): 3-22.
- [9] Ren, C., Zhao, J.G. &Luo, Q.Y. 2017. Glowworm Algorithm for Solving Optimization Problem of Cloud Computing Resource. *Journal of Jilin University (Science Edition)*55(5): 1234-1238.
- [10] Sarker, M.R., Dvorkin, Y. &Ortegavazquez, M.A. 2016. Optimal Participation of an Electric Vehicle Aggregator in Day-Ahead Energy and Reserve Markets. *IEEE Transactions on Power Systems* 31(5): 3506-3515.
- [11] Su, Y.C., Gu, B.W. &Jeong, S.Y. 2016. Advances in Wireless Power Transfer Systems for Roadway-Powered Electric Vehicles. *IEEE Transactions on Industrial Electronics* 63(10): 6533-6545.
- [12] Wang, G.Q., Wang, Z.X.&Wang, Z.Q. 2016a. Research on Optimization of New Electric Vehicle Frame Structure. *Automation & Instrumentation* (7): 67-69.
- [13] Wang, S., Jin, F. &Zhao, D. 2016b. Predicting Consumers' Intention to Adopt Hybrid Electric Vehicles: Using an Extended Version of the Theory of Planned Behavior Model. *Transportation* 43(1): 123-143.
- [14] Yang J.B., Zhang J.Y. &Song P.Y. 2017b. Multi-objective Optimization of Energy Management Strategy for A Tramway with Onboard Energy Storage System. *Journal of Power Supply* 15(5): 137-143.
- [15] Yang, D.R., Chen Y., Liu, S.Y. 2017a. Research on Fault Tolerant Strategy Optimization of Storage System for the Healthcare Big Data. *Journal of China Academy of Electronics and Information Technology*12(5): 546-550.
- [16] Zhou, Y.S., Kong, X.Y. &Zhang, F.T. 2016. Simulation and Test on Starting Fuzzy Control of Electric AMT Clutch. *Computer Simulation*33(12): 173-179.

Deep Drainage Detection System for Inland Vessels Based on Machine Vision

Hechuang Wang*

School of Information Engineering, North China University of Water Resources and Electric Power, Zhengzhou 450045, China

Received OCT 16 2019

Accepted JAN 6 2020

Abstract

In order to prevent inland ships from overdraft, it is necessary to detect the draft depth of inland ships to ensure the safety of navigation. To design a river ship draught depth detection system based on machine vision, it collects accurate and comprehensive visual images of ships through image acquisition module, and provides industrial computer with reasonable detection methods to detect the draft depth of ships. The detection results are stored in the database and displayed in real time. The detection module is composed of FPGA and DSP hardware to realize the system detection process, communication and transaction, and the effective control of the terminal. When the inland water body is clear, the system uses the edge detection based draft depth detection method to effectively detect the ship draft depth. When the inland water body is turbid, the system uses binocular stereo vision three-dimensional detection method to measure the ship draft depth. The test results show that when the inland water body is clear, the error of the intake depth of inland ships detected by the detection system is ± 0.05 m, and when the inland water body is turbid, the error of the system is within ± 0.07 m. This shows that the detection system can accurately detect the intake depth of inland water body in clear and turbid conditions, and the test results are comprehensive and accurate.

© 2020 Jordan Journal of Mechanical and Industrial Engineering. All rights reserved

Keywords: : Machine Vision, Inland Ships, Draft Depth, Water Clarity, Edge Detection, Binocular Stereo Vision;

1. Introduction

At present, due to the decline of water level in many rivers and the transitional cargo loading of shippers, the phenomenon of overdraft of inland ships is becoming more and more common. The phenomenon of overdraft of inland ships refers to the maintenance depth of ships beyond the waters, and the abundant water depth is insufficient to support the normal loading and navigation of inland ships. Overtdraft of inland ships is very harmful, which will damage the structure of the ship itself, and the heavy load will lead to the overdraft of inland ships. Grounding or anchoring of a ship poses a threat to the lives of people on board. The management of ship overdraft behavior has always been a difficulty that has a special focus of inland waterway administration (Baigvand et al. 2015). It is difficult to grasp the actual draft condition of a ship by checking the ship's water gauge or measuring the actual draft in the cabin. This makes it difficult to manage the phenomenon of ship's over-draft. It makes it difficult for the channel administrators to obtain evidence of ship's over-draft. Owners usually argue and deny and refuse to compensate for the loss caused by the channel. How to design an effective ship draft depth detection system to detect and stop the phenomenon of ship over-draft in time is the problem that the waterway administrators need to solve. After the over-draft ship destroys the waterway, the waterway administrators can truly and accurately grasp the

actual information of the ship draft and obtain the evidence of the ship over-draft (Prez et al. 2016).

Inland watercraft draft depth refers to the depth of inland watercraft immersed in water. It is a very important parameter in the field of ship survey. It reflects the buoyancy of inland watercraft in the course of navigation, and uses it to reflect the ship's drainage and cargo carrying capacity. By measuring the intake depth of inland ships, we can know whether there is over-draft phenomenon in inland ships or not. It is convenient for the Inland Ship Administrators to control the phenomenon of over-draft, and it also ensures the personal safety of the staff on board. At present, the detection of intake depth of inland ships is mainly based on manual detection, which mainly draws the intake line on the hull surface to get the intake depth. According to the intake depth, it can be judged whether the ship has over-draft phenomenon or not. In the measurements, the ship needs to be ashore, and the relevant staffs are on board to observe the intake line. This way cannot be separated from manual operation. In order to detect, it is necessary for ships to go ashore, which affects the normal navigation of ships and reduces the efficiency of ships. At the same time, because the ship draft detection line is exposed to the outside, it is eroded by river water, and it becomes ambiguous, which affects the accuracy of manual detection. Moreover, the artificial detection method is greatly affected by weather, and often affects the detection results when the surface wind and waves are large. This method also has one of the biggest drawbacks, that is, the ship's draught line can be modified artificially, which

* Corresponding author e-mail: wanghc0134@163.com.

makes it difficult for the staff to judge whether the ship is in over draught state (Keenan et al. 2015). Therefore, a new detection system is needed to detect the draft depth of inland ships (Li et al. 2015; Bhatt & Pant 2015).

In recent years, with the rapid development and wide application of image processing technology, machine vision has been widely used. Because machine vision has the advantages of non-contact and high efficiency, most scholars adopt machine vision technology to detect the draft depth of inland ships, such as designing a system based on gradient amplitude extraction to detect the depth of the ship's draft line, and tracking code based on color image segmentation. Some scholars use HIS spatial color gradient and heuristic edge extraction algorithm to design a system based on gradient amplitude to extract water lines. However, these systems have some defects. In the process of detection, the above systems select ideal high-definition images, and the scratches on the surface of the ship are small, not natural fields. The general model in this scenario is only suitable for theoretical research under laboratory conditions, but lacks a practical ship draft line detection system (Qureshi & Payne 2016). Chen et al. proposed a draft detection system for inland water vessels based on multi-beam sonar sounding system. Based on sonar ranging technology, the design draft for inland river ships in testing system, complete test system software architecture design and communication protocols, multi-beam sonar sounding system adopting multi-beam sonar sounding data filtering de-noising algorithm filter abnormal data, the system realized the ship draft outline clear and accurate imaging, and digital, real-time display of ship draught, feasibility for inland river ships draft regulation control to a certain extent, but the system exist draft depth, but it has problems in practice, however, it is difficult to promote (Chen et al. 2016). Lu et al. designed a lower computer system based on STM32 and FPGA dual-core structure and an upper computer early-warning software system based on MFC. Based on the propagation model of underwater ultrasonic wave and the diffraction effect of ultrasonic wave, combined with the real-time water level variation information, this system collects the lattice sequence of the draught of navigable ships, and finally calculates the draft depth of navigable ships, but the detection error of this system is large (Lu et al. 2017). Wu et al. proposed a method for ship draft detection based on differential scanning with dual sonar probes. On the basis of detailed analysis of ship curved contour shape, using double differential scanning

sonar sensor technology, detection of important mathematical model is set up, on this basis to design a ship draft detection system, the implementation of inland ship draught detection, but the system is too simple, the existence question of error detection (Wu et al. 2017).

From the point of view of machine vision, this paper designs an inland ship draft depth detection system, which can accurately detect the inland ship draft depth when the inland water body is clear and when the inland water body is turbid. It is widely used and it is applied to the actual ship draft depth detection. This system mainly fills the blank of using machine vision to detect the depth of ship's draught, and is also a further extension of the application scope of machine vision, which has certain applicability and reliability.

2. Materials and methods

2.1. System architecture

The intake depth detection of inland ships based on machine vision is mainly composed of the following modules: image acquisition module, image processing module, detection module, human-computer interaction module and result storage module. The system can not only reflect the characteristics of human recognition of single frame waterline, but also replace the human brain to analyze the results of the waterline. The image acquisition module is similar to the human eye, which obtains the ship draft image and initializes the camera with Opence. The image processing module is equivalent to the human brain nerve, which is used to think, calculate and solve problems. The main functions of the image acquisition module are preprocessing, image denoising, ROI positioning, edge detection or projection positioning, etc. The detection module determines the ship draft line in several wave cycles. The detection module mainly detects the image processed by the image processing module (Goren et al. 2017). Human-computer interaction module is equivalent to human subjective consciousness. After receiving comprehensive information, the final action and decision are made. The results are displayed to users in the form of human-computer interaction, which is convenient for users to observe. Storage module accesses and verifies the current recognition image. The architecture of the detection system is shown in Figure 1.

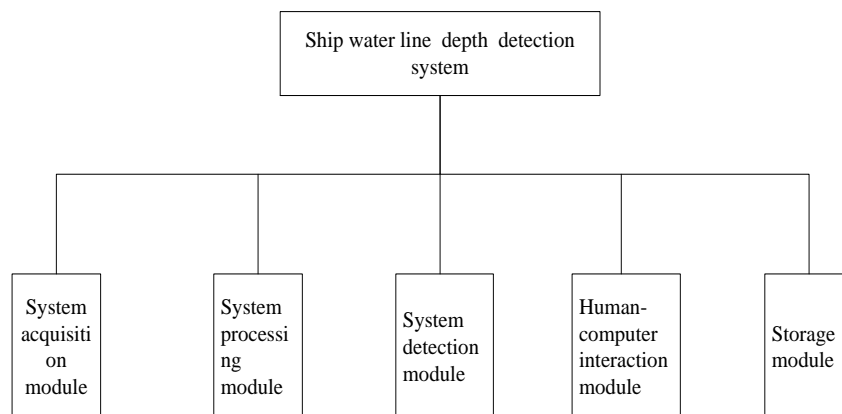


Figure 1. Test system architecture

2.1.1. Image acquisition module

The structure of the image acquisition module in the system is described in Figure 2. From Figure 2, it can be seen that the light source, lens, industrial camera and so on are the important components of the module.

In the image acquisition module, three industrial cameras are set up to acquire accurate and comprehensive visual images of ship draft. The industrial cameras are placed in the same two-dimensional plane perpendicular to the detected ship. When the image acquisition module collects the ship draft image, the encoder rotates with the guide wheel driving, the pulse counter card receives the signal transmitted by the encoder, and the related parameters of the detected ship are stored in the counter card. The counter card sends the trigger command to the camera after running a frame of the image. After the camera collects the image data of the ship draft image, it is provided to the industrial control computer and the reasonable detector is adopted. The method implements the detection

of ship draft depth, and the results are stored in the database and displayed in real time.

2.1.2. Detection Module

This system uses machine vision technology to realize intake detection of inland ships. Machine vision technology is a technology that converts the signal to be measured into image signal by image sensor, and uses special image processing system to process the image signal pertinently and recognize the undetermined results automatically (Haase et al. 2016; Yan 2015). At present, on-line machine vision inspection has become an important part of ship draft depth detection, which has great economic and social benefits. With the development of high-speed image sensor, high-speed DSP and highly integrated FPGA, the technology of high-speed online machine vision is becoming more and more perfect (Zheng et al. 2015). Based on machine vision detection technology, the system designs a depth of draft detection module for inland ships. The principle is shown in Figure 3.

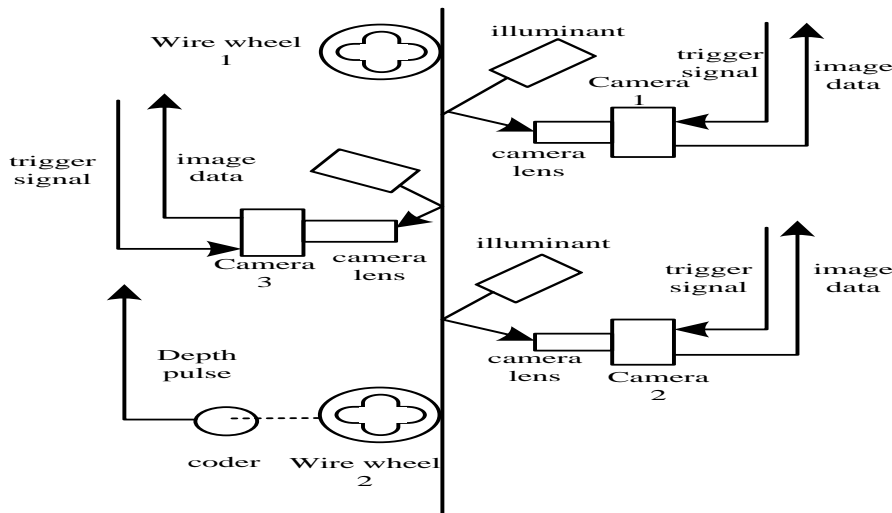


Figure 2. Image acquisition module structure

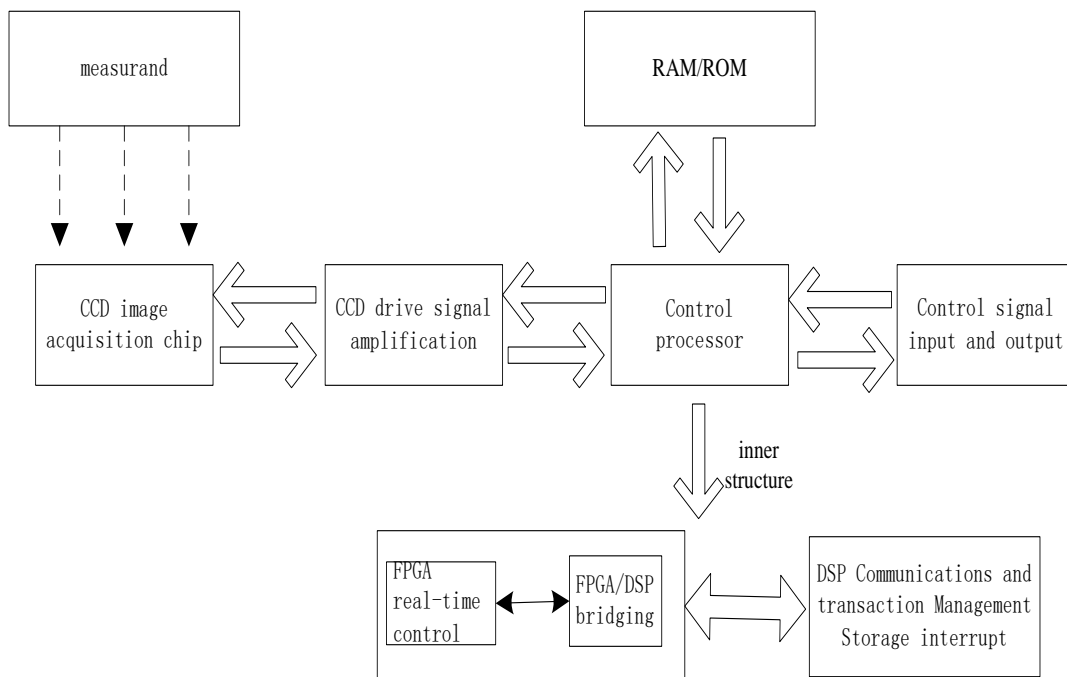


Figure 3. Detection principle of testing system

The core part of the detection module is composed of the hardware of FPGA and DSP. The real-time control of the system is carried out by the FPGA, and the core algorithm is realized. The complex algorithm is completed through the communication, transaction management, storage and terminal management of the DSP with pipeline operation and efficient data processing ability. The bridge connection between the FPGA and the DSP is used to realize seamless connection and improve the efficiency of the system.

2.2. Inspection of inland watercraft drainage depth based on machine vision technology

2.2.1. Method of inland vessel drainage depth detection based on edge detection

Based on edge detection, the position of intake line of inland ship is obtained, and the intake depth of inland ship is calculated by intake line. When the water body of inland river is clear, transparent, bright and the water line state is relatively flat, it is easy to get the target edge by direct edge testing. In order to ensure the extraction of the target water line, it is necessary to obtain as much image gradient information as possible. Therefore, the detection system uses image global information, because histogram technology is an important means of image enhancement, and histogram technology should be adopted. The method corrects the gray level of the image, enlarges the dynamic contrast range of the image, expands the contrast, makes the image clearer and has obvious features. It obtains the image with better effect after the correction. By using the difference of gray level characteristics between the object and background to be extracted from the image, the horizontal gradient information of the whole gray level image is detected according to the direction of Sobel operator, and the appropriate threshold is selected. The image is divided into meaningful regions, and the target is extracted from the image for further analysis (Khalili & Vahidnia 2015). Then the binary image is obtained by Hough line, and the longest line is detected. The midpoint of the detected line is taken as a horizontal line, that is, a single frame draft line, and the draft depth is obtained according to the known draft line.

Firstly, the edge detection of the segmented image is carried out. The commonly used operators of edge detection include Rebert, Sobel, Guass and Canny operators. In view of the comprehensive consideration of edge orientation and sensitivity to interference (Howarth et al. 2015), this paper mainly applies Sobel edge segmentation. Sobel detection operator is an algorithm that uses the adjacent points of the pixel points to obtain gray weights, which mainly depends on the direction of the detection edge and the sensitivity to interference (Howarth et al. 2015). According to the principle that the gradient at the edge points reaches the extreme value, the following equations are needed for edge detection.

$$f_x(x, y) = f(x+1, y-1) + 2f(x+1, y) + f(x+1, y+1) - f(x-1, y-1) - 2f(x-1, y) - f(x-1, y+1) \quad (1)$$

$$f_y = f(x-1, y+1) + 2f(x, y+1) + f(x+1, y+1) - f(x-1, y-1) - 2f(x, y-1) - f(x+1, y-1) \quad (2)$$

$$g(x, y) = |f_x| + |f_y| \quad (3)$$

The Sobel operator template is shown as follows:

$-f_x$	f_0	f_x
$-f_{x+y}$	$g(x, y)$	f_{x+y}
$-f_y$	f_0	f_y

Figure 4. Sobel operator template diagram

Through the above template which detects the draft line, and according to the test results, it can be seen that the introduction of local average value in the algorithm has little impact on noise. Sobel operator is an algorithm with high detection continuity, and can also detect the details of the image very well. So when the inland water surface is calm and the water line is straight, the Sobel detection line along the X direction can often achieve the detection purpose.

The purpose of edge detection is to identify the points with obvious gradient change in gray image. When these points are adjacent and have similar directions, special edge line segments can be constructed by using detection algorithm, but these detection lines are not completely required waterlines. After the detection of scratches and exposure edges of inland river hulls, pseudo-edges will be generated, and some constraints need to be added. At present, Hough transform is the most effective method for line detection. Its advantage is that it is easy to transform geometric figures quickly and efficiently. In the plane rectangular coordinate (x-y), the linear equation can be expressed as $y=kx+b$.

For a fixed point (x_0, y_0) on a straight line, there is a definite equation $y = kx_0 + b$, which represents a straight line in the parameter plane (kx-b). Therefore, a point in the image needs to correspond to a sinusoidal curve in the plane. For all points in the image, Hough transform is used. The final line to be detected must correspond to the point groups where the lines intersect in the parameter plane. The parameter equation $p = x \cos \phi + y \sin \phi$ is usually used to detect the exact position of the intake line of inland ships and get the intake depth of inland ships. However, this system is only suitable for transparent water, i.e. bright water line and relatively flat water line condition.

When the water body is turbid and unstable, that is, the clarity of the water body is not high, the fluctuation of the water line is large, and the brightness of the water line is reduced, it is difficult to detect the draft depth of inland ships by edge detection and Hough transform (Yang et al. 2015). At this time, the detection system uses binocular stereo vision three-dimensional detection method to detect the intake depth of inland ships.

2.2.2. Three-dimensional detection method of binocular stereovision

Binocular stereo vision system is used to detect ship heave. The draft depth of the ship is determined mainly according to the relative position distance between the supply ship and shore base. Two cameras, a computer (or DSP system) and a characteristic object are used in the

binocular stereo vision three-dimensional measurement. The binocular camera of the system is fixed on the crane boom. When installed, the optical axis plane of the two cameras is perpendicular to the horizontal plane. Characteristic objects are placed near the landing point of the cargo on the replenished ship. The relative position between the camera and the characteristic objects can be detected by the binocular stereo vision three-dimensional measurement and detection system (Cheng et al. 2015; Zhou et al. 2015), and the relative height can be obtained. In order to facilitate image processing, the system uses the feature object as a circular color block. The principle of three-dimensional measurement of ship heave by binocular stereo vision is shown in Figure 5. The left camera O-xyz is located at the origin of the coordinate system without rotation, the image coordinate system is OI-XIYI, the effective focal length is f_l , the right camera coordinate is Or-xryrzr, the image coordinate system is Or-XrYr, and the effective focal length is f_r .

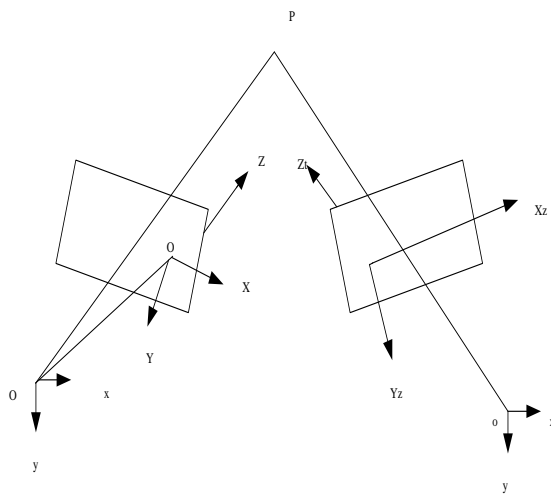


Figure 5. Three-dimensional reconstruction of spatial points in binocular stereo vision measurement

For the same characteristic point P in the process of ship heave, the three-dimensional coordinates of the two cameras are $P_l=(X_l, Y_l)$ and $P_r=(X_r, Y_r)$, respectively. Then the three-dimensional coordinates of the space P point can be expressed as follows:

$$\left\{ \begin{aligned} x &= zX_l / f_l \\ y &= zY_l / f_l \\ z &= \frac{f_l(f_r t_x - X_r t_z)}{X_r(r_7 X_l + r_8 Y_l + f_l r_9) - f_r(r_1 X_l + r_2 Y_l + f_l r_3)} \\ &= \frac{f_l(f_r t_x - Y_r t_z)}{Y_r(r_7 X_l + r_8 Y_l + f_l r_9) - f_r(r_4 X_l + r_5 Y_l + f_l r_6)} \end{aligned} \right\} \quad (4)$$

The space transformation matrix between O-xyz coordinate system and Or-xryrzr coordinate system is Ml:

$$M_l = [R T] \quad (5)$$

$$R = \begin{bmatrix} r_1 & r_2 & r_3 \\ r_4 & r_5 & r_6 \\ r_7 & r_8 & r_9 \end{bmatrix} \quad T = \begin{bmatrix} t_x \\ t_y \\ t_z \end{bmatrix}$$

R and T are rotation matrices and translation vectors between O-xyz coordinate system and Or-xryrzr coordinate system respectively. By calibrating R and T parameters, the

actual coordinate position of P point can be obtained according to the output result of image processing. When the left and right cameras are installed in the detection system, because the optical axes of the two cameras intersect and the plane formed is perpendicular to the plane of the two cameras' images, Or-XrYr rotates θ angle around the Y axis on the basis of coincidence with the O-xyz system and moves to (t_x, t_z) on the xz plane. If the rotation matrix is represented by Euler angles, the following R and T can be obtained.

$$R = \begin{bmatrix} \cos \theta & 0 & \sin \theta \\ 0 & 1 & 0 \\ \sin \theta & 0 & \cos \theta \end{bmatrix} \quad T = \begin{bmatrix} t_x \\ 0 \\ t_z \end{bmatrix} \quad (6)$$

In the binocular ranging system, image processing is the key. The image processing methods are as follows: after the binocular camera obtains the image, in order to make the target feature color block stand out, the image is first enhanced for the characteristic color, and the difference of the image pigmentation value is widened as far as possible (Boss et al. 2017). At the same time, in order to save time and space for subsequent image processing, the color image is converted into gray-scale image, and then binarized. Then, the image is filtered by median filter, the discrete solitary points are removed, and some blank points in the target are repaired. Finally, in MATLAB, the centroid method of region description sub-region is used, that is, the function regionprops (L,'Centroid'), L is the image matrix, and Centroid is the image matrix. The X and Y coordinate vectors of the center of mass of each color block can be obtained from these vectors. According to the maximum area of the feature block, the coordinates $P_l=(X_l, Y_l)$ and $P_r=(X_r, Y_r)$ of the target feature block point in the left and right plane images can be obtained. By substituting X_l, Y_l, X_r and Y_r into the calibrated binocular ranging equation, the spatial coordinates (X, Y, Z) of the target point can be obtained, which directly reflects the relative vertical distance Z between the replenishment vessel (or shore base) and the replenished vessel, i.e. the heave of the inland vessel, and thus the draft depth of the inland vessel can be obtained. The specific steps are shown in Figure 6.

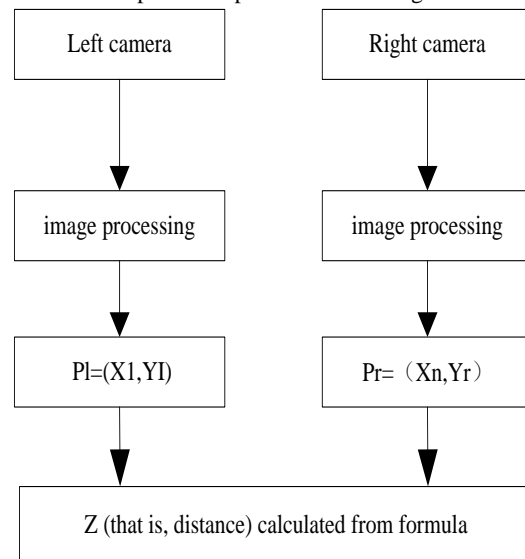


Figure 6. flow chart of system data processing

3. Results

In order to verify whether the detection system in this paper can get the depth of intake line of inland ships for practical needs or not, the detection effect of this system is as follows: if the actual intake depth of an inland ship is detected by video tape, the depth of intake of the ship is detected under clear and turbid conditions, the visual field is 22 s, the frame number is 25 f/s, and the resolution is 720×576 (16: 9). The hardware environment of the experiment is intel pentium. 73 GHz, Windows XP, 1GB memory PC, and software platform: The program is written by using OpenCV visual algorithm library in the environment of VC6.0.

The inland waterway vessel is a 2500-ton inland waterway bulk carrier with a length of 94.57m, the molded breadth of 16m, the moulded depth of 6.2m, maximum loading capacity of 2476 t and speed of 21km/h. The wave height of this test section is 0.5m-1.5m, which corresponds to the level 4 of beaufort wind, and the velocity on the beach in the navigation area is below 3.5m/s. The visual image of the ship is shown in Figure 7.

3.1. Deep drainage line of inland ships based on edge detection

3.1.1. Edge detection, geometric correction experiments and result analysis

When the water body of the inland river is clear, the gray level of the forecasted draft image of the experimental ship needs to be processed when the detection system is used to detect the edge. Histogram technology can treat the gray level of the image as a random number set. The gray level of the image can be modified by histogram to improve the visibility of the image and the contrast of the image while brightening. Thus, the experimental image can be processed. Histogram processing, as shown in Figure 8, can be seen that each histogram shows obvious double peaks, and the minimum gray level is selected as the threshold for effective image segmentation.



Figure. 7 Visual image of ship

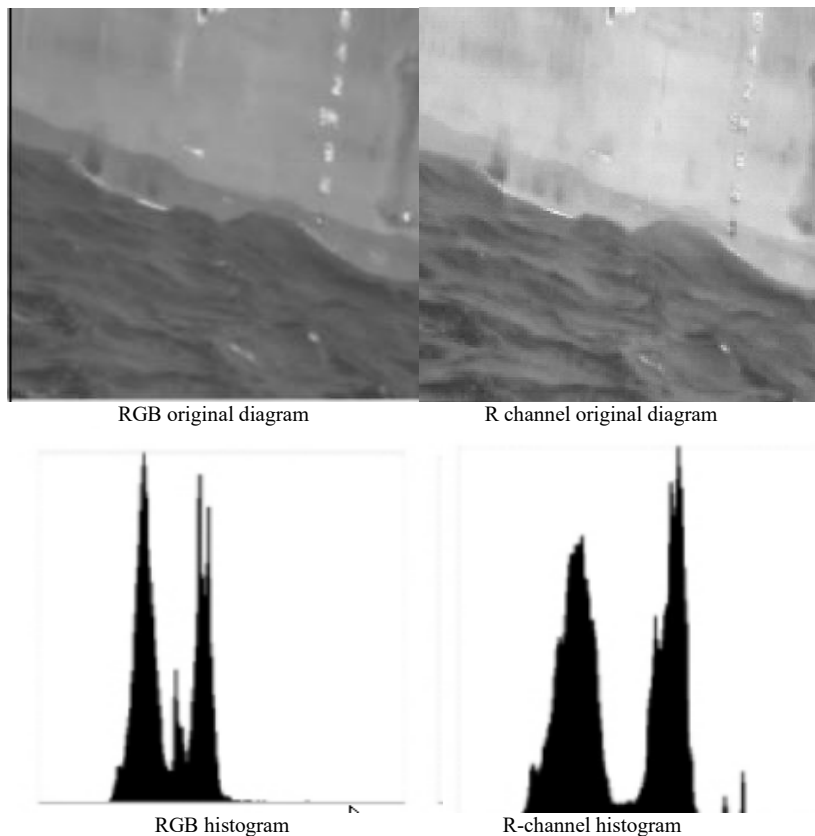


Figure 8. Image cut space selection

The aim of smoothing before edge detection is to improve the signal-to-noise ratio of ship draft image and eliminate noise interference. After verification, Sobel operator is the best edge detection operator. It uses the Gauss filter to smooth the edge. The Gauss filter is a low-pass filter. It can suppress the higher frequency signal, so it can reduce the interference of false edge points. In addition, Sobel operator detects the edges of pixels through edge connection to ensure the integrity of edges. After many experiments, it is found that when the double threshold of Sobel operator is (18, 54), edge detection is the best. After edge detection, it cannot be determined whether the obtained waterline is a real waterline. Hough transform is needed to transform it to get the exact waterline.

3.1.2. Hough transform, draught depth determination experiments and result analysis

The binary image of a single frame image is obtained by Hough transform, and the current draft value is obtained from the suspected water line for detecting the draft depth. The draft line is determined based on the algorithm of converting the curve into a straight line, and then the draft depth is detected. Traditional draught line detection is based on least squares method, but the actual use of least squares fitting is a regression method, processing efficiency is slow, its shortcoming is that if there are some errors deviating from larger points, it will affect the overall fitting effect, resulting in inaccurate detection of draught depth. This detection system uses a method based on edge detection of draught depth detection, according to binary images. The projection is used to determine the draft depth of a single-frame water scale image. The total number of white pixels in each row is counted. The ratio of bright pixels to the total number is set as a threshold to determine the final draft depth of a single-frame image, as shown in Figure 9.

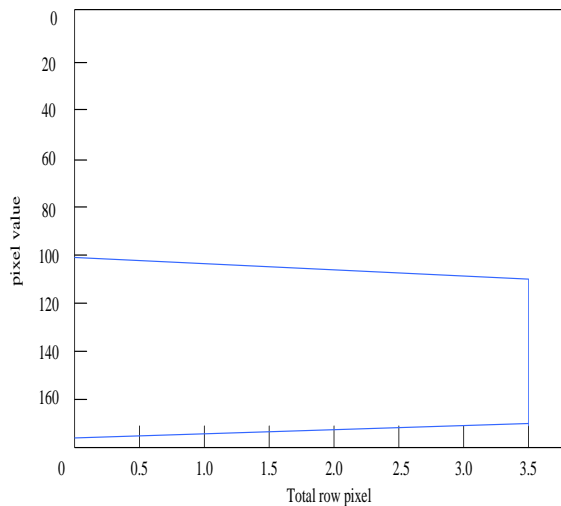


Figure 9 .Horizontal projection graph of bright Pixels

According to Figure 9, the number of pixels after projection of binary image is approximately straight line. When the threshold is set to 50% of the total line pixels, it is exactly the center of the vertical coordinates of the oblique line. Since the first detected draft line may be caused by noise such as scratches on the ship's surface, the horizontal line of the line is fixed as a suspected draft line, and the suspected draft line is scanned downward to check the suspected draft line. If the statistical proportion of continuous bright pixels is more than 50%, the suspected draught line is determined as a single frame draught line.

Otherwise, the detection of the frame is invalid. Then it is tested. The results of manual observation and experiment are compared, the error is calculated as follows:

$$k = f - z \quad (7)$$

Where, f represents the detect draft depth, z represents the actual draft depth.

The experimental error is shown in Table 1.

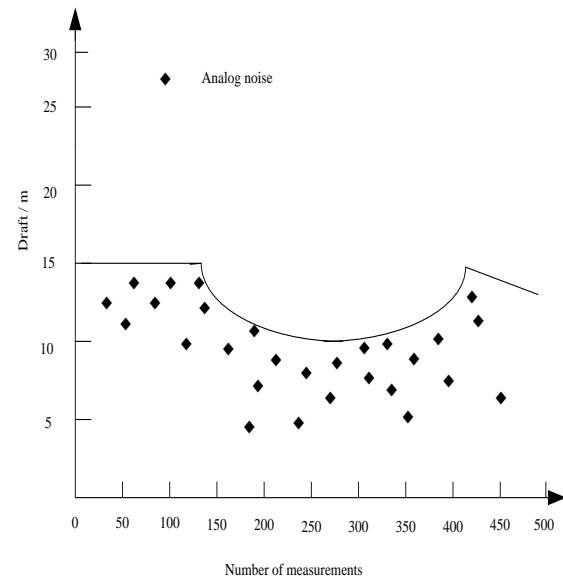
Table 1. Experimental error Analysis

number of times	Detect draft depth/m	Actual draft depth/m	Error/m
1	4.28	4.26	0.02
2	3.13	3.13	0
3	4.47	4.45	0.02
4	2.49	2.30	-0.01
5	4.17	4.18	-0.01
6	3.43	3.45	-0.02
7	4.77	4.76	0.01
8	2.89	2.90	-0.01
9	3.65	3.66	-0.01
10	4.23	4.22	0.01

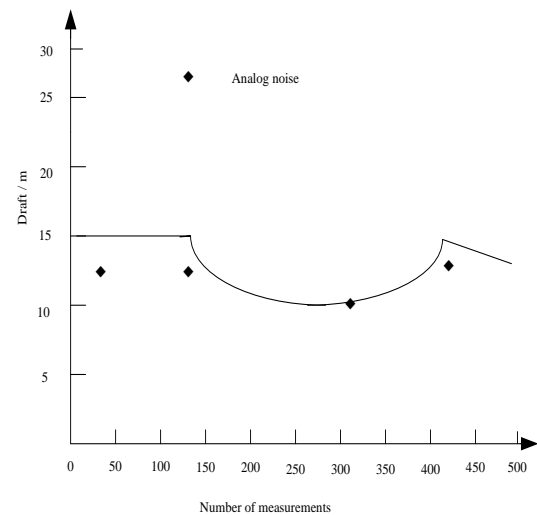
By comparing the measured data and calibration values, it can be concluded that when the water body of the inland river is clear in the experiment, the error of the draft depth value of inland ship detected by the detection system in this paper is $\pm 0.05\text{m}$, which meets the detection requirements. It can be seen that the edge detection method used in this detection system has low error and high accuracy in actual draught line monitoring. To determine the draught depth through the draught line is of great significance to the measurement of the draught depth, and can meet the needs of actual detection.

3.2. Binocular ranging experiment

When the inland water is turbid in the experiment, the effect of the binocular stereo vision three-dimensional detection method used in this system to detect the draft depth of ships is tested. For discrete abnormal data, the median filtering algorithm is used to simulate the ship draught profile and discrete jump data. The simulation steps are divided into three steps. Firstly, the horizontal line and sinusoidal curve are used to simulate the water surface and ship draught profile respectively. Secondly, the uniformly distributed random number is added to simulate the noise. Finally, the median filtering method is applied to deal with the abnormal data. After eliminating a large amount of noise, the input is obtained. The filtered image is shown in Figure 10.



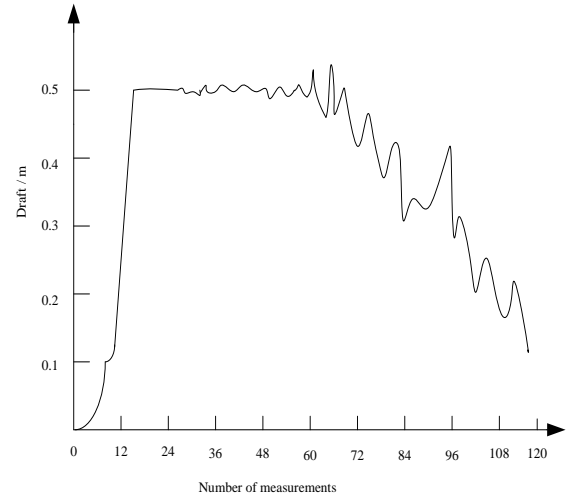
(a) Simulation of ship draft profile before filtering



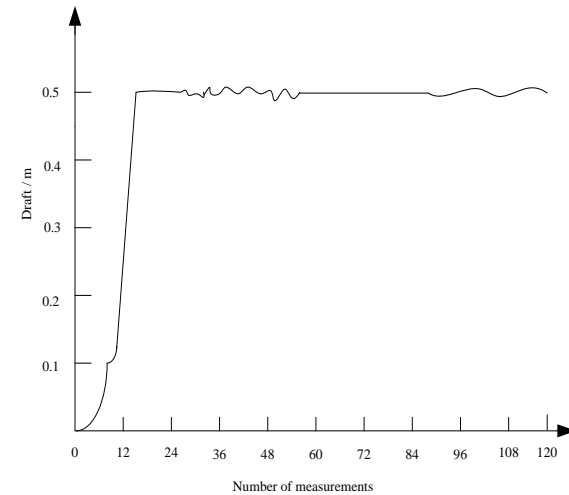
(b) Simulation of ship draft profile after median filtering

Figure 10. Effect of median filter on removing discrete jump anomaly data

From the simulation results of the median filtering algorithm presented in the above figure, it can be seen that the median filtering has good filtering effect on random noise generated in ship draught imaging. The features of the continuous jump abnormal data are concentrated and continuous, and generally distributed in the stern of the ship. The median filtering and other algorithms for random noise are not suitable. For this feature, the curve should be fitted according to the normal data and the abnormal data should be fitted. The centralized area is forecasted, but machine vision technology is used to detect the ship stern according to the image. When detecting the stern, the detection data are all abnormal data. There is no normal data to fit and predict. The least square method is needed to fit and forecast the normal data. The results are shown in Figure 11.



(a) Filter front



(b) After filtering

Figure 11. Least square fitting

The results of anomaly data processing are shown in Figure 11, Figure 11(a) is the continuous jump anomaly data, and Figure 11(b) is the normal data after fitting prediction. It can be seen that the least squares fitting prediction data used in this detection system can effectively identify the continuous anomaly data and obtain the normal data segment.

Based on the normal data of the minimum binary fitting prediction, the experiment of detecting the draft depth of inland ships is carried out. The experimental ships are tested systematically. The feature color blocks are placed in different directions (i.e. space coordinates X, Y) and different distances (i.e. space coordinates Z) of the experimental ships. After obtaining the image coordinates $P_l (X_l, Y_l)$ and $P_r (X_r, Y_r)$ captured by the left and right cameras, the feature points are captured by using MATLAB. After processing, the vertical distance Z from the feature point to the camera can be calculated, as shown in Table 2.

Table2. Detection of draft depth

Number of times	Detect draft depth/m	Actual draft depth/m	Error/m
1	1.39	1.45	-0.06
2	3.22	3.16	0.06
3	4.02	4.27	-0.07
4	4.29	4.28	0.01
5	3.31	3.29	0.02
6	4.31	4.30	0.01
7	2.28	2.31	-0.03
8	3.37	3.32	0.05
9	4.35	4.33	0.02
10	4.32	4.34	-0.02

From several sets of data in Table 2, it can be seen that when the inland water body is turbid in the experiment, the difference between the detection distance and the actual distance of this system is small, all within the range of ± 0.07 m. That is to say, the error between the actual depth of intake and the binocular stereo vision is relatively small, which can measure the actual depth of intake of inland water vessels well. Therefore, binocular stereo vision three-dimensional measurement detection is used in practice. The intake depth of inland ships is maneuverable and accurate, which is superior to manual detection method and reduces the difficulty of detection for ship administrators.

4. Discussions

As a means of transportation, ships play an important role in the transport industry. Drainage depth of inland ships is an important measurement parameter. The actual draft depth of overdraft phenomenon is 5.5m, so no overdraft phenomenon was found during the test in this paper. However, accurate detection of draft depth will reduce the occurrence of overdraft phenomenon, which is conducive to the claim of ship for channel damage, and effectively protect channel resources and smooth channel. At the same time, it can also protect the ship in the normal state of navigation, reduce navigation resistance, and is also an important measure of energy saving and emission reduction. From the point of view of machine vision, this paper designed system overcomes the drawback of traditional artificial observation, get rid of the subjectivity of manual reading scale value, due to the flow speed and reduces the error caused by manual measurement, avoid the water flow rate on the measurement results of adverse effects, improves the accuracy of measurement, obtain more accurate testing data of ship draught.

In this paper, through a lot of research, combined with the convenience of the actual scene and the requirement of sampling stability, according to machine vision technology, the collected images are analyzed. According to the different clarity of river water body, the detection method of inland ship draft depth is designed. For transparent water body, when the water line is bright and smooth, the global image edge detection and Hough line detection are used. Firstly, the S-ray method is used. The experiment shows that when the double threshold of Sobel operator is set at (18, 54), the value obtained by edge detection is the most rational. The suspected waterline can be obtained by edge detection. In order to determine the waterline, Hough

transform should be used to get the binary image of a single image. The total number of white pixels in each line is counted and the proportion of bright pixels is set. From the results, we can see that the statistical proportion of continuous bright pixels is more than 50%, and the suspected draught line is determined as a single frame draught line. Then we compare and analyze the difference between the actual inland ship draught depth and the experimental results. Through the above error analysis, we find that the error value of the two is 0.001m. The error requirement is far less than the expected ± 0.01 m. It can be seen that the edge detection method used in the detection system in this paper can meet the needs of actual detection because of the low error and high accuracy of the actual draft line of the detected ship in the case of clear inland waters.

Aiming at the turbid inland river water body, i.e. the clarity of the river water body is not high, the water line fluctuates greatly and the brightness of the water line is low, so we should use binocular stereo vision three-dimensional measurement method to detect the draft depth of the ship. Firstly, the abnormal data are filtered, and the horizontal straight line and sinusoidal function curve are used to simulate the water surface and the draft profile of the ship respectively. Secondly, the uniformly distributed random number is added to simulate noise. Finally, through median filtering and output filtered image, it can be seen from the output filtered image that the noise generated in the process of ship draught imaging is greatly reduced, that is, median filtering has good filtering effect on random noise generated in the process of ship draught imaging. Least squares are used for regression prediction and fitting processing of information. It is found that after fitting, the connection can be effectively identified. Continuous anomalous data have little influence on the normal data section. Finally, the experimental prediction of the intake depth of inland watercraft is obtained through the processed data. Compared with the actual intake depth of the ship, it is found that the error between the two is relatively small, fluctuating up and down ± 0.1 m, and is close to the actual intake depth of the ship. Therefore, when the water body fluctuates greatly, binocular stereo vision three-dimensional measurement is adopted. It can detect the draft depth of the ship very well.

In this paper, machine vision technology is used to detect the draft depth of inland ships. It can not only accurately detect the draft depth under normal conditions, but also has strong applicability to exposure, scratches on the surface of the ship, and the location of the water trace is not obvious. The detection system in this paper has good prospects for popularization and application in inland river lock, diving controlled channel, port and load reduction base areas where strict control of ship draught is needed. Especially for the design of artificial structures with clear draught control standards, such as ship lock and lift, it plays an important role in ensuring the safety of facilities and smooth navigation.

5. Conclusions

In this paper, according to different river water conditions, different theories are adopted to design the inland ship draft depth detection system, so that the ship managers can efficiently and accurately detect the ship draft depth, and can timely detect the phenomenon of ship over draft, so as to avoid the danger to the river course and the staff on board. In this paper, the detection system uses

machine vision technology to realize the high-precision detection of the draft depth of inland river vessels under clear and turbid water conditions through the detection method of draft depth based on edge detection and binocular stereo vision three-dimensional detection. It provides an important reference for real-time monitoring and early warning of ship draft, and reduces the occurrence of ship grounding, antennae and other safety accidents. The safety of ships and waterways is of great significance to the shipping industry.

Acknowledgement

Foundation item: Scientific and technological project of Henan Province (No. 162102210082); Research Program for Advanced Talents of North China University of Water Resources and Electric Power (No. 40427).

References

- [1] Baigvand, M., Banakar, A., Minaei, S. 2015. Machine vision system for grading of dried figs. *Computers & Electronics in Agriculture* 119 (C):158-165.
- [2] Bhatt, A.K., Pant, D.2015. Automatic apple grading model development based on back propagation neural network and machine vision, and its performance evaluation. *Ai & Society* 30 (1):45-56.
- [3] Boss, Z., Wang, J.L., Ren, X.F. 2017. Design of standard parts recovery system based on machine vision. *Automation and Instrumentation* (8):32-33.
- [4] Chen, Y.D., Chen, F., Tang, W.J. 2016. Simulation study on ship navigation stability control on water. *Computer simulation*33 (11): 203-207.
- [5] Cheng, J., Zhang, X.Y., Li, R.X. 2015. Meta-learning-based software defect prediction and recommendation method. *Journal of China Academy of Electronic and Information Technology* 10 (6):620 -627.
- [6] Goren, O., Calisal, S. M., Danisman, D.B. 2017. Mathematical programming basis for ship resistance reduction through the optimization of design waterline. *Journal of Marine Science & Technology* 22(3):1-12.
- [7] Haase, M., Binns, J., Thomas, G. 2016. Wave-piercing catamaran transom stern ventilation process. *Ship Technology Research* 63(2):71-80.
- [8] Howarth, M.S., Brandon, J.R., Searcy, S.W. 2015. Estimation of tip shape for carrot classification by machine vision. *Journal of Agricultural Engineering Research* 53(2):123-139.
- [9] Keenan, S. J., Diamond, J, Mccluggage, W.G. 2015. An automated machine vision system for the histological grading of cervical intraepithelial neoplasia. *Journal of Pathology* 192(3):351-362.
- [10] Khalili, K., Vahidnia, M.2015. Improving the Accuracy of Crack Length Measurement Using Machine Vision. *Procedia Technology* 19:48-55.
- [11] Li, Z., Mao, T., Liu, T. 2015. Comparison and optimization of pig mass estimation models based on machine vision. *Transactions of the Chinese Society of Agricultural Engineering* 31(2):155-161(7).
- [12] Pérez, L., Rodríguez, Í, Rodríguez, N. 2016. Robot guidance using machine vision techniques in industrial environments: A Comparative Review. *Sensors* 16(3):335.
- [13] Qureshi, W.S., Payne. 2016. Machine vision for counting fruit on mango tree canopies. *Precision Agriculture* 17(3):1-21.
- [14] Chen D.S., Zhu J.H., Li J.X., et al. 2016. Inland ship draft detection based on multibeam echo sounder in pitchup setting. *Port & Waterway Engineering* 34(1):152157.
- [15] Lu L., Xiong M.D., Gao Y.F., et al. 2017. Research on ship draft check system of ship lift. *Yangtze River* 48(20):7174+79.
- [16] Wu J., Shu Y.J., Zhou Y.H. 2017. Ship's draft measurement method based on double probe differential scanning sonar for hanging type side ship. *Transducer and Microsystem Technologies*. 36(6):3234.
- [17] Yan, L.L., Xin, L. I., Luo, Y. 2015. Jacket effects on heave, roll and pitch motions of a new floating deep-draft semisubmersible concept. *Journal of Ship Mechanics* 19(6):664-676.
- [18] Yang, X.F., Lin, Z.Q., Zhou, C.Y. 2015. A review of circulation suppression techniques for modular multilevel converters MMC. *Journal of Power supplies*13 (6): 58-68.
- [19] Zheng, K., Du, C., Li, J. 2015. Underground pneumatic separation of coal and gangue with large size (≥ 50 mm) in green mining based on the machine vision system. *Powder Technology*278:223-233.
- [20] Zhou, Q.S., Chen, J.J., Xu, X.Y. 2015. Coin sorting technology based on machine vision. *Communication Power supply Technology* 32 (4): 74-77.

Regional Coordination Control Method of Rail Transit Signal Based on Unmanned Driver

Yongcheng Wu^{a*}, Changqiong Yang^b, Lanlan Huangfu^c

^aGansu Engineering Research Center of Industrial Transportation Automation, Lanzhou Jiaotong University, Lanzhou 730070, China

^bKey Laboratory of Opt-Electronic Technology and Intelligent Control Ministry of Education, Lanzhou Jiaotong University, Lanzhou 730070, China

^cSchool of Engineering and Automation, Lanzhou Jiaotong University, Lanzhou 730070, China

Received OCT 16 2019

Accepted JAN 3 2020

Abstract

In order to reduce the traffic congestion of driverless vehicles in rail transit and reduce the probability of traffic accidents of driverless vehicles, a coordinated regional control method based on driverless rail transit signal is proposed. The operation structure of driverless rail transit is designed based on vehicle network technology. The vehicle information is obtained by radio frequency identification equipment and the wireless communication technology is used. Instructions are conveyed to the built-in speed controller and steering controller of the vehicle. Vehicle speed, steering and running phase are controlled by the unmanned automatic tracking control module and the signal priority control module of the unmanned vehicle. The photoelectric sensor is used in the unmanned automatic tracking control module to convert the test results of the collected rail traffic signal into the lateral deviation to obtain the driving advance of the vehicle. Aiming at the information, adding the "driver" model to automatically control the state of the vehicle; the signal priority control module of the driverless vehicle chooses the vehicle to restore the priority request through the signal priority request and processing flow, adjusts the vehicle operation phase, and ensures the driverless vehicle to pass as first as possible according to the signal priority strategy of the rail transit. The experimental results show that the difference between the angle command and the actual angle is 20°. Within the range, the front wheel angle error does not exceed 1.45°. The average stability of the method is 0.9747, and the stability is good.

© 2020 Jordan Journal of Mechanical and Industrial Engineering. All rights reserved

Keywords: Driverless; Rail Transit; Signal Area; Coordination Control; Automatic Tracking; Priority Control;

1. Introduction

Rail transit is a kind of transportation means that carries run on "specific" tracks, which also produces support and guidance. Transportation develops with the development of society. Safety is a concern for all people. In order to ensure the safety of no vehicles in rail transit, it is necessary to coordinate the control of vehicles in the signal area of rail transit so as to realize the safe travel of vehicles [1]. Unmanned driving technology just meets the actual requirements. Unmanned driving technology refers to the use of on-board sensors to obtain relevant data and information in the course of driving, according to the acquired information, to process, analyze, and control the steering and speed of the vehicle, so as to make the vehicle run safely on the road. Since the 1970s, developed countries have begun to study driverless cars and made some progress. As early as the 1980s, China began to develop driverless cars. In 1992, it developed the first driverless car in China, which marked a new technological breakthrough in the field of driverless vehicles in China [2]. This means that the level of driverless vehicles in China has been improved. It is at the advanced level in the world. Unmanned driving has three advantages. Firstly, it can achieve precise control of rail transit transportation, avoid artificial abnormal operation [3]. Secondly, it can save

manpower and material resources and liberate a large number of labor forces. In addition, it can prevent rail transit accidents. Because unmanned vehicles can adapt to narrower streets, there will be no traffic jams and reduce energy and save a lot of money for the government [4].

Unmanned vehicle control technology is a multi-disciplinary and multi-industry integrated technology [5], which integrates vehicle engineering, computer technology, automatic control theory, architecture theory and other theories and technologies. It has not only huge military value, but also broad industrial and civil value. It is a national computer science, recognition mode and intelligence. The development level of technology can be controlled, which is also an important symbol to measure a country's scientific research strength and industrial level [6]. Therefore, it is necessary to study the coordinated control method of unmanned driving in signal area of rail transit.

2. Materials and methods

2.1. Design of unmanned rail transit based on vehicle networking technology

2.1.1. Design of operation structure of unmanned rail transit

Unmanned rail transit consists of control center and individual vehicle [7]. The control center should load

* Corresponding author e-mail: 18693103237@163.com.

transmitter, central processing unit, GIS live analysis and alarm. The control center receives the signal from the vehicle, transmits the information to the central processing unit for processing, and gives orders to the vehicle by combining the GIS geographic reality analysis. If an accident occurs, the alarm will automatically alert the relevant departments to take measures [8]. Individual vehicles should be equipped with radio frequency identification equipment to acquire surrounding information. Secondly, receivers should be installed to transmit vehicle reality and receive commands. In addition, relevant controllers should be installed to control vehicle acceleration, deceleration and braking. Induction system and digital image processing technology should also be installed, which can not only automatically switch doors for passengers to get on and off, but also can monitor vehicle driving situation in real time and report to the control center. Vehicle individuals should include automatic tracing module and vehicle signal priority control module to realize vehicle unmanned automatic tracing and signal priority control [9]. The operation design structure of unmanned rail transit is shown in Fig. 1.

In Fig.1,the control center give orders to the vehicle individual, then the Transceiver convey information back to the control center.

2.1.2. Unmanned rail transit operation process

In the course of driving, vehicle information is acquired by sensing the surrounding vehicles according to the radio frequency identification equipment [10]. The wireless communication technology report is sent to the control center for processing. The control center calculates the auto-tracing and vehicle signal priority control strategy, analyses the speed predetermined value, the angle predetermined

value and the vehicle running condition, and transmits the instructions to the built-in speed controller and steering controller of the vehicle through the wireless communication technology. Through the unmanned auto-tracing control module and the unmanned vehicle, the control center transmits the instructions to the speed controller and steering controller of the vehicle. Vehicle signal priority control module to achieve precise parking and rail connection [11]. Vehicle driving data in the form of images are available in the vehicle. If an accident occurs, the vehicle-related central processing unit will report the situation to the control center through wireless communication, and the control center will analyze and make instructions [12]. The operation flow chart of unmanned rail transit is shown in Fig. 2.

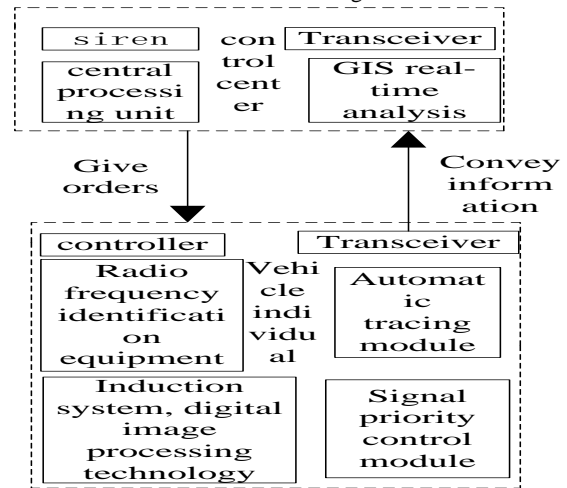


Figure 1. Operational design structure of unmanned rail transit

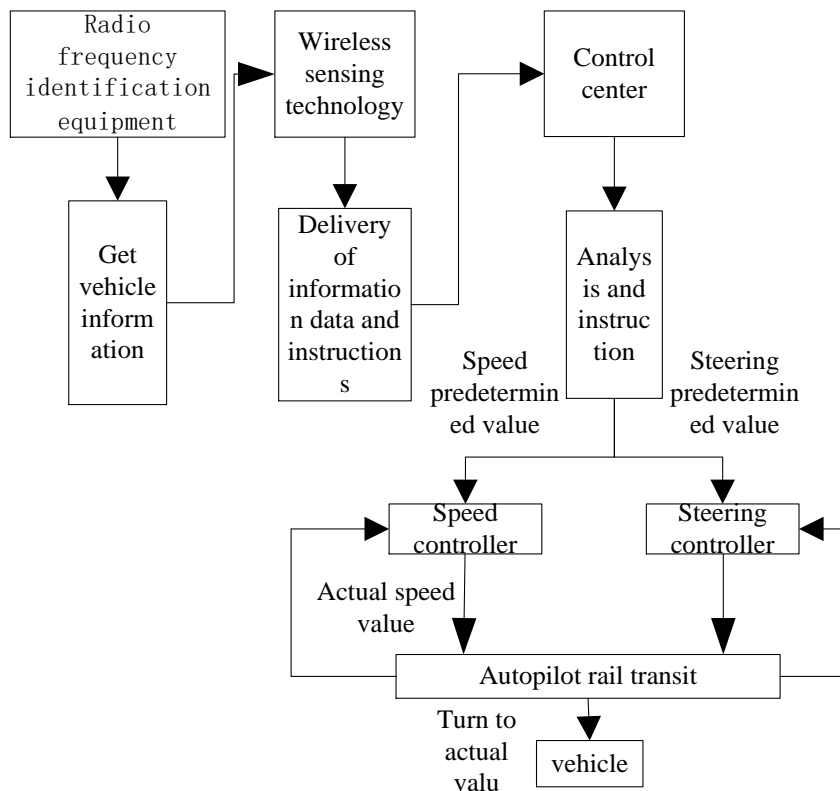


Figure 2. Flow chart of unmanned rail transit

2.2. Unmanned automatic tracking control module

2.2.1. Composition of automatic tracking module

The automatic tracing module of an unmanned electric vehicle is mainly composed of sensor module, control module and actuator [13]. The structure of the module is shown in Fig. 3.

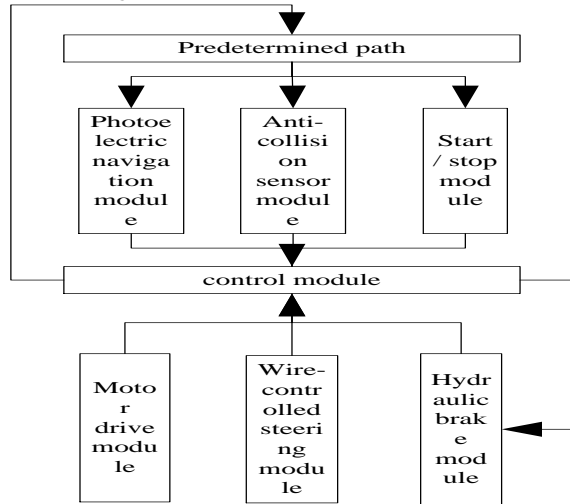


Figure 3. Structure diagram of automatic tracing module for self-driving electric vehicle

The sensor module is mainly composed of photoelectric navigation module, collision prevention sensor module and start/stop module. The control module is mainly composed of Micro Auto Box controller from dSPACE Company. The actuator mainly consists of click-drive module, line-controlled steering module and hydraulic braking module. Photoelectric navigation module is mainly composed of light source, photoelectric sensor, shading accessories, signal acquisition and power supply, among which the light source is the most important part [14].

The light source part adopts 48 high-brightness white light LED. For the photoelectric sensor, adopts 40 photo resistors (5 mm in diameter, working temperature range: -30°C-+70°C) with 2% precision cds5562 are arranged at an equidistance of 7.68 mm. Based on the principle that the resistance value decreases when the light intensity of the photosensitive resistance is enhanced, the voltage change at both ends of the photosensitive resistance is measured through the half-bridge partial voltage to reflect the intensity of light as well as the change of light intensity [15]. The measuring circuit of photosensitive resistance is shown in Fig. 4.

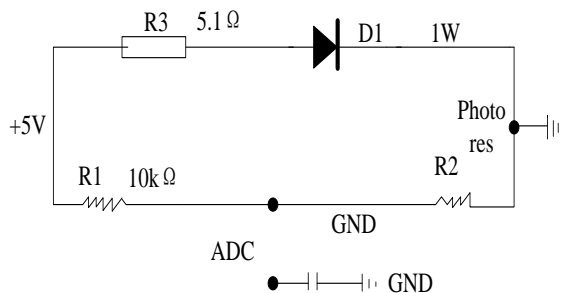


Figure 4. measuring circuit of Guang Min resistance

The system uses visible light source, so outdoor sunlight and adjacent light source will interfere with the signal in the

module, and the path sensor module needs to be shaded. By adding a black plastic sleeve to each photosensitive resistor to avoid interference from adjacent light sources, the interference of sunlight to the unmanned automatic tracking control module can be prevented [16].

2.2.2. Principle of automatic tracing control

The principle of automatic tracking driving control is shown in Fig. 5. The control module controls the vehicle steering according to the preview information of preview point P. The speed of the current car is the acceleration, and K_p is the upper controller, and $M(s)$ and $F(s)$ are the control module and the actuator, respectively. $M_g(s)$ is the train quality:

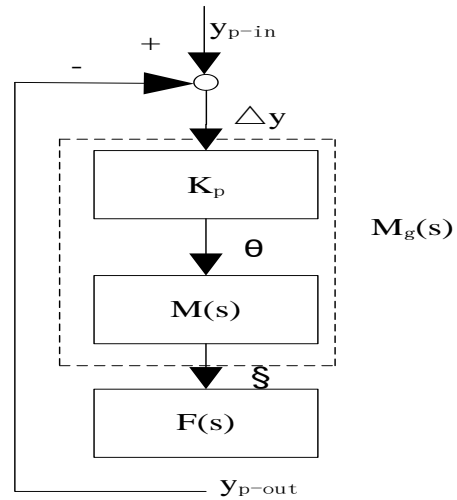


Figure 5. principle of auto-track-seeking driving control for vehicles

The function of the controller module is to convert the test results of photoelectric sensors into transverse Δy , obtain the preview information of vehicle driving, add the “driver” model, automatically control the state of the vehicle, carry out program design, and control the vehicle driving according to the predetermined conditions [17].

2.2.3. Lateral deviation calculation

The controller assigns 40 sensor channels to the corresponding digital y_i ($i=1, 2, \dots, 40$), compares the received 40 channel data with the preset threshold U , and obtains the corresponding control threshold a_i as follows:

$$a_i = \begin{cases} 1 & U_i > U \\ 0 & U_i \leq U \end{cases} \quad (1)$$

Then the lateral deviation Δy is expressed as:

$$\Delta y = d \sum_{i=1}^{40} y_i a_i \sum_{i=1}^{40} (a_i - 20) \quad (2)$$

In the formula, d denotes the distance between adjacent photoelectric sensors.

2.2.4. Vehicle model

The horizontal vertical excitation of the left and right wheels of an automobile is the same, and the vehicle is symmetrical about the longitudinal axis of the vehicle, that

is, the vehicle does not have roll vibration, no lateral displacement, no yaw vibration, and is regarded as a vehicle body system for the consistency of the motion between the passenger and the vehicle body. And the body system is regarded as a rigid sprung mass regardless of the effect of the engine and the drive train on the body. The body's contact mass is zero, that is, the front and rear parts of the body are independent of each other. The axle and the main wheel associated with it are considered to be unsprung masses and the wheels are in point contact with the road surface on the centre line. due to the damping of the tire with respect to the damping of the vehicle shock absorber, And therefore only the stiffness of the tire is taken into account. By the above assumptions, the complex vehicle system becomes a relatively simple two-degree-of-freedom suspension system simplified model. The two-degree-of-freedom vehicle model and the preview point p model are used to express the transfer function of the vehicle model as follows:

$$F_{\zeta}(s) = \frac{0.012s + 2.17}{0.0001s^3 + 0.04s^2 + 2.93s} \quad (3)$$

2.2.5. Driver model

Under zero initial condition, the ratio of Laplace transform of output of linear time-invariant system to Laplace transform of input is defined as the transfer function of linear time-invariant system. Namely: The exact model transfer function of driver linear control is simplified as follows:

$$M_R(s) = K_R \frac{1 + T_2s}{1 + T_1s} e^{-s\tau} \quad (4)$$

In the formula, K_R denotes the human factor, T_2 denotes the lead time, T_1 denotes the lag time, and τ denotes the delay time. Considering the sampling frequency (2 ms) of the controller, the delay link can be neglected, so the transfer function of the driver model is changed to:

$$M_R(s) = K_R \frac{1 + T_2s}{1 + T_1s} = K_P K_M \frac{1 + T_2s}{1 + T_1s} \quad (5)$$

The driver model essentially consists of two parts, one is the proportional link K_P , which is mainly the proportional gain in angle conversion, the other is a correction link

$M(s) = \frac{K_M(1 + T_2s)}{1 + T_1s}$, in which K_M is the correction gain coefficient.

(1) Proportional link

According to the angle conversion, the relationship between the angle β of pinion and the lateral deviation Δy measured by the sensor is as follows:

$$\beta = i_w \arctan \frac{2L\Delta y}{(\Delta y^2 + D^2)^2 - 4L^2\Delta y^2 - B\Delta y} \quad (6)$$

In the formula, i_w represents the transmission ratio of the gear-rack steering system of a vehicle, $i_w = 13.8$. According to the definition of parameters of driverless electric vehicle, the relationship between steering gear angle and transverse deviation of photoelectric sensor is as follows:

$$\beta = f(\Delta y) = K_p \Delta y = 6135\Delta y \quad (7)$$

(2) Correction link

Through practical research, it is found that the stability of the method is enhanced after the correction step. The open-loop coefficient transfer function $G_1(s)$ expression without correction link is formula (8).

$$G_1(s) = K_p F_{\zeta}(s) = \frac{6135(0.012s + 2.17)}{0.0001s^3 + 0.04s^2 + 2.93s} \quad (8)$$

The transfer function $G_2(s)$ of the open-loop system with the correction link is expressed as an expression (9).

$$G_2(s) = M_R(s)F_{\zeta}(s) = \frac{4046(0.012s + 2.17)(0.2s + 1)}{(0.0001s^3 + 0.04s^2 + 2.93s)(0.4s + 1)} \quad (9)$$

2.3. Signal priority control module of unmanned vehicle

2.3.1. Signal priority request and processing flow

The signal priority control module of driverless vehicle consists of the following parts:

- (1) Vehicle-mounted equipment. It includes vehicle information module, signal priority module and WIFI antenna.
- (2) Signal control module of driverless vehicle road intersection. It includes signal controller of driverless vehicle, information acquisition module (four groups of detectors: request detector P1, request detector P2, request detector P3, request detector P4) and special signal lamp.
- (3) Road signal control module at intersection. It includes traffic signal controller, traffic signal lights and intersection correlation detector and other equipment.
- (4) Central control module. It includes driverless vehicle signal center and road traffic signal control center.

The P1 detector is set at the S_{P1} position from the parking line of the driverless vehicle. The driverless vehicle passes through the P1 point and immediately sends out a priority traffic request. The signal machine gives priority to the recovery. The P2 detector is set at the S_{P2} position from the parking line of the driverless vehicle. This signal is sent out. The signal machine should ensure the response of the priority traffic confirmation if the priority traffic is ensured. The signal plane should adjust the phase before

point D, the P3 detector should be set 2 meters behind the parking line of the driverless vehicle to detect whether the driverless vehicle enters the intersection, the P4 detector should be set at the exit, and the distance from the intersection is about 35 meters, which is used to verify that the driverless vehicle passes through the intersection smoothly [18]. Expressed by formula as follows:

$$S_{P2} = S_b + S_{r+s} \tag{10}$$

$$S_{r+s} = v_{t2}(t_r + t_s) + \frac{1}{2}a(t_r + t_s)^2 \tag{11}$$

$$v_{t2} = v_0 + at_p \tag{12}$$

$$S_{P1} = S_{P2} + v_1 t_p + \frac{1}{2}at_p^2 \tag{13}$$

In the formula, S_b denotes the braking distance of driverless vehicle (about 60 m), S_{r+s} denotes the driving distance of vehicle response time and module response redundancy time, t_r denotes the driving time of driverless vehicle, takes 2 s, t_s denotes module response redundancy time, takes 1 s, v_1 denotes the speed of driverless vehicle at P1, a denotes deceleration acceleration (negative value), t_p denotes the minimum phase time (Depending on the actual configuration of the intersection), v_{t2} represents the speed of the driverless vehicle at point P2.

2.3.2. Signal control strategy

According to the delay time, full load rate and operation scheduling plan of driverless vehicles, the priority of driverless vehicles at intersections is divided into three levels: high priority at level 1, low priority at level 2 and no priority at level 3. When two conflicting traffic priority requests are received at the same intersection, the higher priority requests are responded to. According to the regional traffic demand and background traffic of driverless vehicles, the current road service level is judged in real time. When the priority request is received, the priority signal of driverless vehicles is determined according to the current service level. Generally, the first-level priority requests should ensure the first-level priority, the second-level priority requests should consider whether to ensure the first-level priority according to the actual situation, and the third-level priority requests should consider not to ensure the first-level priority. Therefore, the signal control of driverless vehicles at intersections should adopt conditional active signal priority [19].

Active control signal priority strategies usually include green light extension, red light shortening, insertion phase and jump phase. On the premise of guaranteeing the minimum green light time of intersecting road phase and the safe green light interval between phases, according to the real-time arrival time of driverless vehicles and the current stage of signal control, the selection rules of signal control strategy for driverless vehicles are formulated, as shown in Table 1.

Table 1. General signal control policy selection rule

Regional traffic condition	Priority 1	Priority 2	Priority 3
Normal	1/2/3/4	½	
More congestion	1/2/3/4	½	
Congestion	1/2		
Stop up			

Note: No-no priority, 1-green light extension, 2-red light shortening, 3-insertion phase, 4-jump phase.

(1) The green light is extended. When the driverless vehicle arrives at the end of the traffic phase (green light), the module extends the length of the notification phase to make the driverless vehicle pass smoothly.

(2) The red light is shortened. When the driverless vehicle arrives at the non-traveling phase, the module opens the traveling phase ahead of time (the green light turns on early), and tries to let the driverless vehicle pass preferentially.

(3) Insert phase. When an unmanned vehicle is detected to arrive at a non-passing phase, a special phase for unmanned vehicle is inserted after the end of the current phase. The length of the phase is calculated for the whole vehicle of the unmanned vehicle only. When the insertion phase is finished, the subsequent phase interrupted by the insertion phase is continued and the original phase sequence is run.

(4) Jump phase. When an unmanned vehicle arrives at its non-passing phase, it jumps directly to the driving phase of the unmanned vehicle at the end of the current phase with the minimum release time. At that time, the signal of the Chang'an Cleaning Detector and the whole vehicle can be calculated. When the driving phase of an unmanned vehicle ends, it runs in the original phase sequence [20].

3. Results

3.1. Automatic tracking control effect

During the experiment, an unmanned electric prototype car was used to drive counterclockwise along the trajectory shown in Fig. 6, and its speed was maintained at 5 km/h.

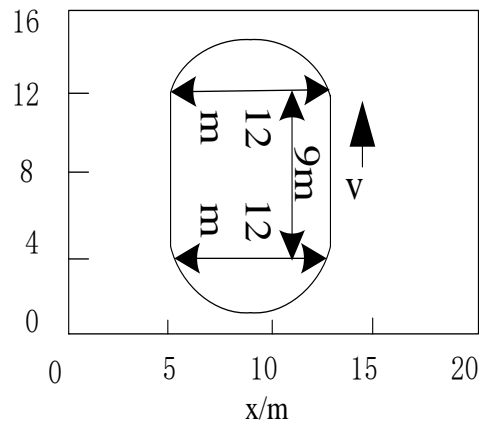


Figure 6. Vehicle experiment path

Through the above experimental path, two ways are used to test the effect of this method on the automatic tracking control of the experimental driverless vehicle. Firstly, the effect of this method on the automatic tracking control of the driverless vehicle is judged by detecting the difference between the angle command and the actual angle. The test results are shown in Fig. 7.

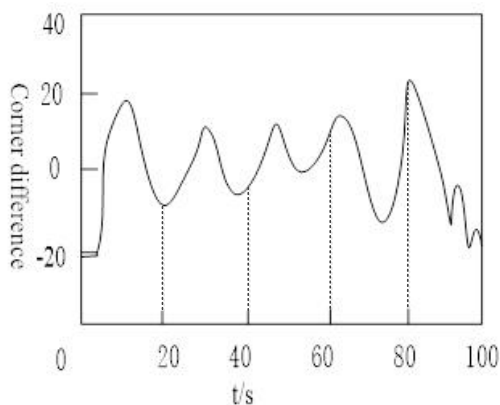
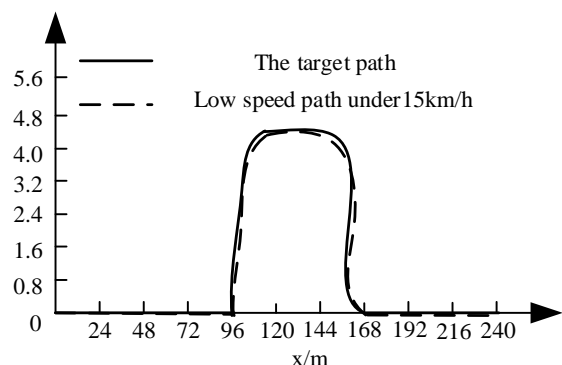
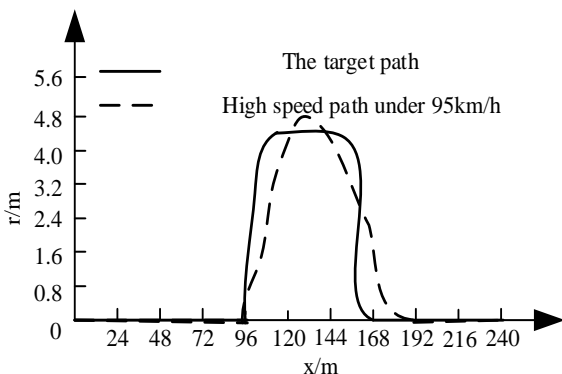


Figure 7. Corner instruction and actual corner difference

From Fig. 7, it can be seen that the difference between the measured angle command and the actual angle during the whole experiment is 20°. Within the range, that is, the front wheel angle error does not exceed 1.45°. It can be seen that the control effect of this method is better for the experimental unmanned vehicle. Secondly, starting from the experimental speed of the driverless vehicle itself, the effect of this method on the automatic tracking effect of the driverless vehicle is validated. The tracking results at low speed of 15 km/h and high speed of 90 km/h are selected and compared to test the control effect of this method on the automatic tracking of the driverless vehicle at different speeds. The results of driverless vehicle tracking at two speeds are shown in Fig. 8.



(a) Automatic tracing effect at low speed



(b) Automatic tracking effect at high speed

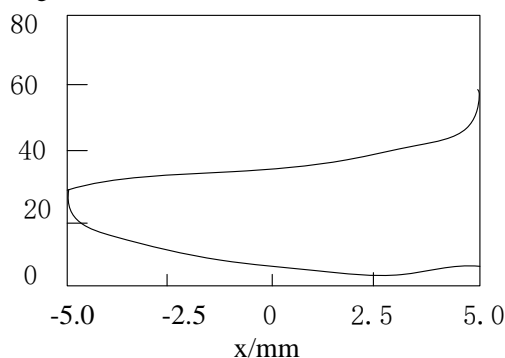
Figure 8. Automatic tracking effect at different speeds

From Fig. 8, it can be seen that although the auto-tracing effect of driverless vehicles at high speed is slightly lower

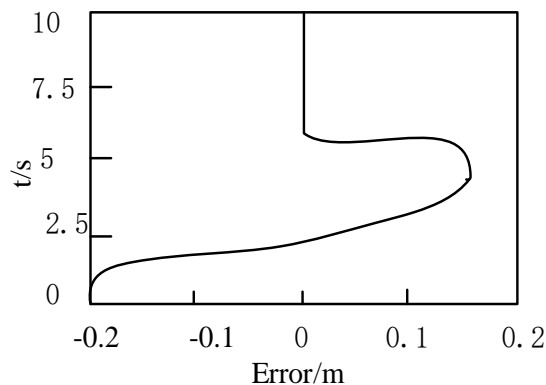
than that of driverless vehicles at low speed, the error of auto-tracing at different speeds is smaller and the effect of auto-tracing is better. It shows that the method in this paper has better effect of controlling the auto-tracing of driverless vehicles. The method in this paper is more effective and can realize the auto-tracing effect of driverless vehicles. Vehicle automatic tracing control ensures the safe and smooth operation of driverless vehicles in the signal of rail transit area.

3.2. Horizontal control in the process of automatic tracking control

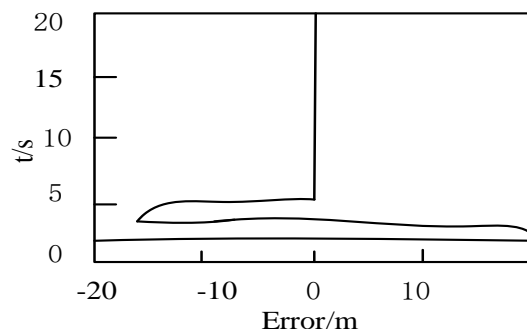
In order to test the effect of horizontal control of unmanned vehicle in this method, it is necessary to detect the rear wheel speed, lateral displacement tracking error and front wheel rudder angle of experimental unmanned vehicle in the process of lateral driving. The test results are shown in Fig. 9.



(a) Rear wheel speed



(b) Transverse displacement tracing error



(c) Front wheel rudder angle

Figure 9. Horizontal control result

From Fig. 9, it is known that when the longitudinal speed of the car body changes, even when the longitudinal speed

is zero, the driverless car body can still track the established track automatically in the lateral direction, with better dynamic characteristics and stable tracking accuracy, which shows that the lateral control effect of the driverless car body under the automatic tracking control is better.

3.3. Contrast of three methods of signal control

In order to verify the signal control status of the intersection, a city intersection is selected for detection. The effectiveness of this method in signal priority control of driverless vehicles is tested by comparing the method, timing signal control method and first-come-first-service control method. The test results are shown in Table 2.

As can be seen from Table 2, compared with the first-come-first-served control method and the timing signal control method, the evaluation indexes have been greatly improved after using the priority control signal method. The average traveling time of emergency driverless vehicle in this method is 10.11% less than that of first-come-first-service control method, and the average traveling time of ordinary driverless vehicle is 17.6% less, and the average stopping time is 17.6% less than that of the first-come-first-service control method. The number of vehicles decreases by 21.56%, which shows that the method of priority control signal has better effect, and the first-come-first-service control method has worse effect. At the same time, the excessive start-up and stop behavior of driverless vehicles under the control of first-come-first-service method is liable to cause traffic accidents.

Compared with the method of timing signal control, the evaluation index of each phase has been improved after using the method of priority control signal. The average passing time of emergency driverless vehicle in this method is 13.1% less than that of timing signal control method, the average passing time of ordinary driverless vehicle is 14.5% less, and the average parking times are 20.6% less. This shows that this method has priority. The effect of control signal is good. To sum up, the priority control signal based on this method can realize the priority of driverless vehicles on the right of passage at intersection time and reduce the interference of driverless vehicles to other vehicles.

3.4. Method energy consumption comparison

In order to verify the low energy consumption of this method in controlling unmanned vehicles, the method, the control method based on fuzzy control and the control method based on image processing technology are compared. The comparison results are shown in Fig. 10.

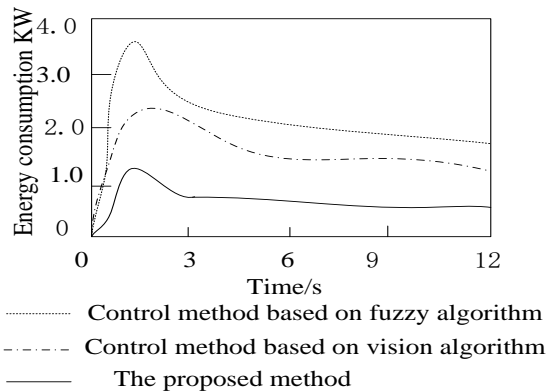


Figure 10. Energy consumption comparison results

As can be seen from Fig. 10, the energy consumption of this method is lower than that of the two comparison methods at the same time. That is, this method can effectively optimize the energy consumption while effectively controlling the unmanned vehicle, and reduce the energy consumption of controlling the unmanned vehicle.

Table 2. Comparison of results between three methods

Control strategy	Numb er of experi ments	Emergency of driverless passage (seconds/vehicle)	Average time of driving vehicles(seconds/veh icle)	Average passage of ordinary self-parkin ge times/s
Timing signal control method	1	45.6	50.1	0.87
	2	44.8	49.8	0.84
	3	44.1	49.1	0.85
	4	43.8	48.9	0.81
	5	43.1	48.6	0.83
	6	42.6	47.5	0.8
	7	41.7	47.1	0.79
	8	41.3	46.9	0.76
	Mean value	43.37	48.50	0.81
	Varian ce	2.21	1.47	0.0012
First-come-first-serve control method	1	40.6	60.5	0.91
	2	40.1	59.7	0.89
	3	39.5	54.3	0.87
	4	38.9	55.6	0.85
	5	39.1	57.8	0.81
	6	38.7	58.6	0.92
	7	38.2	59.4	0.86
	8	37.9	54.1	0.85
	Mean value	39.12	57.50	0.87
	Varian ce	0.83	6.30	0.0012
This paper method	1	31.9	50.1	0.7
	2	31.5	49.6	0.65
	3	31.1	49.7	0.71
	4	30.1	49.3	0.76
	5	30.9	48.1	0.79
	6	30.4	48.6	0.67
	7	30.8	48.5	0.68
	8	30.5	47.6	0.64
	Mean value	30.9	48.9375	0.7
	Varian ce	0.30	0.66	0.0009

3.5. Method stability comparison

In order to verify the control performance of the proposed method, the stability of the three methods is compared and analyzed, and three road types are set up: straight line, turn around and bend. The stability of driverless vehicle acceleration controlled by three methods is analyzed. The results of acceleration comparison are shown in Table 3.

From Table 3, it can be seen that under the three road types, several experiments have been carried out. Compare the average value of the Forthright, Turn-around turn, and the Winding course, the mean stability of the proposed method is $(0.9762+0.9725+0.9752)/3=0.9747$. According to the above calculation, the mean stability of the two methods is 0.7081 and 0.4792 respectively. Through comparison, it is found that on three different types of roads, this method controls the driverless vehicle. Vehicle stability is the best.

Table 3. Comparative results of different methods for controlling self-driving vehicles

Number of experiments	This paper method		Self-driving vehicle Control method based on Fuzzy Control			Control method of self-driving vehicle based on Image processing Technology			
	Forthright	Turn-around	Winding course	Forthright	Turn-around	Winding course	Forthright	Turn-around	Winding course
1	0.99	0.95	0.99	0.78	0.79	0.73	0.59	0.58	0.54
2	0.98	0.97	0.97	0.65	0.74	0.74	0.54	0.51	0.51
3	0.99	0.98	0.98	0.69	0.71	0.71	0.51	0.53	0.42
4	0.96	0.96	0.96	0.74	0.75	0.76	0.49	0.54	0.48
5	0.97	0.99	0.97	0.71	0.68	0.71	0.43	0.47	0.49
6	0.95	0.98	0.99	0.73	0.67	0.69	0.42	0.42	0.4
7	0.99	0.96	0.98	0.61	0.71	0.68	0.49	0.41	0.39
8	0.98	0.99	0.96	0.64	0.69	0.69	0.46	0.49	0.38
Mean value	0.9762	0.9725	0.9752	0.6937	0.7175	0.7137	0.4912	0.4937	0.4512

4. Discussions

Unmanned vehicle is an integral part of intelligent transportation system in the future. It is necessary to

coordinate and control the unmanned vehicle in the signal area of rail transit. Therefore, this paper proposes a coordinated control method for driverless vehicles in the signal area of rail transit. Firstly, the operation structure and process of the driverless rail transit are designed based on the vehicle network technology. The driverless rail transit is composed of control center and individual vehicle. The most important part of the individual vehicle is the automatic tracking control module and the vehicle signal priority control module. Individual vehicle loads radio frequency identification equipment, obtains surrounding information, installs relevant controllers, controls vehicle acceleration, deceleration and braking, installs induction system and digital image processing technology. It can not only automatically switch doors to facilitate passengers getting on and off, but also monitor vehicle driving situation in real time, so as to report to the control center. According to the received information, the control center can divide the vehicle into several parts according to the geographical conditions of GIS. At the same time, the control center also calculates the vehicle speed predetermined value, the corner predetermined value and the vehicle operation condition through the automatic tracking and the vehicle signal priority control strategy. In the light source part of the unmanned auto-tracking control module, the interference of sunlight on the unmanned auto-tracking control module is reduced by shading the path sensor module. Through the calculation of lateral deviation, the preview information of the vehicle is obtained, and the vehicle model and driver model are constructed to control the vehicle running according to the predetermined conditions. The signal priority control module of the driverless vehicle detects whether the driverless vehicle passes through the intersection by establishing the signal priority request and processing flow, and ensures that the driverless vehicle passes through the intersection as first as possible through the signal control strategy.

The experimental results show that the difference between the measured and actual corners of the driverless vehicle controlled by this method is 20°. Within the range, that is, the front wheel angle error does not exceed 1.45°. From the point of view of different speeds of driverless vehicles, the error of automatic tracing is smaller and the effect of automatic tracing is better, which shows that the method in this paper has better effect in controlling the automatic tracing of driverless vehicles. The method in this paper is more effective and can realize the control of the automatic tracing of driverless vehicles and ensure that the driverless vehicles can communicate in the rail transit area. It is safe and smooth to drive on board. In addition, by detecting the rear wheel speed, lateral displacement tracking error and front wheel rudder angle under lateral control, it is found that the driverless vehicle body controlled by this method can still track the established track automatically in the lateral direction when the longitudinal speed of the vehicle body changes, even when the longitudinal speed is zero. The dynamic characteristics are good, and the stable tracking accuracy can reach zero static error. It is shown that the lateral control effect of this method under automatic tracing control is better. Compared with the method in this paper, the control method based on fuzzy control and the control method based on image processing technology, it is found that the energy consumption of this method is lower and the stability is higher, and the control effect of this method is better.

5. Conclusions

This paper presents a coordinated regional control method for urban rail transit signal based on unmanned driving. The operation structure of unmanned rail transit is designed based on vehicle network technology. The operation flow of unmanned rail transit is given. The most important part of the operation structure of unmanned rail transit is the unmanned automatic tracking control module and the signal priority control module of unmanned vehicle. The automatic tracking control module obtains the preview information of the driverless vehicle by calculating the lateral deviation, and realizes the automatic tracking control of the driverless vehicle by combining the vehicle model with the driver model. The signal priority control module of the driverless vehicle establishes the signal priority request and processing flow, detects whether the driverless vehicle passes through the intersection smoothly, and ensures that the driverless vehicle passes as first as possible through the signal control strategy. This method has good control effect on automatic tracing and signal optimization control of driverless vehicles. The method also has high effectiveness. It can realize automatic tracing control of driverless vehicles and ensure the safe and smooth running of driverless vehicles in the signal of rail transit area.

Acknowledgment

The paper was supported by School Level, Youth Science Foundation of Lanzhou Jiaotong University, (NO: 2017039)

References

- [1] Jia, H., Park, B.B., Lee, Y.J. 2015. Coordinated transit signal priority supporting transit progression under Connected Vehicle Technology. *Transportation Research Part C Emerging Technologies* 55(4):393-408.
- [2] Li, S., Xu, R., Yang, R. 2017. Optimizing urban rail transit network operation plans based on transport capacity coordination. *Journal of Southeast University* 47(5):1048-1054.
- [3] Ghanim, M.S., Abulebdeh, G. 2015. Real-Time Dynamic Transit Signal Priority Optimization for Coordinated Traffic Networks Using Genetic Algorithms and Artificial Neural Networks. *Journal of Intelligent Transportation Systems* 19(4):327-338.
- [4] Ye, B.L., Wu, W., Mao, W. 2015. A method for signal coordination in large-scale urban road networks. *Mathematical Problems in Engineering* (3-4):1-15.
- [5] Meng, M., Chen, S., Zhang, L. 2017. Coordinated Control Strategy for Power Supply System of Urban Comprehensive Transportation. *High Voltage Engineering* 43(6):2069-2079.
- [6] Cao, Z., Yuan, Z., Li, D. 2016. Synchronization and coordination optimization model of urban rail transit. *Journal of Southeast University* 46(1):221-225.
- [7] Chen, Z., Weselinski, L.J., Adil, K. 2017. Applying the power of Reticular Chemistry to finding the missing alb-MOF platform based on the (6, 12)-coordinated edge-transitive net. *Journal of the American Chemical Society* 139(8):3265-3274.
- [8] Gonzales, E.J. 2015. Coordinated pricing for cars and transit in cities with hypercongestion. *Economics of Transportation* 4(1-2):64-81.
- [9] Guo, J., Sun, M., Wang, T. 2015. Transportation development and congestion mitigation measures of Beijing, China. *Mitigation & Adaptation Strategies for Global Change* (5):651-663.
- [10] Wu, W., Liu, R., Jin, W. 2016. Designing robust schedule coordination scheme for transit networks with safety control margins. *Transportation Research Part B* 93(4):495-519.
- [11] Gabriel, E., Skitzki, J. 2015. The Role of Regional Therapies for in-Transit Melanoma in the Era of Improved Systemic Option. *Cancers* 7(3):1154-1177.
- [12] Jian, G.J., Lu, L., Sun, L. 2015. Optimal allocation of protective resources in urban rail transit networks against intentional attacks. *Transportation Research Part E* 84(2):73-87.
- [13] Guo, B., Gan, W., Fang, W. 2015. Using Hand Grip Force as a Correlate of Longitudinal Acceleration Comfort for Rapid Transit Trains. *Sensors* 15(7):15755-15771.
- [14] Chen, Z.S., Zhou, J.T., Tim, T.K. 2016. Alignment control for a long span urban rail-transit cable-stayed bridge considering dynamic train loads. *Science China Technological Sciences* 59(11):1759.
- [15] Gao, Z.Y., Fang, J.J., Zhang, Y.N. 2015. Control of urban rail transit equipped with ground-based supercapacitor for energy saving and reduction of power peak demand. *International Journal of Electrical Power & Energy Systems* 67(9):439-447.
- [16] Jiao, Z.D., Gan, C.H. 2015. Risk Assessment of Crowd Crushing and Trampling Accidents in Urban Rail Transit Station Based on DEA. *Applied Mechanics & Materials* 730(1):327-330.
- [17] Wang, R.W., Xun, J., Ning, B. 2019. A train positioning method based on received. *Signal Strength for Urban Rail Transit* 7(1):36-44.
- [18] Ning, B., Jing, X., Gao, S. 2015. An Integrated Control Model for Headway Regulation and Energy Saving in Urban Rail Transit. *IEEE Transactions on Intelligent Transportation Systems* 16(3):1469-1478.
- [19] Bagherian, M., Mesbah, M., Ferreira, L. 2015. Using delay functions to evaluate transit priority at signals. *Public Transport* 7(1):61-75.
- [20] Yao, L.L., Chen, R., Guo, J. 2015. Modeling and Verification of TSSM-Based CBTC Zone Controller for Urban Rail Transit. *Journal of Southwest Jiaotong University* 50(1):27-35.

Unmanned Vehicle Route Tracking Method Based on Video Image Processing

Yiyi Zhu, Na Guo*

School of Digital Media and Creative Design, Sichuan University of Media and Communications, Chengdu 611745, China

Received OCT 16 2019

Accepted JAN 7 2020

Abstract

Most unmanned vehicle path tracking methods ignore video image processing, resulting in a lot of interference information and severe distortion in the original video image, unable to accurately obtain road information, and reducing the accuracy of path tracking. This paper proposes a vehicle path tracking method based on video image processing. The original road condition image is filtered by median filtering method to reduce the interference of noise on image quality; the filtered road condition image is binarized to distinguish the image from the target image and the background image; and the boundary contour of the binary image is extracted by four neighborhood method to obtain the required road condition feature information. At the same time, the computational complexity is reduced. Based on the road condition characteristic information, the preview deviation angle and path curvature are calculated by preview point sequence; the driving speed is determined according to the path curvature, and the longitudinal control is realized; the preview deviation angle is converted into the control quantity of front wheel rotation angle by Pure Pursuit algorithm, and the lateral control is realized. The experimental results show that the driverless vehicle can track the reference trajectory quickly with different reference speeds, and then its position deviation is controlled within 0.05 m. The average energy consumption of path tracking is 355.13 J, which shows that the driverless vehicle using this method can achieve precise path tracking with low energy consumption.

© 2020 Jordan Journal of Mechanical and Industrial Engineering. All rights reserved

Keywords: Video Image; Driverless; Vehicle; Path Tracking; Preview Deviation Angle; Path Curvature;

1. Introduction

In 2017, the World Health Organization assessed road traffic safety in 182 countries around the world. The assessment reports that about 1.24 million people in the world lose their lives in road traffic accidents every year, and nearly 50 million people are injured in traffic accidents. These deaths and injuries have an inestimable impact on the families of victims. It has caused irreparable tragedy to their lives and even their work. The World Health Organization says road traffic accidents are expected to be the seventh leading cause of death in the world by 2030 unless sustained action is taken. Statistical data show that more than 90% of traffic accidents are caused by human factors, such as violation traffic rules, fatigue caused by long-term repetitive driving, limitations of human drivers' perception and congenital delays in driving emergency response [1]. The main causes of road traffic accidents are the wrong operation behavior and so on, and these conditions also lead to a series of traffic problems, such as traffic jams. In order to avoid these problems, it is necessary for vehicles to have advanced functions, such as self-identification of roads, self-planning of driving paths, and self-control of driving, so that drivers can be freed from complex environmental information and cumbersome driving behavior, and get a safer driving experience. Improving the safety technology and safety performance of driving vehicles and reducing road traffic accidents has become a social issue of common concern to governments and research institutions, which is

also one of the important issues facing the development of science and technology [2].

Unmanned vehicles are mainly used to improve road traffic safety, reduce traffic congestion, and to reduce vehicle fuel consumption and environmental pollution. Many countries in the world are supporting the research in the field of driverless vehicles and intelligent transportation technology, mainly including the control research of driverless vehicle path tracking, lane maintenance, vehicle lane change and so on. The purpose of path tracking is to make the vehicle travel along the desired path while ensuring the lateral stability of the vehicle. Its control algorithm is the key of path tracking. The path tracking control algorithm is particularly important for the driverless vehicle. Therefore, path tracking is a key technology in the research direction of the driverless vehicle [3]. Early path tracking methods, such as geometric path planning and rolling path method, are more suitable for indoor robots [4]. However, because the driverless vehicle is a non-holonomic constrained vehicle body, which is constrained by turning radius, angular speed and so on, the path tracking method mentioned above is not applicable to the driverless vehicle. Therefore, unmanned vehicle path tracking method has become a hot research topic of relevant scholars. Jeon et al. took the change rate of lateral deviation and lateral deviation as input of the fuzzy controller, and the former wheel rotation angle as output of the controller to control the driverless vehicle running along the desired path [5]. For example, adopt adaptive sliding mode controller to realize path tracking of unmanned vehicle, and eliminate control

* Corresponding author e-mail: sccm_gn@163.com.

system jitter and external interference according to Lyapunov stability theory [6]. Ojha et al. used model predictive control and forward feedback control to achieve four-wheel steering driverless vehicle path tracking [7] with the objective of minimizing lateral deviation. Depatla uses robust H output feedback control to track the driverless vehicle's path without considering the driverless vehicle's lateral speed. Simultaneously, simulation experiments are carried out. However, there is a big deviation between the theoretical results and the actual situation [8].

Unmanned vehicle path tracking is mainly composed of path recognition, steering control and speed control, and all of these are based on video image processing. Various methods of unmanned vehicle path tracking proposed in the above literature neglect video image processing, resulting in a large number of interference information and serious distortion in the original video image, so the processor cannot be directly used, and cannot accurately acquire road condition information and reduce the accuracy of path tracking. In this paper, a path tracking method for driverless vehicle based on video image processing is proposed. The driverless vehicle receives the preview information processed by video image processing technology, establishes a preview point sequence search model according to the current posture and the relative motion relationship between the preview point sequence and the path. It uses the strategy of multi-point preview to predict the curvature change of the path, and controls the vehicle according to certain rules. Through Pure Pursuit algorithm [9], the control quantity of front wheel rotation angle is calculated to control the steering of driverless vehicle. Finally, the effectiveness of the proposed tracking method is verified by experimental analysis.

2. Unmanned vehicle path tracking method

2.1. Video image processing technology

2.1.1. Wave filtering

Due to the influence of noise, the road condition images collected by the camera contain a lot of interference information. In order to reduce the interference of noise on image quality, software filtering method is used to smooth the image. Median filtering is a method of replacing the gray value at the noise point with the median value of gray value. This method can protect the edge of the image and filter out the noise at the same time. The filtering effect is better than that of mean filtering. Because the subsequent contour extraction requires high image quality [10], the median filtering method is selected in the video image processing technology of tracking unmanned vehicle path.

2.1.2. Binarization

In order to reduce computational complexity, save processing time and extract road information more intuitively, the filtered image should be binarized to get binary image. The gray value and threshold of the pixels in the image should be compared, and the image can be divided into two parts: the target image and the background image [11]. Threshold selection is critical. If the threshold is too high, too many target points are misclassified as background; if the threshold is too low, too many background points are misclassified as targets. Threshold is divided into static threshold and dynamic threshold. The specific process is shown in Fig. 1.

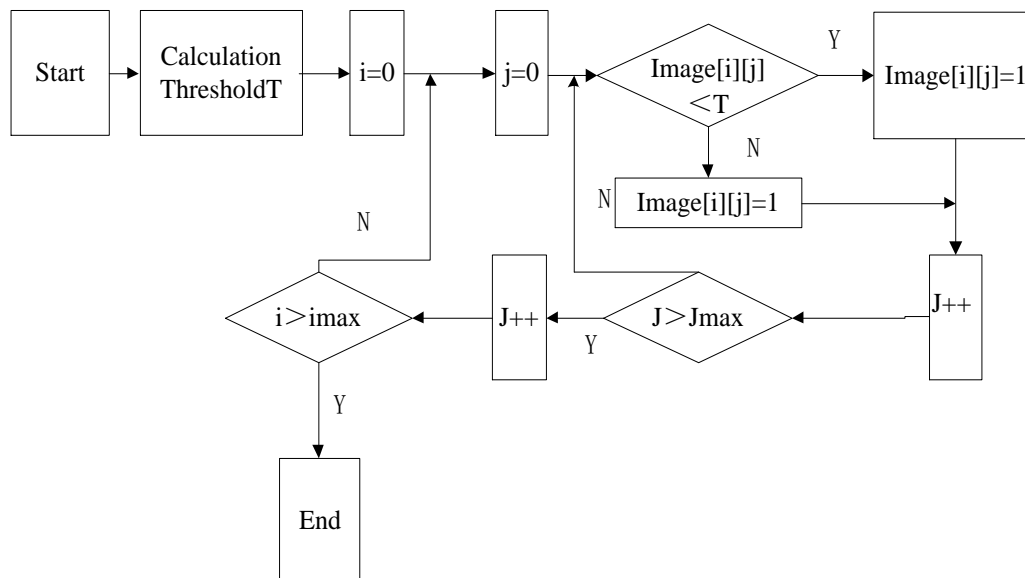


Figure 1. Flow chart of binarization

In Fig. 1, T denotes the threshold, i denotes the image row, j denotes the image column, and $\text{Image}[i][j]$ denotes the gray value at (I,J) . When the gray value at this point is less than the threshold, the value is zero, indicating that the image at that point is the background; on the contrary, the value is 1, denoting that the number of data for the target image is equal to i is reduced by 1, and j_{\max} is equal to the amount of data for j by 1.

In the process of binarization, a dynamic threshold is selected, which is adapted to the driving environment of an unmanned vehicle in real time. The dynamic threshold is obtained by Otsu method, that is, the best threshold is selected from 0 to 255 in turn, and the image is divided into two parts, background and target, so that the variance between the two parts is maximized. The greater the variance between background and target, the greater the difference between the two parts of the image, that is, the best threshold [12]; on the contrary, the selection of threshold is unreasonable. Therefore, to maximize the variance between classes means that the probability of misclassification is the smallest, and Otsu method is simple to calculate, time-consuming and not easily affected by image brightness and contrast [13]. Calculate the normalized histogram p_i of the input image, that is:

$$p_i = \frac{n_i}{N} \quad (1)$$

Among them, n_i and N are target image and background image respectively.

For $k=1, 2, \dots, 255$, the cumulative sum $p_i(k)$ and the cumulative mean $m(k)$ are calculated.

$$p_i(k) = \sum_{i=0}^k p_i \quad (2)$$

$$m(k) = \sum_{i=0}^k ip_i \quad (3)$$

The global gray values are calculated by the above formulas.

$$m_G(k) = \sum_{i=0}^{255} ip_i \quad (4)$$

For $k=1, 2, \dots, 255$, calculate the inter-class variance $\sigma_B^2(k)$:

$$\sigma_B^2(k) = \frac{[m_G P_1(k) - m(k)]^2}{P_1(k)[1 - P_1(k)]} \quad (5)$$

The optimal dynamic threshold is obtained to maximize the k of $\sigma_B^2(k)$.

$$\sigma_B^2(k) = \max_{0 \leq k \leq 255} \sigma_B^2(k) \quad (6)$$

If the gray level histogram is obviously bimodal, the gray value at the trough between the two peaks is selected as the threshold value. This method is suitable for processing images with obvious double peaks and deep valley bottom. For single peak histogram, the histogram with no obvious double peaks or wide flat valley bottom is not effective [14]. In practical applications, the image is often affected by noise, which results in two obvious peaks. Otsu method is chosen to calculate the threshold because of the complex and changeable road conditions in the driving process of driverless vehicles.

2.1.3 Contour extraction

If all binary images are analyzed and processed, the computational complexity is large and the processing speed is slow. In order to simplify the analysis and processing steps and accelerate the response speed of video image processing, the four-neighborhood method should be used to extract the boundary of binary image. If the current pixel value is 1, then the current binary image is the target image; if the four pixels of the binary image are 1, then the current pixel value is 0, and the binary image is the background image, otherwise the current pixel value is unchanged [15]. This method can effectively retain the road condition information required by driverless vehicles.

After the unmanned vehicle obtains the required road condition information through video image processing, it obtains the path preview information in the road condition information through multi-point sequence. The path preview information includes lateral position deviation, preview deviation angle, path curvature and so on, and finally realizes the path tracking of the unmanned vehicle.

2.2. Unmanned vehicle path tracking

2.2.1. Relative motion model of unmanned vehicle-path

After simplification and abstraction, the relative motion model of driverless vehicle-path is established as shown in Fig. 2.

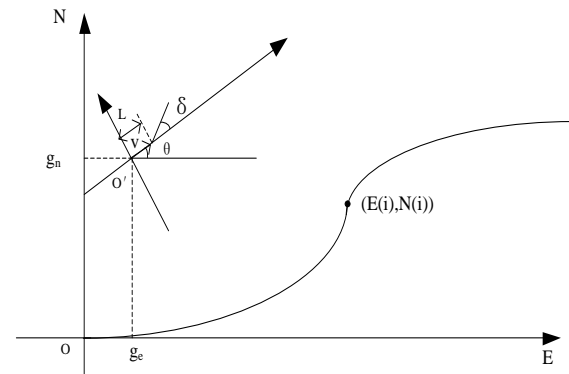


Figure 2. Relative motion model of driverless vehicle and path

Among them, E , N and O are global coordinates, E axis is in the positive East direction, N axis is in the positive North direction. The local coordinate system $XO'Y$ is established with the midpoint of the rear axle as the origin of the coordinate, which specifies the forward direction of the X axle as the vehicle's direction; δ is the front wheel rotation angle; θ is the heading angle, that is, the angle between the vehicle's forward direction and the E axle; v is the forward speed; and L as the wheelbase. The road condition information obtained by video image processing technology is actually a series of ordered longitude and latitude coordinates, which are transformed from WGS-84 coordinate system to plane rectangular coordinate system. Then the starting point of the trajectory point sequence is used as the origin of coordinate to establish the global coordinate system. The coordinates of the trajectory point of the driverless vehicle in the global coordinate system are expressed as $(E(i), N(i))$ and i is the sequence number of trajectory points. The target path tracked by an unmanned vehicle is given in the form of the above point sequence. If the position coordinate of the midpoint of the rear axle of an unmanned vehicle is (g_e, g_n) in the global coordinate

system, the kinematics model of the unmanned vehicle can be expressed as follows:

$$\begin{cases} g_e = k \cdot \cos \theta \\ g_n = k \cdot \sin \theta \\ \theta = \frac{k \cdot \tan \theta}{L} \end{cases} \quad (7)$$

2.2.2. Preview deviation angle and path curvature

In the process of manual driving, the driver’s eyes constantly preview the forward path, and determine the direction, angle and speed of the vehicle according to the relevant information of the forward path, so that the vehicle can approach the forward path as far as possible [16]. For the problem of path tracking control of unmanned vehicle, the concept of path curvature and preview deviation angle is introduced by referring to manual driving behavior. Assuming that the angle between the moving direction of an unmanned vehicle and the line connecting the preview tracking point and the current position point is the angle, the angle is defined as the preview deviation angle by literature investigation. At the same time, through actual investigation and analysis, it is found that the lateral control problem of path tracking can be transformed into the tracking problem of preview deviation angle [17]. A multi-point preview strategy is proposed to describe the curvature change at the preview tracking point of the target path. In addition to selecting a preview point as the tracking point on the target image path after video image processing, the other preview points are only used to describe the curvature change of the path and obtain the curvature of the front path. Firstly, the preview point search algorithm model is established as shown in Fig. 3.

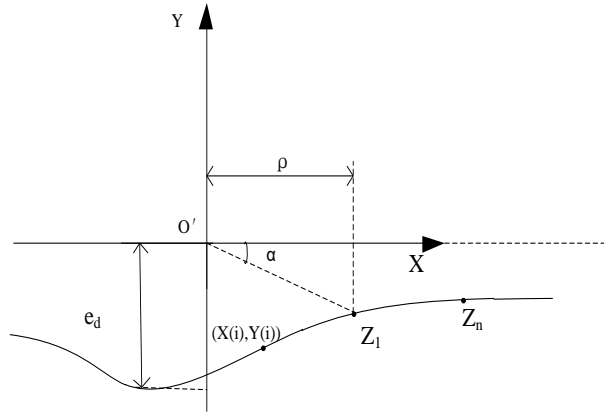


Figure 3. Model of preview point search algorithm

In Fig. 3, ρ is the preview distance, e_d is the lateral position deviation, that is, the distance deviation between the current position and the tracking path trajectory, and Z_j is the preview point sequence acquired on the target path, that is, the trajectory point sequence. Taking the unmanned vehicle as the reference object, the trajectory point sequence is transformed into the local coordinate system $XO'Y$, then the coordinates of the trajectory point sequence in the local coordinate system are expressed as $(X(i), Y(i))$, and the coordinates satisfy the following equation:

$$\begin{bmatrix} X(i) \\ Y(i) \end{bmatrix} = \begin{bmatrix} \cos \theta & \sin \theta \\ -\sin \theta & \cos \theta \end{bmatrix} \cdot \begin{bmatrix} E(i) - g_e \\ N(i) - g_n \end{bmatrix} \quad (8)$$

The steps of searching preview tracking points Z_1 are as follows: first, the trajectory points are transformed into local coordinate system by formula (8), then the nearest points are found in the sequence of trajectory points describing the target path, which is the starting point of this search; secondly, starting from the starting point, along the direction of the vehicle body, one point is found in the sequence of trajectory points in turn to satisfy the following requirements:

$$[X(z_1) - \rho][X(z_1 + 1) - \rho] \leq 0 \quad (9)$$

In the formula, z_1 is the ordinal number of the points satisfying formula (9) in the sequence of trajectory points. This point is preview tracking point z_1 , which can complete a preview tracking point search. When the vehicle moves to a new position, repeat the above steps and complete a new search. After confirmation, α was determined immediately. It is found that the driver mainly controls the speed according to the change of road curvature [18]. Therefore, in order to control the longitudinal speed of the driverless vehicle, it is necessary to find the remaining multiple preview points z_j , where $j=1,2,\dots, N$, z_j determines the degree of curvature of the path through multiple preview points. In the local labeling system $XO'Y$, it is convenient to express the curvature change of the target path with a broken line, as shown in Fig. 4.

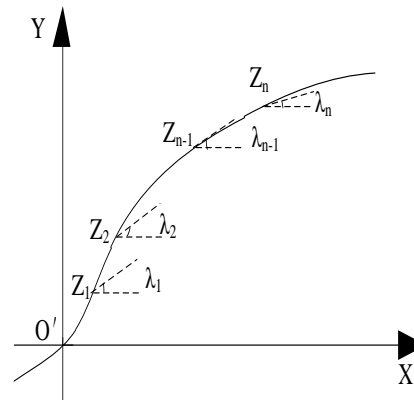


Figure 4. Schematic diagram of path bending degree calculation

The path curvature C is defined to describe the degree of path curvature at the preview point sequence.

$$C = \sum_{j=1}^{n-1} |\lambda_{j+1} - \lambda_j| \quad (10)$$

In the formula, λ_j denotes the angle between the tangent at the preview point z_j and the driving direction of the driverless vehicle, and $|\lambda_{j+1} - \lambda_j|$ denotes the relative variation of the tangent angle, which is used to describe the change of the curvature of the path and the degree of curvature of the road. The curvature of the path increases when the direction of the path changes unilaterally or swings left and right. Among them, z_j can be selected by equal interval number, that is, a preview point can be selected by a certain number of path sequence points at each interval. The number of preview points can be selected

according to the degree of sparsity of the sequence points describing the target path. The sum of Euclidean distances between the interval points can be used as an index to select the number of intervals.

2.2.3. Implementation of path tracking

According to preview deviation angle and path curvature, the driverless vehicle path tracking is carried out. The main control variables in the process of path tracking are the front wheel rotation angle and longitudinal speed. The control system of unmanned vehicle is a typical time-delay, non-linear and unstable system, and the preview control action has obvious predictability, which is obviously superior to the traditional control algorithm based on information feedback [19]. The framework of the proposed path tracking algorithm is shown in Fig. 5.

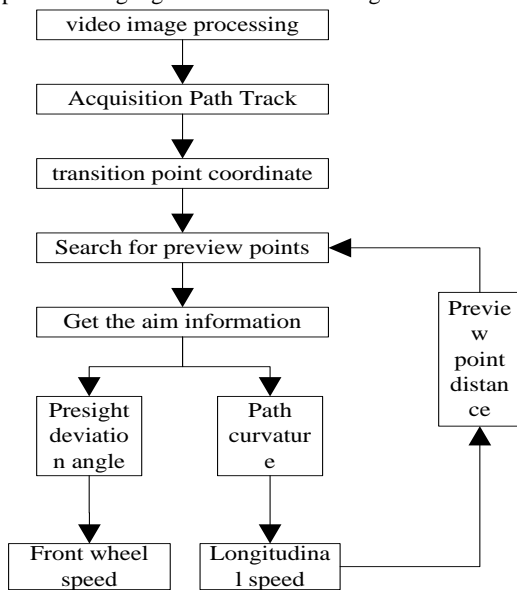


Figure 5. Path tracking algorithm

As can be seen from Fig. 5, after video image processing of the target path image of an unmanned vehicle, the path information is acquired according to the processed image acquisition path trajectory, and the path information is converted into the road point coordinates. The preview information of preview angle and path curvature is obtained by searching preview point in the road point coordinates. The speed and longitudinal direction of the front wheel of an unmanned vehicle are determined by preview point information. The speed is controlled, and the distance of the preview point is obtained according to the information of the preview point. It is more important to determine the preview distance and the lateral and longitudinal control speed. The following is a detailed analysis of the determination of the preview distance and the lateral and longitudinal control speed. (1) The determination of the preview distance.

Preview distance directly affects the accuracy of path tracking, and its selection is very important. The smaller preview distance can make the driverless vehicle track the path more accurately and can track the path with larger curvature. The larger preview distance can reduce the overshoot of the driverless vehicle in the tracking process and improve the tracking stability. The preview distance can be determined according to the longitudinal speed of the driverless vehicle. In addition, the preview distance is usually saturated at the minimum and maximum, so the relationship between the preview distance and the

longitudinal speed of an unmanned vehicle can be expressed by empirical formulas:

$$\rho = \begin{cases} av + l_{\min}, & 0 \leq v \leq \frac{(l_{\max} - l_{\min})}{a} \\ l_{\max} & v > \frac{(l_{\max} - l_{\min})}{a} \end{cases} \quad (11)$$

In the formula, l_{\min} and l_{\max} represent the minimum and maximum preview distance respectively, and a is a constant. The preview distance can be obtained by the above formula.

(1) Longitudinal control based on path curvature

In the local coordinate system, λ_j can be expressed as:

$$\lambda_j = \arctan \frac{X_r(p_i + 1) - Y_i(p_i)}{X_r(p_i + 1) - X_r(p_i)} \quad (12)$$

In the formula, (X_r, Y_r) is the coordinate of the preview point in the local coordinate system. After calculating the curvature C from formula (10) and formula (12), only considering the effect of curvature change on vehicle speed, the larger the C , the smaller the vehicle speed; conversely, the greater the vehicle speed v . Vehicle speed may not exceed a certain value of v_{\max} under certain conditions. Therefore, in order to ensure that the speed v decreases significantly with the increase of curvature C , the calculation of vehicle speed is as follows:

$$v = \left(1 - \frac{C}{k_c}\right)^2 v_{\max} \quad (13)$$

In the formula, k_c is constant. If the path is given, the curvature C at each point of the path and the maximum and minimum curvature C_{\max} and C_{\min} of the whole path can be calculated offline, then the selection range of k_c is $C_{\min} < k_c < C_{\max}$.

(2) Horizontal control based on Pure Pursuit algorithm

Taking the midpoint of the rear axle as the tangent point and the longitudinal symmetrical axis of the driverless vehicle as the tangent line, the deflection angle of the front wheel is calculated by the geometric relationship of the preview deviation angle, so that the driverless vehicle can travel along the arc passing through the preview point, and the preview deviation angle tends to zero [19]. By applying the sine theorem, we can get that:

$$\frac{l_d}{\sin(2\alpha)} = \frac{R}{\sin(\frac{\pi}{2} - \alpha)} \quad (14)$$

$$\frac{l_d}{\sin \alpha} = 2R \quad (15)$$

Where R is the radius.

Formula (14) can also be expressed as:

$$\kappa = \frac{2 \sin \alpha}{l_d} \quad (16)$$

In the formula, l_d is the distance between the current position and the preview point Z_1 , and κ is the arc curvature. According to the simplified Ackerman vehicle model, the front wheel angle δ can be expressed as:

$$\delta = \arctan(\kappa L) \tag{17}$$

According to formula (14) and formula (15), the control quantity of front wheel rotation angle based on Pure Pursuit algorithm can be obtained as follows:

$$\delta = \arctan \frac{2L \sin \alpha}{l_d} \tag{18}$$

In the formula $l_d = \rho \cdot \cos \alpha$, after the introduction of the formula (18), there is only one adjustable parameter, i.e. preview distance ρ , which makes the algorithm easy to implement and adjust.

3. Results

3.1. Analysis of the effect of road information processing

In order to study the validity of image processing technology in this paper, the road condition information before and after image processing should be compared, and the comparison results are shown in Fig. 6.

As can be seen from Fig. 6, there is obvious noise in the original road condition image, which is not conducive to the subsequent extraction of path information. After using the median filter in this method to filter out the noise points, the noise points in the image are obviously reduced, and the original contour boundary of the image is retained. The object and background can be effectively separated by binarization. At the same time, the contour extraction method not only retains the road feature information, but also greatly simplifies the amount of image information, which shows that the method in this paper has a good effect in processing the video image information.

3.2. Analysis of path tracking effect

Two methods are used to test the effect of this method on experimental driverless vehicle path tracking. Firstly, the effect of driverless vehicle path tracking under this method is judged by detecting the difference between the driverless vehicle corner command and the actual corner. The test results are shown in Fig. 7.

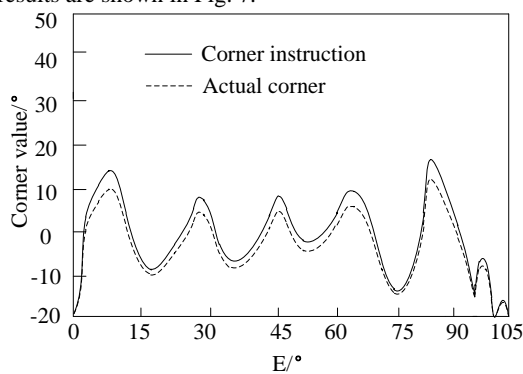


Figure 7. Corner instruction and actual Corner difference

It can be seen from Fig. 7 that in the whole experiment process, the difference between the measured angle instruction and the actual angle is very small, which shows

that the control accuracy of this method is high, and it has a good effect on the path tracking of driverless vehicles.

Secondly, starting from the speed of the driverless vehicle itself, the effect of this method on the path tracking of the driverless vehicle is verified. The results of unmanned vehicle path tracking at low speed of 18 km/h and high speed of 93 km/h are compared to detect the impact of this method on the unmanned vehicle path tracking at different speeds. The path tracking of an unmanned vehicle at two speeds is shown in Fig. 8.

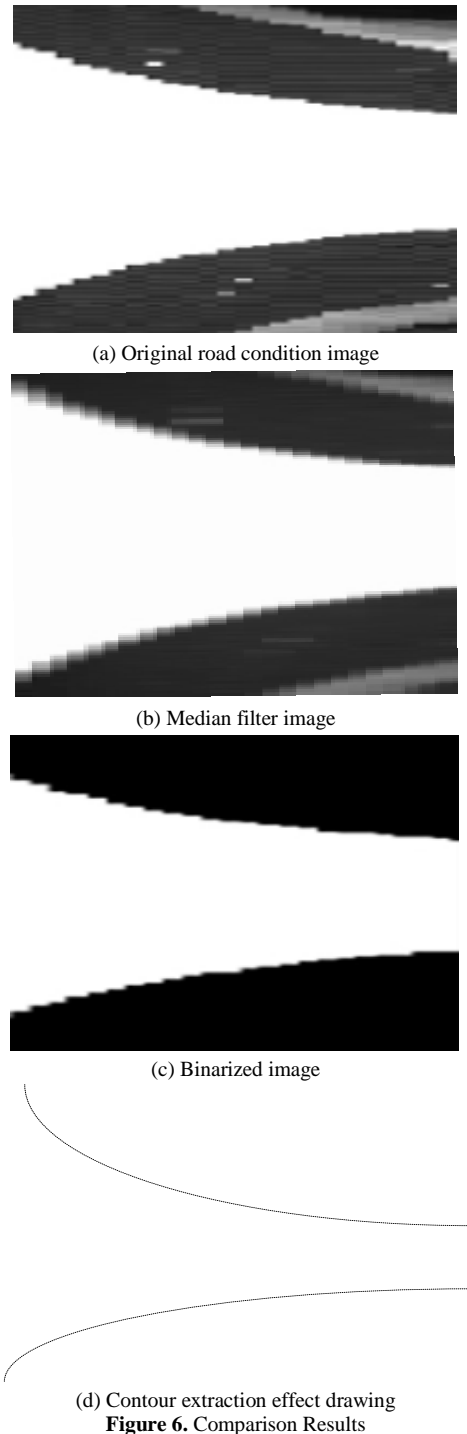
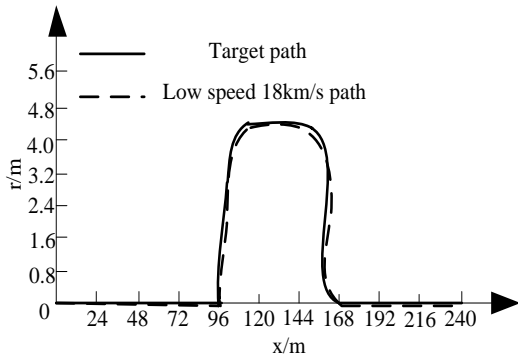
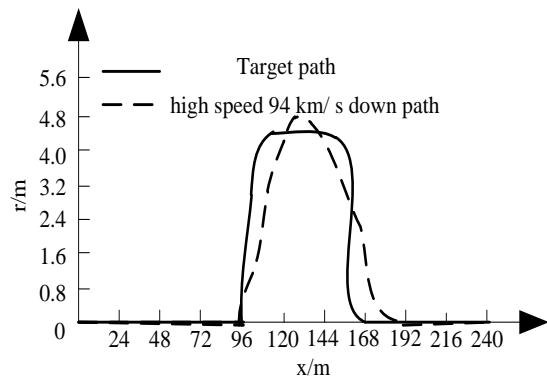


Figure 6. Comparison Results



(a) Automatic tracing effect at low speed



(b) Automatic tracking effect at high speed

Figure 8. Automatic tracking effect at different speeds

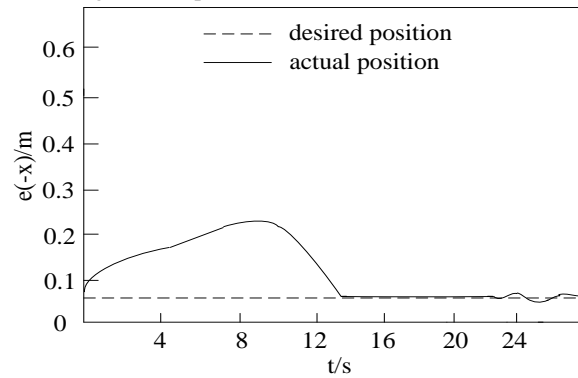
From Fig. 8, it can be seen that although the path tracking effect of driverless vehicles at high speed is slightly lower than that of driverless vehicles at low speed, the path tracking errors at different speeds are relatively small, which shows that the path tracking effect of driverless vehicles using this method is better, and the effectiveness of this method is higher. After using this method, driverless vehicles can carry out the path tracking. Accurate and effective path tracking ensures safe and smooth driving of driverless vehicles.

3.3. Analysis of posture deviation at different velocities

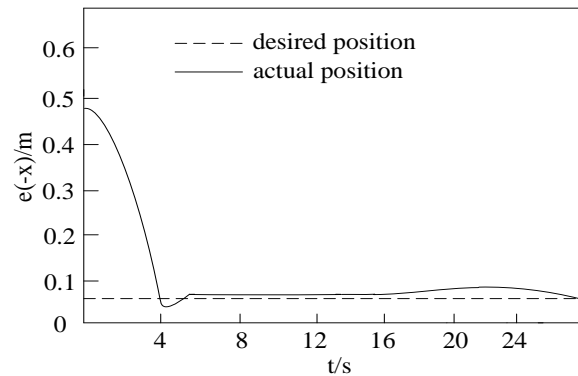
Through the above experiments, it is found that the path tracking effect of unmanned vehicle is better after using this method. In order to further verify the path tracking accuracy of this method, it is necessary to analyze the position and attitude deviation of unmanned vehicle at different speeds. In this experiment, the position and attitude deviation of unmanned vehicle at 18 km/h and 94 km/h are mainly studied. The test results are shown in Fig. 9.

From Fig. 9, it can be seen that the driverless vehicle can quickly track the reference trajectory when the initial position of the vehicle is different from the reference trajectory and the reference speed is different. Under the condition of low reference speed, the actual trajectory of the vehicle is closer to the reference trajectory, and the position and attitude deviation after tracking the reference trajectory is smaller; under the condition of high reference speed, the vehicle still has good tracking effect, and the improvement of the reference speed does not lead to the decline of tracking performance. Therefore, this method can realize the rapid tracking of the reference trajectory of the

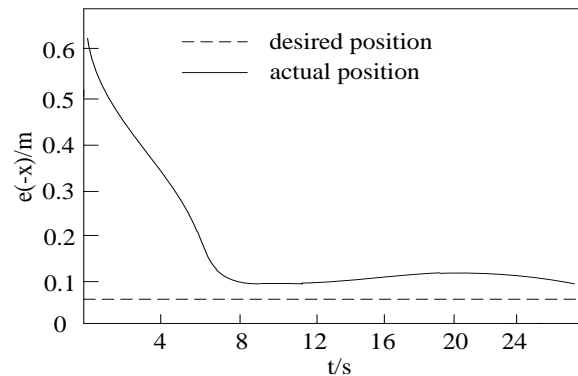
unmanned vehicle, and has strong robustness to the change of the longitudinal speed of the unmanned vehicle.



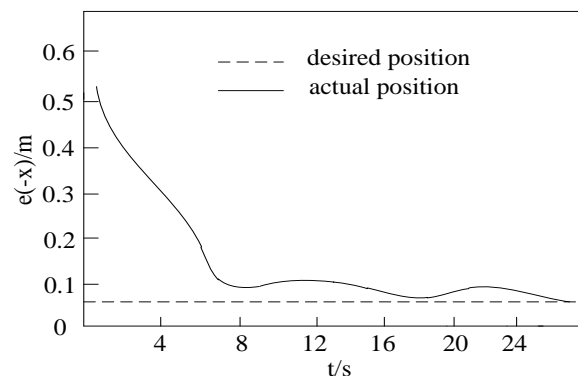
(a) 18 km/h lateral position deviation



(b) 18 km/h longitudinal position deviation



(c) 94 km/h lateral position deviation



(d) 94 km/h longitudinal position deviation

Figure 9. Position and position deviation of different speed

3.4. Energy consumption analysis of vehicle route tracking based on this method

In order to verify the low energy consumption of driverless vehicle path tracking under this method, it is necessary to compare the energy consumption of the proposed method with the vehicle path tracking method based on Fuzzy annealing and the vehicle path tracking method based on neural network. In order to improve the accuracy of this experiment, many experiments are needed, and the results are shown in Table 1.

Table 1. Comparison of energy consumption/J

Number of experiments	The method	Vehicle path tracking method based on Fuzzy annealing	Vehicle path tracking method based on Neural Network
1	356	598	981
2	359	601	983
3	348	609	979
4	340	593	986
5	357	612	975
6	361	619	949
7	352	621	936
8	368	599	991
Mean value	355.13	606.50	972.50

According to the data in Table 1, the energy consumption of the method in this paper is 368J, the energy consumption of vehicle path tracking method based on fuzzy annealing is 621J, and the energy consumption of vehicle path tracking method based on neural network is 991J. The highest consumption value is significantly lower than the two traditional methods. And the average energy consumption of this method is 355.13J, which is much lower than the two traditional methods. Through the above data analysis, it can be concluded that the method in this paper can save energy consumption, because the method in this paper uses the four-neighborhood method to extract the boundary contour of the binary image, thereby obtaining the required road condition feature information. According to the obtained information, the preview deflection angle and the curvature of the path can be calculated, and the precise tracking control of the path of the unmanned vehicle can be realized, thereby reducing the probability of the occurrence of the path deviation and further reducing the energy consumption.

4. Discussions

According to the above analysis, the advantages of the drone path tracking method based on video image processing proposed in this paper are:

(1) Through this method, the collected road video image is filtered to reduce the influence of noise on image quality. Binary image processing can reduce the amount of calculation, save processing time, extract road information more intuitively, select dynamic threshold in the process of binarization, and can follow the driving environment of unmanned vehicles. Real-time adjusting the dynamic threshold has strong adaptability to the environment. The dynamic threshold is obtained by Otsu method, which is

convenient to distinguish the background and the target of the image, so that the corrected image can accurately restore the road condition information. This image processing technology can adapt to various complex road conditions and provide material guarantee for subsequent acquisition of preview points.

(2) Most of the traditional path tracking methods pay little attention to the horizontal and vertical control of unmanned vehicles. However, the method in this paper performs path tracking of unmanned vehicles based on the preview deviation angle and path curvature. The main control variables in the path tracking process are the front wheel rotation angle and the vertical speed. By extracting multiple preview points on the target path to obtain the preview information of the path, the vertical and horizontal control of the driverless car is realized.

5. Conclusions

In order to solve the problems of image distortion and low path tracking accuracy when using traditional methods to track unmanned vehicles, a method for unmanned vehicle path tracking based on video image processing is proposed. The analysis of the experimental results shows that the method in this paper effectively improves the accuracy of path tracking, and the energy consumption is low, indicating that the method has high practical application value. However, the method in this paper does not take into account the issue of tracking efficiency, so the following will focus on tracking efficiency as the research focus for method optimization.

References

- [1] García-Pulido, J. A., Pajares, G. & Dormido, S. 2017. Recognition of a landing platform for unmanned aerial vehicles by using computer vision-based techniques. *Expert Systems with Applications an International Journal* 76(16):152-165.
- [2] Jeong, S., Ko, J. & Kim, M. 2016. Construction of an unmanned aerial vehicle remote sensing system for crop monitoring. *Journal of Applied Remote Sensing* 10(2):26-27.
- [3] Huang, H., Long, J. & Yi, W. 2017. A method for using unmanned aerial vehicles for emergency investigation of single geo-hazards and sample applications of this method. *Natural Hazards & Earth System Sciences* 17(11):1-28.
- [4] Peng, L., Liu, J. 2018. Detection and analysis of large-scale WT blade surface cracks based on UAV-taken images. *IET Image Processing* 12(11):2059-2064.
- [5] Jeon, D., Kim, D. H. & Ha, Y. G. 2016. Image processing acceleration for intelligent unmanned aerial vehicle on mobile GPU. *Soft Computing - A Fusion of Foundations. Methodologies and Applications* 20(5):1713-1720.
- [6] Example, F. 2017. An Open Data Platform for Traffic Parameters Measurement via Multirotor Unmanned Aerial Vehicles Video. *Journal of Advanced Transportation* 2017(1852):1-12.
- [7] Ojha, T., Misra, S. & Raghuvanshi, N. S. 2015. Wireless sensor networks for agriculture: The state-of-the-art in practice and future challenges. *Computers & Electronics in Agriculture* 118(3):66-84.
- [8] Depatla, S., Buckland, L. & Mostofi, Y. 2015. X-Ray Vision with Only WiFi Power Measurements Using Rytov Wave Models. *IEEE Transactions on Vehicular Technology* 64(4):1376-1387.
- [9] Zhang, W., Wei, S. & Teng, Y. 2017. Dynamic Obstacle Avoidance for Unmanned Underwater Vehicles Based on an Improved Velocity Obstacle Method. *Sensors* 17(12):27-42

- [10] Jabbarpour, M. R., Zarrabi, H. & Jung, J. J. 2017. A Green Ant-based method for Path Planning of Unmanned Ground Vehicles. *IEEE Access* 5(99):1820-1832.
- [11] Yang, D. W. 2018. Detail-enhanced target segmentation method for thermal video sequences based on spatiotemporal parameter update technique. *IET Image Processing* 13(1):216-223.
- [12] Hsia, C. H., Liou, Y. J. & Chiang, J. S. 2016. Directional Prediction CamShift algorithm based on Adaptive Search Pattern for moving object tracking. *Journal of Real-Time Image Processing* 12(1):183-195.
- [13] Oliveira, T., Aguiar, A. P. & Encarnação, P. 2016. Moving Path Following for Unmanned Aerial Vehicles with Applications to Single and Multiple Target Tracking Problems. *IEEE Transactions on Robotics* 32(5):1062-1078.
- [14] Long, Y., M, Q. X. & Xu, W. Y. 2017. A numerical method for analyzing the permeability of heterogeneous geomaterials based on digital image processing. *Journal of Zhejiang University-SCIENCE A* 18(2):124-137.
- [15] Wang, W. H., Cheng, D. & Chen, B. 2017. The Application Research of Histogram of SAR Images Processing. *Journal of China Academy of Electronics and Information Technology* 12(1):90-95.
- [16] Xiang, Y. H., Fu, X. W. & Tian, J. 2016. Porosity evaluation for porous electrodes using image processing. *Chinese Journal of Power Sources* 40(3):572-574.
- [17] Shen, Y. X., Wu, J. & Wu, D. h. 2017. Fault Diagnosis Technology for Three-level Inverter Based on Reconstructive Phase Space and SVM. *Journal of Power Supply* 15(6):108-115.
- [18] Zheng, Z. Q. 2019. Continuous track control of intelligent vehicle based on inversion method. *Automation & Instrumentation* 231(1):135-137.
- [19] Gao, L. F., Li, C. 2016. Palmprint Recognition Based on Features Weighted and Kernel Principal Component Analysis. *Journal of Jilin University (Science Edition)* 54(06):1361-1366.
- [20] Wu, M., Zhang, F. T. & Wen, G. L. 2016. The Control Strategy Research of Unmanned Vehicles Steering-by-Wire System. *Computer Simulation*, 33(12):163-168.

Acceleration Sensor Abnormality Detection Method for Axle Box of Unmanned Vehicle

Jianhu Gong

School of Data and Computer Science, Guangdong Peizheng College, Guangzhou 510830, China

Received OCT 16 2019

Accepted JAN 20 2020

Abstract

The method of detecting the acceleration sensor anomaly of the axle box of unmanned vehicle is studied in this paper. The condition monitoring device needs to install the acceleration sensor on the bogie, which collects the acceleration sensor signal of the axle box of the vehicle. According to each frequency, the vertical vibration acceleration of the axle box with the vertical vibration acceleration of the bogie frame are compared to detect the shock absorber anomaly of axle box; the quasi-double-layer chloroprene rubber filter is used to isolate the high frequency component of shock acceleration signal, while the low frequency component is retained. The vertical displacement of the axle box is obtained by integrating the vertical vibration acceleration of the collected axle box twice. The displacement is the rail corrugation. The sliding variance window statistical algorithm of axle box acceleration is used to obtain the sliding variance of axle box acceleration, and find out the line problems and their corresponding positions. The results show that when the vibration frequency of axle box vibrator is higher than 7.5 Hz, the amplitude ratio of axle box acceleration under the condition of throttle hole blockage and insufficient hydraulic oil is inconsistent with that under the intact condition. At this time, the shock absorber of axle box is abnormal. When the frequency is higher than 8 Hz, the acceleration response ratio of axle box under the three conditions moves towards the same direction, but there are obvious differences. At this time, the shock absorber of axle box attenuates and has abnormal vibration. Based on the analysis of sliding variance of vertical acceleration of axle box before and after rail pre-grinding at 300 km/h speed level, it is concluded that the variance of axle box acceleration decreases, and the effect of rail pre-grinding on improving the smoothness of rail welded joints is very obvious. When the vehicle derails, the vertical vibration acceleration waveform of axle box and the vibration acceleration waveform of bogie on ballast track show that the absolute value of negative peak vibration acceleration is greater than that of positive peak vibration acceleration.

© 2020 Jordan Journal of Mechanical and Industrial Engineering. All rights reserved

Keywords: Unmanned vehicle; Sensor; Axle box; Acceleration; Abnormal detection; Inertia principle;

1. Introduction

In recent years, with the increasing demand for active safety and intelligence of automobiles in the market, the huge social and economic value of unmanned driving has become increasingly prominent. More and more enterprises and scientific research institutions actively participate in and promote the development of the field of unmanned driving [1]. At present, there is no formal mass production and sales of completely unmanned vehicles, but a considerable number of experimental vehicles can achieve highly autonomous driving behavior through environmental awareness, such as starting, acceleration, braking, lane tracking, lane change, collision avoidance, and parking, etc. [2]. For the definition of unmanned driving, it divides unmanned driving into five levels, namely advanced auxiliary driving, specific function assistance, combined function assistance, highly automatic driving, and completely unmanned driving. At present, most of the vehicles are still at the stage of combined function assistance. There is still a long way to go to accomplish the production of completely unmanned vehicles.

Vibration sensors are also called vibration detectors. They are similar to seismographs that record seismic and

atomic bomb explosion waves. They are the most common ones used in sensors. This kind of sensor detects the target mainly by capturing the ground vibration signal caused by the movement of human or maneuvering target through the vibration probe (also called seismograph) of the device [3]. Vibration sensor has a long detection distance and high sensitivity. At the same time, the vibration sensor also has a certain target resolution[4]. It can distinguish not only man-made vibration and natural disturbance, but also people and targets. Usually, vibration sensor is used to collect abnormal acceleration signals of vehicles[5].

Foreign scholars have done a lot of research on the detection of acceleration sensor anomaly of axle box of unmanned vehicle in this field: Morys established a vehicle-track coupling model, believing that wheel non-circularization would cause a great change in vertical force of wheel and rail, stimulate bending vibration of axle pair, and then lead to lateral sliding of wheel and lateral stripping of material between wheel and rail surface. However, this model did not compare the difference between the amplitude-frequency domain and the frequency domain. Johansson et al. established a three-dimensional numerical model of vehicle-track dynamic interaction and wheel wear feedback coupling. By analyzing the frequency spectrum of wheel-rail force at 50km/h running speed, it was found that

* Corresponding author e-mail: gscilw@163.com.

the larger peak value at 40 Hz came from the vertical resonance of wheel-rail coupling system, corresponding to the fifth, sixth and seventh order polygon wear of wheel, but it did not consider using the statistical analysis method of axle box acceleration sliding variance window to achieve a comprehensive evaluation of track status (sliding variance peak method); CLAUS et al. believed that when the speed exceeds 200 km/h, the third and fourth order polygon wear of wheels could cause significant vibration of the vehicle body at 70 Hz to 100 Hz. Although the purpose of axle box detection was achieved, the repeated impact of trains passing track joints was not considered. Bad sensors or zero drift would lead to the distortion of test signals. Therefore, the method of detecting the acceleration sensor anomaly of axle box of unmanned vehicle studied in this paper provides an effective basis for ensuring the safe operation of unmanned vehicle.

2. Definition of Algorithm

2.1. System Structure of Monitoring Device and Abnormal Detection of Shock Absorber of Axle Box

2.1.1. Structure of Condition Monitoring Device

Figure 1 is the basic structure of the condition monitoring device.

The device assumes that acceleration sensors are installed on bogies, and in order to improve the accuracy of diagnosis and increase monitoring items [6], the way of installing axle box acceleration sensors on specific axles is also studied.

2.1.2. Structure of Monitoring System

The system structure is shown in Figure 2.

Figure 2 shows that the accelerometer measures the vibration acceleration of the axle box of a vehicle, the

analog processing is carried out by signal amplifier to quantify the data acquisition card, and the speed sensor collects the train speed [7]. Then the acceleration signal of the axle box is processed by digital processing technology, including noise reduction, digital integration and high-pass filtering. Finally, the waveform of corrugation is obtained.

2.1.3. Abnormal Detection of Shock Absorber of Axle Box

The following will introduce the application of numerical simulation technology to research and test the shock absorber of axle box if there is a fault, which will have an impact on the operation safety. Therefore, a numerical simulation model of single vehicle with 17 degrees of freedom is established. The model assumes that the body shown in Figure 3 is a rigid body with a running speed of 275 km/h. According to the input parameters [8,9], the “white” noise concerned in vehicle vibration modes is listed as a band-limited waveform when the frequency reaches 80 Hz, which is used as track irregularity.

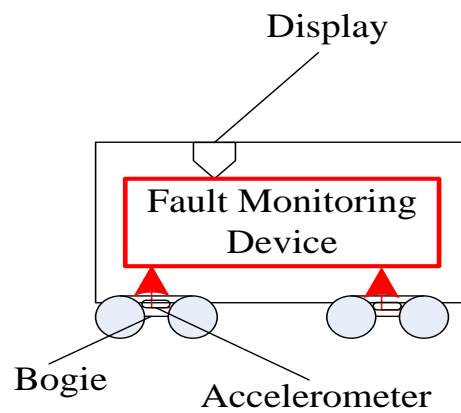


Figure 1. Basic Structure of Condition Monitoring Device

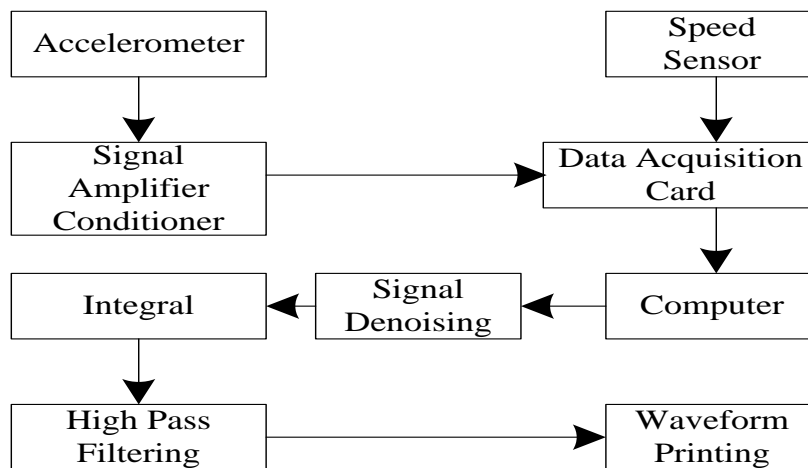


Figure 2. Structure Diagram of Monitoring System

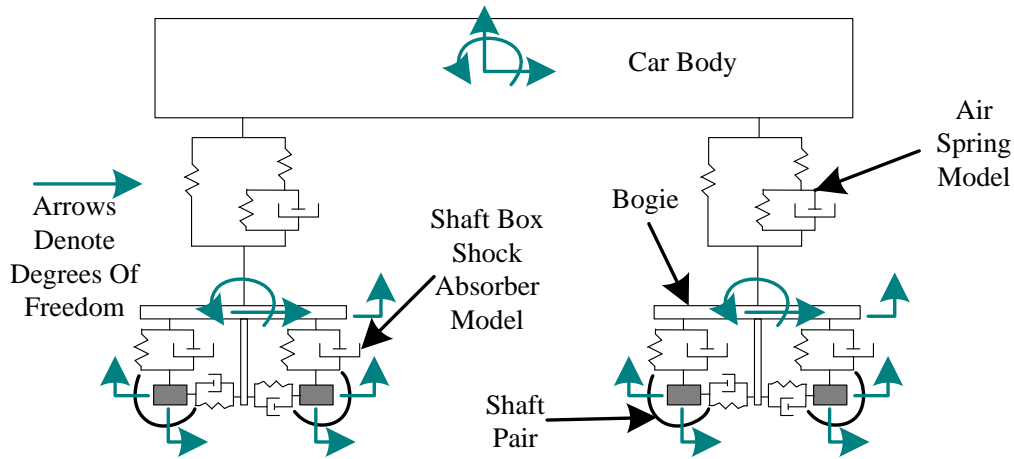


Figure 3. A Numerical Simulation Model for the Vertical System of a Bicycle

The detection method is to compare the vertical vibration acceleration of the newly built or maintained bogie with that of the running bogie according to each frequency. In addition, for vehicles with vertical vibration acceleration sensor of axle box installed for bearing detection, the vertical vibration acceleration of axle box can also be detected by comparing the vertical vibration acceleration of axle box with the vertical vibration acceleration of bogie frame according to each frequency. The former has the advantage that it is not necessary to install vertical acceleration sensor on axle box, but it is necessary to compare track irregularities to the same extent. Because the ratio of vertical vibration acceleration of axle box to the vertical vibration acceleration of bogie frame is used [10], the latter has the advantage of not being affected by track irregularity.

2.2. Impulse Isolation Filter and Detection Principle

2.2.1. Structure and Characteristic Analysis of Impulse Isolation Filter

In order to simulate and reproduce the vibration state of the train running on the rolling vibration test bench, it is necessary to measure the vibration acceleration signal of the train's axle box on the spot. In order to reproduce the vibration of a train running on a straight track, it is necessary to isolate the shock wave when the train passes through the rail seam [11]; the shock acceleration value of the train passing through the rail seam is more than 400 g, while the vibration acceleration of the train running on a straight track is usually less than 10 g. In order to ensure the test accuracy, a sensor with a measuring range of about 15 g should be selected. In addition, in the process of on-line measurement, the repeated impact of rail joint will damage the sensor or cause zero drift, which will lead to the distortion of the test signal. Therefore, in the process of measuring vehicle's axle box acceleration signal, isolation filtering of impact acceleration becomes an urgent research topic. In order to ensure the validity of the measured signal, it is required that the amplitude-frequency characteristics of the impulse isolation filter have good linear smoothness in the low frequency band, and that it should have as steep attenuation characteristics as possible in the high frequency band; at the same time, the cut-off frequency of the filter should be low; when the high frequency components of the impulse acceleration signal are isolated, the low frequency

components can be easily processed [12]. According to these requirements, a quasi-double-layer chloroprene rubber filter with good filtering characteristics is designed after repeated analysis and experimental comparison of various shock isolation filters.

The typical spectrum lines of train's axle box vibration and shock are shown in Figure 4 and Figure 5 shows the ideal amplitude-frequency characteristics.

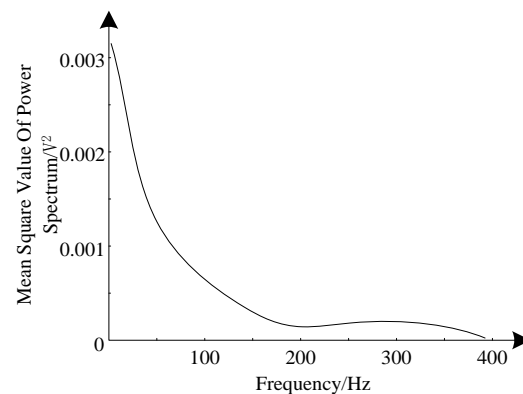


Figure 4. Vibration and Shock Power Spectrum Axle Box

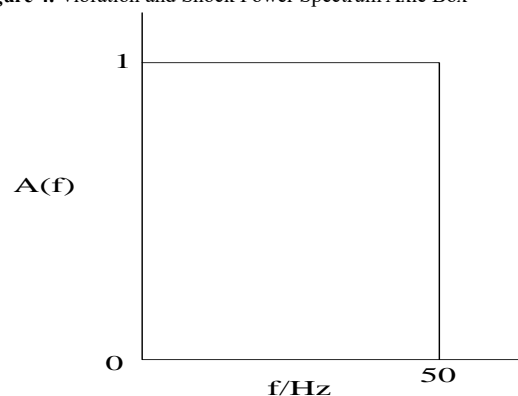


Figure 5. Characteristics of Ideal Impulse of Isolation Filter

As can be seen from Figure 4, the frequency range of shock spectrum is generally below 300 Hz. Considering that the frequency range of vibration acceleration signal of train's axle box due to track irregularity is generally below 50 Hz. It is required that the amplitude-frequency

characteristics of the shock isolation filter designed be linear at least before 50 Hz.

The structure of the shock isolation filter is shown in Figure 6. The upper and lower layers of the filter are tightly bonded with the middle layer through 502 glue. The middle layer is 8 mm thick and has a small crack in the chloroprene rubber isolation layer. It can also be called quasi-double rubber filter. The dynamic characteristics of single-layer rubber filter can be described by the physical model shown in Figure 7. Its mathematical equation of motion is as follows:

$$m\ddot{x} + c\dot{x} + kx = P_0 \cos \omega t \tag{1}$$

The transfer rate of acceleration can be calculated from the formula.

$$A = \frac{\sqrt{1 + \left(2 \frac{c}{C_c} \cdot \frac{\omega}{\omega_m}\right)^2}}{\sqrt{\left(1 - \frac{\omega^2}{\omega_m^2}\right)^2 + \left(2 \frac{c}{C_c} \cdot \frac{\omega}{\omega_m}\right)^2}} \tag{2}$$

In formula (2), $\omega_m = \sqrt{k/m}$ is the natural frequency and $C_c = 2\sqrt{mk}$ is the critical damping coefficient. For chloroprene rubber, the elastic coefficient k is independent of frequency, and the product of damping coefficient C and vibration frequency is constant. The formula (2) can be simplified as follows:

$$A = \frac{\sqrt{1 + l^2}}{\sqrt{\left(1 - \frac{\omega^2}{\omega_m^2}\right)^2 + l^2}} \tag{3}$$

In formula (3), $l = (\omega c)/k$ is a constant, and the acceleration transfer rate A here is the amplitude-frequency characteristic $A(f)$ of the filter. The curve is shown in Figure 8. From the curve of Figure 8, it can be seen that the amplitude-frequency characteristics of single rubber layer cannot meet the requirements of impulse signal filtering that the transmission rate at resonance is small, and the transmission rate curve should drop steeply after crossing the resonance region. Considering the above-mentioned single-layer isolation filter system according to these requirements shows many shortcomings. In this paper, a quasi-double rubber filter is designed on the basis of a large number of analysis and experiments [13]. The filter can effectively meet the requirements of shock isolation filter.

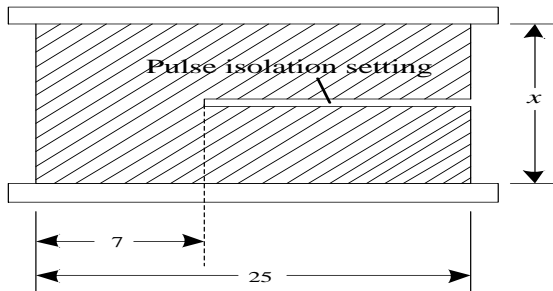


Figure 6. Structural Sketch of Impulse Isolation Filter

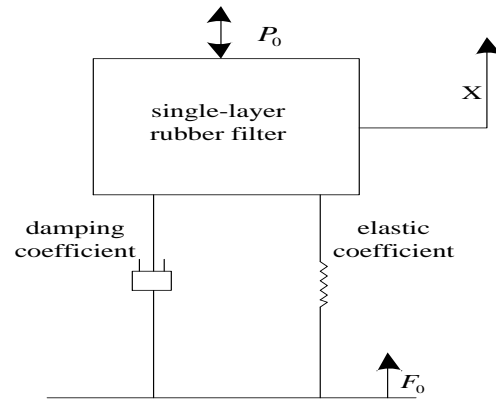


Figure 7. Physical Model of Dynamic Response of Single Layer Rubber

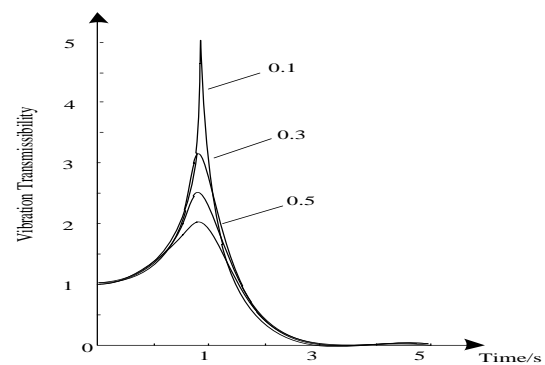


Figure 8. Acceleration Transfer Rate of Monolayer Rubber

2.2.2. Detection Principle

At present, there are two main detection methods for track irregularity: chord measurement method and inertial reference method. The transfer function of the chord measurement method is not always equal to 1, which cannot correctly reflect the real track irregularity [14]. In this paper, the inertia reference method is adopted. The traditional principle of inertia reference method is to install acceleration sensors on the train body. When the vibration frequency of axle box is very high and far higher than the natural frequency of mass spring system composed of vehicle body and wheel axle box, according to the principle of inertia, the vehicle body cannot move up and down along with the axle box, so the vehicle body becomes a static reference which can be used for measurement. Therefore, the displacement of axle box relative to vehicle body is track irregularity without the wheel leaving the rail. However, the vibration frequencies of the axle box caused by rail corrugation are not all much higher than the natural frequencies of the system [15]. When the wavelength is longer or the driving speed is lower, the axial vibration frequencies caused by rail corrugation are not high enough, and the vehicle body will move with it, and the measurement datum will be lost. For this reason, another kind of axle box acceleration integration method based on inertia principle that seems to be more convenient and feasible is proposed, that is, the second integration of the collected vertical vibration acceleration of axle box, indicating that the vertical displacement of the axle box is equal to the rail corrugation, and its detection schematic diagram is shown in Figure 9.

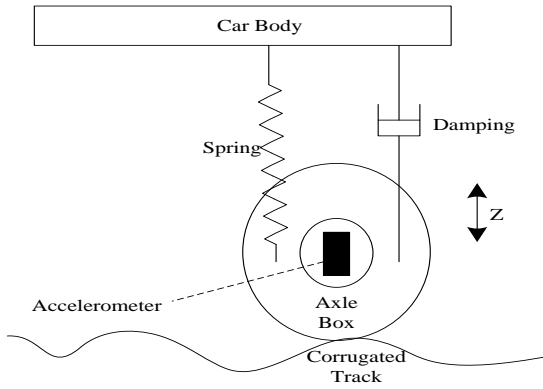


Figure 9. Principle Diagram of Inertial Constant Method

The acceleration vibration signal collected by the acceleration sensor installed on the axle box directly reflects the irregular state of the track. The vertical displacement Z obtained by integration is the wave wear value.

$$Z = \int \int \ddot{Z} dt dt \quad (4)$$

At this time, the inertial reference line is the axle box, so the integral value Z is the track wave wear value.

2.3 Statistical Algorithm of Sliding Variance Window for Axle Box Acceleration and Selection of Sliding Window Width

2.3.1 Statistical Algorithm of Sliding Variance Window for Axle Box Acceleration

Variance is the average of the square of the difference between each data and the average. For a group of data $X_n = \{x_1, x_2, x_3, \dots, x_n\}$, the definition of variance $D(X_n)$ is shown in formula (5):

$$D(X_n) = \frac{\sum_{i=1}^n (x_i - \bar{x})^2}{n} \quad (5)$$

In formula (5), \bar{x} is the mean of the array X_n .

For the measured axle box acceleration data $a = \{a_1, a_2, a_3, \dots, a_N\}$, as shown in Figure 10, assuming the sliding window width is M , then $M < N$, and the calculation results of sliding variance are shown in Formula (6):

$$S = \{S_1, S_2, S_3, \dots, S_{N=M+1}\},$$

$$S_k = \frac{\sum_{i=k}^{k+M-1} (a_i - \bar{a}_k)^2}{M} \quad (6)$$

In formula (6), there are:

$$\bar{a}_k = \frac{\sum_{i=k}^{k+M-1} a_i}{M} \quad (7)$$

According to formula (7), formula (8) can be obtained as:

$$a_{k+1}^- = \bar{a}_k - \frac{a_k}{M} + \frac{a_{k+M}}{M} \quad (8)$$

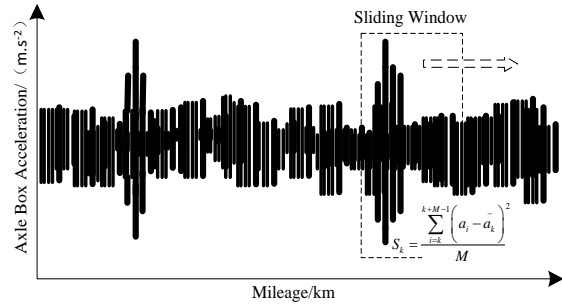


Figure10. Sliding Variance of Vertical Acceleration of Axle Box

2.2.3. Selection of Sliding Window Width

Formula (6) and formula (7) show that the key of sliding variance statistical algorithm is to determine the width of sliding window M . Two ways are considered to determine the width of sliding window M , one is to determine M (time window) based on time, as formula (9):

$$M = \frac{T}{dt} = Tf \quad (9)$$

Another method is to determine M (distance window) based on distance, as formula (10):

$$M = \frac{L}{dl} = \frac{Lf}{v} \quad (10)$$

In formula (10), L is the length of the line to be covered by the sliding window, with the unite of m ; dl is the length of the line corresponding to the sampling interval, with the unite of m ; f is the sampling frequency, with the unite of Hz ; v is the speed of the vehicle, with the unite of m/s .

At the same speed, there is a one-to-one correspondence between the time window and the distance window [16,17]. Dynamic detection corresponds the peak value of vehicle dynamic response to the position of the line. Through the sliding variance of axle box acceleration, the line diseases and their corresponding positions can be found out. The distance window is more suitable. For the distance window, the selection of L is very important, L is too small to cover the overall response caused by a certain line excitation, and L is too large to weaken the response caused by specific line excitation. The response of typical line excitation links such as welded joints and turnouts in the speed range of 200 km/h to 350 km/h is analyzed. The response length is generally 10 m to 20 m. Therefore, it is reasonable to choose 20 m for L .

3. Results

3.1. Abnormal Vibration Detection of Shock Absorber Attenuation of Axle Box

In order to investigate the change trend of bogie's vertical vibration acceleration when the shock absorber of axle box is abnormal, the numerical simulation is carried out at first. Therefore, under the condition of insufficient hydraulic oil, it is assumed that the damping coefficient of one axle box damper in eight axle box dampers of a vehicle is 0. When the throttle hole is blocked, the damping coefficient of one of the eight axle box dampers in a vehicle is assumed to be twice as high as that of the intact axle box

dampers. Based on the above assumptions, the damping coefficient of the shock absorber of axle box is calculated. Figure 11 is an example of using the method of amplitude ratio to detect the abnormality of shock absorber of axle box. Figure 12 is an example of using the method of response ratio to detect the abnormality of shock absorber of axle box.

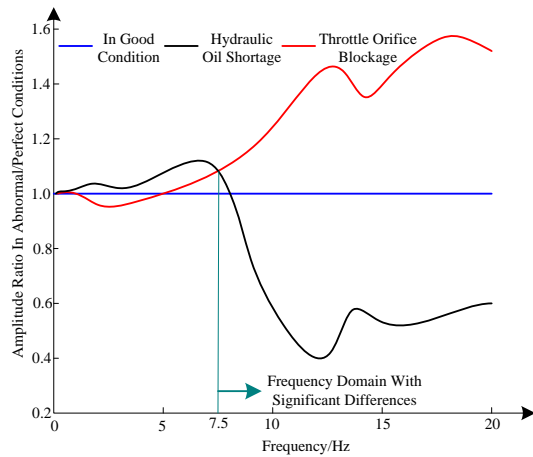


Figure 11. Detection of Shaft Box Shock Absorber Abnormality by Amplitude Ratio

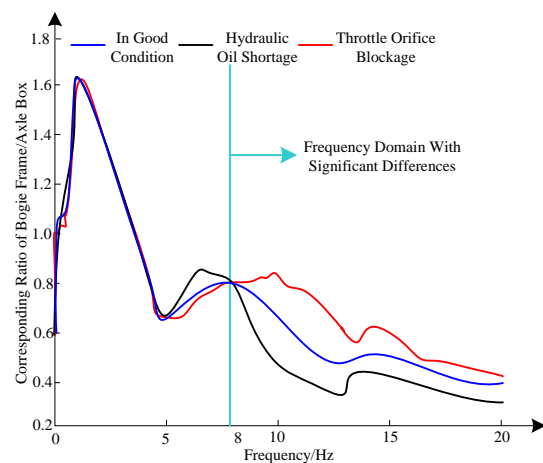


Figure 12. Detects Abnormal Vibration Attenuation of Axle Box Damper Based on Response Ratio

In Figure 11, the amplitude ratio of intact state (abnormal/intact) at each frequency is 1. From the difference of vibration attenuation characteristics of axle box dampers, in the frequency domain higher than 7.5 Hz, with the increase of vibration frequency of axle box dampers, when the throttle hole is blocked, the amplitude ratio of axle box acceleration is higher than 1, and when the hydraulic oil is insufficient, the amplitude ratio is lower than 1, which is inconsistent with the amplitude ratio of intact condition. Therefore, the shock absorber of axle box is in an abnormal state. It can be considered that the failure of the shock absorber of axle box can be judged by comparing the difference of vibration reduction characteristics in the frequency domain with the amplitude frequency domain above 7.5 Hz.

Figure 12 is an example of using response ratio method to detect the abnormality of shock absorber of axle box. From about 5 Hz, the response ratio is different, and there is also difference at 8Hz, but the difference is basically 0. After 8 Hz, the normal state, throttle hole blockage and hydraulic oil shortage show a decreasing trend with the

increase of vibration frequency of the axle box's shock absorber. Although the amplitude ratio of the three is consistent, there are obvious differences. Therefore, the shock absorber of axle box is in abnormal state, and the frequency domain above 8Hz is used, which can determine the failure of shock absorber of axle box.

3.2. Line Detection by Using Sliding Variance Peak Method of Axle Box Acceleration

The main factors affecting vehicle dynamic response include vehicle type and state, vehicle speed and line disturbance. When determining the threshold value of sliding variance of axle box vertical acceleration for line detection, it should correspond to vehicle type, state and running speed. In fact, the sampling frequency of vertical acceleration of axle box also directly affects the calculation result of sliding variance. The sliding variance of the vertical acceleration of a trailer's axle box is calculated when a comprehensive inspection vehicle runs at the speed level of 300 km/h in the initial stage of a high-speed railway joint commissioning test. The sampling frequency of the axle box acceleration is 100 Hz. Statistical analysis of the length of the line is 220 km, and there is a total of about 2200 rail welded joints and 6 groups of turnouts. The peak value of sliding variance of axle box vertical acceleration corresponding to all welded joints and turnouts is calculated. Table 1 shows the peak value of sliding variance greater than the threshold value and its proportion when the threshold value is different.

Table 1. Statistical Result of Sliding Variance of Vertical Acceleration of Axle Box in 220 km Line Section

Threshold Value/(m ² ·s ⁻⁴)	The Number of Sliding Variance Peaks Greater than the Threshold	Proportion of the Number of Sliding Variance Peaks Greater than the Threshold %
10000	0	0
8000	2	0.09
6000	5	0.22
5000	23	1.03
4000	67	2.99
3000	199	8.89
1000	1730	77.3
500	2237	99.96

The peak values of sliding variance of axle box vertical acceleration corresponding to 99% of welded joints and 6 groups of turnouts are between 500 m²/s⁴ and 5000 m²/s⁴. If 99% confidence probability corresponds, the threshold value is 5000 m²/s⁴. Table 2 lists the location of the line whose peak value of sliding variance of axle box vertical acceleration is more than 6000 m²/s⁴ and the corresponding line condition.

Table 2. Route Locations of Vertical Acceleration Sliding Variance Peak of Greater than 6000 m²/s⁴

Peak Value of Sliding Variance of Vertical Acceleration Route of Axle Box/(m ² ·s ⁻⁴)	Corresponding Route Location	Corresponding Line Condition
8673	K823+940	Welded Joint
8468	K832+040	Welded Joint
6437	K762+520	Welded Joint
6275	K761+450	Switch
6013	K837+240	Welded Joint

The peak value of sliding variance of axle box vertical acceleration passing through all turnouts at a speed level of 300 km/h of a comprehensive testing vehicle in the initial stage of a high-speed railway joint commissioning test is made statistical analysis, in which the sampling frequency of axle box acceleration is 1000 Hz. Table 3 shows the peak value of sliding variance greater than the threshold value and its proportion when the threshold value is different.

Table 3. Statistical Results of Peak Sliding Variance of Axle Box Vertical Acceleration at Turnout

Threshold Value/(m ² ·s ⁻⁴)	The Number of Sliding Variance Peaks Greater than the Threshold	Proportion of the Number of Sliding Variance Peaks Greater than the Threshold %
20000	0	0
15000	2	5.3
10000	3	7.9
8000	4	10.5
5000	16	42.1
4000	27	71.0
3000	31	81.6
2000	38	100

The peak value of sliding variance of axle box vertical acceleration corresponding to all turnouts ranges from 2000 m²/s⁴ to 20000 m²/s⁴, and the peak value of sliding variance of axle box vertical acceleration greater than 8000 m²/s⁴ has only 4 turnouts, accounting for about 10% of all turnouts. If 90% confidence probability corresponds, the threshold value is 8000 m²/s⁴.

Rail pre-grinding can eliminate decarburization layer on rail surface, short wave irregularity during rolling and rail surface defects during construction, and improve the smoothness of rail welded joints. Figure 13 shows the sliding variance of vertical acceleration of axle box at the speed level of 300 km/h before and after rail pre-grinding in 10 km section of a high-speed railway.

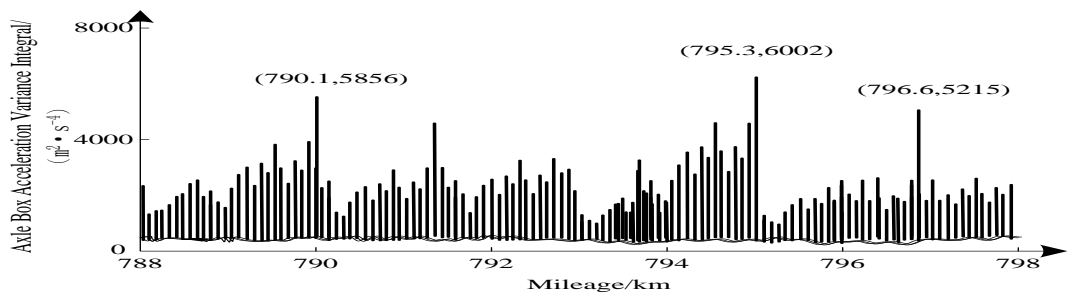
Figure 13 shows that the effect of rail pre-grinding on improving the smoothness of rail welded joints is very

obvious. After rail pre-grinding, the transient vibration energy of wheel pairs at rail welded joints generally decreases by 5-10 times.

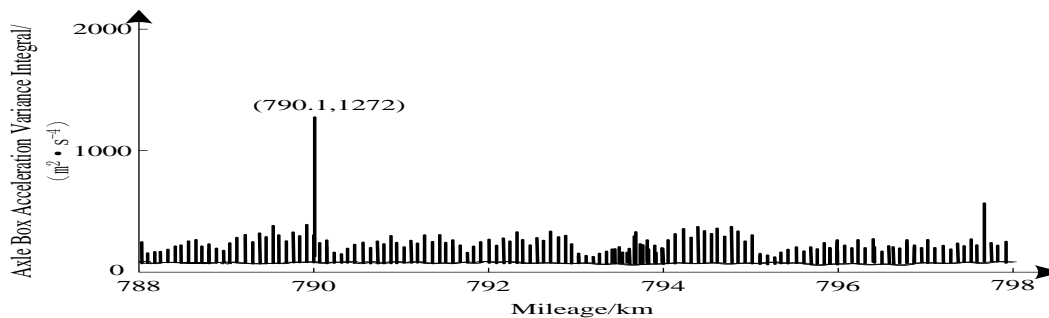
3.3. Derailment Detection

3.3.1. Basic Ideas

In previous research work, a method of comparing the frequency of acceleration exceeding the critical value and the cumulative value of current and previous acceleration is proposed. In order to improve the detection accuracy of derailment, this paper focuses on the different phenomena of peak vibration acceleration at specific parts of the vehicle and the positive and negative asymmetry of the inherent vibration acceleration when derailment occurs. The peak vibration acceleration here refers to the maximum vibration acceleration in a certain period of time. This method considers that “if the running speed and track state are determined, the magnitude of positive/negative peak vibration acceleration of bogie frame and vehicle body can be roughly determined”. According to the combination of running speed level (e.g. step length 10 km/h) and each track state (classification) (e.g. line interval level), the statistical average value and standard deviation value of peak vibration acceleration are established in advance. In the database, by comparing the database data with the peak vibration acceleration of the running time in turn, the abnormality of the running device can be detected. In addition, according to the positive and negative asymmetry of vibration acceleration waveform and other factors, it is determined whether derailment will occur. The following is the confirmation of the sample distribution (the distribution of vibration acceleration in normal condition) which belongs to the first stage of the same-level method, and the method for quantifying the degree of deviation of vibration acceleration from normal condition when derailed by checking the distribution of vibration acceleration in normal condition.



(a) Before Grinding



(b) After Grinding

Figure 13. Sliding Variance of Vertical Acceleration of Axle Box before and after Rail Grinding in the Same Line Section

3.3.2. Research on Detection Method

(1) Normal operation

Firstly, the statistical distribution of peak vibration acceleration in normal operation is confirmed. Figure 14 is the vertical vibration acceleration waveform of the freight vehicle body with a 2-axle bogie in normal operation. Figure 15 and Figure 16 show the peak vibration acceleration of the waveform calculated at regular intervals, respectively, and the statistical results of peak vibration acceleration are expressed in terms of frequency distribution. Table 4 gives the mean and standard deviation of normal operation.

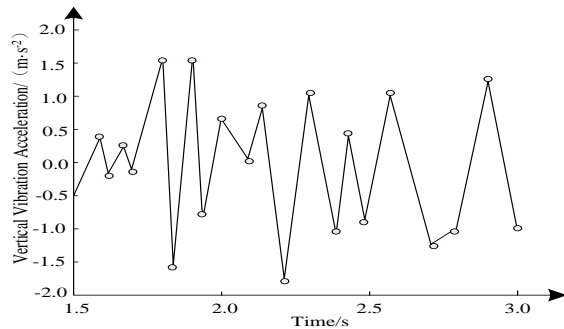


Figure 14. Vertical Vibration Acceleration Waveform of Vehicle Body in Normal Operation

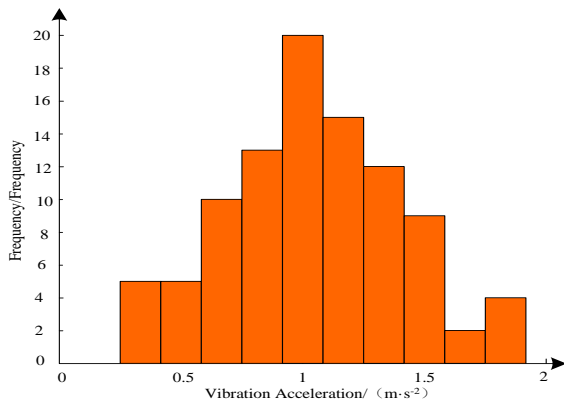


Figure 15. Frequency Distribution of Positive Peak Vibration Acceleration

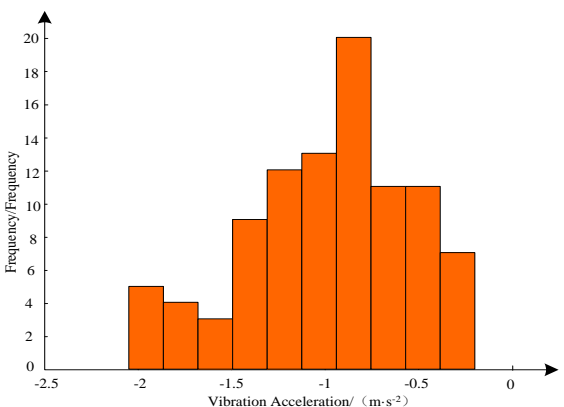


Figure 16. Frequency Distribution of Negative Peak Vibration Acceleration

Table 4. Average and Standard Deviation of Vertical Vibration Acceleration of Vehicle Body under Normal Operation

	Average Value	Standard Deviation
Positive Peak Vibration Acceleration/(m·s ⁻²)	1.07	0.36
Negative Peak Vibration Acceleration/(m·s ⁻²)	-1.00	0.43

The number of sampling samples is about 100, which is not enough, but the peak vibration acceleration shown in Figure 15 shows a normal distribution. From the negative peak vibration acceleration shown in Figure 16, the distribution shape is approximately lognormal distribution and F distribution. The higher the frequency around the average is, the more it deviates from the average, and the lower the frequency distribution is. According to these conditions, the more the deviations from the average are, the greater the possibility of anomalies is.

Table 4 gives the mean and standard deviation of normal operation. In addition, the vehicle speed corresponding to the test data of derailment is 9 km/h, so the comparison with the vertical vibration acceleration of the vehicle body under normal operation at this speed is in line with the requirements. However, because the data of freight vehicle running at 9 km/h in derailment test cannot be obtained, as the data of normal operation, the same data of freight vehicle running at 60 km/h with 2-axle bogie are used. The vibration acceleration of vehicle body increases with the increase of speed, so the derailment detection described below is conservative, and it is considered that there is no problem to compare with the vibration acceleration of 60 km/h running speed.

(2) Derailment operation

Figure 17 shows the vertical acceleration waveform of the vehicle body when the truck derails. In this paper, the acceleration is in the downward direction, and the acceleration waveform is processed in the same way as in normal operation. The peak vibration acceleration (Formula (11), (12)) is compared with the standard deviation in normal operation.

$$\alpha p > 30\sigma p \tag{11}$$

$$\alpha n < -50\sigma n \tag{12}$$

In the formula, σp is the standard deviation of positive peak vibration acceleration in normal operation, with the unit of m/s²; σn is the standard deviation of negative peak vibration acceleration in normal operation, with the unit of m/s²; αp is the positive peak vibration acceleration when derailing, with the unit of m/s²; αn is negative peak vibration acceleration when derailing, with the unit of m/s². In addition, Figure 17 is the vibration acceleration of the vehicle body when derailing, and Figure 18 is the vibration acceleration of the replaced bogie when running on ballast track.

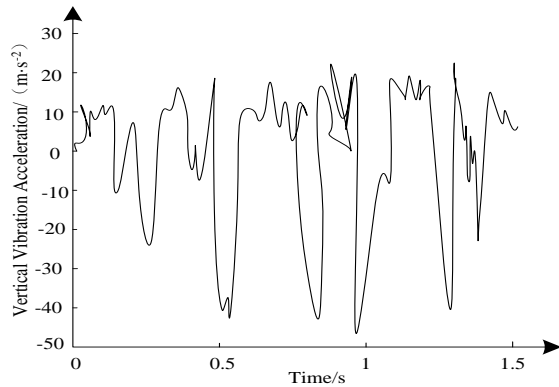


Figure 17. Vibration Acceleration of Car Body When Derailing

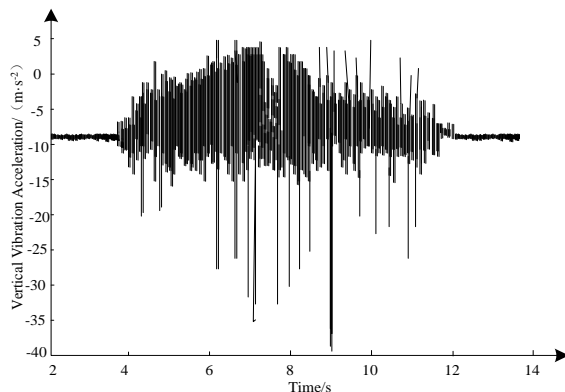


Figure 18. Vibration Acceleration of Replaced Bogie Running on Ballast Track

From Fig. 14 and 17, it can be seen that the vertical vibration acceleration of axle box fluctuates between $-1.8 \text{ m}\cdot\text{s}^{-2}$ and $1.7 \text{ m}\cdot\text{s}^{-2}$ in normal operation, with a small fluctuation range. When the vehicle derails, the vertical vibration acceleration of axle box fluctuates irregularly between $-45 \text{ m}\cdot\text{s}^{-2}$ and $22 \text{ m}\cdot\text{s}^{-2}$. The fluctuation range is very large, and the absolute value of negative peak vibration acceleration is greater than that of positive peak vibration acceleration. When derailment occurs, the vertical vibration acceleration of axle box is abnormal. After installing acceleration sensor on the bogie after replacement, it runs on ballast track. Figure 18 is the vibration acceleration of the replaced bogie running on ballast track. The vertical vibration acceleration shown in Figure 18 is the same as that shown in Figure 17. When the vehicle derails, the absolute value of the negative peak vibration acceleration is greater than the positive peak vibration acceleration, and the vertical vibration acceleration of the axle box is abnormal. In Figure 18, the reason for the formation of vibration acceleration waveform is that ballast and sleepers cause the wheel to be impacted in the upward direction, which is the waveform with unique characteristics when the vehicle derails. In addition, the sleepers are usually laid at intervals of 34 to 44 per 25 m. Assuming that the running speed is 9 km/h when derailment is considered, it can be considered that the wheel of the test vehicle passes through a sleeper at intervals of 0.30 s to 0.23 s . In Figure 17, the time interval of negative peak vibration acceleration is about 0.25 s , which is consistent with the time when the wheel passes through the sleeper. Therefore, it can be considered that the impact of sleepers and wheels results in negative peak vibration acceleration of the vehicle body. It can be seen that the accuracy of derailment detection can be improved by

considering the time when the wheel passes through the sleeper. In addition, even on slab (ballastless) track, the accuracy of derailment detection can be improved if the track information is used as the basis.

4. Conclusions

This paper studies the detection method for acceleration sensor anomaly of axle box of unmanned vehicle. This method takes the failure of bogie parts directly related to operation safety and the sliding variance peak value of dynamic response index of railway vehicle as the influencing factors to judge the acceleration sensor anomaly detection of axle box of unmanned vehicle, to achieve the acceleration sensor anomaly detection of axle box of unmanned vehicle.

(1) From the difference of vibration attenuation characteristics of axle box dampers, in the frequency domain above 7.5 Hz , the amplitude ratio of axle box acceleration under the condition of throttle hole blockage and insufficient hydraulic oil is inconsistent with that under the intact condition, which indicates that the axle box damper is abnormal at this time. Therefore, the difference of vibration attenuation characteristics in this frequency domain can be determined by comparing the amplitude frequency domain above 7.5 Hz . When the response ratio method is used to detect the shock absorber abnormality of the axle box, the frequency domain of the response ratio difference is more than 8 Hz . When the response ratio of the axle box acceleration is higher than 8 Hz , the response ratio of the axle box acceleration under the three conditions is consistent, but there are obvious differences, which indicate the shock absorber abnormality of the axle box. Therefore, the failure of shock absorber of axle box can be judged by using the difference of response rate in frequency domain above 8 Hz . Therefore, comparing the difference of vibration attenuation characteristics of axle box damper and using the method of response ratio to detect the abnormality of axle box damper, can well judge the abnormal condition of axle box acceleration, so as to realize the abnormal detection of axle box sensor acceleration of unmanned vehicle.

(2) Rail pre-grinding has obvious effect on improving the smoothness of rail welded joints. Based on the sliding variance of vertical acceleration of axle box at 300 km/h speed level, the instantaneous vibration energy of wheelset at rail welded joints after rail pre-grinding generally decreases by 5-10 times, and the variance of axle box acceleration significantly decreases. The variance of axle box acceleration reflects the vibration energy of wheelset. It can effectively characterize the influence of line excitation on the vibration state of wheelset.

(3) When derailment occurs, the vertical vibration acceleration waveform of axle box and the vibration acceleration waveform of replaced bogie running on ballast track are both the absolute value of negative peak vibration acceleration greater than that of positive peak vibration acceleration, and the vertical vibration acceleration of axle box is abnormal.

Reference

- [1] Sun, Q.; Zhang, B.; Li, Y.P.; Chen, C.J. Wavelength-Fixing Mechanisms for Detecting the Wheel Polygon-Shaped Fault Onsite. *Journal of Railway Science and Engineering*, 15, 2018, 2343-2348.

- [2] Wang, S.F.; Zhang, D.W. Analysis of Limit Relationship between Vehicle Speed and Front Wheel Angle. *Machinery Design & Manufacture*, 9,2017 , 237-240.
- [3] Xu, N.; Ren, Z.S.; Xu, R. Time and Frequency Domain Response and Vibration Transfer Characteristics of High-Speed EMU. *Journal of the China Railway Society*, 41, 2019, 31-40.
- [4] SHI Chunfei;SUN Yi;WANG Xiaoping. Study on Highly Sensitive Detection of Polarization Controlled Light Intensity Modulated SPRi Sensor[J]*Chinese Journal of Sensors and Actuators*. 30,2017,1152-1157.
- [5]LIU Yong-yong LI Guo-ping ZUO Guo-kun.Design of force sensor signal acquisition and processing system based on STM32[J].*Transducer and Microsystem Technologies*. 36,2017,112-115.
- [6] Dong, W.; Huang, W.; Xing, Z.Y.; Long, J.; A Rail Corrugation Detection Method Based on Wavelet Packet-Energy Entropy. *Railway Standard Design*, 62, 2018, 52-58.
- [7] Li, C.B.; Lou, J.J.; Zhang, Z.H.; Xia, J.M. Experimental Study on Vibration Characteristics of a Star-Type Compressor. *Journal of Wuhan University of Technology (Transportation Science & Engineering)*,42, 2018, 23-28.
- [8] Yang, Y.; Ding, J.J.; Li, F.; Jiang, K. Effect of Equivalent Stiffness of Resilient Wheel on Vehicle Dynamic Performance. *China Railway Science*,39, 2018,65-72.
- [9] Huang, Y.S.; Deng, S.E.; Zhang, W.H.; Hu, J.; Sun, L.M.; Ma, Z.K. Influence of Impact Loads on the Dynamic Characteristics of Plastic Cages in Railway Axle Bearings. *Journal of Vibration and Shock*, 37, 2018,172-180.
- [10] Cha, H.; Ren, Z.S.; Xu, N. Vibration Performance of High-Speed Vehicles with Axle Box Bearing. *Journal of Mechanical Engineering*,54, 2018,144-151.
- [11] Wang, W.J.; Li, G.Q.; Han, J.C.; Li, Q.Z. Influence Rule of Dynamic Stress of High-Speed Train Gearbox Housing. *Journal of Traffic and Transportation Engineering*, 15,2019, 85-95.
- [12] Dai, M.Z.; Gao, C.F. Framework Performance Evaluation Based on Hadoop, Spark and Flink Large-Scale Data Analysis. *Journal of China Academy of Electronics and Information Technology*, 13,2018, 149-155.
- [13] Guo, Q.Y.; Kang, J.S.; Feng, J.H.; Zhou, G.F. Current Development and Trend of Rail Transit Vehicle Traction Control. *Journal of Power Supply*, 15, 2017, 40-45.
- [14] An, Y.P.; Zhao, J.C.; Liu, J.N. Research on Control of Lithium-Ion Battery Charge and Discharge Based on Bi-Directional DC/DC Converter. *Chinese Journal of Power Sources*,41, 2017,208-210.
- [15] Yu, F.H. Design and Analysis of Intelligent Three Dimensional Parking Lot Control System Based on PLC Technology. *Automation & Instrumentation*, 231, 2019, 86-88.
- [16] Wang, D.X.; Teng, J.K. Authentication Scheme Based on Aggregate Signature in VSNS. *Journal of Jilin University (Science Edition)*, 56, 2018, 657-662.
- [17] Liu, B.; Luo, X.; Zhu, J. Research on Simulation of Planning Obstacle Avoidance Path for Automated Vehicles. *Computer Simulation*, 35, 2018, 105-110.

Driving Pattern Recognition of Hybrid Electric Vehicles Based on Multi-hierarchical Fuzzy Comprehensive Evaluation

Qingyong Zhang^{a,b,*}, Zhenfei Lu^a, Yaru Wang^a, Weiping Lin^a

^aSchool of Mechanical and Automotive Engineering, Fujian University of Technology, Fuzhou 350118, China

^bFujian Key Laboratory of Automotive Electronics and Electric Drive, Fujian University of Technology, Fuzhou 350118, China

Received OCT 16 2019

Accepted FEB 2 2020

Abstract

Energy management strategy is a key technology which affects the fuel economy of hybrid electric vehicles (HEVs), which is greatly affected by the complex driving environment of vehicles, and further research is needed in the aspect of comprehensive consideration of vehicle driving pattern. In this paper, the multi-mode driving control is defined as the control strategy which switches a current driving control algorithm to the algorithm optimized in a recognized driving pattern. Based on the analysis of vehicle drive cycle, the driving pattern is defined according to the randomness of vehicle drive cycle. Four representative driving patterns are selected, which are composed of two urban driving patterns, two express way driving pattern. A total of 14 characteristic parameters are chosen to characterize the driving patterns. The multi-hierarchical comprehensive evaluation based on fuzzy comprehensive evaluation for vehicle drive conditions is introduced, which in driving decides periodically the representative driving pattern that is closest to a current drive cycle by comparing the correlation related to 14 characteristic parameters. The hierarchical system of vehicles driving patterns characteristic parameters is set up. Using an actual drive cycle as an example, the working condition is evaluated using the weighted average of fuzzy comprehensive evaluation model with comprehensive consideration of the influence of multiple factors. The analysis of vehicle drive cycle can be used to guide the design of HEVs powertrain and the multi-mode control algorithm using real-time online identification of driving pattern can be developed to optimize the performance of HEVs.

© 2020 Jordan Journal of Mechanical and Industrial Engineering. All rights reserved

Keywords: Drive cycle; driving pattern; fuzzy evaluation; multi-mode control;

1. Introduction

The actual drive cycle of vehicles is random and uncertain which considerably affects the emissions and fuel efficiency of HEV, and especially the driving cycle and driving habits that have more sensitive influence on HEV than internal combustion engine vehicles. Currently, most of the hybrid power train parameters matching and control strategy optimization are obtained based on the analysis of a specific drive cycle. If the drive control strategy of HEV is not suitable for current drive cycle, it will have worse performance of fuel consumption and emissions than internal combustion engine vehicles (Song *et al.*, 2016).

The hybrid buses have the characteristics of fixed driving route and strong cycle repeatability, which can realize the on-line identification and application of control strategy and typical working conditions. The selection of HEV powertrain structure, parameter matching, and test development must be based on the reasonable actual drive cycle. Additionally, the simulation analysis and performance verification of the whole vehicle should be conducted on the basis of the drive cycles (Luo *et al.*, 2007).

The existing recognition methods of working condition mainly include neural network recognition method, fuzzy inference recognition method, etc (Montazeri-Gh M and Mahmoodi-k M, 2015). It needs a lot of data training to identify the working condition accurately by using neural network. However, due to the complexity of the actual

working condition and many emergencies, it is difficult to obtain a large number of accurate data samples for its learning. The driving pattern recognition based on fuzzy discrimination can contain all kinds of information. It can make the same kind of signals achieve different effects under different operations by changing the fuzzy rules, and has good following and filtering characteristics (Hao *et al.*, 2016).

Yang (2014) established a classification and identification sample by dividing the standard working conditions, and established a working condition identifier based on the limit learning machine to complete the identification of the cycle working conditions. Lian (2016) proposed an adaptive control strategy based on fuzzy on-line identification for a parallel hybrid electric bus. The algorithm of fuzzy on-line identification is designed to identify the actual driving conditions of the vehicle. The corresponding optimal control parameters are called according to the results of condition identification. The experimental results showed that the designed fuzzy recognition method can complete the recognition of driving condition type. In order to overcome the lack of adaptability of PHEV powertrain control strategy in complex driving cycle, Chen (2017) proposed a route-based fuzzy adaptive control strategy of PHEV and the results showed that the method can improve the economic performance.

Vehicle have random actual working conditions and the characteristics of fuzzy information, which can be described and studied using fuzzy set. Due to the large amount of

* Corresponding author e-mail: zhqy@fjut.edu.cn.

calculation, many kinds of parameters and wide range of features, fuzzy recognition algorithm is applied in this study. It can recognize by quantifying the membership characteristics of computational data and standard data, which can eliminate the interference of noise array and accurately reflect the belonging of recognition object. In addition, fuzzy recognition has the advantages of fast calculation speed and strong real-time performance, which is applicable to the identification of driving conditions in this study.

The drive cycles of vehicles are not only the characteristics manifested by vehicle itself, but also evaluators' understanding of vehicle performance from different purposes. It can be understood as the evaluation subjects' qualitative descriptions of objective phenomenon. In order to make the evaluation object of qualitative description distinguished and compared, some quantitative standards are needed.

2. Multi-mode Drive Control

Multi-mode drive control is defined as a kind of control strategy, and it can convert the present drive control algorithm into the optimized algorithm of representative driving pattern after identification (Lei *et al*, 2017). By contrast, single mode control is the control strategy that only has one drive control algorithm. The use of driving pattern recognition can make drive control strategy periodically adapted to current drive mode. To achieve this goal, simulation or experiment was conducted on the four typical driving patterns, and then the control parameters in the working index were optimized, thereby reducing fuel consumption and improving emission performance. These control parameters were stored in the vehicle control unit memory (Zhang & Xiong, 2015).

Control parameters are composed of weighting factors of working indexes, which are used to determine the indexes such as engine power. In actual driving, control parameters change to be the ones most suitable for current driving pattern according to the results of driving pattern recognition (Jeon *et al*, 2002).

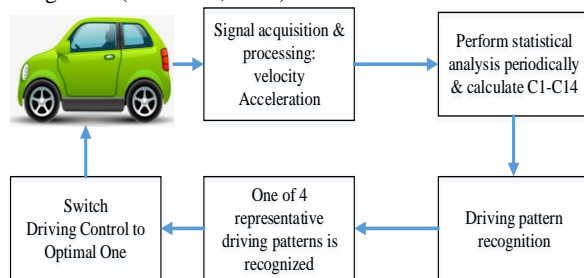


Figure 1. Multi-mode control principle diagram.

Fig.1 shows the multi-mode drive control diagram. First of all, each representative driving pattern control parameters were optimized so as to reduce fuel consumption and emissions. Such process could be finished through simulation. Thus, velocity and acceleration signals were stored in the vehicle control unit memory through the sensor measurement. The characteristic parameters were obtained through the statistical analysis of stored signals at short intervals. These results, as the input of fuzzy evaluation of vehicle drive cycles, recognized current driving pattern as one of four representative typical driving patterns. According to the result of driving pattern recognition, the drive control algorithm was turned into the optimized algorithm (Nicolas *et al*,2016).

3. Multi-hierarchical Comprehensive Evaluation Method Based on Fuzzy Comprehensive Evaluation

The basic idea of fuzzy comprehensive evaluation is to make reasonable comprehensive evaluation using fuzzy linear transformation principle and maximum degree of membership, and considering various factors related to the evaluated object (Liu *et al*, 2013).

It is assumed that there are m factors related to the evaluated object, and it is expressed with $U = \{u_1, u_2, \dots, u_m\}$ and named as the factor set. It represents m properties of the object. Besides, it is assumed that there are n possible comments, and it is expressed with $V = \{v_1, v_2, \dots, v_n\}$ and named as the evaluation set.

For the significance of comprehensive evaluation, when the individual factor u_i is considered, the membership degree of u_i evaluation for the evaluation v_j is $r_{ij} (j = 1, 2, \dots, n)$; for the result through the generalized fuzzy "and" operation ($a_i \wedge r_{ij}$) expressed with r_{ij}^* , when various factors are comprehensively considered, the membership degree of u_i evaluation for v_j means the adjustment on r_{ij} when the influence degree a_i of factor u_i on the total evaluation is considered. Finally, the adjusted membership degree is comprehensively processed through generalized fuzzy "or" operation so as to obtain reasonable comprehensive evaluation results.

When there are many elements in factor set U , the importance coefficient of each factor is correspondingly smaller, and it is often difficult to distinguish the superiority order of things in the system, and impossible to obtain meaningful evaluation results. For this kind of situation, the elements in factor set U can be divided into several categories according to certain properties; people can first make comprehensive evaluation on each kind of factors (fewer elements), and then conduct high-level comprehensive evaluation of the "class" element among the evaluation results (Shen *et al*, 2009). The specific method is as follows:

Assuming the importance degree subset of U_i is A_i , and the comprehensive evaluation matrix of k_i factors in U_i for V is R_i , the first level model $M(\wedge, \vee)$ is selected for the fuzzy comprehensive evaluation on U_i . It is assumed that the fuzzy comprehensive evaluation set of U_i is as follows:

$$B_i = A_i * R_i = (b_{i1}, b_{i2}, \dots, b_{in}) \quad (i = 1, 2, \dots, N) \tag{1}$$

Assuming importance degree fuzzy subset of $U = \{U_1, U_2, \dots, U_N\}$ factor is as follows:

$$A = \{A_1, A_2, \dots, A_N\} \tag{2}$$

Based on Equation (1), the second level comprehensive evaluation matrix is constructed:

$$R = \begin{pmatrix} B_1 \\ B_2 \\ \vdots \\ B_N \end{pmatrix} = \begin{pmatrix} A_1 * R_1 \\ A_2 * R_2 \\ \vdots \\ A_N * R_N \end{pmatrix} \tag{3}$$

Then, the second level fuzzy comprehensive evaluation for U is as follows:

$$B = A * R = (b_1, b_2, \dots, b_n) \tag{4}$$

Finally, using the principle of maximum membership degree, the level (evaluation) corresponded by the maximum b_i is the best evaluation result.

4. The Classification of Vehicle Drive Mode

4.1. Vehicle Characteristic Parameters of Drive cycle

Vehicle driving pattern can be described with a variety of standard. This paper defines it with drive cycle working condition, and describes it with the recommended parameters in Table 1^[5]. For vehicle driving cycle, the factor set was $U = [C1, C2, \dots, C14]$. Because there are many factors and the weight need to meet $\sum \alpha_i = 1$, the weight of some factors would be smaller. Therefore, the factor set is further classified, and then factors within each level are comprehensively evaluated; finally, the high level of comprehensive evaluation is conducted on the evaluation results.

Table 1. Fourteen characteristic parameters of driving patterns.

Parameters	Meaning
C1	Average circling speed [km/h]
C2	Average operating speed after removing the parking time, $V > 0.5 \text{ km/h}$ [km/h]
C3	Parking time /total time [%]
C4	Accelerating kinetic energy under unit mass and distance (PKE) [m^2/s^2]
C5	Average acceleration [m/s^2], $a > 0.1 \text{ m}/\text{s}^2$
C6	Average deceleration [m/s^2], $a < -0.1 \text{ m}/\text{s}^2$
C7	The number of parking per kilometer
C8	Average start-stop time (from starting and parking) [s]
C9	Acceleration time/total time [%]
C10	Deceleration time /total time [%]
C11	Acceleration standard deviation [m/s^2]
C12	Deceleration standard deviation [m/s^2]
C13	Maximum speed [km/h]
C14	Speed standard deviation [km/h]

In Table 1, C4 denotes the speed kinetic energy under unit mass and unit travel distance. The calculation formula is as follows:

$$PKE = \sum \frac{V_f^2 - V_i^2}{x}, \frac{dV}{dt} > 0 \tag{5}$$

In Equation (5), V_f and V_i respectively denote the start and final speed for each time of acceleration; x is the total travel distance.

C5 denotes the average acceleration of the whole acceleration process; C6 denotes the average deceleration of the whole deceleration process; C11 is acceleration standard deviation. For the selected driving pattern, the average acceleration of each driving pattern (C5) was firstly solved, the square root of the squares of the sum of each value and

average deviation is the acceleration standard deviation. Similarly, C12 is the deceleration standard deviation; C14 is the corresponding average circling speed standard deviation, which can refer to the calculation of acceleration standard deviation.

Four representative driving patterns are selected, including two urban driving patterns and two highway drive patterns, shown in Fig. 2. And the dynamic performance of each driving pattern was sorted, which concretely describes the composition of each driving pattern and the statistics characteristics of the speed curve.

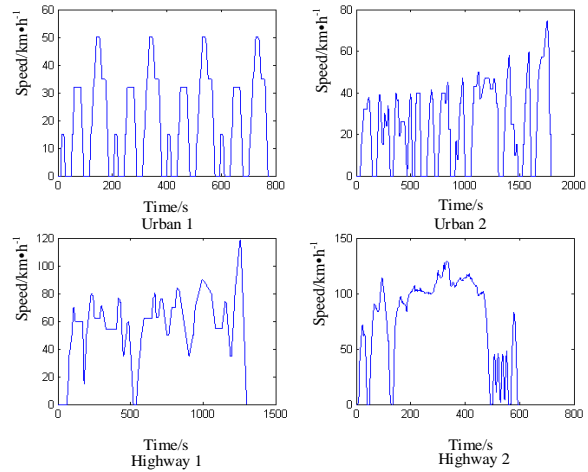


Figure 2. Four driving patterns.

The four specific driving patterns are described using the parameters specified in Table 1, and the specific values are shown in Table 2.

Table 2. Characteristic Parameter Values of Four Driving Patterns.

Characteristic Parameter	Urban 1	Urban 2	Highway 1	Highway 2
C1/ $\text{km} \cdot \text{h}^{-1}$	18.73	24.57	57.22	77.15
C2/ $\text{km} \cdot \text{h}^{-1}$	28.1	31.95	61.22	82.65
C3/%	30.8	23.12	6.96	6.66
C4/ $\text{m} \cdot \text{s}^{-2}$	0.2918	0.1612	0.2102	0.4573
C5/ $\text{m} \cdot \text{s}^{-2}$	0.13	0.1	0.1	0.28
C6/ $\text{m} \cdot \text{s}^{-2}$	-0.13	-0.1	-0.1	-0.29
C7	4	7.25	0.3	0.38
C8/s	45	120	607.5	109.4
C9/%	21.5	30.87	34.08	40.61
C10/%	18.5	28.2	32.62	40.27
C11/ $\text{m} \cdot \text{s}^{-2}$	0.1493	0.1493	0.1493	0.1493
C12/ $\text{m} \cdot \text{s}^{-2}$	-	-	-0.1578	-0.1578
C13/ $\text{km} \cdot \text{h}^{-1}$	50	74.52	118.43	129.2
C14/ $\text{km} \cdot \text{h}^{-1}$	47.84	47.84	47.84	47.84

4.2. The Classification of Factor Set and Determination of Weight

The fuzzy evaluation of vehicle drive cycles involves many factors, so the factors involved are divided into several categories in accordance with certain attributes, and then ordered from low to high level, as shown in Fig.3. Comprehensive evaluation is first conducted on the early

levels of each kind, and then higher level of comprehensive evaluation is implemented on the class of evaluation results of each type so as to obtain the quantitative evaluation results that accorded with the actual situations.

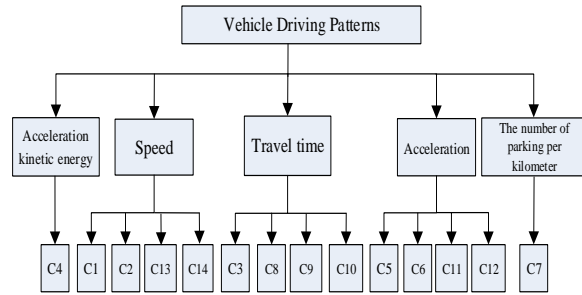


Figure 3. The hierarchical system of vehicles driving patterns Characteristic parameters.

For the weight of the characteristic parameters that described the vehicle driving pattern, the weight value shown in Table 3 are adopted.

Table 3. Characteristic Parameters and the Weight of Four Driving Patterns.

First level index and weight	Second level index and weight	Weight
Speed	Average circling speed	0.33
	Average speed after removing the parking time	0.33
	Maximum speed	0.17
	Speed standard deviation	0.17
	Parking time/total time	0.4
	Average start-stop time (from starting to parking)	0.2
Travel time	Acceleration time/total time	0.2
	Deceleration time/total time	0.2
	Average acceleration	0.33
	Average deceleration	0.33
Acceleration	Acceleration standard deviation	0.17
	Deceleration standard deviation	0.17
	accelerating kinetic energy under unit mass and unit distance	1
	The number of parking per kilometer	0.05
	The number of parking per kilometer	1

4.3. The Determination of Evaluation Set

Evaluation sets is a direct description and representation form of each level factors evaluation results. It is necessary to establish the corresponding evaluation set for each level of factors. It is determined the evaluation structure of various factors in the model are four grades, namely, 4 elements in V (m = 4) are expressed with V = {V1, V2, V3 and V4}.

The second level of factors are the base factors of comprehensive evaluation, namely, the direct survey

evaluation factors. And the first level factor and the total target are the comprehensive reflection about the evaluation results of several factors. Evaluation sets represent the comprehensive evaluation results in the form of membership degree, and can fully reflect the evaluation.

For the fuzzy evaluation of vehicles working mode, four driving patterns are adopted as the evaluation result. Therefore, the key problem was how to determine the membership degree of elements in the factor sets. By taking Parameters C1 and C2 as examples, the membership function of driving pattern parameters is listed below.

(1) Average circling speed

Normal distribution is used as the membership function of average circling speed, and the average value is the average circling speed obtained by calculation. Besides, the variance is the average cycling speed standard deviation of four driving patterns. With urban drive cycle 1 as an example, the normal distribution value is listed in Equation (6):

$$\mu(C1) = e^{-\left(\frac{x-18.73}{47.84}\right)^2} \tag{6}$$

The membership degree curve of average circling speed under the four driving patterns is shown in Fig. 4.

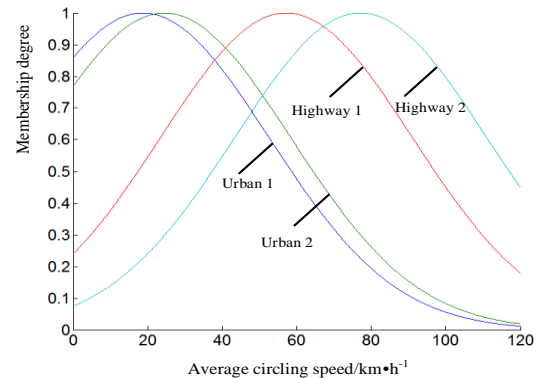


Figure 4. Membership Curve of Vehicles Average Circling Speed.

(2) Average speed after removing the parking time

Being similar to C1, with urban driving pattern 1 as an example, the normal distribution was taken, and the average is the average running speed after removing parking time, the variance is the average speed standard deviation of the four driving pattern2. The membership of average speed after removing the parking time is shown in Equation (7).

$$\mu(C2) = e^{-\left(\frac{x-28.1}{44.65}\right)^2} \tag{7}$$

The membership curve of average speed after removing the parking time under the four driving pattern is shown in Fig.5.

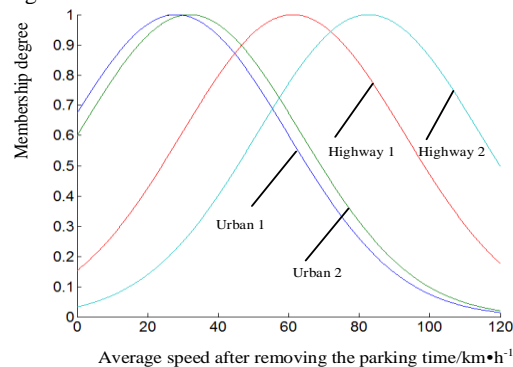


Figure 5. Membership curve of vehicle average speed after removing the parking time

Similarly, the characteristic parameters membership functions under the four driving pattern could be obtained, as shown in Table 4.

Table 4. Membership functions of characteristic parameters under four driving patterns.

	Urban 1	Urban 2	Highway 1	Highway 2
C1	$e^{-\left(\frac{x-18.75}{47.84}\right)^2}$	$e^{-\left(\frac{x-24.57}{47.84}\right)^2}$	$e^{-\left(\frac{x-57.22}{47.84}\right)^2}$	$e^{-\left(\frac{x-77.15}{47.84}\right)^2}$
C2	$e^{-\left(\frac{x-28.1}{44.65}\right)^2}$	$e^{-\left(\frac{x-31.95}{44.65}\right)^2}$	$e^{-\left(\frac{x-61.22}{44.65}\right)^2}$	$e^{-\left(\frac{x-82.65}{44.65}\right)^2}$
C3	$e^{-\left(\frac{x-0.308}{0.2087}\right)^2}$	$e^{-\left(\frac{x-0.2312}{0.2087}\right)^2}$	$e^{-\left(\frac{x-0.0696}{0.2087}\right)^2}$	$e^{-\left(\frac{x-0.0666}{0.2087}\right)^2}$
C4	$e^{-\left(\frac{x-0.2918}{0.2249}\right)^2}$	$e^{-\left(\frac{x-0.1612}{0.2249}\right)^2}$	$e^{-\left(\frac{x-0.2102}{0.2249}\right)^2}$	$e^{-\left(\frac{x-0.4573}{0.2249}\right)^2}$
C5	$e^{-\left(\frac{x-0.13}{0.1493}\right)^2}$	$e^{-\left(\frac{x-0.1}{0.1493}\right)^2}$	$e^{-\left(\frac{x-0.1}{0.1493}\right)^2}$	$e^{-\left(\frac{x-0.1}{0.1493}\right)^2}$
C6	$e^{-\left(\frac{x+0.13}{0.1578}\right)^2}$	$e^{-\left(\frac{x+0.1}{0.1578}\right)^2}$	$e^{-\left(\frac{x+0.1}{0.1578}\right)^2}$	$e^{-\left(\frac{x+0.29}{0.1578}\right)^2}$
C7	$e^{-\left(\frac{x-4}{5.7633}\right)^2}$	$e^{-\left(\frac{x-7.25}{5.7633}\right)^2}$	$e^{-\left(\frac{x-0.3}{5.7633}\right)^2}$	$e^{-\left(\frac{x-0.38}{5.7633}\right)^2}$
C8	$e^{-\left(\frac{x-45}{450.2385}\right)^2}$	$e^{-\left(\frac{x-120}{450.2385}\right)^2}$	$e^{-\left(\frac{x-607.5}{450.2385}\right)^2}$	$e^{-\left(\frac{x-109.4}{450.2385}\right)^2}$
C9	$e^{-\left(\frac{x-0.215}{0.1378}\right)^2}$	$e^{-\left(\frac{x-0.3087}{0.1378}\right)^2}$	$e^{-\left(\frac{x-0.3408}{0.1378}\right)^2}$	$e^{-\left(\frac{x-0.4061}{0.1378}\right)^2}$
C10	$e^{-\left(\frac{x-0.185}{0.1574}\right)^2}$	$e^{-\left(\frac{x-0.282}{0.1574}\right)^2}$	$e^{-\left(\frac{x-0.3262}{0.1574}\right)^2}$	$e^{-\left(\frac{x-0.4027}{0.1574}\right)^2}$
C11	$e^{-(x-0.1493)^2}$	$e^{-(x-0.1493)^2}$	$e^{-(x-0.1493)^2}$	$e^{-(x-0.1493)^2}$
C12	$e^{-(x+0.1578)^2}$	$e^{-(x+0.1578)^2}$	$e^{-(x+0.1578)^2}$	$e^{-(x+0.1578)^2}$
C13	$e^{-\left(\frac{x-50}{64.396}\right)^2}$	$e^{-\left(\frac{x-74.5}{64.396}\right)^2}$	$e^{-\left(\frac{x-118.4}{64.396}\right)^2}$	$e^{-\left(\frac{x-129.2}{64.396}\right)^2}$
C14	$e^{-(x-47.84)^2}$	$e^{-(x-47.84)^2}$	$e^{-(x-47.84)^2}$	$e^{-(x-47.84)^2}$

5. Case Study

By taking one actual drive cycle as the example, the fuzzy evaluation is conducted and the speed curve is shown in Fig. 6.

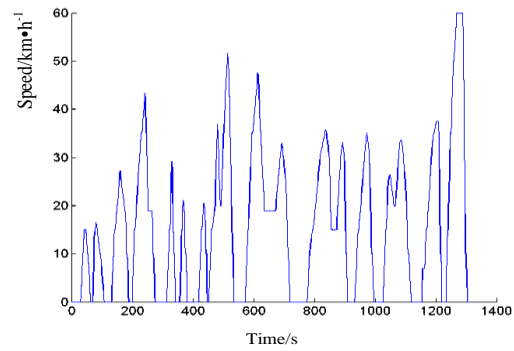


Figure 6. Speed curve of the vehicle drive cycle to be Evaluated

The characteristic parameters of the working condition are as follows:

$$U = \{16.1, 19.83, 30.37, 0.285, 0.11, -0.11, 2.5, 67.64, 0.3485, 0.2336, 0.1539, -0.1643, 60, 54.135\}$$

After bringing the value to Table 4, the membership of the factors in different driving patterns could be obtained. Multi-hierarchical fuzzy evaluation is conducted according to the classification method shown in Table 3. In accordance with the classification method shown in Table 3, second level indexes are comprehensively evaluated in the first place. The evaluation matrix of the second layer was established.

By definition, the second level indexes evaluation matrix are respectively as follows:

$$R_1 = \begin{bmatrix} 0.99 & 0.97 & 0.48 & 0.2 \\ 0.97 & 0.93 & 0.42 & 0.13 \\ 0.98 & 0.95 & 0.44 & 0.32 \\ 0 & 0 & 0 & 0 \end{bmatrix}$$

$$R_2 = \begin{bmatrix} 0.99 & 0.87 & 0.28 & 0.27 \\ 0.99 & 0.98 & 0.24 & 0.99 \\ 0.39 & 0.92 & 0.99 & 0.84 \\ 0.90 & 0.91 & 0.71 & 0.32 \end{bmatrix}$$

$$R_3 = \begin{bmatrix} 0.98 & 1 & 1 & 0.27 \\ 0.98 & 1 & 1 & 0.27 \\ 1 & 1 & 1 & 1 \\ 1 & 1 & 1 & 1 \end{bmatrix}$$

The weight matrix are as follows:

$$A_1 = [0.33 \quad 0.33 \quad 0.17 \quad 0.17]$$

$$A_2 = [0.4 \quad 0.2 \quad 0.2 \quad 0.2]$$

$$A_3 = [0.33 \quad 0.33 \quad 0.17 \quad 0.17]$$

By using fuzzy transformation and the first model, namely:

$$b_j = \bigvee_{i=1}^m (a_i \wedge r_{ij}) \quad (j = 1, 2, \dots, n)$$

The corresponding results could be obtained:

$$B_1 = A_1 \circ R_1 = [0.33 \quad 0.33 \quad 0.33 \quad 0.2]$$

$$B_2 = A_2 \circ R_2 = [0.4 \quad 0.4 \quad 0.28 \quad 0.27]$$

$$B_3 = A_3 \circ R_3 = [0.33 \quad 0.33 \quad 0.33 \quad 0.27]$$

After combining the evaluation results of the second level indexes with the membership functions of two independent index, the evaluation matrix of the first level indexes are obtained as follows:

$$R = \begin{bmatrix} 0.33 & 0.33 & 0.17 & 0.17 \\ 0.4 & 0.2 & 0.2 & 0.2 \\ 0.33 & 0.33 & 0.17 & 0.17 \\ 1 & 0.74 & 0.9 & 1 \\ 0.94 & 0.51 & 0.86 & 0.87 \end{bmatrix}$$

The weights allocation of the first level indexes is as follows:

$$A = [0.3 \quad 0.25 \quad 0.3 \quad 0.1 \quad 0.05]$$

After conducting fuzzy transformation, the corresponding results could be found:

$$B = A \circ R = [0.3 \quad 0.3 \quad 0.2 \quad 0.2]$$

The fuzzy evaluation results obtained through the first model have the same membership degree for the urban driving pattern 1 and 2. Because the main element decided type fuzzy comprehensive evaluation model considers only the main influencing factors, and ignores the influence of other factors, it is more suitable for the situation that the single evaluation optimization could be the optimal comprehensive evaluation.

In order to comprehensively consider the effect of multiple factors, the weighted average fuzzy comprehensive evaluation model is adopted.

$$b_j = \sum_{i=1}^m (a_i \cdot r_{ij}) \quad (j = 1, 2, \dots, n)$$

The second level indexes are evaluated, and the following results are obtained:

$$B_1 = A_1 \circ R_1 = [0.8143 \quad 0.7885 \quad 0.3718 \quad 0.1633]$$

$$B_2 = A_2 \circ R_2 = [0.852 \quad 0.91 \quad 0.5 \quad 0.538]$$

$$B_3 = A_3 \circ R_3 = [0.9868 \quad 1 \quad 1 \quad 0.5182]$$

The evaluation matrix of the first level indexes are as follows:

$$R = \begin{bmatrix} 0.8143 & 0.7885 & 0.3718 & 0.1633 \\ 0.8520 & 0.91 & 0.5 & 0.538 \\ 0.9868 & 1 & 1 & 0.5182 \\ 1 & 0.74 & 0.9 & 1 \\ 0.94 & 0.51 & 0.86 & 0.87 \end{bmatrix}$$

The weights allocation of the first level indexes is as follows:

$$A = [0.3 \quad 0.25 \quad 0.3 \quad 0.1 \quad 0.05]$$

After conducting fuzzy transformation, we could find

$$B = A \circ R = [0.9 \quad 0.86 \quad 0.67 \quad 0.48]$$

Visibly, the selected actual drive cycle is closer to the selected urban driving pattern 1.

Seen from the results above, the fuzzy comprehensive evaluation method can be effectively used to distinguish the working conditions of vehicles. The characteristic parameters of the selected driving mode meet the needs of the actual working conditions and the characteristics of the randomness of the actual working conditions. On this basis, combining with other information such as driver's intention, the energy management strategy based on condition adaptation can meet the real-time control and optimization of vehicle management strategy under various conditions. The results can be used not only in hybrid vehicles, but also in electric vehicles and fuel cell vehicles.

6. Conclusions

Due to the fuzzy characteristics of vehicle driving data, this paper proposes a method of vehicle driving pattern recognition based on fuzzy discrimination.

Firstly, the principle of multi-mode drive control is introduced. Besides, the multi-level comprehensive evaluation based on fuzzy comprehensive evaluation for vehicle drive cycle is introduced. The results of comprehensive evaluation are judged according to the maximum membership principle; The vehicle driving pattern is defined with the drive cycling working condition.

Four typical driving patterns are selected to define the typical driving pattern of HEV, including two urban drive cycles and two highway drive cycles. The driving patterns are described using 14 representative characteristic parameters (C1 - C14), which are closely related to the speed, acceleration, and so on. According to the composition of drive cycles and the statistical characteristics for each speed curve, the characteristic parameters of four driving patterns are defined; The factors relating to four driving patterns are divided into five categories according to property, and the weights of their characteristic parameters are selected. The evaluation sets of evaluation results of factors at various levels are established. The membership functions of driving pattern parameters are determined; With a certain actual drive cycle as an example, the working condition is evaluated using the weighted average of fuzzy comprehensive evaluation model with comprehensive consideration of the influence of multiple factors.

Based on the analysis of the historical driving data, the energy management strategy based on multi-hierarchical fuzzy comprehensive can judge the driving condition type of the current and future vehicles in a short time, and dynamically adjusts the control strategy according to the condition type to achieve the adaptive energy management strategy.

Acknowledgments

This project is supported by the project grant from natural science foundation of Fujian province (2015J01179), the projects of technological innovation and strategic emerging industries of Fujian provincial economic and trade commission, the projects of industry-university collaboration of Fuzhou municipal economic and trade commission.

References

- [1] Chen Z., Xiong R., Cao J.(2016). Particle swarm optimization-based optimal power management of plug-in hybrid electric vehicles considering uncertain driving conditions[J]. *Energy*, 96:197-208.
- [2] Chen H., Guo J., Chu L.(2017). Research on route-based fuzzy adaptive control strategy of PHEV[J]. *Automobile technology*, (4):40-44.
- [3] Hao J., Yu Z., Zhao Z.(2016). Optimization of key parameters of energy management strategy for hybrid electric vehicle using DIRECT algorithm[J]. *Energies*, 9(12): 997.
- [4] Jeon, S.I., Jo, S.T., Park, Y.I. & Lee, J.M. (2002). Multi-mode driving control of a parallel hybrid electric vehicle using driving pattern recognition. *Journal of Dynamic Systems, Measurement, and Control*, 124(3):141-149.
- [5] Lei, Z.Z., Qin, D.T., Liu, Y.G., Peng, Z.Y. & Lu L.L. (2017). Dynamic energy management for a novel hybrid electric

- system based on driving pattern recognition. *Applied Mathematical Modelling*, 45(5):940-954.
- [6] Liu, W., Zhao, Y., Ruan, M., & Wang, W. (2013). Fuzzy comprehensive evaluation and verification for handling stability of vehicle. *China Mechanical Engineering*, 24 (19):2681-2686.
- [7] Lian J., Chang J., Li L.(2016). Adaptive control strategy of parallel hybrid electric bus based on Fuzzy n-line identification[J]. *Journal of Beijing University of Technology*, 36(3): 264-270.
- [8] MontazeriM. &Mahmoodi-k M.(2015). Development a new power management strategy for power split hybrid electric vehicles[J]. *Transportation Research Part D: Transport and Environment*, (37): 79-96.
- [9] Nicolas, D., Maxime, R., Dubois, Renaud, D. & Alain, De. (2016). Blended Power Management Strategy Using Pattern Recognition for a Plug-in Hybrid Electric Vehicle. *International Journal of Intelligent Transportation Systems Research*, 14(2):101-114.
- [10] Song, W., Zhang, X., Tian, Y. & Xi L.H. (2016). Driving pattern recognition and charging management-based Intelligent control strategy for extended-range electric vehicles. *Journal of Automotive Safety and Energy*, 7(2):224-229.
- [11] Shen, Y., Huang, J., Fang Z., Yang, X. (2009). Study on two-layered evaluation methods for vehicle running state based on fuzzy theory. *In: IEEE Intelligent Vehicles Symposium*. Xi'an, 1232-1235.
- [12] Yang G.(2014). Energy Management Strategy of Plug-in Hybrid Electric Vehicle Based on the Recognition of Driving Intention and Working Condition. Chongqing: Chongqing University
- [13] Zhang, S. & Xiong, R. (2015). Adaptive energy management of a plug-in hybrid electric vehicle based on driving pattern recognition and dynamic programming. *Applied Energy*, 155(1):68-78.

Vibration Fatigue Analysis and Optimization Design of a Light-truck Urea Box Bracket

Zhenqi Yu ^{a,b}, Huifang Jia ^b, Xingyuan Huang ^{a*}

^aSchool of Mechatronics Engineering-Nanchang University-Nanchang 330031, China

^bProduct Development & Technical Center-Jiangling Motors Co., Ltd-Nanchang 330001, China

Received OCT 16 2019

Accepted FEB 2 2020

Abstract

In order to solve the cracking problem of a light truck urea box bracket, firstly, the time domain - acceleration signal of the excitation end is collected and converted to frequency domain - acceleration signal, and the frequency response of the urea box bracket is analyzed based on the frequency - acceleration curve of the washboard road, the results show that the maximum stress of the urea box bracket exceeds the yield strength of the material. Then based on the power spectral density curve to do vibration fatigue analysis, the analysis results show that the fatigue life of the urea box bracket does not meet the design requirements and is the same as the cracking position. Furthermore, based on the neighborhood cultivation multi-objective genetic algorithm, the multi-objective optimization analysis of the thickness value of each bracket of the urea box is carried out. The optimum thickness is obtained, the maximum stress of the urea box bracket is lower than the material yield strength, the fatigue life value exceeds the engineering requirement value, and the total weight of the urea box bracket is reduced, achieved the purpose of light weight design. Finally, the bench test of the urea box bracket was carried out, the actual life is close to the simulation value. While it carries on the vehicle road durability verification, the test results show that the vibration amplitude of the urea box bracket is obviously reduced and no cracking after the test, so the cracking problem of the urea box bracket is solved successfully. The method of vibration fatigue analysis and the idea of structural optimization are provided.

© 2020 Jordan Journal of Mechanical and Industrial Engineering. All rights reserved

Keywords: the urea box support bracket, acceleration spectrum, frequency response, vibration fatigue, optimization;

1. Introduction

In accordance with the provisions of the new state regulations, in order to reduce the content of nitrogen and oxygen compounds in the exhaust gas, to achieve environmental protection purposes. The existing light truck type vehicle needs to install the Urea box ^[1], and as the key support part of the urea box, the urea box support bracket plays a key role in the safety of the vehicle in the driving process. The random excitation of the road in the driving will usually cause the forced vibration of the structure, so among the automobile components and weld crack damage in the road test and the user feedback, most of them are fatigue damage ^[2,3].

The cracking phenomenon of a light truck urea box bracket occurs during the road test (the cumulative mileage is 39845 km), as shown in Fig. 1, it can be known from Figure 1 that the cracking position is located at the transition of the circular tube, where is easy to occur stress concentration, and the crack source is gradually formed under the joint action of the alternating force torque and the gravity field, with the increase of the excitation frequency, the crack expands, the final cracking occurs, and the crack location of the section color is deep, the test mileage is long, so the preliminary judgment is fatigue cracking, it is

urgently needed to find the cause of cracking, and put forward feasible optimization scheme.

Bao Xiaodong et al. ^[4]Through collecting road load spectrum and finite element static strength analysis of heavy truck urea box bracket, put forward the bench test method of bracket fatigue verification. However, no finite element method for vibration fatigue analysis is proposed which has certain one sidedness. Liu Longtao et al. ^[5] analyzed the modal and strength characteristics of an airborne structure by using finite element software ANSYS. The vibration fatigue was calculated by using finite element analysis results and empirical formula, but no more theoretical optimization method was proposed. Li Minhao et al. ^[6] carried out the random vibration fatigue analysis of the vehicle body auxiliary bracket, and carried out the experimental benchmark, which was consistent with the experimental results. Finally, the structure was optimized to effectively improve the fatigue life of the structure under random vibration.

In this paper, frequency response analysis and vibration fatigue analysis to the urea box bracket is carried out, and also optimization analysis based on optimization platform is carried, finally to carry out bench test and vehicle road durability test for the optimization scheme, through which to provide theoretical method for future new product development.

* Corresponding author e-mail: huangxingyuan001@126.com.



Figure 1. Cracking of urea box bracket

2. Frequency response analysis principle

Frequency response analysis adopts the array superposition method [7]. The main idea is to transform and coordinate of the dynamic equations of the n degree-of-freedom system, replace the original finite element nodal coordinates with the matrix coordinates, and then obtain the uncoupled n single degree-of-freedom equations through the modal matrix transformation, and solve them individually, and then superimpose the solution to get the results of the dynamic response.

The general solution of displacement of each node in free vibration is:

$$\delta = \delta_{01} \cos(\omega_1 t + \varphi_1) + \delta_{02} \cos(\omega_2 t + \varphi_2) + \dots + \delta_{0n} \cos(\omega_n t + \varphi_n) \quad (1)$$

In the formula ω_n is the n th natural frequency of the structure, δ_{0n} is the relative vibration amplitude, φ_n is the phase angle.

After solving the natural frequencies and the natural array of undamped free vibration, the displacement vector $\delta(t)$ is regarded as a linear combination of the array δ_{0i} , that is, the transformation is introduced:

$$\delta(t) = \delta_{01} x_1(t) + \delta_{02} x_2(t) + \dots + \delta_{0n} x_n(t) = \Delta X(t) \quad (2)$$

In the formula Δ is array matrix:

$$\Delta = [\delta_{01} \delta_{02} \delta_{03} \dots \delta_{0n}] \quad (3)$$

$X(t)$ is the array matrix amplitude vector:

$$X(t) = \{x_1(t) x_2(t) x_3(t) \dots x_n(t)\}^T \quad (4)$$

Substitute it into dynamic equation, the equation can be simplified into n uncoupled single degree-of-freedom vibration formula by using the orthogonality of eigenvector:

$$m_i \ddot{x}_i + c_i \dot{x}_i + k_i x_i = f_i \quad (i = 1, 2, \dots, n) \quad (5)$$

Solve each equation, and substitute x_i into it, superimpose n array, then can get the dynamic response of the structure.

3. Collection of acceleration of excitation end

An acceleration sensor is arranged at the front and rear ends of the connection position between the frame longitudinal beam and the urea tank bracket respectively. The acceleration sensors direction X, Y and Z are in the same direction as the vehicle, that is, the front end of the

whole vehicle points to the rear end is X positive direction, the main driving side points to the co-driver side is the Y positive direction, and the bottom points to the roof is the Z positive direction. According to the vehicle road durability test specifications, road tests were carried out on short slope road, washboard road, stone road and convex road, to collect the vibration acceleration of the frame longitudinal beam excitation end of each road. By comparing and analyzing the time-domain acceleration curves of each road surface, it can be seen that the acceleration of the washboard road is the largest, as shown in Figure 2. Based on Ncode software, it is converted to frequency-domain acceleration curve, as shown in Figure 3. From the figure 3, it can be seen that the maximum vibration acceleration in X, Y and Z directions is 1.21 g, 1.03 g and 0.24 g respectively. The collected road acceleration is a time-domain load and belongs to a dynamic load, which is different from simply applying a static load such as a force to the urea box bracket, which can better reflect the real working load of the urea box bracket.

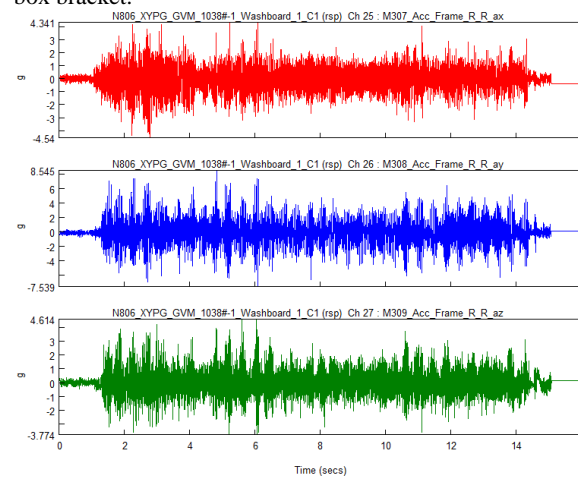


Figure 2. Time domain - acceleration curve of the frame longitudinal end on washboard road

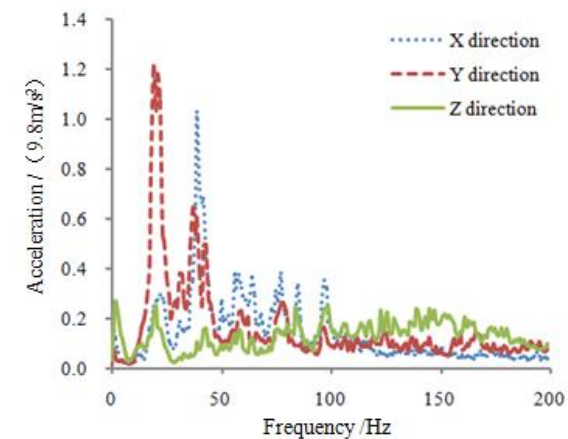


Figure 3. Frequency domain - acceleration curve of frame longitudinal end on washboard road

4. Frequency response analysis of urea box bracket

4.1. Establishment of finite element analysis model

Based on finite element pretreatment software Hypermesh [8] Import the three-dimensional model of frame longitudinal beam, the urea box and the Urea box bracket, among which the urea box bracket includes the bottom plate, the front bracket 1, the front bracket 2, the medium

bracket, the rear bracket, the circular tube and the reinforcing plate bracket, and so on, according to the vehicle road spectral acceleration gathering point position section the corresponding frame longitudinal beam, clean the middle surface of the longitudinal beam, the urea box and the urea box bracket of the frame at the same time, and use the 3 mm shell element to divide it into grid. The bolt Connection adopts RBE2+BEAM+RBE2 element to simulate, and the welding connection is simulated by HEXA (ADHESIVE) element. The material of urea box is plastic, its elastic modulus is 2.1E+5 MPa, Poisson ratio is 0.28, density is 7.01E-9 Ton/mm³, the quality of urea box is 20.8 kg, the material of urea box bracket is Q235, its yield strength is 235 MPa, tensile strength is 375 MPa, The material of the pipe is 20#, its yield strength is 245 MPa, the tensile strength is 410 MPa, based on above to establish the finite element analysis model of the Urea box support, as shown in Figure 4.

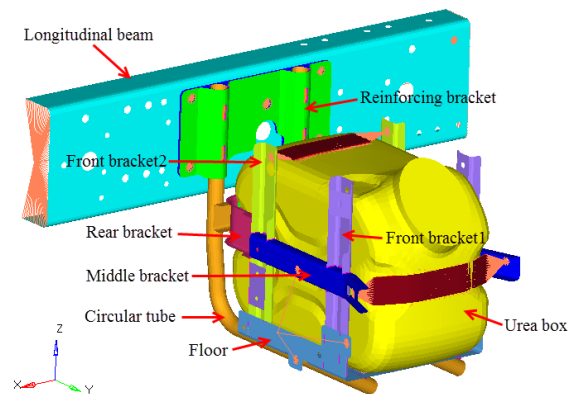


Figure 4. Finite Element analysis model of Urea box bracket

4.2. Analysis results

Taking the frame longitudinal beam, the rear ends as the excitation source, the frequency-acceleration curve of X, Y and Z direction of the frame longitudinal beam on the washboard road is imported into the Nastran software, the frequency range is set to 0-80 Hz and to do frequency response analysis based on it, and the frequency-stress curve of the urea box bracket is obtained, as shown in Figure 5. It can be seen from Figure 5 that when the excitation frequency is 19.6 Hz, the stress of the urea box bracket reaches the maximum. As shown in Figure 6, which is the stress cloud diagram of the urea box bracket at 19.6 Hz. For Figure 6 we can know that the maximum stress of the urea box bracket is 332.4 MPa, and the maximum stress position is in accordance with the actual crack position, exceeding the material yield strength (235 MPa), which is not meeting the strength design requirement and there is the fatigue cracking risk. The strength analysis results can help us find the weak position of the urea tank bracket on the real working load .

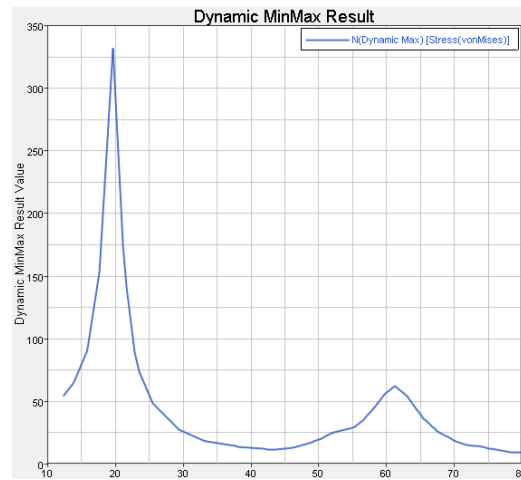


Figure 5. Frequency-stress curve of urea box bracket

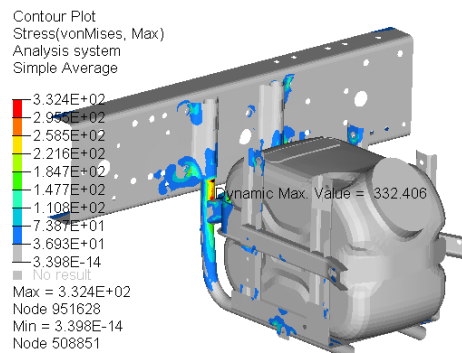


Figure 6. Stress cloud diagram of urea box support

5. Random vibration fatigue analysis theory

The power spectrum density function is the frequency domain description of stable random process, based on the spectral distance of which can obtain statistical information [9, 10], the *i* order spectral distance is:

$$m_i = \int_0^{+\infty} f^i G(f) df \tag{6}$$

In the formula, *f* is the vibration load frequency, *G(f)* is the vibration load function.

According to Miner linear cumulative damage theory [11, 12], the fatigue damage value of the structural part is:

$$D = \sum D_i = \sum \frac{n_i}{N_i} \tag{7}$$

In the formula: *n_i* is the cycle times of stress level *S_i*, *N_i* is the life of the structural part under stress level *S_i*, when the cumulative damage reach 1 it become invalid.

For continuous state, the stress gcycle times in stress range (*S_i*, *S_i* + Δ*S_i*) within time *T* is:

$$n_i = E(P)TP(S_i)\Delta S_i \tag{8}$$

In the formula, *E(P)* is expected value of peak value of random response signal, *T* is action time of random

response, $P(S_i)$ is probability density function of stress amplitude S_i .

Based on Dirlik probability density function [13, 14] and Miner linear cumulative damage theory, the random vibration fatigue damage of the structure is:

$$D = E(P) \frac{T}{S} \int S^b P(S) dS \quad (9)$$

In the formula, D is the vibration fatigue damage of the structure, $E(P)$ is the expected value of stress peak

value, $P(S)$ is the stress amplitude probability density function, b, k, T are the relevant parameters of material and load travel.

6. Vibration fatigue analysis of urea box bracket

In order to obtain the fatigue life of urea box support bracket more truly, the vibration fatigue analysis was carried out based on the theory of vibration fatigue analysis and the acceleration load spectrum of different road. The yield strength and tensile strength of Q235 and 20# steels are input by Ncode software, and the S-N fatigue curves are fitted automatically. At the same time, the time-domain acceleration load curves of short slope road, washboard road, stone road and convex road are converted into PSD load curves based on Ncode. Since the time domain-acceleration load curve is a dynamic load, the PSD load curve is also a dynamic load. PSD curve of short wave road as shown in Figure 7.

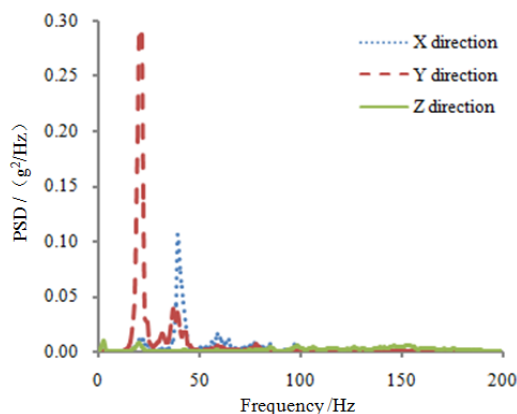


Figure 7. PSD curve of short wave road

Based on Nastran software, the unit load is applied at both ends of the longitudinal beam of the frame to obtain its frequency stress transfer function, and then the PSD dynamic load curves of four kindroads are imported into Ncode software to carry out vibration fatigue analysis. As shown in Figure 8, which is fatigue life cloud diagram of the urea box bracket, its life is $9.23E+4$ times, this reflects the times that the urea box bracket can work normally under actual road loads, which is lower than the engineering requirement of $3.0E+5$ times. It does not meet the fatigue design requirements, and the maximum stress position of the frequency response analysis is consistent with the actual cracking position. In summary, the cracking of urea box bracket is caused by vibration fatigue, which has reshaped its failure mode.

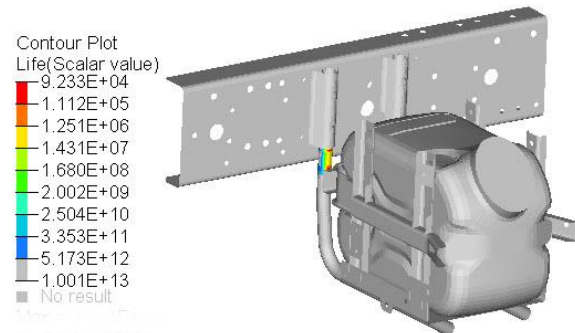


Figure 8. Fatigue life cloud diagram of urea box bracket

7. Multi-objective optimization design

7.1. Optimization model

In order to improve the fatigue and strength properties of urea box bracket and reduce its weight at the same time, take the thicknesses of the bottom plate of urea box bracket, front bracket 1, front bracket 2, middle bracket, rear bracket, circular tube and reinforcing plate bracket as design variables, take the minimization of urea box bracket maximal stress, maximization of vibration fatigue life and the minimization of its weight as target functions, take the bracket life bigger than 5.0×10^5 , bracket stress lower than 235 MPa and bracket total weight smaller than 7.2 kg as constraint condition, to build the optimization model as:

$$\begin{aligned} & \text{Maximum Life (a,b,c,d,e,f,g)} \\ & \text{Minimum Stress (a,b,c,d,e,f,g)} \\ & \text{Minimum Mass (a,b,c,d,e,f,g)} \\ & \text{Subject to Life (a,b,c,d,e,f,g)} > 3.0E+5 \\ & \text{Subject to Stress (a,b,c,d,e,f,g)} < 210 \\ & \text{Subject to Mass (a,b,c,d,e,f,g)} < 2.3 \\ & 1.0 \leq a \leq 4.0, \quad 1.0 \leq b \leq 4.0, \quad 1.0 \leq c \leq 4.0, \quad 1.0 \leq d \leq 4.0, \\ & 1.0 \leq e \leq 4.0, \quad 1.0 \leq f \leq 4.0, \quad 3.0 \leq g \leq 6.0 \end{aligned} \quad (10)$$

In the formula *Life* is the life of urea box bracket, *Mass* is the urea box bracket total weight, *a* is the thickness of bottom plate, *b* is the thickness of front bracket 1, *c* is the thickness of front bracket 2, *d* is the thickness of middle bracket, *e* is the thickness of rear bracket, *f* is the thickness of circular tube, *g* is the thickness of reinforcing plate bracket.

7.2. Optimization methods

Isight software [15] is used to integrate Hypermesh software, Nastran software and Ncode software, as shown in Figure 10. In the Hypermesh module, the command flow of grid cell division of urea box bracket is imported, and the thickness of the bottom plate, the front bracket 1, the front bracket 2, the middle bracket, the rear bracket, the circular tube and the reinforcing plate of the urea box bracket are parameterized as input variables. In the Frequency Response module, the command flow of frequency response analysis based on the collected load spectrum and frequency response analysis based on the unit load is imported. The vibration fatigue command flow based on the actual acceleration signal is imported into the Vibration Fatigue module. The urea box bracket optimization problem belongs to multi-objective problem. Neighborhood cultivation multi-objective genetic algorithm [16,17] deems each objective function as equally important, and crosses each other by grouping after sorting, so as to realize adjacent

propagation, enhance the cross-propagation probability of the optimal solution set, and accelerate the convergence to the maximum extent and reduce the calculation time. Therefore, in the Optimization module, neighborhood culture multi-objective genetic algorithm is selected to carry out multi-objective optimization analysis of urea box bracket.

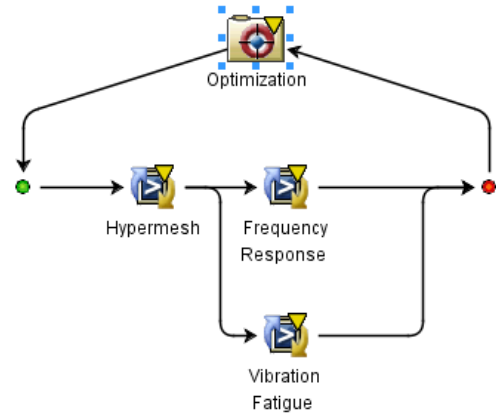


Figure 9. Isight Optimization Platform

7.3. Optimization result

After 158 times of iterations, the optimal thickness of each bracket in the urea box was obtained, as shown in Table 1, the comparison of the parameters before and after optimization. According to table 1, the best thickness of urea box bottom plate is 1.6 mm, the best thickness of front bracket 1 is 1.4 mm, the best thickness of front bracket 2 is 1.4 mm, the best thickness of middle bracket is 1.6 mm, the best thickness of rear bracket is 3.0 mm, the best thickness of circular tube is 3.2 mm, and the best thickness of reinforcing plate bracket is 4.2 mm. At the same time, after optimization, the total weight of the urea box stent is 5.8 kg, which is 23.7% less than that before optimization, achieving the goal of lightweight and saving production costs.

Table 1. Parameters comparison before and after optimization

	Before optimization	After optimization
Floor <i>a</i> /mm	2.0	1.6
Front bracke1 <i>b</i> /mm	2.0	1.4
Front bracke2 <i>c</i> /mm	2.0	1.4
Middle bracke <i>d</i> /mm	2.0	1.6
Rear bracket <i>e</i> /mm	3.5	3.0
Circular tube <i>e</i> /mm	2.0	3.2
Reinforcing bracket <i>e</i> /mm	4.5	4.2
Mass <i>m</i> /kg	7.6	5.8
Stress σ /MPa	332.4	188.4
Life <i>N</i> /cycles	92334	302958

As shown in Figure 10, which is the maximum stress distribution cloud diagram of the urea box bracket, after optimization the maximal stress of urea box bracket is 188.4 MPa, which is 43.3% lower than that before optimization, and less than the yield strength of the material and meets the strength performance requirements.

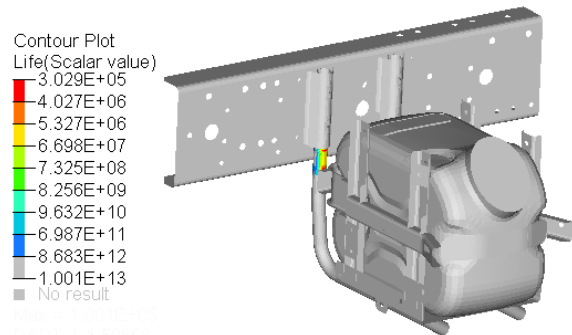


Figure 10. stress cloud picture of urea box bracket after optimization

As shown in Figure 11, which is the vibration fatigue life cloud diagram of the urea box bracket after optimization, it can be known from Figure 11 that the life of the urea box bracket reaches 3.03E+5 times, which is larger than the engineering requirement. Compared with that before the optimization, the life of the urea box bracket is increased by 2.28 times, and its fatigue performance is significantly improved meeting the fatigue design requirements.

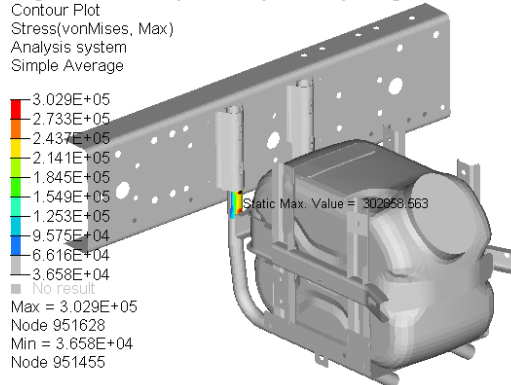


Figure 11. the fatigue life cloud diagram of urea box bracket after optimization

8. Bench test verification

The structure of the urea box bracket optimized by frequency response analysis was used to estimate its fatigue life through vibration fatigue analysis.. In order to verify the accuracy and reliability of the analysis results, a vibration bench test was carried out on the optimum structure of the urea box bracket (Figure 12). The PSD load of the bench test is consistent with the fatigue analysis load. When the bench vibration frequency is 3.64E+5, a crack was found in the urea box bracket. The error rate between the bench test times and the fatigue simulation analysis value is 16.7%.The results of the bench test show that the vibration fatigue analysis method has high accuracy.



Figure 12. bench test of urea box bracket

9. Vehicle road durability verification

In order to verify the reliability of urea box bracket optimization scheme in real road work, the samples were made according to optimization value, the samples before and after optimization were installed on two test vehicles as shown in Figure 13. In order to better compare the urea box bracket vibration situation before and after optimization, a vibration acceleration sensor is installed on the outside of urea box bracket to collect the acceleration signal. According to durability test provision, the road tests were done on short slope road, washboard road, stones road, convex road, by comparing the acceleration signal on each road we can know, the acceleration of the urea box bracket in the Z direction on washboard road is the largest, as shown in Figure 14, which is the frequency domain – acceleration curve of urea box bracket in Z direction on washboard road before and after optimization. It can be known from Figure 14 that before optimization the acceleration of urea box bracket in Z direction maximum is 1.92 g, after optimization it is 0.98 g, which decreased by 48.9% compare to that before optimization, the vibration amplitude is reduced significantly. After the vehicle road durability test (the cumulative test mileage is 10000 km), the urea box bracket has not cracked after optimization, therefore, the optimization scheme of the urea box bracket has high reliability, and the whole analysis and optimization method has high accuracy, and solved the cracking problem successfully and effectively.



Figure 13. optimization scheme of urea box bracket

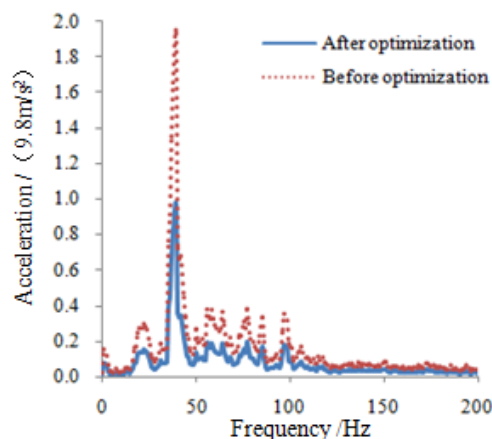


Figure 14. frequency domain acceleration curve of urea box bracket before and after optimization

10. Conclusion

In this paper, concerning the cracking problem of a light truck urea box bracket, the vibration acceleration of the longitudinal beam end is collected, then the frequency response is analyzed, and then the vibration fatigue is analyzed based on the power spectral density, and meanwhile the multi-objective optimization is carried out on the basis of the optimization platform, and finally the bench test and the vehicle road durability verification are carried out.

(1) The acceleration signal of the frame longitudinal end is collected on short slope road, washboard road, stone road and convex road, in which the maximum acceleration of X, Y and Z direction of washboard Road is 1.21 g, 1.03 g and 0.24 g respectively.

(2) Based on Ncode, the measured time domain - acceleration curve is converted to the frequency - acceleration curve, which is used as excitation to analyze the frequency response of the urea box bracket, the urea box bracket achieves the maximum at 19.6 Hz, the maximum stress is 332.4 MPa, which is greater than the material yield strength, and does not meet the strength design requirement, and it is the same as the actual cracking position.

(3) The time domain - acceleration curve of each road is converted into power spectral density curve, and the vibration fatigue analysis of the urea box bracket is carried out, its life is $9.23E+4$ times, which is less than the engineering requirement value and is consistent with the actual cracking position.

(4) Based on Isight optimization platform, the optimum value of each bracket thickness is obtained by multi-objective optimization of the thickness of the urea box bracket. After optimization, the maximum stress of the urea box bracket is 188.4MPa, the life of the urea box bracket is $3.03E+5$ times. Compare to that before the optimization, the stress value is reduced by 43.3% and its life expectancy has been increased 2.28 times; The total weight of the urea box bracket is 5.8 kg, the weight of which has been reduced by 23.7% compare to that before the optimization, and the aim of lightweight is achieved, the optimization effect is obvious, and it can meet both the fatigue and strength design requirements.

(5) After bench test of the optimization scheme of the urea box bracket, it cracks at vibration times of $3.6E+5$, which is close to simulation value. Meanwhile after vehicle durability test, the urea box has not crack, the acceleration in Z direction of urea box bracket is reduced by 48.9% comparing to that before optimization, the vibration amplitude decreased obviously, which successfully solves the cracking problem.

References

- [1] Lee J, Theis JR, Kyriakidou EA. 2019. Vehicle emissions trapping materials: Successes, challenges, and the path forward. APPLIED CATALYSIS B-ENVIRONMENTAL, 243: 397-414.
- [2] João P D, Stephen E, Americo C, Shweta D, Abraham N, Fisseha M., Haileyesus B. . 2019. Parametric probabilistic approach for cumulative fatigue damage using double linear damage rule considering limited data. International Journal of Fatigue, 127.
- [3] Gharaibeh MA, Pitarresi JM. 2019. Random vibration fatigue life analysis of electronic packages by analytical solutions and Taguchi method. MICROELECTRONICS RELIABILITY, 102.

- [4] Bao X D, Zhang X N. 2017. Design and fatigue verification of urea box bracket for heavy commercial vehicle. *Mechanical Design and Manufacturing*, (03): 212-214, 218.
- [5] Liu L T, Li C R, Cheng Q and Qiao L. 2013. Random vibration fatigue analysis of a structural part. *Vibration and Impact*, 32 (21): 97-101.
- [6] Li Mi H, Deng S B, Liu X Z and Yuan H Q. 2018. Finite element analysis and optimization of random vibration of vehicle body control module bracket. *Modern Manufacturing Engineering*, (06): 64-68.
- [7] Zhu H J, Yang J and Zhang Y Q. 2018. Modeling and optimization for pneumatically pitch-interconnected suspensions of a vehicle. *Journal of Sound and Vibration*, 432: 290-309.
- [8] Marzbanrad J and Hoseinpour A. 2017. Structural optimization of macpherson control arm under fatigue loading. *Tehnicki Vjesnik-Technical Gazette*, 24(3): 917-924.
- [9] Fragkoulis V C, Kougioumtzoglou, I A, Pantelous, AA. 2016. Linear Random Vibration of Structural Systems with Singular Matrices, 142(02).
- [10] Li J. 2009. Random vibration theory and application in new progress. Tongji University Press
- [11] Yao W X. 2003. Structure fatigue life analysis. National Defence Industry Press
- [12] Hassanifard S and Feyzi M. 2017. Experimental and numerical investigation of fatigue damage accumulation in composite laminates. *International Journal of Damage Mechanics*, 26 (6): 840-858.
- [13] Xue X T and Chen N Z. 2018. Fracture mechanics analysis for a mooring system subjected to Gaussian load processes. *Engineering Structures*, 162: 188-197.
- [14] Durodola J F, Ramachandra S, Gerguri S and Fellows N A. 2018. Artificial neural network for random fatigue loading analysis including the effect of mean stress. *International Journal of Fatigue*, 111: 321-332.
- [15] Zhu H J, Yang J and Zhang Y Q. 2018. Modeling and optimization for pneumatically pitch-interconnected suspensions of a vehicle. *Journal of Sound and Vibration*, 432: 290-309.
- [16] Bandyopadhyay K, Hariharan K, Lee M G and Zhang Q. 2018. Robust multi objective optimization of anisotropic yield function coefficients. *Materials & Design*, 156: 184-197.
- [17] Ilka R, Alinejad-Beromi Y and Yaghobi H. 2018. Cogging torque reduction of permanent magnet synchronous motor using multi-objective optimization. *Mathematics and Computers in Simulation*, 153: 83-95.

Application of Improved Particle Swarm Optimization in Gear Fault Diagnosis of Automobile Transmission

Aibing Wang^a, Jianwei Liang^{b*}, Yapeng Liu^c

^aAutomotive Engineering Department, Hebei Jiaotong Vocational & Technical College, Shijiazhuang 050035, China

^bDepartment of Mechanics and Electrics, Shijiazhuang Vocational Technology Institute, Shijiazhuang 050081, China

^cDepartment of Information Science and Engineering, Hebei Vocational College of Labour Relations, Shijiazhuang 050091, China

Received OCT 16 2019

Accepted FEB 29 2020

Abstract

The current fault diagnosis method has the problems of long time and low recognition rate of fault diagnosis for the gear fault diagnosis of automobile transmission. For these problems, a fault diagnosis method for gear of automobile transmission based on improved particle swarm optimization algorithm is proposed in this paper. The speed information of gear fault vibration signal is extracted. The extracted speed information is used for uniform angular resampling of gear fault vibration signal and converted to angular domain signal. The cyclostationary demodulation analysis is carried out to the angular domain signal, and the slice demodulation is performed at each order of the fault feature of the cyclic autocorrelation function. Compound fault diagnosis of gearbox is achieved based on slice demodulation spectrum of each slice signal. In order to improve the accuracy of fault diagnosis and reduce the time of fault diagnosis, the CGA algorithm is introduced. The CGA acceleration operator is introduced in every step of iterations of particle swarm optimization, so that the local search ability of particle swarm optimization can be improved. The local convergence speed and convergence accuracy of PSO can be greatly improved. Simulation results show that the proposed method can effectively shorten the time of fault diagnosis and improve the efficiency of fault diagnosis and recognition.

© 2020 Jordan Journal of Mechanical and Industrial Engineering. All rights reserved

Keywords: Improved particle swarm optimization; automobile transmission; gear fault diagnosis;

1. Introduction

Gear is an essential part of mechanical equipment to transmit power and change speed and direction. It has strong bearing capacity, accurate and reliable transmission, and large transmission power and speed of gear [1, 2]. Once a failure occurs, it will cause the mechanical equipment to fail. If it is diagnosed in advance, it can effectively avoid accidents, eliminate continued damage, and save a lot of maintenance costs [3]. The automobile gearbox is the main driving part of the car. Accurately monitoring the running status of the transmission, and forecasting the possible faults in advance are important for product improvement, testing equipment, and personnel safety [4]. How to efficiently diagnose the gear fault of transmission has become the primary problem of current research.

In recent years, some new algorithms for fault diagnosis have been proposed by scholars. In the literature [5], a new gear fault diagnosis method which reflects the complexity or nonlinearity of the signal, which is called partial mean multiscale fuzzy entropy (PMMFE), is proposed. PMMFE is proposed based on multiscale fuzzy entropy. Although multiscale fuzzy entropy contains temporal pattern information at different scales, the representation of signals with similar feature is not ideal at most scales. PMMFE synthetically considers fuzzy entropy of multiple scales. By using the skewed distribution characteristics of fuzzy entropy at different scales, the complexity or nonlinearity of signals can be quantitatively characterized, and the characteristics of signal can be reflected more accurately.

However, the gear fault vibration signal in gearbox is multi-source vibration signal, so the feature extraction must be carried out after the original signal of gear vibration is separated. The adaptive and sparsest time-frequency analysis (ASTFA) method can effectively separate the original signal of gear fault vibration according to the initial phase function determined by the gear meshing frequency. The combination of ASTFA and PMMFE is applied in gear fault diagnosis. The fault vibration signal of gear in the gearbox is separated by ASTFA, and the multiscale fuzzy entropy of the signal is calculated. The fault diagnosis of the gear is accomplished by calculating the PMMFE based on the multiscale fuzzy entropy. This method is not ideal for most of the similar feature signals, resulting in low recognition rate. In the literature [6], a gear fault diagnosis method based on two classes of features of kurtosis and intrinsic mode component energy and least squares support vector machine is proposed. Based on ensemble empirical mode decomposition, the effective IMF components of the measured gear vibration signal are extracted to calculate energy characteristics and kurtosis values. Two classes of feature vectors in time and frequency domain are built. Secondly, the two class feature vectors in time-frequency domain of the 3 kinds of states of the normal gear, the tooth root crack and the broken tooth are taken as the input to build the gear fault diagnosis model for the gear fault identification. However, this method cannot accurately identify the type of fault. In the literature [7], a dual-tree complex wavelet denoising fault diagnosis method based on morphological component analysis is proposed. The wavelet transform coefficients of different layers are

* Corresponding author e-mail: 595900302@qq.com.

obtained by dual-tree complex wavelet transformation of the fault signal with strong background noise. The wavelet coefficients with the obvious periodicity are selected for MCA denoising. After the single parameter reconstruction of the denoised coefficients, the fault feature signal can be obtained. The envelope analysis of the denoised signal can determine the fault feature frequency of the signal. However, this method can effectively remove strong background noise in signals. In the literature [8], a gear fault diagnosis method based on adaptive stochastic resonance and sparse coding shrinkage algorithm is proposed. Correlation kurtosis is used as a measure function of stochastic resonance to detect periodic impact components. The periodic impact features in the signal is adaptively extracted by using genetic algorithm. On this basis, the sparse coding contraction algorithm is used to further denoise the random resonance detection results, thus highlighting the impact feature and completing the fault identification of the gear. However, this method has a long fault diagnosis time.

For these above problems, a gear fault diagnosis method for automobile transmission based on improved particle swarm optimization algorithm is proposed in this paper. The main research is described as follows.

(1) The rotational speed information of gear fault vibration signal is extracted.

(2) The extracted speed information is used for uniform angular resampling of gear fault vibration signal and converted to angular domain signal. The cyclostationary demodulation analysis is carried out to the angular domain signal, and the slice demodulation is performed at each order of the fault feature of the cyclic autocorrelation function. Compound fault diagnosis of gearbox is achieved based on slice demodulation spectrum of each slice signal.

(3) To improve the accuracy of fault diagnosis and reduce the time of fault diagnosis, the CGA algorithm is introduced. The CGA acceleration operator is introduced in the iterations of particle swarm optimization. Then the local search ability of particle swarm optimization can be improved and the local convergence speed and accuracy of PSO can be greatly improved.

2. Fault Diagnosis Method

2.1. Gear Feature Parameter Extraction Method Based on VMD Algorithm

In the fault diagnosis of gearbox, because the original vibration signal of the gear is not easy to distinguish the gear fault mode, it is particularly necessary to extract the feature parameters of the gear vibration signal. Therefore, a gear feature parameter extraction method based on VMD is proposed.

In order to reduce the influence of other idle gears on the vibration response of gearbox, the single-stage fixed shaft gearbox is selected as the simulation object. The schematic diagram of single-stage fixed shaft gearbox is shown in Figure 1, where the red path represents the transmission path of meshing vibration of fixed shaft gearbox: meshing point gear bearing box sensor.

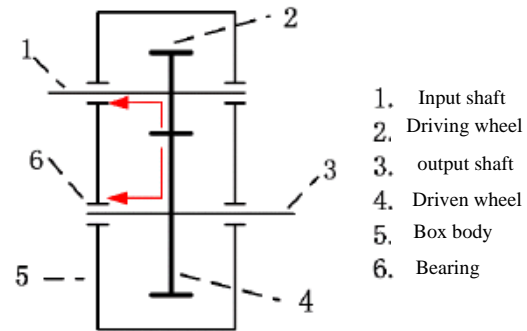


Figure 1. Schematic diagram of gear box

The gear can be regarded as a vibration system with the gear tooth as the spring and the gear body as the mass. The exciting force of the self-excited vibration of the system is caused by the periodic change of gear stiffness, gear assembly error and torque change. Once generated, the gear will generate the torsional vibration in the circumferential direction and the bending vibration of the gear shaft, resulting in the gear noise corresponding to the meshing frequency.

In the VMD algorithm, the concept of intrinsic mode function (IMF) in EMD algorithm is applied and redefined. The IMF in the VMD algorithm is made as amplitude modulated and frequency modulated signal, which is expressed as

$$u_i(t) = A_i(t) \cos \phi_i(t) \quad (1)$$

where $A_i(t)$ is a non-negative envelope function, that is, $A_i(t) \geq 0$, $\phi_i(t)$ is a non-decreasing function, that is, $\phi_i(t) \geq 0$.

The instantaneous frequency $w_i(t) = \phi_i'(t)$ and $A_i(t)$ is far less than the phase $\phi_i'(t)$, that is, $u_i(t)$ can be considered as a harmonic signal with the amplitude $A_i(t)$ and the frequency $w_i(t)$ in the $[t - \delta, t + \delta]$ ($\delta = 2\pi / \phi_i'(t)$) region.

In order to construct the variational model, the following steps are needed.

(1) The Hilbert transform is used to transform all the modal

functions $u_i(t)$ into the corresponding analytic signals, so as to obtain the unilateral spectrum of the signal.

(2) All modal functions are demodulated to the corresponding baseband according to the estimated center frequency and the exponential correction method.

(3) In order to obtain the constrained variational model given by Eq. (2) and Eq. (3), the bandwidth of each band must be used. The bandwidth can be obtained based on Gaussian smoothing demodulation signal, that is, the square root operation of the L_2 norm gradient.

$$\min_{\{u_i\}, \{w_i\}} \left\{ \sum_i \|\partial_t \left[\left(\partial(t) + \frac{j}{\pi t} \right) \times u_i(t) \right] e^{-jw_i t} \|_2^2 \right\} \quad (2)$$

$$\sum_i u_i = f \quad (3)$$

In order to solve the optimal solution of the constrained variational model given by Eq. (2) and Eq. (3), the

augmented Lagrange function is constructed by penalty factor a , which is given by

$$L(\{u_i\}, \{w_i\}, \lambda) = \alpha \sum_i \left[\delta(t) + \frac{j}{\pi t} \times u_i(t) \right] + f(t) - \sum_i u_i(t) \quad (4)$$

where λ is the Lagrange multiplier, a is the penalty factor.

In order to obtain the extremal solution of Lagrange function, it is necessary to transform it from time domain to frequency domain. The modal component and frequency domain is calculated by using as follow:

$$u_i^{n+1}(w) = \frac{f - \sum_{i \neq k} u_i(w) + \frac{\lambda(w)}{2}}{1 + 2\alpha(w - w_i)} \quad (5)$$

$$w_i^{n+1} = \frac{\int_0^\infty w |u_i(w)|^2 dw}{\int_0^\infty |u_i(w)|^2 dw} \quad (6)$$

(4) The alternating direction multiplier algorithm is used to obtain the optimal solution of the constrained variational model. The original analytical signal is decomposed into k modal components. The steps of solving the optimal solution are as follows:

- 1) Initialize $\{u_i^1\}$, $\{w_i^1\}$, λ^1 , n , and $\lambda^1 = n = 0$.
- 2) Iteratively update u_i and w_i by using Eq. (5) and Eq. (6).
- 3) Iteratively update λ^{n+1} by using Eq. (7).

$$\lambda^{n+1}(w) \leftarrow \lambda^n(w) + \tau \left[f(w) - \sum_i u_i^{n+1}(w) \right] \quad (7)$$

- 4) When $\sum_i \|u_i^{n+1} - u_i^n\|_2^2 / \|u_i^n\|_2^2 < \varepsilon$ is satisfied, the iteration stops, otherwise it returns to step 2) to continue the iteration, and finally to output k modal components.

VMD is compared with EMD and LMD. The decomposition of EMD and LMD signals is recursive filtering mode, while VMD is a non-recursive and variational mode decomposition method, which can make the decomposed modal component no longer cause modal aliasing [9]. Therefore, VMD has excellent robustness in noise signal processing. Through properly controlling the convergence condition of VMD, the sampling effect is much lower than that of EMD and LMD. In addition, VMD can effectively separate the signals with similar frequencies.

The vibration signal of gear is decomposed by VDM, and several modal components of different components are successfully separated. The singular features are extracted by using modal component. But there is a problem in the VMD algorithm. The parameters k and a in the algorithm need to be set in advance depending on personal experience [10]. If the number of modal decomposition k is not set reasonably, the modal separation after decomposition will be different from the actual situation. According to a priori knowledge, the decomposition of EMD algorithm can adaptively adjust the number of the decomposed modal components. By using the EMD decomposed signal, the

decomposition parameter k of VMD can be obtained according to the EMD decomposition result.

The feature extraction of gear includes two steps:

- 1) With Optimal parameter combination, the collected vibration signal of the gear is decomposed by VDM, and the k modal components are obtained.
- 2) The gear speed information is extracted by using the VMD-based gear feature parameter extraction method, which is given by

$$\begin{cases} A = USV^T = U \left[\sum_x 0 \right] V^T \\ U \times U = I_k, V \times V^T = I_n \end{cases} \quad (8)$$

where $\sum_x = \text{diag}(\delta_1, \delta_2, \dots, \delta_k)$ and the feature vector of gear fault $D = (\delta_1, \delta_2, \dots, \delta_k)$.

2.2. Gear Fault Diagnosis Method Based on CPP Algorithm

The CPP algorithm, order tracking and cyclostationary demodulation method are combined to diagnose the gear fault. The gearbox fault is composed of partial fault of gear and partial fault of bearing in wheel box [11]. The process of the fault diagnosis is described as follows.

If the statistical characteristics of non-stationary random signal $x(t)$ change periodically or periodically with time, $x(t)$ is called cyclostationary signal. Autocorrelation function of asymmetrical form of the signal $x(t)$ is given by

$$R(t, \tau) = E \{ x(t) x^*(t + \tau) \} \quad (9)$$

where τ is the time delay, $E \{ \cdot \}^*$ is the mean operation, and $*$ denotes conjugate.

Assume the signal satisfies time ergodicity, the signal is sampled with the sampling period, and then it can be expressed as an average of time:

$$R(t, \tau) = E \{ x(t) x^*(t, \tau) \} = \lim_{N \rightarrow \infty} \frac{1}{(2N+1)} x^*(t + nT_0) \quad (10)$$

where T_0 is the sampling period, N is the sampling length.

In the case of the fixed τ , the correlation function $R(t, \tau)$ is a function of time, with a period of T_0 .

Therefore, the Fourier series expansion of $R(t, \tau)$ is given by

$$R(t, \tau) = \sum_\alpha R_\alpha(\tau) \exp(i2\pi\alpha t) \quad (11)$$

where α is the cycle frequency, which includes zero cycle frequency and non-zero cycle frequency. The zero cycle frequency represents the stationary part of the signal, and the non-zero cyclic frequency represents cyclostationarity of the signal.

Fourier coefficient in Eq. (11) is given by

$$R_{\alpha}(\tau) = \lim_{T \rightarrow \infty} \frac{1}{T} \int_{T_{12}}^{T_{12}+T} x(t) x^*(t+\tau) \exp(i2\pi\alpha t) dt \quad (12)$$

where T is the sampling interval, $T = (2N+1)T_0$, $R_{\alpha}(\tau)$ is the cyclic autocorrelation function, which is the joint function of cycle frequency α and time delay τ . The AM signal expression is as follows:

$$AM(t) = Q[1 + B \cos(2\pi f_n t)] \cos(2\pi f_z t) \quad (13)$$

where, f_n is the modulation frequency of AM signal, f_z is the carrier frequency of AM signal, Q is the amplitude of carrier signal, B is the spectrum of AM modulation signal

Eq. (13) is substituted into Eq. (12), cyclostationary demodulation analysis of angular domain signal is expressed as

$$\lim_{T \rightarrow \infty} \frac{1}{T} \int_{T_{12}}^{T_{12}+T} \exp(iw_1 t) \exp(iw_2 t) dt = 0 (w_1 \neq w_2) \quad (14)$$

Compound fault diagnosis of gearbox is obtained according to slice demodulation spectrum of each slice signal, which is expressed as

$$R_{\alpha}(\tau) = \begin{cases} \frac{A^2}{2} \cos(2\pi f_z \tau) & \alpha=0 \\ \frac{A^2 B}{2} \cos(2\pi f_n \tau) & \alpha = \pm f_n \\ \frac{A^2 B^2}{8} \cos(2\pi f_n \tau) & \alpha = \pm 2f_n \end{cases} \quad (15)$$

From Eq. (15), the non-zero value of the cyclic autocorrelation function $R_{\alpha}(\tau)$ is only located at the cycle frequency $\alpha=0$, $\alpha = \pm f_n$, $\alpha = \pm 2f_n$, etc. At other cycle frequencies, the value of cyclic autocorrelation function $R_{\alpha}(\tau)$ is zero.

When the gear in gearbox has partial fault, the rotational frequency modulation phenomenon will occur in its vibration signal. When local fault occurs in rolling bearing, the feature frequency modulation of bearing fault will occur in its vibration signal [12]. Therefore, when the gear box and bearing local fault occur simultaneously in the gearbox, the diagnosis of the composite fault of the gear box containing the local fault of the gear and the local fault of the bearing can be diagnosed according to the difference of the modulation frequency of the two defaults.

The cyclostationary demodulation analysis method can extract modulation information of amplitude modulated signal according to the modulating frequency of each amplitude modulated signal. However, for the non-stationary signals with varying speed, the second-order statistics change with time and do not satisfy the second-order cyclostationary assumption. Then the cyclostationary demodulation method is no longer applicable, and the signal needs to be stabilized in advance. The computed order tracking method can effectively realize signal stabilization by resampling the signal. But the computed order tracking method needs to predict the speed information of the signal.

Therefore, combining the CPP algorithm, order tracking and cyclostationary demodulation method, a gear fault diagnosis method based on CPP and cyclostationary demodulation is proposed for analysis of local fault of gear and local fault of rolling bearing. Assume the measured fault vibration signal of gear is $x(t)$, the number of gear teeth is T , then the steps of gear fault diagnosis based on CPP and cyclostationary demodulation are described as follows.

(1) The meshing frequency $f_z(t)$ of gear box is extracted from the vibration signal $x(t)$ of gear fault by CPP method. The rotational frequency curve $f_r(t)$ of the shaft can be obtained by dividing the meshing frequency $f_z(t)$ with the number of the gear teeth T .

(2) According to the estimated frequency curve $f_r(t)$, the order analysis of the vibration signal $x(t)$ is carried out to obtain the angular domain signal $x(\theta)$.

(3) The cyclostationary demodulation of the angular domain signal $x(\theta)$ is carried out to obtain the cyclic autocorrelation function $R_{\alpha}(\tau)$.

(4) The cyclic autocorrelation function $R_{\alpha}(\tau)$ is sliced separately at the order of gear fault cycle and the order of bearing failure cycle. The slice signal is demodulated and analyzed, and its slice demodulation spectrum is obtained.

(5) If there is a significant peak in the rotational frequency order or its frequency doubling order in the slice demodulation spectrum of the gear fault cycle order, it is determined that a local fault occurs in the gear. If in the slice demodulation spectrum of the rolling bearing fault cycle order, the fault order of the rolling bearing appears obvious peak, it is determined that there is a local fault in the gear bearing.

2.3. Introducing CGA Algorithm to Improve the Local Convergence Speed and Convergence Accuracy of Particle Swarm Optimization Algorithm

Particle swarm optimization algorithm is based on the simulation of migration and gregarious foraging process. The mathematical expression is described as follows. Assume target search space is d -dimensional and the population consists of m particle groups. The velocity of the i th particle is $V = (v_{i1}, v_{i2}, \dots, v_{id})$ and the position vector is $X = (x_{i1}, x_{i2}, \dots, x_{id})$, the searched optimal location of the population is $P_g = (p_{g1}, p_{g2}, \dots, p_{gd})$, the current searched optimal position of the i th particle is $P_i = (p_{i1}, p_{i2}, \dots, p_{id})$. The particle expression is as follows:

$$v_{id}(t+1) = v_{id}(t) + c_1 r_1 (p_{id} - x_{id}(t)) + c_2 r_2 (p_{id} - x_{id}(t)) \quad (16)$$

$$x_{id}(t+1) = x_{id}(t) + v_{id}(t+1) \quad (17)$$

where the range of the value of i is $[1, m]$, the range of the value of d is $[1, D]$, r_1 and r_2 are random numbers with uniform distribution in $[0, 1]$, c_1 and c_2 are acceleration factors, which is non-negative number, P_{id} is the current searched optimal position of the i th particle, v_{id} is the current velocity of the i th particle, $x_{id}(t)$ is the current position of the i th particle.

Although particle swarm optimization is an excellent global optimization algorithm, it is not good to process the discrete optimization problem, and easy to fall into local optimum [13]. It will lead to long time and low recognition rate of fault diagnosis. The CGA acceleration operator is introduced in iterations of particle swarm optimization, so that the local search ability of particle swarm optimization can be improved. The specific implementation process is as follows.

$$v_{id}(k+1) = \chi \left[w(k) v_{id}(k) + c_1 r_1 (p_{id} - x_{id}(k)) + c_2 r_2 (p_{ag} - x_{id}(k)) \right] \quad (18)$$

$$x_i(k+1) = x_i(k) + \varphi_1(k) \times v_i(k+1) + \varphi_2(k) \times \mu \times d_i(k) \quad (19)$$

where μ is influence scale factor of CGA, which is a fixed value in $(0, 1]$, χ is the constraint factor, which is a constant in $(0, 1]$, $d_i(k)$ is the direction of the conjugate gradient or the steepest descent direction, φ_1 and φ_2 are the scale factors of the relative influence of CPP algorithm. The selection of φ_1 and φ_2 influences the overall performance of the algorithm. The selection of φ_1 and φ_2 are given by

$$\varphi_1(k) = \frac{k_{max} - k}{k_{max}} \quad (20)$$

$$\varphi_2(k) = \frac{k}{k_{max}} \quad (21)$$

where k is the number of current evolutionary generation, k_{max} is the maximum number of current evolutionary generation. $\varphi_1(k) + \varphi_2(k) = 1$. $\varphi_1(k)$ and $\varphi_2(k)$ are variables and change with k . The purpose is to dynamically adjust the update of each particle and determine the influence of the basic CPP algorithm and CGA.

The specific steps of the improved particle swarm algorithm are as follows.

- (1) Initialize all particles. Randomly determine the initial position and velocity of each particle. Particle swarm optimization is designed to optimize the target value of the desired error for a given optimization problem [14, 15].
- (2) Design the fitness function of population.
- (3) Calculate the initial fitness value of each particle and determine the optimal position of the initial individual of each particle. Initialize global optimal position and calculate $\varphi_1(k)$, $\varphi_2(k)$, and initial gradient and initial search direction of each particle.

(4) The current generation is the k th generation, $k = k_1, \dots, k_{max}$. If $k = 1$, the initial fitness value of the current generation of each particle is the initial fitness value. The individual optimal position of each particle is the initial individual optimal position, and the global optimal position is the initial global optimal position. If $k \neq 1$, the fitness value of the current generation of each particle is calculated by fitness function. Then the optimal location $P_{id}(k)$ and global location $P_{gd}(k)$ of each particle are updated with the next steps.

(5) Update the individual optimal position $P_{id}(k)$.

(6) Update the global optimal position $P_{gd}(k)$.

(7) Calculate the conjugate gradient $d_i(k)$ of the current generation of each particle. Then calculate $\varphi_1(k)$ and $\varphi_2(k)$ by using Eq. (20) and Eq. (21).

(8) Update the velocity and position of each particle by using Eq. (18) and Eq. (19).

(9) Calculate new gradient $g_i(k)$ and search direction $d_i(k)$.

(10) The number of evolutionary iterations plus 1.

(11) Check whether the condition is satisfied. If it is satisfied, the optimization ends. Otherwise, go to step (4) for loop executing, until the optimal number of evolution k_{max} is reached or the optimization error corresponding to the global optimal particle is less than the given error.

3. Experimental Results and Analysis

In order to prove the validity of the proposed algorithm, a simulation experiment is carried out. The test platform of gear box fault detection system is built by using PCI1712 data acquisition module.

In the gearbox, about 60% of the faults are caused by gear faults. The three faults of the gear are identified, which are no fault, tooth root crack, and broken tooth. The 2, 4, and 6 gear position were selected in the frequency domain feature signal extraction. The amplitudes at the side band $f_s + n f_z$ of the 1, 2, and 3 bearing are A_{ij1} , A_{ij2} , and A_{ij3} , where $f_z(t)$ is the meshing frequency of the gear, f_z is the rotational frequency of the bearing, $n = 1, 2, 3$, $i = 2, 4, 6$ is the gear position, $j = 1, 2, 3$ is the number of the bearing. Because there are two pairs of gears on the 2 bearing and 3 bearing, 1 and 2 represent two meshing frequencies respectively. So, the input of the network is a 15-dimensional vector. The schematic of the transmission is shown in Figure 2. the sensor accelerometer is shown in figure 3. The transmission vibration data is shown in Table 1.



Figure 2. Schematic of the transmission Figure 3 Sensor Accelerator

In CATIA, a 3D model of gearbox components is established, which is endowed with specific material attributes, and local coordinate system is added to the 3D model according to the relative position relationship; the 3D model of the components is imported into LMS virtual lab software, and the geodetic coordinate system is added to the motion module to simulate the gearbox workbench; the coordinates on the components are one-to-one corresponding, which is based on the actual situation. For the inter contact relationship, four fixed pairs are added between the earth and the gearbox box, and rotating pairs are added between the driving wheel and the driven wheel and the earth respectively; bushing force is added at the bearing to simulate the rolling bearing, and joint position driver is added on the rotating pair between the driving wheel and the earth to simulate the gear drive.

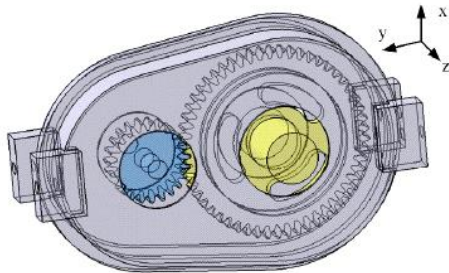


Figure 4. Dynamic model of gear box multi-rigid body

Set the gear breaking or eccentric fault on the driving wheel and driven wheel respectively, and record the gear breaking of driving wheel as condition 1, the gear breaking of driven wheel as condition 2, and the common fault as condition 3.

Table 1. transmission vibration data

Vibration parameters	Working condition 1	Working condition 2	Working condition 3
Swing around X-axis at front box bearing	334.02	351.65	-
Box swinging around X-axis	413.45	410.34	211.93
Tilt vibration of xoy surface of front box diaphragm	446.25	447.53	-
Inclined vibration of box on xoy surface	528.93	526.12	273.65
Reciprocating vibration of front box rib in Y-axis direction	647.78	643.38	384.65

Because these data have different units and orders, the input variables are normalized. Experimental data are collected with MATLAB R2007, and 12 sets of data are collected, of which 9 sets used as training samples and 3 sets as test samples. During the training process, the CPP package of MATLAB is called. The CPP network design function selects newbre, and the feature samples in the training samples are used as input variables of the CPP network, and the gear state is used as the output of the network. The following form is used: No fault (1, 0, 0), gear crack (0, 1, 0), and broken tooth (0, 0, 1). The training set finally determines that when the expansion constant is 0.0838, the training effect is the best, and the network output is consistent with the actual output.

In order to verify the effectiveness of the experiment, the data shown in Table 2 is used as the test sample set, and the gear state is used as the output of the network to verify the built CPP network model. The results are shown in Table 3. In Table 1, S represents the number of the data, S1, S2, and S3 are the number 1, 2, and 3 of the data, T represents feature sample, C represents gear fault, Nf represents no fault, Gc represents gear crack, Bt represents broken tooth. In Table 3, Ao represents actual output, No represents network output, result represents diagnosis results.

Table 2. Test sample

S	T	C
S1	0.2102 0.096	Nf
	0.1358 0.2602	
	0.1002 0.7534	
	0.090 0.0388	
	0.1452 0.0129	
	0.160 0.2453	
S2	0.511 0.1320	Gc
	0.2594 0.19 0.712	
	0.2802 0.1500	
	0.1297 0.1002	
	0.1892 0.2531	
	0.0876 0.0059	
S3	0.1802	Bt
	0.0993 0.0803	
	0.1003	
	0.2600 0.2236	
	0.1202 0.1172	
	0.1103 0.0684	
	0.0623 0.2598	
	0.2603 0.1169	
	0.0050 0.1003	
	0.1521 0.2283	
0.3206		

Table 3. Diagnosis results

S	Ao	No	result
S1	1 0 0	0.9815 0 0	Nf
S2	0 1 0	0 0.9736 0	Gc
S3	0 0 1	0.0286 0.0268 1	Bt

From Table 3, it can be seen that, the first set of data errors are 0.0185, 0, and 0, respectively, the second sets of data errors are 0, 0.0264, and 0, respectively, and the second sets of data errors are -0.0286, -0.0268, and 1, respectively. It shows that the error between the actual output and the network output is relatively small, and the diagnosis result is consistent with the gear fault, indicating that the diagnosis result is correct.

The fault diagnosis time of the proposed method is compared with that of the literature [5] method and the literature [6] method. The comparison results are shown in Fig. 5, Fig. 6, and Fig. 7.

From Fig. 5, Fig. 6, and Fig. 7, it can be seen that, when the number of samples is 9, the fault diagnosis time of the proposed method is 3s, the literature [5] method is 10s, and the literature [6] method is 8s. The fault diagnosis time of the proposed method is the least, which shows that the proposed method can effectively shorten the fault diagnosis time.

Table 4. Fault diagnosis accuracy rate of different methods

Method	Accuracy rate of fault diagnosis (%)					
	Normal state	Tooth root crack of intermediate shaft	Ulnar wear of intermediate shaft	Root wear of output shaft	Ulnar wear of output shaft	Accuracy rate of diagnosis (%)
The proposed method	100	98.0	95.0	90.0	95	95.6
The literature [5] method	98.0	90.0	90.0	80.0	75.0	86.6
The literature [6] method	99.0	85.0	81.0	79.0	65.0	81.8
The literature [7] method	99.0	80.0	75.0	70.0	68.0	78.4

In order to further verify the fault diagnosis performance of the proposed method, the fault recognition rate of the proposed method, the literature [5] method, the literature [6] method, and the literature [7] method is compared. In the case of different faults, the comparison results of fault recognition rate of different methods are shown in Table 4.

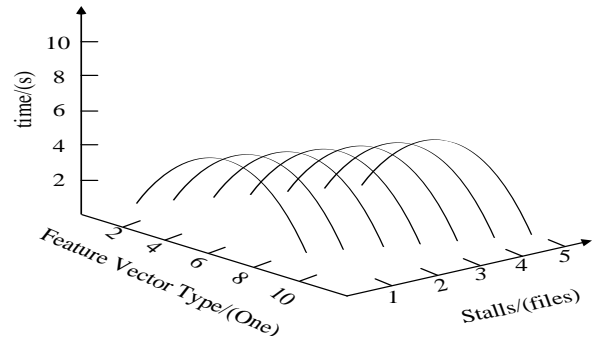


Figure 5. The fault diagnosis time of the proposed method

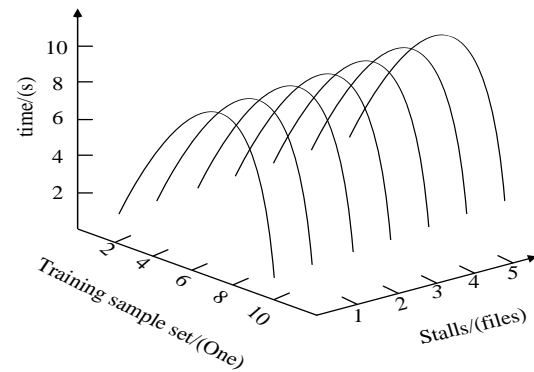


Figure 6. The fault diagnosis time of the literature [5] method

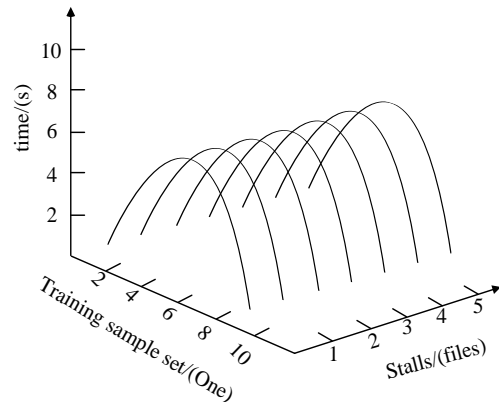


Figure 7. The fault diagnosis time of the literature [6] method

From Table 4, it can be seen that, when the different faults of transmission gear occur, the fault recognition rates of different methods are different. When the tooth root crack of intermediate shaft of the transmission is cracked, the fault diagnosis accuracy of the proposed method is 98%, the literature [5] method is 90%, the literature [6] method is 85%, and the fault literature [7] method is 80%. The fault recognition rate of literature [7] method is the lowest. The diagnostic accuracy of the proposed method is 95.6%, the literature [5] method is 86.6%, the literature [6] method is 81.8%, and the literature [7] method is 78.4%. The diagnosis accuracy of the proposed method is obviously better than other methods. The improved particle swarm algorithm significantly improves the fault diagnosis performance of the proposed method.

4. Conclusions

In the process of driving, the gears, shafts and bearings in the gearbox often fail because of the frequent shifting. According to the relevant statistics, among all the automobile faults, about 60% of the automobile transmission faults are caused by gear failure. At present, the fault diagnosis method of automobile transmission gear has the problems of long diagnosis time and low recognition rate. In order to solve these problems, a fault diagnosis method based on improved particle swarm optimization algorithm is proposed. The speed information of gear fault vibration signal is extracted, which is used for uniform angle resampling of gear fault vibration signal and converted into angle domain signal. The cyclic stationary demodulation of the diagonal domain signal is analyzed, and the fault characteristics of the cyclic autocorrelation function are demodulated by slice. Based on the slice demodulation spectrum of each slice signal, the composite fault diagnosis of gearbox is realized. In every iteration of particle swarm optimization algorithm, CGA acceleration operator is introduced to optimize the fault diagnosis results and realize the fault diagnosis of automobile transmission gears. The simulation results show that compared with the traditional method, this method has higher fault diagnosis efficiency and shorter fault diagnosis time. This method provides a new idea for the further development of fault diagnosis technology of automobile transmission gears, improves the accuracy of fault identification, reduces the time of fault diagnosis, and ensures the driving safety.

The fault detection and diagnosis technology of automobile transmission gear usually completes the diagnosis under a single condition, which has good effect. However, in practice, due to the relatively cumbersome mechanical mechanism and the interference of other elements, many diagnosis technologies are difficult to fully use. In the future work, for the fault diagnosis of different specifications of gears, we should continue to try to improve the accuracy of fault diagnosis of automobile transmission gears.

References

- [1] F. Cheng, Y. Peng, L. Qu, et al. Current-based fault detection and identification for wind turbine drivetrain gearboxes. Estimation Method for TDCS in Low SNR Conditions. *Computer Simulation*. 53 (2017) 878 887.
- [2] Singh. A, Parey. A. Gearbox fault diagnosis under fluctuating load conditions with independent angular re-sampling technique, continuous wavelet transform and multilayer perceptron neural network. *Iet Science Measurement & Technology*. 11 (2017) 220 225.
- [3] M. Zhao, M. Kang, B. Tang, et al. Deep residual networks with dynamically weighted wavelet coefficients for fault diagnosis of planetary gearboxes. *IEEE Transactions on Industrial Electronics*. 65 (2018) 4290 4300.
- [4] J. M. Ha, J. Park, K. Na, et al. Toothwise fault identification for a planetary gearbox based on a health data map. *IEEE Transactions on Industrial Electronics*. 65 (2018) 5903 5912.
- [5] B. Q. Li, J. S. Cheng, Z. T. Wu, et al. Gear fault diagnosis method based on the adaptive and sparsest time-frequency analysis method and partial mean multi-scale fuzzy entropy. *Journal of Vibration Engineering*. 29 (2016) 928 935.
- [6] J. G. Wang, Y. Z. Yang, B. Qin, et al. Gear fault diagnosis research based on kurtosis and IMF energy feature fusion and least squares support vector machine. *China Measurement & Testing Technology*. 42 (2016) 93 97.
- [7] Y. G. Xu, G. L. Zhao, C. Y. Ma, et al. Denoising method based on dual-tree complex wavelet transform and MCA and its application in gear fault diagnosis. *Journal of Aerospace Power*. 31 (2016) 219 226.
- [8] J. M. Li, J. F. Zhang, Y. Z. Zhang, et al. Fault diagnosis of gears based on adaptive stochastic resonance and sparse code shrinkage algorithm. *China Mechanical Engineering*. 27 (2016) 1796 1801.
- [9] H. Malik, R. Sharma. Transmission line fault classification using modified fuzzy q learning. *IET Generation Transmission & Distribution*. 11(2017) 4041 4050.
- [10] J. M. Johnson, A. Yadav. Complete protection scheme for fault detection, classification and location estimation in hvdc transmission lines using support vector machines. *IET Science Measurement & Technology*. 11 (2017) 279 287.
- [11] S. Asgharigovar, H. Seyedi. Adaptive cwt-based transmission line differential protection scheme considering cross-country faults and ct saturation. *IET Generation Transmission & Distribution*. 10 (2017) 2035 2041.
- [12] Y. Lei, F. Jia, J. Lin, et al. An intelligent fault diagnosis method using unsupervised feature learning towards mechanical big data. *IEEE Transactions on Industrial Electronics*. 2016 (2016) 3137 3147.
- [13] Z. Zhe, C. Yang, C. Wen, et al. Analysis of PCA-based reconstruction method for fault diagnosis. *Industrial & Engineering Chemistry Research*. 55(2016) 7402 7410.
- [14] F. Wu, J. Zhao. A real-time multiple open-circuit fault diagnosis method in voltage-source-inverter fed vector controlled drives. *IEEE Transactions on Power Electronics*. 31(2016) 1425 1437.
- [15] Y. L. Wang, Q. Luo, H. Y. Ji. Research on fault diagnosis algorithm for vibration signals of electromechanical equipment. *Computer Simulation*. 34 (2017) 414M419



الجامعة الهاشمية



المملكة الأردنية الهاشمية

المجلة الأردنية
للمهندسة الميكانيكية والصناعية

JJIMIE

مجلة علمية عالمية محكمة
تصدر بدعم من صندوق البحث العلمي

<http://jjmie.hu.edu.jo/>

ISSN 1995-6665

المجلة الأردنية للهندسة الميكانيكية والصناعية

المجلة الأردنية للهندسة الميكانيكية والصناعية: مجلة علمية عالمية محكمة تصدر عن الجامعة الهاشمية بالتعاون مع صندوق دعم البحث العلمي والابتكار - وزارة التعليم العالي والبحث العلمي في الأردن.

هيئة التحرير

رئيس التحرير

الأستاذ الدكتور محمد سامي الأشهب

مساعد رئيس التحرير

الدكتور احمد المقدادي

الدكتور مهند جريسات

الأعضاء

الأستاذ الدكتور طارق العزب

جامعة البلقاء التطبيقية

الاستاذ الدكتور محمد الوديان

جامعة العلوم والتكنولوجيا الاردنية

الاستاذ الدكتور جمال جابر

جامعة البلقاء التطبيقية

الاستاذ الدكتور محمد تيسير هياجنه

جامعة العلوم والتكنولوجيا الاردنية

الأستاذ الدكتور محمد الطاهات

الجامعة الاردنية

الدكتور علي جوارنه

الجامعة الهاشمية

فريق الدعم

المحرر اللغوي

الدكتور بكر محمد بني خير

تنفيذ وإخراج

م . علي أبو سليمة

ترسل البحوث إلى العنوان التالي

رئيس تحرير المجلة الأردنية للهندسة الميكانيكية والصناعية

الجامعة الهاشمية

كلية الهندسة

قسم الهندسة الميكانيكية

الزرقاء - الأردن

هاتف : 00962 5 3903333 فرعي 4147

Email: jjmie@hu.edu.jo

Website: www.jjmie.hu.edu.jo